Random collagen-like biomimetic nanostructures: Fabrication, characterization and application for biosensors

Dissertation

zur Erlangung des Grades

des Doktors der Naturwissenschaften

der Medizinischen Fakultät

der Universität des Saarlandes

Homburg (Saar) 2024

vorgelegt von

Bharat nath Nowduri

geb. am 26.11.1990 in Abu Dhabi, Vereinigte Arabische Emirate

Tag der Promotion : 31.07.2024

Dekan : Prof. Dr. M.D. Menger

Berichterstatter : Prof. M. Hoth

Prof. H. Madry

Prof. A. Offenhäusser

Abstract

Functionalization of biosensor surfaces with nanostructures is a well-established approach to promote biological entities to adhere, grow and proliferate. The natural adhesion surface of cells is composed of extracellular matrix biomolecules and the organization of the bio-nanostructures is completely random. Therefore, this study focuses on fabrication of randomly organized nanostructures inspired from the dimensions and orientation of natural collagen fibers with nanoimprint lithography. The biomimetic nanostructures subsequently grown by electroplating the nanoimprinted surfaces replicate the topographical randomness of the natural collagen fibers in lateral dimension and organization, but not axial dimension. The nanostructures significantly influence the surface properties by amplifying free surface energy by 33 % and reduction in impedance magnitude by 54 % for frequencies below 1 kHz. The surface modifications open nanostructuring opportunities for biosensor application such as in-vitro microelectrodes used for electrophysiological studies. The biomimetic nanostructured microelectrodes show reduction in impedance magnitude at 1 kHz by 41 % for densely-packed nanostructures. Electrophysiological experiments with mice enteric neurons show a 3-fold amplification in seal impedance and an increase of 35 % in extracellular signal-to-noise ratio. Finally, cell biological experiments show 270 % increase in neuronal growth and up to 50 % increase in focal adhesion coverage induced by the nanostructures.

Zusammenfassung

Die Funktionalisierung der Oberflächen von Biosensoren mit Nanostrukturen ist ein etablierter Ansatz, um die Haftung, das Wachstum und die Vermehrung biologischer Komponenten zu fördern. Die natürliche Adhäsionsfläche von Zellen besteht aus Biomolekülen der extrazellulären Matrix, wobei die Organisation der biologischen Nanostrukturen völlig zufällig ist. Daher konzentriert sich diese Arbeit auf die Herstellung von zufällig organisierten Nanostrukturen, die von den Abmessungen und der Ausrichtung natürlicher Kollagenfasern inspiriert sind und mit Nanoimprintlithografie (NIL) hergestellt werden. Die biomimetischen Nanostrukturen, die durch Galvanisierung der zuvor mittels NIL-geprägten Oberflächen aufgewachsen werden, replizieren die topografische Zufälligkeit der Kollagenfasern in Bezug auf die laterale Dimension und Organisation, jedoch nicht die axiale Dimension. Die Nanostrukturen beeinflussen die Oberflächeneigenschaften erheblich, indem sie die freie Oberflächenenergie um 33 % erhöhen und die Impedanz bei Frequenzen unter 1 kHz um 54 % verringern. Die Oberflächenmodifikationen eröffnen Nanostrukturierungsmöglichkeiten für Biosensoranwendungen wie in-vitro Mikroelektroden, die für elektrophysiologische Studien verwendet werden. Die biomimetisch nanostrukturierten Mikroelektroden zeigen eine Verringerung der Impedanz bei 1 kHz um 41 % für dicht gepackte Nanostrukturen. Elektrophysiologische Experimente mit Darmneuronen von Mäusen zeigen eine dreifache Verstärkung der Dichtungsimpedanz und einen Anstieg des extrazellulären Signal-Rausch-Verhältnisses um 35 %. Schließlich zeigen zellbiologische Experimente eine Zunahme des neuronalen Wachstums um 270 % und eine Zunahme der fokalen Adhäsionsabdeckung um bis zu 50 %.

Declaration of original authorship

I hereby declare on oath that this dissertation is my own original work except were otherwise indicated. All data or concepts drawn directly or indirectly from other sources have been correctly acknowledged. This dissertation has not been submitted in its present or similar form to any other academic institution either in Germany or abroad for the award of any other degree. I furthermore declare with my signature that I

- did not practice any sorts of "plagiarism"-activities listed in the information sheet "Avoiding plagiarism" of the Faculty of Natural Sciences and Technology,
- documented all methods, data and work processes truthfully and
- did not manipulate any data.

Zweibrucken, Bharat nath Nowduri

place, date Signature

Table of contents

1. Introduction

History of electronic biosensors in medicine can be dated to 1962 when American scientist Leland Clark developed the first blood glucose sensor based on the application of Clark-type oxygen electrode [1]. Consequently, biosensors as a research field grew in prominence aided by emerging technologies. Electronic biosensors can be broadly classified based on their sensing mechanisms namely, physical (e.g. thermometer) [2-3], biochemical (e.g. enzyme-based sensors) [4-5], optical (e.g. SpO_2 sensors) [6-7], electrophysiological (e.g. microelectrode arrays) [8], etc. Among these examples, electrophysiological sensors were of particular interest to researchers as they were exclusively used for sensing electrogenic activity in cells such as neurons and cardiomyocytes. In most of these applications, both in vivo and in vitro environment, the cells are in direct contact with the conductive surface of the sensor. Therefore, an optimized interface between the cells and the electrode surface was essential for enhanced sensor signal transmission. Micro- and nanostructuring of the sensor surface has been a well-established technique to enhance the cell interface, as it mimics the natural rough environment of cell adhesion [9-10]. 'Biological' nanostructuring of the conductive surfaces was performed using coating techniques based on biomolecules such as laminin, collagen and other extracellular matrix (ECM) proteins [11-13]. These coating methods were standardized, easy-to-use and proved to be effective in improving coupling of cells to the surface [11-13]. But over an extended period of culture duration, the biomolecules were confronted with a major risk of detachment in extreme conditions, such as pH and temperature [14-15]. The engineering solution to this problem was the replacement of natural nanostructures with synthetic durable nanostructures fabricated by microsystems technologies.

Depending upon the electrode material and application of biosensor, there are several fabrication methodologies to develop different types of nanostructures. With current state-of-the-art fabrication technologies, nanostructures with spatial resolution smaller than 100 nm have been developed for biosensor functionalization [16-18]. For example, conducting polymer nanostructures were chemically deposited on silicon-based FET biosensors for enhanced signal sensitivity [19]. In another example, 'ice-like' dendritic gold nanostructures deposited by electroless plating on a gold electrode were used for functionalization of DNA sensor for Enterococcus faecalis detection [20]. With limitless opportunities in methods and materials to structure the sensor surface, it is essential to examine the natural adhesion surface of cells and understand the cellular preference in their native environment.

For instance, cellular components in vertebrae body sit on a cushion of supporting film called basement membrane. The basement membrane is composed of a complex organization of ECM biomolecules such as integrins, laminin, proteoglycans, fibrillin and collagen fibrils. These components give the overlying cells mechanical stability and a platform to grow, adhere and migrate. Examination of the basement membrane surface profile with AFM measurements reveals

several nanotopographical features such as pores, ridges, wells, tubes, and pillars [21]. The dimensions of these features vary from ten to a several hundred nanometers and more importantly there exists no symmetry in the orientation of the nanostructures [22]. On the contrary to the natural adhesion surface, current structuring methods are designed to develop symmetric and organized nanostructures with defined structure dimensions and periodicity. Therefore, this study explores opportunities to fabricate synthetic nanostructures with random structural dimensions and asymmetric organization.

Randomness in nanostructuring can be interpreted in terms of anisotropy in dimensions (axial and lateral) and organization of the structures. For instance, nanostructures represent a one-dimensional randomness when asymmetry exists in either lateral dimension or axial dimension, two-dimensional randomness when asymmetry exists in both lateral, as well as, axial dimension and three-dimensional randomness when asymmetry also exists in the spatial organization. For instance, the natural adhesion surface of the basement membrane can be interpreted to represent a three-dimensional randomness pattern [21-22]. Mimicking the natural adhesion surface by nanostructuring methods has been previously performed to an extent by preparing nanorough surfaces and nanoporous surfaces by chemical etching methods [23]. But such surfaces do not completely represent a true biomimetic surface, as presence of general roughness is not the only characteristic of a natural adhesion surface. A more suitable approach to fabricate biomimetic nanostructures would be to mimic the exact dimensions and organization of the biomolecular nanofeatures.

Collagen is dimensionally the biggest biomolecule present in the extracellular matrix composite and it has the largest presence in comparison to other biomolecules such as fibronectin, laminin, etc. [24]. Existence of collagen in mammalian systems can be briefly classified to different types based on the amino acid chain organization (type I, type II etc.) and their structural hierarchy ranging from individual fibrils to large bundles of composite fascicles [25]. Collagen fibers are characterized by their exceptional mechanical strength [26] and thermal stability [27]. These properties allow collagen molecules to be used in mechanoforming processes such as polymer hot embossing and electrospinning [28]. Using soft lithography methods, the collagen fibers have been successfully mimicked onto polymers such as polydimethylsiloxane [28-29]. But most biosensor surfaces are developed with conductive materials (such as metals and semiconductors). Therefore, conventional lithography methods would have to be combined with mechanoforming methods such as nanoimprint lithography to replicate collagen fibers to metallic biomimetic nanostructures.

Nanoimprint lithography (NIL) is a novel nanostructure fabrication method based on mechanical deformation of a UV curable or thermoplastic polymer with exceptional structure resolution [30-31]. The two main components of NIL are a mechanical template containing the micro- and nanopattern and a nanoimprintable polymer cured by the apparatus (UV or temperature). The

nanostructure pattern on the mechanical template is compressed on the imprint polymer and the molded polymer is used to grow nanostructures by chemical deposition [32], physical deposition [33] or electrodeposition methods [34]. Nanostructured surfaces fabricated by NIL have been previously used for several biosensor applications such as biofuel cells [35], axon guiding platforms [36] etc. Conventional NIL templates are fabricated by high resolution e-beam lithography and Gaussian beam pattern generators [37]. Interestingly, the collagen molecules are mechanically strong and thermally stable and hence they could be used as a master stamp in NIL. Subsequently by nanostructure growth, nanostructures mimicking the structural dimension and organization of natural collagen fibers can be fabricated on metal biosensor surfaces.

Microelectrode arrays (MEAs) are microscaled electrophysiological biosensors used to communicate with electrogenic cells such as neurons and cardiomyocytes. They can be used in vitro and in vivo environment for extracellular activity recording and for electrical stimulation purposes. MEAs possess a unique advantage of recording the extracellular activity of the neuronal tissue without puncturing the cell membrane (as done in patch clamp measurements) and hence integrity of the cell cytoplasm is maintained. Moreover, MEAs can be used to measure extracellular activity from several locations of a larger tissue for longer periods of time with excellent spatiotemporal resolution. Active surface area of a microelectrode is a critical parameter in determining its efficiency in signal transmission. From ohmic relations, it is known that larger area results in smaller surface impedance of the electrode [38]. But at the same time, the widened microelectrodes compromise the density of electrodes in an array, which in turn results in loss of spatial resolution of recording. An effective method to increase the active surface area of the microelectrode without changing its dimensions is the introduction of conductive nanostructures on the electrode surface [39]. Enhanced effective surface area of the metal electrode can be electrochemically correlated to enlarged surface capacitance and reduced surface resistance, which could result in improving the signal-to-noise ratio for electrophysiological recordings [40]. Nanostructuring of MEAs for improved signal transmission properties has been popular over the past few decades, where researchers have structured electrode surfaces with a large variety of materials such as metals, polymers, ceramics etc. For example, nanoimprint lithography and gold electroplating has been used for fabrication of gold nanostructures with different shapes such as tubes, pillars, mushrooms on microelectrode surfaces, which resulted not only in significant reduction in impedance, but also tighter adhesion of cells to the electrode surface [41]. A stronger adhesion results in a smaller gap between the electrode and the cell, which in turn results in reduced ohmic loss of electrical information [42].

Although there have been several examples illustrating the benefits of nanostructures for improved electrophysiological performance of microelectrodes, there has been very limited research revealing the mechanics of the enhancement in cell-nanostructure interaction. Neurons, like most eukaryotic cells, consist of a cell body with nucleus and several organelles enclosed by

the cell membrane. Cell membrane proteins form a complex micromechanical framework which senses and reacts to external stimuli such as surface topography [43]. When in contact with nanostructures (natural or synthetic), the cell body and cell membrane adapt their interaction by biochemical signaling, which in turn results in modified cell adhesion [44]. Tighter adhesion of neurons to the culture surface has been previously investigated by monitoring the development of focal adhesion complexes (FACs). Formation and maturation of FACs range can widely differ depending on the depth, width, pitch and isotropy of nanostructures [45]. With fluorescence microscopy it is possible to map the development of the FACs and subsequently correlate the cell adhesion to nanostructures. Such a study in collaboration with high resolution electron microscopy will be extremely useful in understanding the biomechanical interaction of cells with the nanostructures [46], which in turn would greatly contribute in improving the efficiency of nanostructure development for electronic biosensors.

The objective of this thesis is to explore opportunities to fabricate randomly organized biomimetic nanostructures on the surface of biosensors and later to apply the same to surface of microelectrode arrays used for electrophysiological applications. Another important aspect of this thesis is to investigate the biomechanical interaction of cells with the biomimetic nanostructures. In Chapter 2, essential theoretical knowledge useful for understanding the motivation, experiments, results and discussion sections of this thesis is explained. In Chapter 3, experimental methods used in this study for the fabrication and characterization of random nanostructures and their subsequent application on microelectrode surfaces are presented. In Chapter 4, development of randomness pattern derived from natural collagen fiber network is described, which then is used to fabricate the random nanostructures with gold electroplating. In Chapter 5, application of the biomimetic nanostructuring process on microelectrode surfaces is described. Apart from fabrication of the nanostructured microelectrodes, improvements in the impedance properties and adhesion of cells are also illustrated. Finally, results from electrophysiological experiments with enteric neuronal culture are presented. In Chapter 6, the interaction of cells with the biomimetic nanostructures is investigated with fluorescence microscopy. Firstly, neuron-glial cell growth assay is illustrated on the nanostructured surfaces. Then a comprehensive analysis on growth and maturation of FACs for the cells on the biomimetic nanostructures is presented. Finally in Chapter 7, discussions which could be implemented for further improvements in the nanostructuring and future applications in biomedical engineering and tissue engineering are illustrated.

2. Theoretical background

In this chapter, essential theoretical knowledge to understand the fabrication, characterization and subsequent application of the biomimetic nanostructured surfaces has been presented. Firstly, a brief introduction to neuronal anatomy and electrophysiology of has been presented. Then, the principles of cell-surface interactions to the nanostructures have been described. Afterwards, working principle of the nanoimprint lithography used for nanostructure fabrication has been described. Finally, a brief explanation of physicochemical and biological characterization methods has been presented.

2.1. Anatomy and electrophysiology of neurons

2.1.1. Neuron: Structural unit of nervous system

Neurons are the fundamental excitatory cells of the brain and nervous system responsible for communicating information with the external world. Nervous system exists as primitive cerebral ganglion in early eukaryotes like Coelenterates, to highly complex brain and spinal cord systems with several billion neurons in evolved mammals such as humans. Neurons ideally are composed of three main components: a cell body or soma, an axon and several dendrites (**Figure** 2.1). Soma contains central nuclei, typical cell organelles and granular bodies called Nissl's granules which help in internal regulation of neuron protein synthesis. Axon is a singular long extension that protrudes from the cell body which directs the transmission of information in to the neuron. Dendrites are several branches of short fibers which protrude out of the cell body that transmit information out of the neuron. The distal end of the axon is terminated to several branches called synaptic knobs which consists of synaptic vesicles containing essential neurotransmitters. Depending upon the number of axons and dendrites, the neurons can be briefly classified as apolar (without dendrites or axons), unipolar (one axon and no dendrite), bipolar (one axon and one dendrite) or multipolar (one axon and two or more dendrites). Apart from neurons, non-excitatory cells such as glial cells exists in the nervous system, which support neuronal growth and are responsible for several functions such as insulating axons with myelin sheath (made of oligodendrocytes or Schwann cells). Other glial cells such as astrocytes and satellite cells share the function of supporting and protecting neurons.

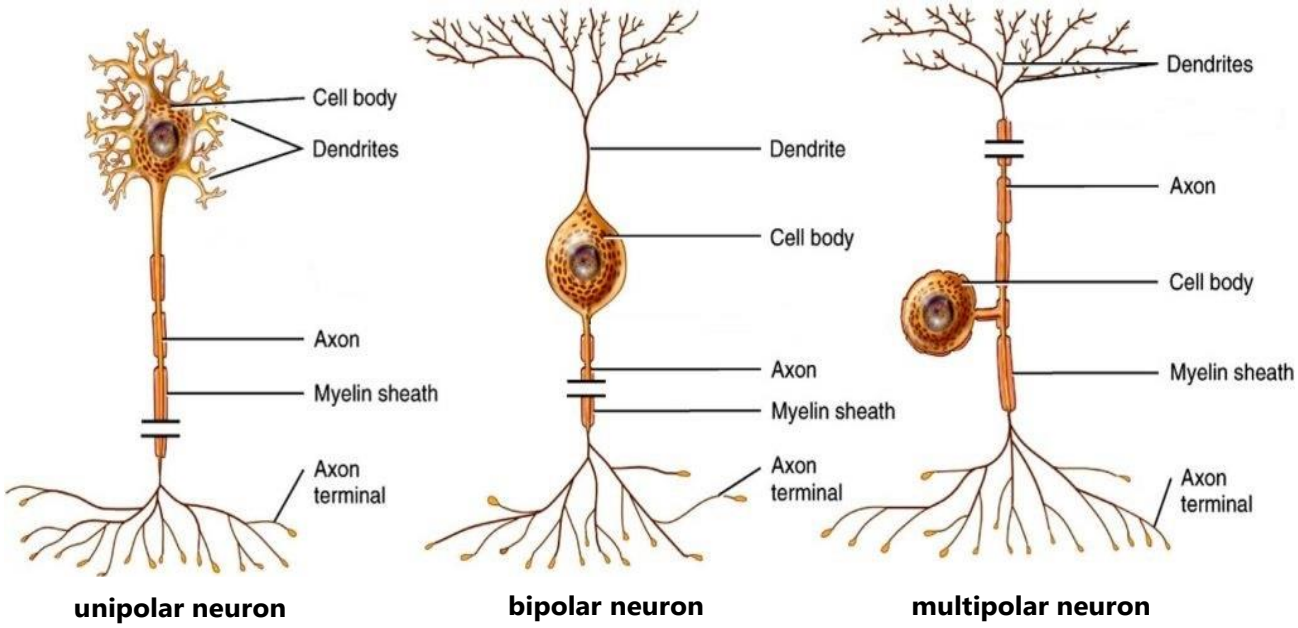

Figure 2.1. Illustration of neuronal classification based on anatomy (adapted from [47]).

2.1.2. Functional classification of mammalian nervous system

Nervous system in mammals can be broadly classified to central and peripheral nervous system based on its function (**Figure** 2.2). Central nervous system (CNS) consists of the brain and spinal cord, which acts as the central processing unit of the coordination and control. Peripheral nervous system (PNS) is a collective of all the neurons in the organism excluding the central nervous system. The main function of PNS is to transmit information from CNS to the rest of the body. PNS consists of cranial nerves (nerve segments emerging from brain), spinal nerves (nerve segments emerging from spinal cord), visceral nerves (segments emerging to and from viscera) and ganglia clusters. PNS can be further classified based on its function to somatic nervous system and autonomic nervous system. Somatic nervous system comprises of sensory and motor fibers from the skin, skeletal muscles and joints. Autonomic nervous system coordinates involuntary motor control of organs and body functions. Autonomic nervous system can be classified to sympathetic system (adjusts our bodies for situations of increased physical activity), parasympathetic nervous system (adjusts our bodies for energy conservation activities) and enteric nervous system (that regulate the activity of the gastrointestinal tract). Enteric nervous system is composed of both parasympathetic fibers and sympathetic fibers which form two plexuses within the wall of the intestine: submucosal plexus (found in the submucosa of the intestines) and myenteric-plexus (found in the muscularis externa). Neurons from mammalian myenteric plexus have been used in this study for the electrophysiological application of biomimetic nanostructures.

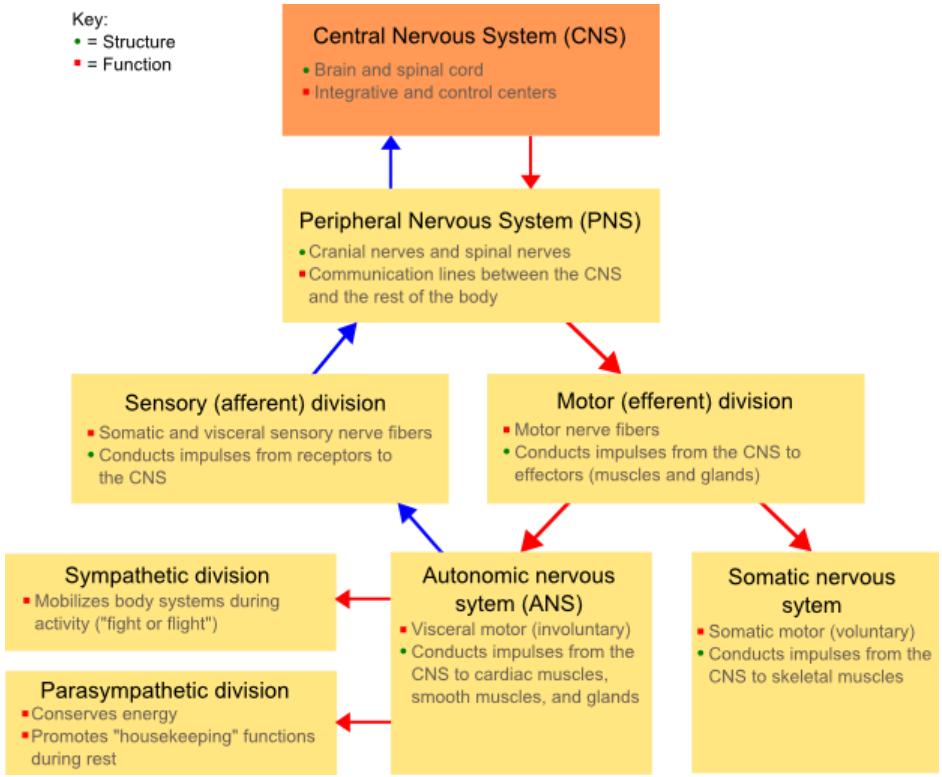

Figure 2.2. Functional classification of mammalian nervous system (adapted from [48]).

2.1.3. Generation and conduction of action potential

Cell membrane in neurons is composed of a lipid bilayer with several membrane proteins embedded on its surface. The membrane acts as an electrical insulator between ionic charge concentrations present inside and outside the cell cytoplasm. Also present on the cell membrane are selectively permeable ion-channels. When the neuron is not conducting an impulse, it exists in a resting state and the membrane is permeable to K^+ ions and impermeable to Na^+ ions, as well as, negatively charged proteins present in the cytoplasm. At the same time the fluid outside has an excess of Na^+ ions, thus forming an ion concentration gradient at the membrane. To maintain this concentration gradient, a sodium-potassium pump present on the membrane transports three Na^+ ions outwards for two K^+ ions into the cell [49]. This results in the outside surface of the membrane being positively charged and the inside surface negatively charged. The electrical potential difference existing due to this ion concentration gradient during the resting stage is called resting membrane potential. When the neuron is stimulated by an external source (e.g., neurotransmitters), the membrane at the stimulation site becomes permeable to Na^+ ions, which leads to large influx of positively charged Na^+ ions into the cytoplasm. This leads to depolarization in the ionic concentrations of the membrane. The change in electrical potential difference due to the concentration gradient depolarization is known as the action potential, which in fact is the conducting nerve impulse (**Figure** 2.3a). At the site next to the point of action potential generation, the membrane still exists in resting state. Therefore, the current flows to the neighboring site from a positive to negative gradient on outside and vice versa in opposite direction on the inside, thus completing the electrical flow of circuit. This current flow at the membrane travels across the length of the neuron, which is the mechanism of nerve impulse conduction. The change in membrane potential is short-lived, as the permeability and direction of ion flow immediately reverses causing the initial site at the membrane to repolarize back to resting potential and available for further stimulation.

Conduction of impulses between neurons takes place with fluid-filled cell membrane junctions known as synapse. The gap between the neurons is known as a synaptic cleft and the conduction takes place by electrical or chemical means (**Figure** 2.3b). When the synaptic cleft is very small, the impulse electrically jumps from one neuron to another, hence triggering the post synaptic neuron. When the synaptic cleft is larger, signaling molecules known as neurotransmitters are released from the pre-synaptic neuron into the synaptic cleft, which is received by the post synaptic neuron by its specific receptors. The binding of the neurotransmitters on the receptors triggers the change in the ion channel concentration and leads to the conduction of nerve impulse. Inhibitory neurotransmitter result in increase in membrane potential, whereas excitatory neurotransmitter cause depolarization. Dopamine and serotonin are examples of inhibitory neurotransmitters, whereas epinephrine and norepinephrine are examples of excitatory neurotransmitters.

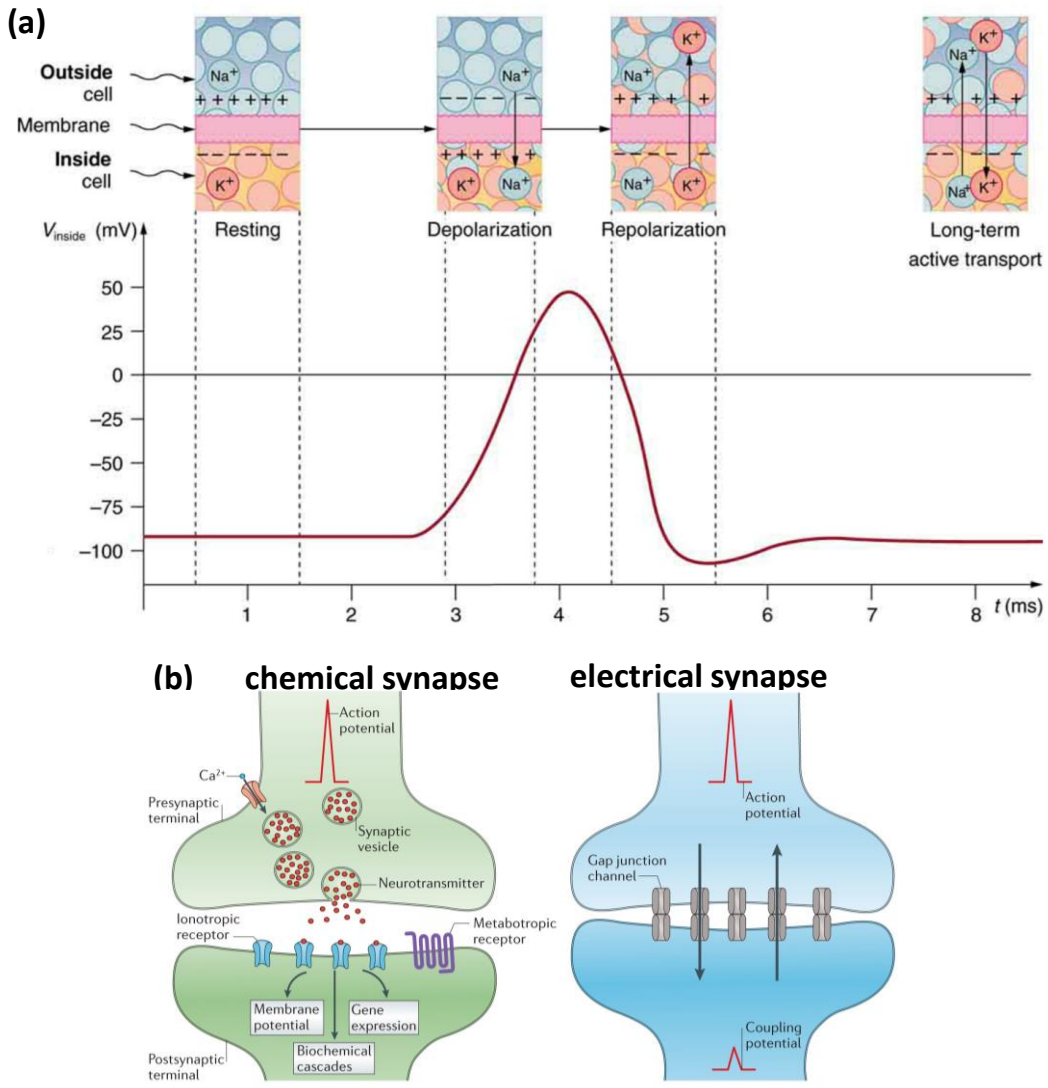

Figure 2.3. (a) Transmission of action potential across the neuronal membrane (adapted from [49]). (b) Chemical and electrical synapse for neuronal impulse conduction (adapted from [50]).

2.1.4. Action potential measurement from neurons

Extracellular and intracellular activity transmitted in the neurons, such as action potentials, single-unit recordings, bursts, postsynaptic potentials etc., can be recorded with excellent temporal resolution of a single neuron (both in vitro and in vivo environments) with state-of-the-art microsystems technologies [51-55].

2.1.4.1. Intracellular action potential measurement: Patch clamp apparatus

The first intracellular measurement of neural activity was performed by German scientists Bert Sakmann and Erwin Neher in 1975, when they developed the first patch clamp apparatus to measure single channel currents across a membrane path of a frog skeletal muscle, for which they were awarded the Nobel prize in physiology and medicine in 1991 [56]. A single ion channel

conducts around 10 million ions per second which accounts to a current of just a few picoamperes. A thin glass or quartz pipette with a blunt end is sealed onto the membrane with a suction applied to create a high resistance seal in giga-ohm range (**Figure** 2.4a) [57-58]. This suction allows the ions to flow through the glass pipette, where a saline immersed silver electrode measures the ion current, which is then amplified and recorded.

Depending upon the mode of seal formation, patch clamp methods can be used in different configurations (**Figure** 2.4b) [59]. In cell-attached mode, the membrane patch is left intact and the electrode is loosely attached on to it. In whole-cell mode, the membrane is disrupted by application a large suction in the glass pipette. By doing so the electrode interface becomes a part of the interior of the cytoplasm. It is also possible to record current just from a small patch instead of the complete cell which helps in isolated activity measurements of single channel. This can be achieved either in inside-out mode [60], where a patch of the membrane is separated from cell and measured. Or outside-out mode [59], where the pipette is set up in whole-cell configuration and then retracted, causing a rupture and rearrangement of the membrane in the extracellular domain. Despite its popular application in intracellular activity measurement, patch clamp method cannot be adapted for long-term neural network studies, as rupture of cell membrane by the patch electrode leads to cell deformation and ultimately cell death [61].

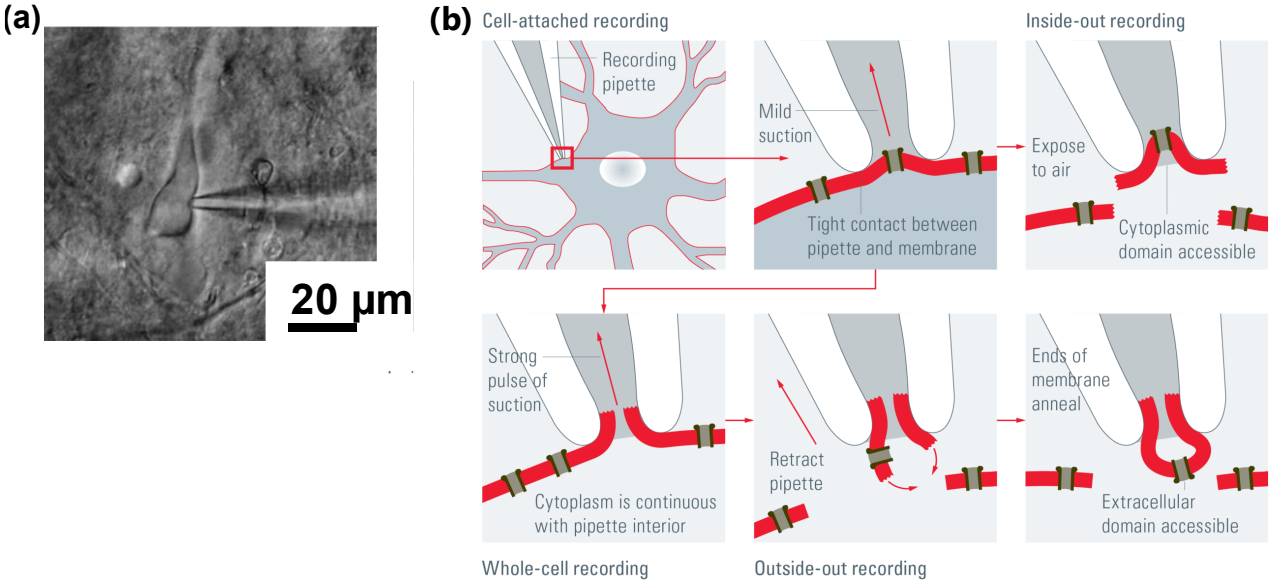

Figure 2.4. (a) Microscopy image of the patch clamp suction tube into neuronal cell body (adapted from [58]). (b) Illustration of different modes of patch clamp for intracellular activity measurements (adapted from [59]).

2.1.4.2. Extracellular action potential measurement

Measurement of electrical activity in neurons can be performed without disturbing the cell membrane with extracellular recording methods. Although the amplitude of action potential signals is significantly smaller than intracellular measurements, these methods are extremely versatile and electrical activity from several neurons can be measured simultaneously for longer periods. The most common method of extracellular measurements is performed by microelectrode arrays, although other devices such as field-effect transistors and cuff electrodes are also popular in application [62-63].

2.1.4.3. Microelectrode arrays (MEAs): Design and fabrication

MEAs are 2D planar electrode arrays used to measure extracellular activity in neuronal culture. Dimensions of the microelectrode range between few hundred nanometers to several microns [64-65]. The surface area of the 2D array and microelectrode density determine the spatial resolution of the extracellular activity measurements. The basic design of a MEA consists of a cell culture chamber with a planar culture surface embedded with an array of microelectrodes (**Figure** 2.5).

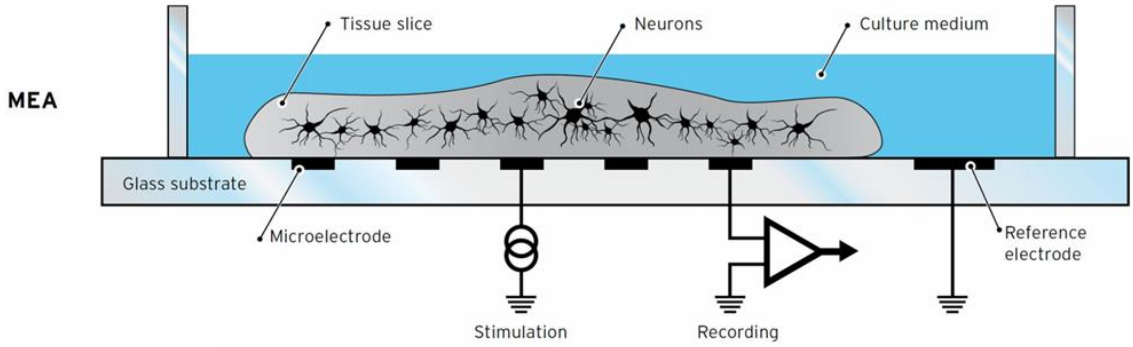

Figure 2.5. Schematic illustration of neuronal culture seeded on the surface of a microelectrode array (adapted from [66]).

The microelectrodes are connected on the exterior to a signal acquisition system with amplifiers, filters and signal processing units. The planar electrodes are isolated with a layer of biocompatible dielectric material such as chemical vapor deposited silicon oxide-silicon nitride thin films, parylene C, polyimide, SU-8 polymer etc. The first reported MEA was developed in the year 1972, where American Scientist P. A. Springer fabricated 30 electrodes disposed on two lines 50 μm apart to successfully measure extracellular activity in cardiomyocytes of chick embryo [67]. Choice of materials for substrate, electrodes, connection tracks and passivation dielectric is diverse depending upon the application of the MEAs. For in vitro applications, rigid substrates such as glass and quartz are used, whereas flexible polymers such as polyimide are used for in vivo applications. Likewise, conductive ceramics such as TiN and ITO are used as electrode material for

high signal-to-noise ratio (**Figure** 2.6a) [68] and for material robustness, microelectrodes are fabricated with noble metals such as gold. With current state-of-the-art technologies, MEAs have been realized up to a density of 16384 electrodes, spread over a surface area of 2 mm^2 (**Figure** 2.6b) [69].

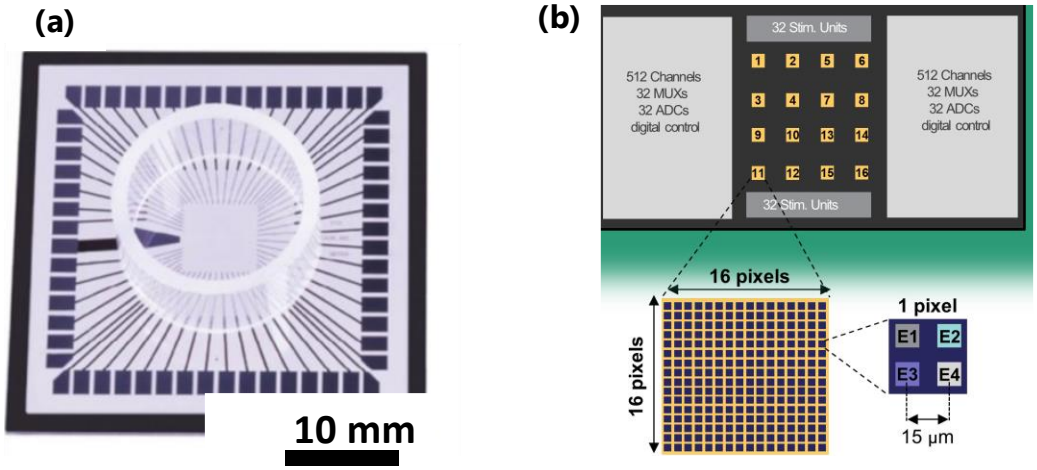

Figure 2.6. (a) Commercial TiN MEAs fabricated by Multichannel Systems GmbH (adapted from [68]). (b) CMOS chip with 16384 microelectrodes and 1024 channels (adapted from [69]).

2.1.4.4. Electrical properties of MEAs

To optimize the signal transmission in microelectrodes, it is essential to understand the electrical properties of its individual components and their overall contribution to the improvement in signal transmission. Such an analysis can be effectively performed by development of an electrical equivalent circuit, where the charge-transfer mechanisms at the electrode can be realized to active and passive electrical components (**Figure** 2.7a). Microelectrodes measure the electrical activity of cells through a fluid culture medium. This can be simulated in the equivalent circuit by a voltage source transmitting an AC signal through a conductive electrolyte medium. The schematic of microelectrode consists of three main parts: electrode surface, the passivation layer surrounding the electrode and the connection tracks. Since the electrode surface and the connection tracks are made of highly conductive materials, the material resistance contributed by them are negligible compared to the large impedances contributed by charge-transfer components.

Charge-transfer at the electrode-electrolyte interface occurs significantly by the presence of an electrical double-layer at polarized electrode surface formed by the hydrated ions present in the electrolyte (**Figure** 2.7b) [70]. The charge-transfer across the double-layer occurs by both reactive and diffusive pathways. Apart from these components, there also exists other parasitic capacitances originating from closely located microelectrodes (such as passivation layer ($C_{passivation}$), etc). But in comparison to charge-transfer and diffusive impedances, the parasitic components do not contribute largely to the global electrode impedance of the microelectrodes. Therefore, a

simplified version of the electrical equivalent circuit described by Randel's model is generally used in literature to characterize the charge-transfer properties of MEAs [71]. The first component of this model is the double-layer capacitance (C_{dl}) formed by the dielectric film of hydrated ions the charged electrode surface [70]. The second component is the charge-transfer resistance (R_{ct}) characterized by chemical reactions and transfer of electrons at the electrode surface. The third component is the complex diffusive impedance, also known as Warburg impedance (W) [72]. Finally, a resistive component contributed by the ionic conductivity of the electrolyte (R_s). From the electrical equivalent circuit and AC small signal analysis, the complex impedance spectrum of the microelectrode can be evaluated. And with further evaluation of the real and imaginary parts of the complex impedance spectrum, impedance magnitude and phase spectra can also be determined.

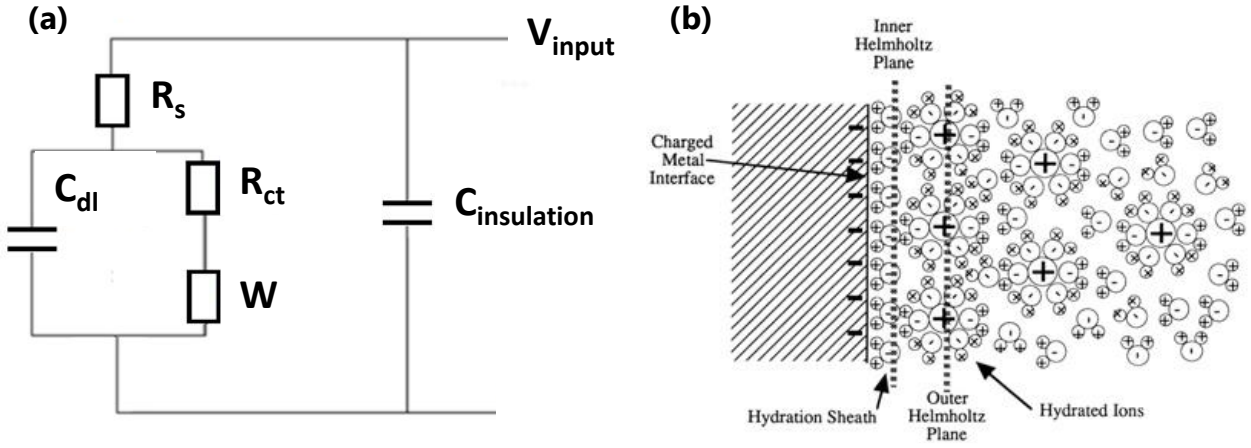

Figure 2.7. Schematic illustration of (a) electrical equivalent circuit and (b) Helmholtz double-layer of the microelectrode interface with a conductive electrolyte (adapted from [70]).

It is known from Ohmic relations that larger surface area reduces the overall impedance of electrode. But by increasing the area of the microelectrode, the density of electrodes is reduced and hence the spatial resolution of measurement is compromised. Considering the size of electrogenic cells in general, Hughes et al described an electrode area of 20 µm × 20 µm to be suitable to meet this trade-of [73]. An effective method to increase the electrode surface area without changing its dimension is the introduction of nanostructures on its surface. Presence of nanostructures reduces the global impedance of microelectrode by enhancing its capacitive properties [74] and reducing the charge-transfer resistance [75]. Effect of nanostructures on microelectrode impedance can be mathematically modelled into the Randel's circuit and the physicochemical mechanisms can further evaluated. Examples of reduction in impedance magnitude spectrum induced by nanostructured surface profile of platinum black and columnar TiN microelectrodes in comparison to platinum smooth microelectrodes can be seen in **Figure** 2.8 [76].

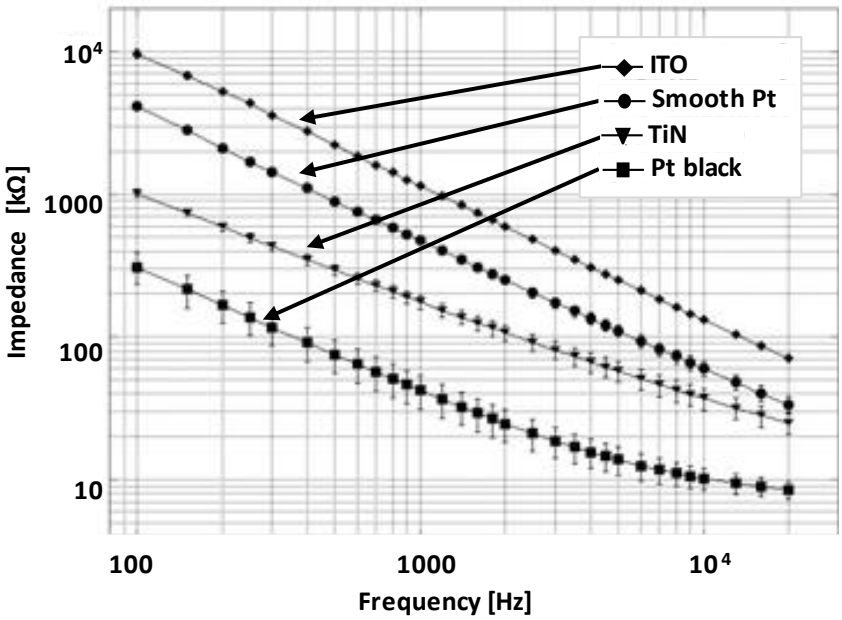

Figure 2.8. Impedance spectroscopy measurements for three different kinds of nanostructured microelectrodes in comparison with unstructured smooth platinum microelectrode (adapted from [76]).

2.2. Cell interaction with nanostructured surfaces

Another important aspect of this study is to understand the interaction and adhesion of cells, especially neurons to artificial nanostructured surfaces. Adhesion of cells to a surface is essential for cell communication and regulation, which is of fundamental importance in the development and maintenance of tissues [77].

2.2.1. Focal adhesion complexes (FACs)

Cell interaction with artificial surfaces can be explained by means of extracellular matrix (ECM) proteins pre-adsorbed on its surface [78]. The transmission of extracellular and extracellular forces between cell and the ECM occurs through localized sites formed by the transmembrane proteins called integrins [79]. The integrins bind to the ECM biomolecules of the surface and activates the Rho GTPase family (including Rho, Rac, and Cdc42), which in combination with other molecular adaptors (such as vinculin, tensin, talin) are bound to the actin cytoskeletal fibers, forming complex biomolecular clusters called focal adhesion complexes (FACs) (**Figure** 2.9) [80]. FACs act as anchors for the cell membrane on the adhesion surfaces, which consequently determines the shape of the nucleus and cell cytoskeleton. FACs transmit tensile and compressive forces by a process called mechanotransduction, which is essential for the cell signaling in migration, proliferation and differentiation for tissue organization, maintenance and repair [77]. In the case of electrogenic cells such as neurons, the improved adhesion additionally modulates the ion channel activity [81].

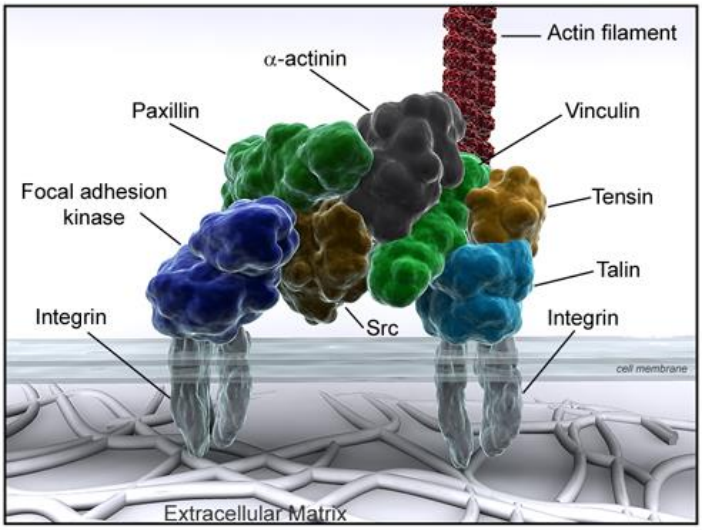

Figure 2.9. Illustration of the focal adhesion complex composition (adapted from [80]).

Cell adhesion on in vitro surfaces takes places as a static process where the cells are planted on artificial adhesion surfaces coated with ECM molecules (e.g., glass slides, petri dish). Static adhesion of cells is characterized by 3 stages (**Figure** 2.10) [77]. The first stage is the electrostatic sedimentation of cells guided by hydrophilicity of the surfaces [78]. The strength of interactions is weak and no cytoskeletal changes occur, letting the cells keep its shape. In the second stage the integrins of the cell membrane bind to the ECM molecules adsorbed on the surface leading to flattening to the cell shape, but not cell spreading [77]. In the final stage the integrins activate the molecular adaptors in the cytoplasm leading to the formation of active FACs with the actin cell cytoskeleton [80]. The cells complete their spreading on the surface and the mechanotransduction of internal forces signal the cell cycle events such as migration, proliferation and differentiation [82]. In the case of neuronal cells these events can further result in formation of robust neuronal networks during differentiation, which would lead to enhanced extra- and intracellular signaling. Presence of nanostructures has shown in literature to affect the cell interaction by modulating the formation and growth of FACs as well as altering the static adhesion cycle [77].

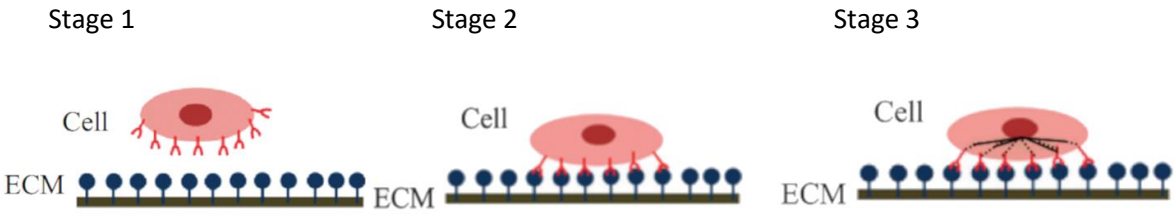

Figure 2.10. Stages of static adhesion of cells on a naturally nanostructured (with extracellular matrix) in vitro surface (adapted from [77]).

2.2.2. Influence of nanostructure shape and orientation on cell interaction

Ability of cells to sense physical cues in nanoscale range and subsequently modify its adhesion behavior has led to immense interest in nanostructured surfaces for biological studies. The topographical features of the nanostructures can be characterized by their axial dimension, lateral dimension and pitch. The nanostructure orientation can be classified to isotropic and anisotropic depending on its topographic features [83]. Isotropic nanostructures have uniform dimensions in all directions, whereas, anisotropic nanostructures follow directionality in their organization (**Figure** 2.11). Studies have shown that several features of cell adhesion (such as FACs, cytoskeletal organization, nuclei shape, etc.) are dependent on the isotropy of the nanostructures [46, 84-86]. For example, the behavior of neuronal shape was largely influenced by the orientation of the polymeric nanostructures on which the embryonic neurons were seeded [86]. In another example, shape of the nanostructures activated membrane proteins and influenced the subsequent cell attachment (**Figure** 2.12a-b). Mushroom shaped nanostructures were used on microelectrode surfaces for enhanced neuronal adhesion and impedance reduction [87]. It was hypothesized that the cells grew around the nanostructures through a phagocytosis like engulfment mechanism (**Figure** 2.12a). After the initial contact to the surface, the actin filaments surrounded the stalk of the nanostructures forming a ring-shaped structure, and the integrin regulated FACs were formed around the head of the structures leading to stabilized adhesion (**Figure** 2.12b) [88].

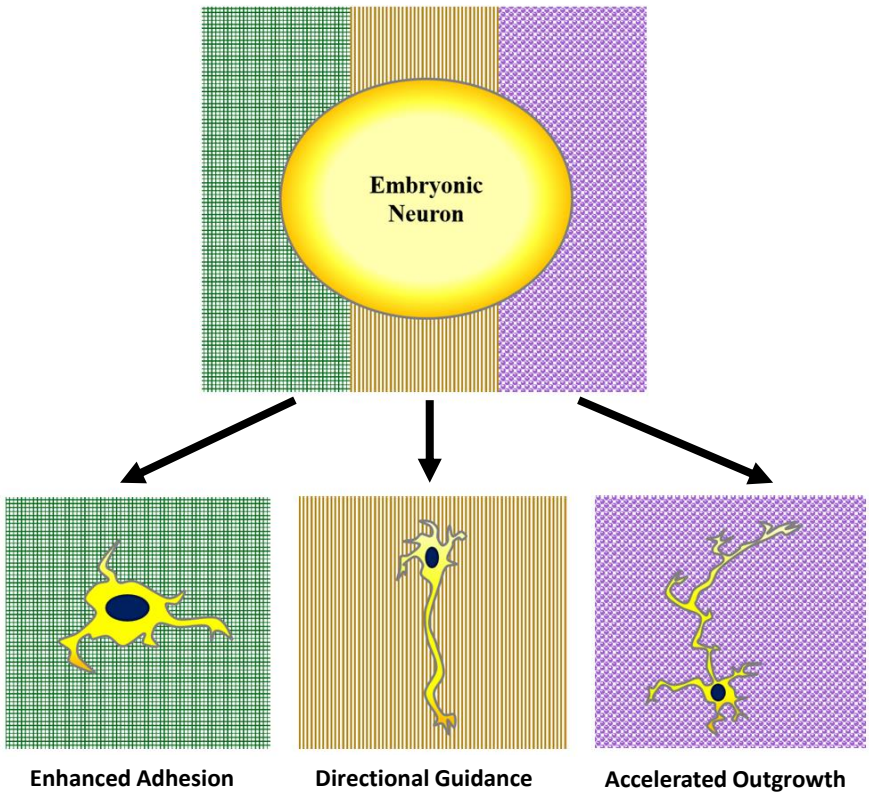

Figure 2.11. Illustration of nano-grooves fabricated with photolithography with different topographies and the neuronal processes adaptation (adapted from [83]).

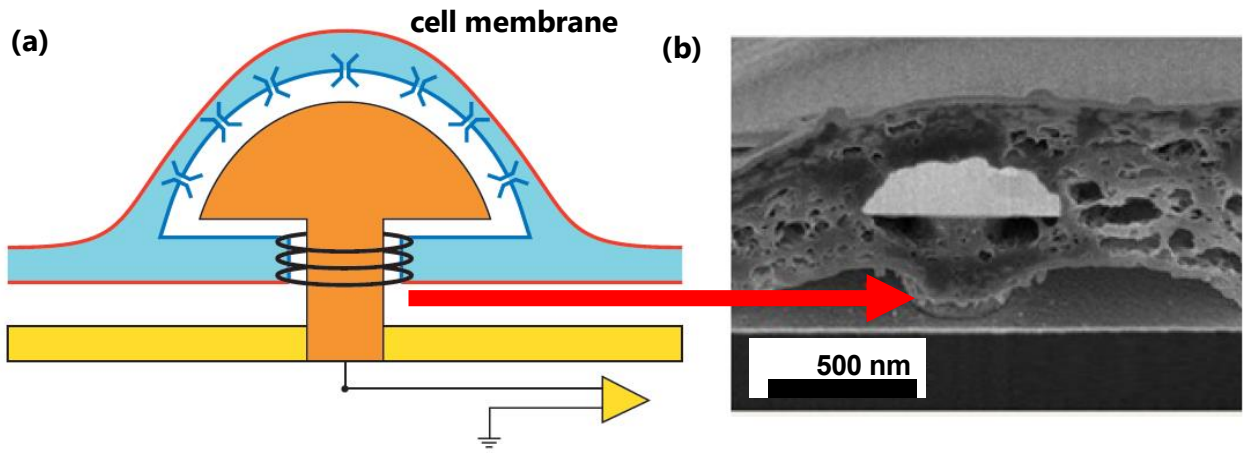

Figure 2.12. (a) Schematic illustration and (b) scanning electron microscopy image of actin filaments of neurons wrapping around mushroom-shaped microelectrode fabricated with electrodeposition (adapted from [88]).

2.2.3. Electrical characterization of the cell-electrode interface

In recent times, electrical equivalent circuit has been implemented to characterize adhesion of neurons to nanostructured electrode surfaces [89-90]. Such an analogue consists of three key components: neuron, nanostructured electrode surface and seal gap between neuron and electrode (**Figure** 2.13a). As established in the previous section, transmission of charge to the electrode occurs in both capacitive and resistive mechanisms [70]. Therefore in this analogue, the electrode surface is characterized by a resistive electrode impedance. The neuron membrane interfacing the electrode surface is designated as junctional membrane and the membrane not interfacing the electrode is designated as non-junctional membrane. Both these membranes are characterized by their individual resistive and capacitive components [89]. Action potentials propagating in the neurons are transmitted through both junctional and non-junctional membranes, but only the current flowing through junctional membrane is transmitted to the electrode for sensing. The space between neuron and electrode is filled with ionic fluid and this gap is characterized by a resistive component known as seal impedance [89]. The electrical analogue circuit has been used to correlate the coupling efficiency of action potentials (APs), post synaptic potentials (PSPs) and slow membrane oscillations (example waveforms in **Figure** 2.13b) with the seal impedances of the microelectrodes [89]. By experimental methods, it was revealed that coupling of neurons to the electrode surface with nanostructures was significantly enhanced due to the reduced seal gap and increased seal impedance, especially for low frequency signals (such as PSPs and membrane potentials) (**Figure** 2.13c-d) [89].

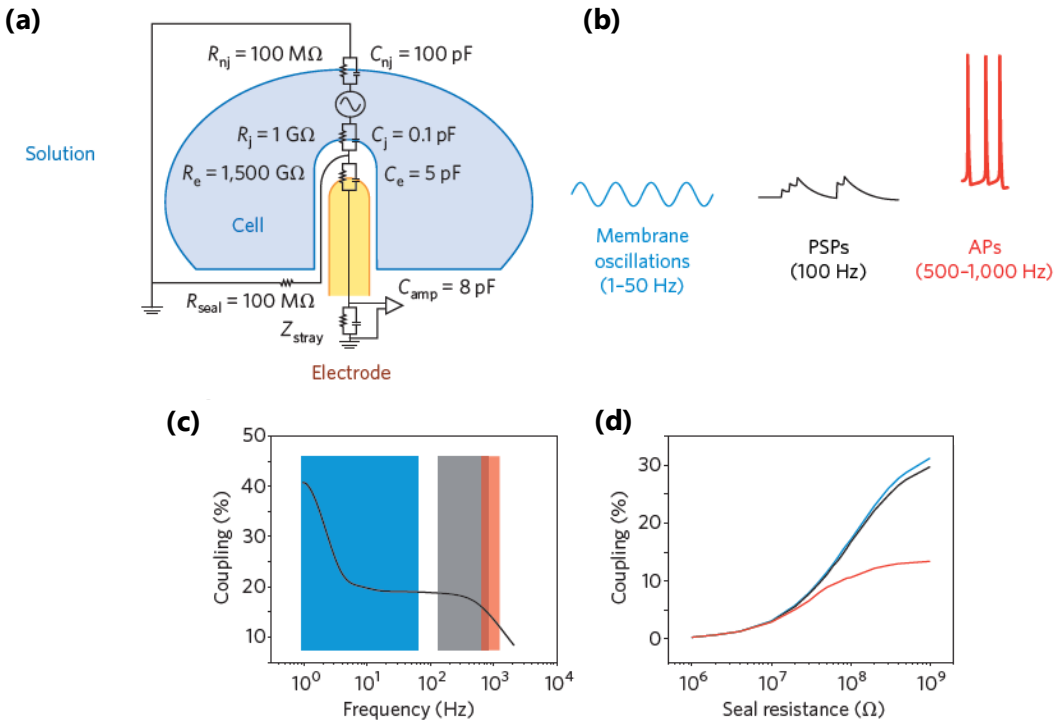

Figure 2.13. (a) Schematic illustration of electrical equivalent circuit of microelectrode interfacing with electrogenic cell culture (adapted from [89]). (b) Illustrations of waveform and frequency range of different electrogenic activities. (c) Dependence of coupling efficiency on the electrogenic activity and (d) dependence of coupling efficiency on seal resistance (adapted from [89]). Color of the marked regions in (c) and (d) are related to the signal frequencies described in (b).

2.3. Nanoimprint lithography

Nanoimprint lithography (NIL) is a nanopatterning method used to fabricate micro- and nanostructures with high throughput and excellent resolution at relatively lower costs [30,91]. NIL works on the principle of mechanical deformation of polymers and subsequent curing to generate brittle nanostructures. The mechanical deformation is performed with a master mold containing the micro/nanopattern. Depending on the curing methods used on the deformed polymer, NIL can be classified to UV-NIL or Thermal-NIL (**Figure** 2.14). Thermal NIL is used with a thermoplastic polymer characterized by polymer chains associated by weak intramolecular forces. When the thermoplastic polymer is heated to a temperature larger than its glass transition threshold, the intramolecular forces disintegrate yielding the polymer to be in viscous fluidic state. The viscous polymer can then be reshaped by application of mechanical pressure with the master mold by methods such as injection molding, compression molding etc. Upon reduction of temperature, the polymers are brought back to brittle solid state, but do not regain their original undeformed shape. On the other hand, UV-NIL uses low viscous fluidic precursors composed of UV-curable monomers instead of thermoplastic polymers for mechanical deformation. Monomers in the deformed film are cross-linked by UV light resulting in formation of brittle polymer films. UV-NIL possess an

advantage over thermal NIL for substrates which are sensitive to high temperature. But such an apparatus would require the master mold to be transparent to UV light. Finally, the solid deformed polymers are used for nanostructuring either by top-down (e.g., chemical vapor deposition [92], physical vapor deposition [93]) or bottom-top (e.g. electroplating [94], self-assembled monolayer polymers [95]) fabrication methods to generate nanopatterns with spatial resolution as small as 10 nm [30, 91].

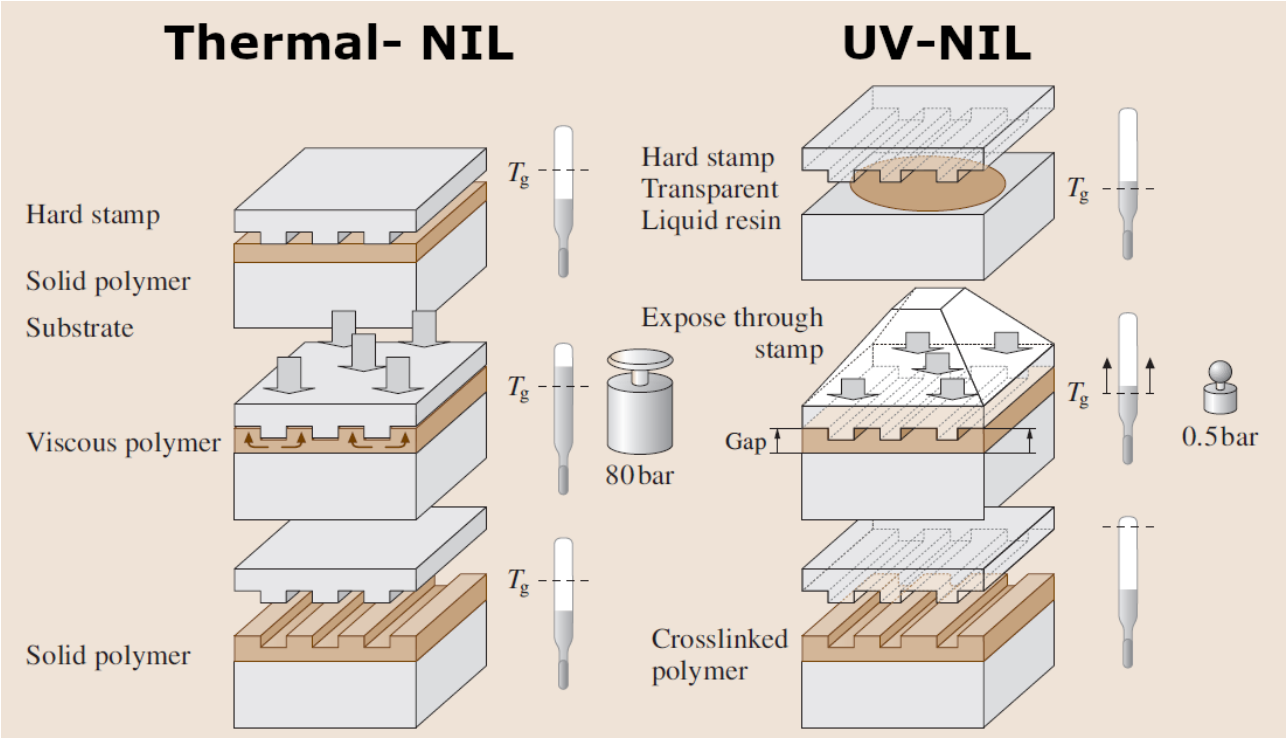

Figure 2.14. Schematic representation of the functional principle for thermal nanoimprint lithography and UV nanoimprint lithography (adapted from [91]).

2.3.1. Nanostructuring with NIL for biosensor functionalization

With the emergence of a wide variety of novel biocompatible materials for NIL purposes, the scope of nanostructuring has found enormous application in several fields of bioengineering [96]. For instance, UV-NIL has been used to fabricate micro-/nanostructures with biocompatible hybrid polymers for development of 3D culture surfaces for neurons (**Figure** 2.15a) [97]. Results showed enhancement not only in stronger adhesion of neurons on 3D nanostructured surfaces, but also significant changes in growth and differentiation life cycles of the cells [97]. In another example, thermal NIL was used to fabricate gold nanostructures on top of microelectrodes used for electrophysiological applications (**Figure** 2.15b) [41]. The nanostructures not only improved the adhesion of cells to the electrode surface but also contributed to reduction of global electrode impedance. Large scale fabrication of the nanostructured surfaces with NIL has also been popular

in recent times, due to the advent of ingenious industrial approaches such as roll-to-roll fabrication and laser assisted direct imprint [98].

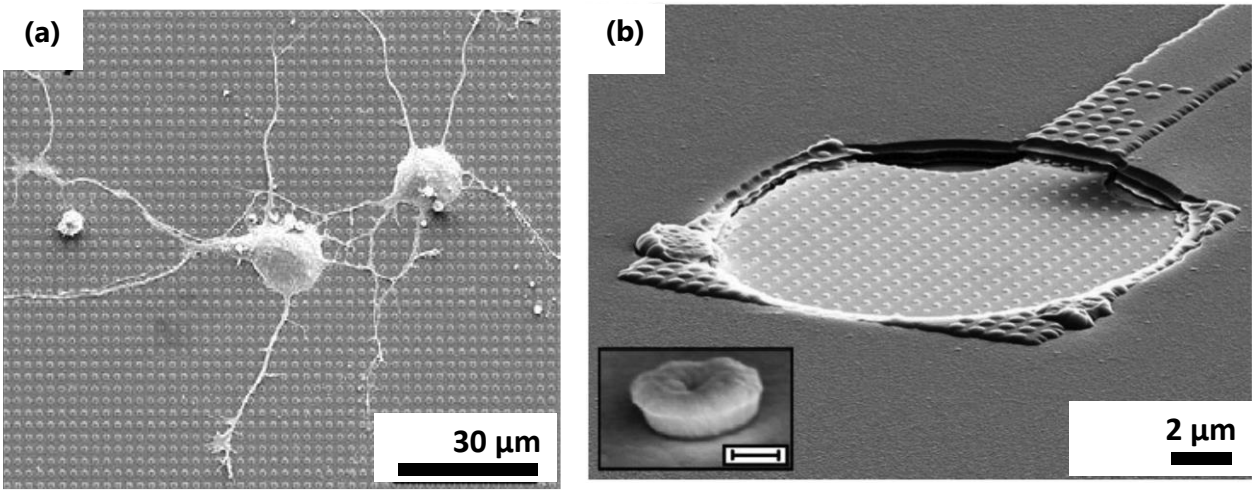

Figure 2.15. Examples of nanostructures fabricated with nanoimprint lithography for bio-analytical applications with (a) biocompatible polymer (adapted from [97]) and (b) electrodeposited nanostructures on microelectrode (inset scale bar 200 nm) (adapted from [41]).

2.4. Topographical randomness

The main objective of this study is to fabricate random nanostructures and hence it is essential to understand the interpretation of randomness, especially in the context of topographical dimensions and organization. Randomness in mathematics is expressed as the probability of predicting the outcome of a situation over several trails of an experiment. In case of 3D nanostructures on a planar surface, the degree of order and randomness can be explained in terms of the predictability of its axial dimension, lateral dimension and the intra-structural distances [46, 99]. Although there is no specific standardized test which can quantitatively determine randomness of 3D nanostructures, it can be interpreted with Gaussian distribution of the geometrical nanofeature dimensions. This approach has been illustrated with an array of circular cylindrical structures on a planar surface with defined diameter and height. **Figure** 2.16a shows the cylindrical structures with uniform diameter, height and intra-structural distance, whereas **Figure** 2.16b shows variance in the cylinder diameter across the structure array. When the diameter of the cylinder structures are represented in the form of normalized Gaussian distribution (**Figure** 2.16c), the ratio of standard deviation to its mean (also known as coefficient of variation) could be used as the quantitative parameter determining the extent of randomness. The dimensions of a highly random nanostructure array would have larger coefficient of variation with smaller probability density function, whereas a highly organized nanostructure array would have a smaller coefficient of variation with larger probability density function.

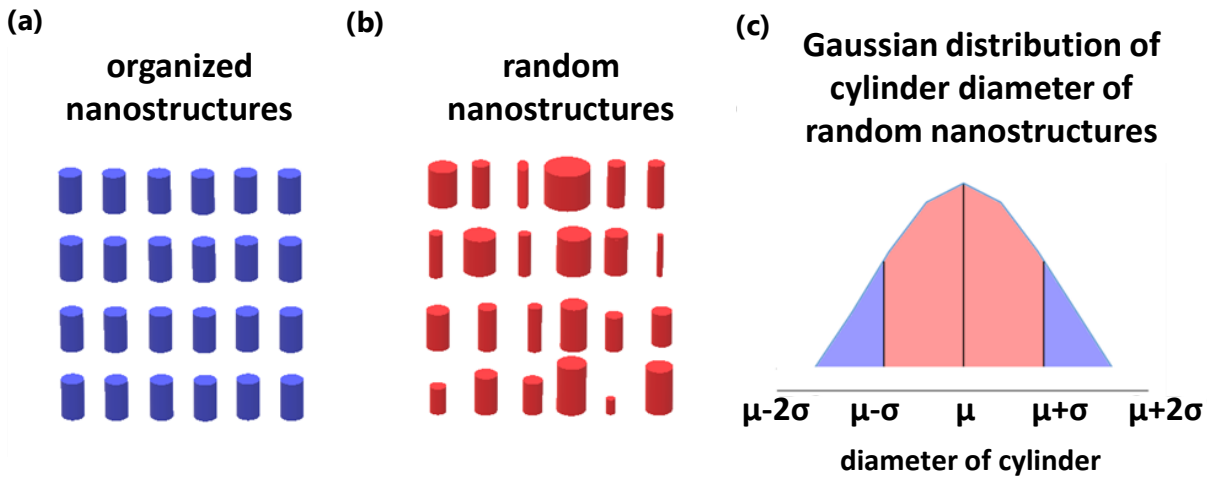

Figure 2.16. Illustration of cylindrical nanostructures with (a) uniform lateral dimension (diameter) and (b) variable lateral dimension (diameter). (c) Gaussian distribution of the cylinder diameter of random nanostructures in (b). **μ** represents the mean and **σ** represents the standard deviation of the cylinder diameter.

Depending upon the number of geometrical parameters of the nanostructures varying in the arrangement, the randomness pattern be classified to 1D, 2D or 3D. The example of cylindrical nanostructures on planar surface (**Figure** 2.16a) has been used in this study for illustrating this perspective of randomness evaluation. The cylinders are characterized by 1 lateral dimension (diameter), 1 axial dimension (height) and the organization (intra-structural distance). If one geometric dimension is showing variance in the array (**Figure** 2.17a height of the cylinder), the nanostructure array is entitled to possess 1D randomness. Likewise, if two geometric dimensions show variance in the array (in **Figure** 2.17b diameter and height of cylinder) the nanostructure array can be entitled to possess 2D randomness. If variance exists in axial dimension, lateral dimension, as well as, organizatoin of the nanostructures, the array can be entitled to possess 3D randomness (**Figure** 2.17c).

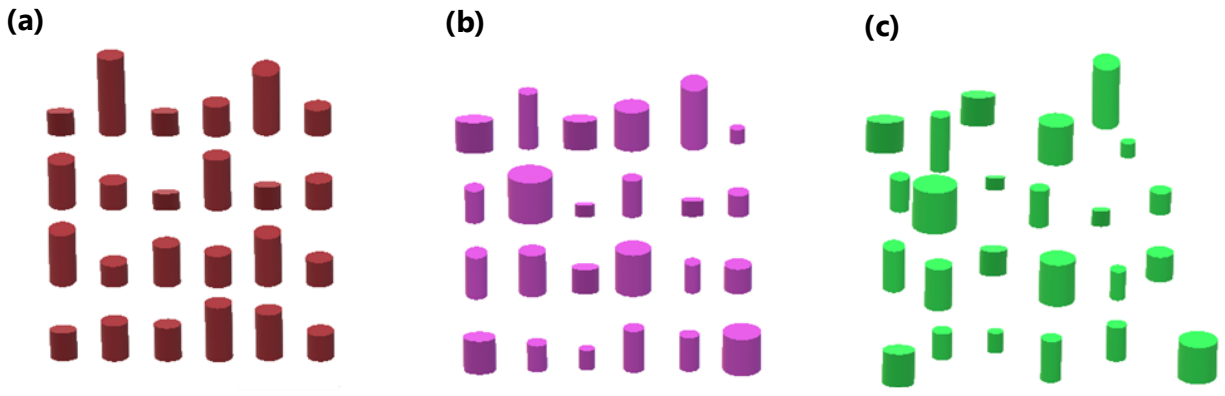

Figure 2.17. Schematic of cylindrical nanostructures depicting (a) 1D randomness, (b) 2D randomness and (c) 3D randomness.

Illustration of this perspective of topographical randomness can be observed in asymmetric nanostructures developed in literature. For example, Fuhrmann et al developed silicon nanowires produced by nanosphere lithography and molecular beam epitaxy (**Figure** 2.18a) [100]. The nanowires have homogenous volume across the substrate surface, but follow no discernible pattern in spatial organization, which is a representative of 1D randomness profile. In another example, Ji et al developed heterogeneous nanostructures through the photo-cleavage of pre-stabilized self-assemblies (**Figure** 2.18b) [101]. The nanostructures follow no discernible spatial organization pattern and also the lateral dimensions are not uniform hence illustrating 2D randomness. Finally, Shin et al fabricated random nanostructures as a scattering layer on organic light emitting diodes where the nanostructures are organized in an entirely random orientation and the volume of individual structure is also completely asymmetric, representing 3D randomness (**Figure** 2.18c) [102]. Interestingly, the biological nanostructures present in the basement membrane of the natural cell adhesion surface consists of 3D topographical components such as ridges, wells, tubes, and pillars (**Figure** 2.18d). The dimensions of these topographical components vary from within ten to a several hundred nanometers [21-22] and the orientation represents 3D randomness.

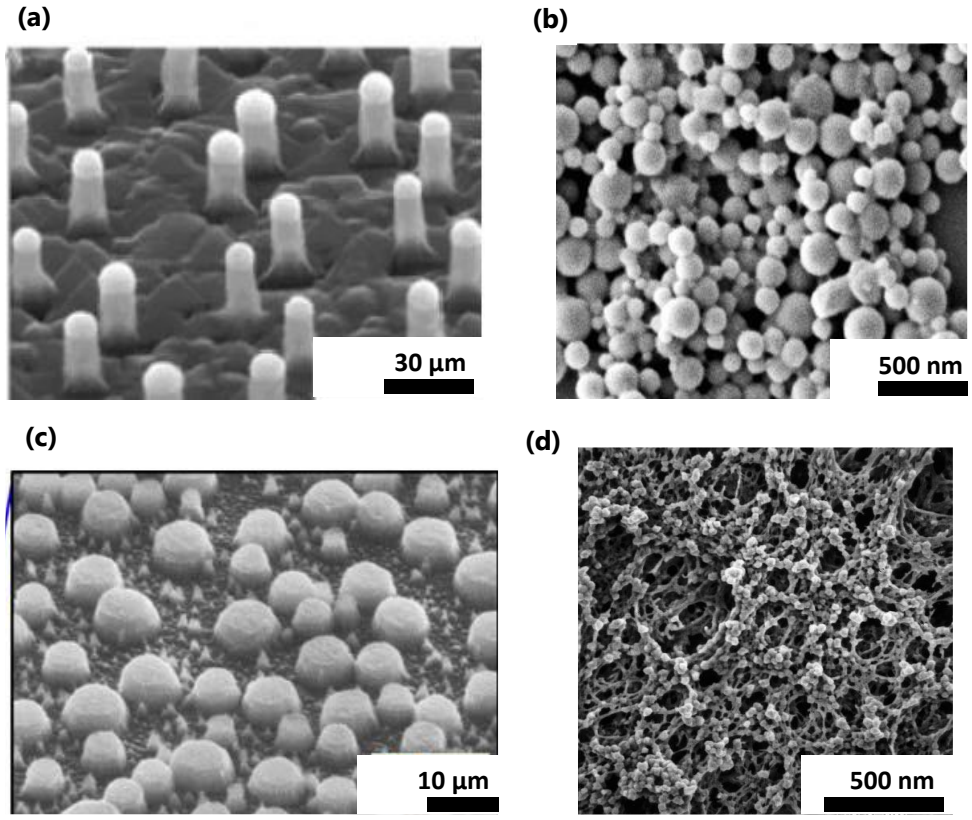

Figure 2.18. Examples of synthetic random nanostructures depicting (a) 1D randomness (adapted from [100]), (b) 2D randomness (adapted from [101]) and (c) 3D randomness (adapted from [102]). (d) Rhesus macaque corneal epithelium basement membrane depicting 3D randomness (adapted from [21]).

2.5. Surface characterization methods

2.5.1. Atomic force microscopy

Atomic force microscopy (AFM) is a high-resolution scanning probe microscopy with demonstrated resolution in the order of fraction of nanometers. It combines the principles of piezoelectric effect and optical position sensing to measure various topographical features of a surface such as roughness, surface profile, electromagnetic properties etc. [103]. In comparison to optical and electron microscopy methods, AFM does not use lenses or beam irradiation which allows the spatial resolution of measurement not be limited by the light diffraction aberrations.

The main components of the AFM apparatus include a small spring like cantilever with an extremely sharp tip at its free end with surface diameter measured to be as small as 1 nm, a piezoelectric element which oscillates position of the cantilever as it traverses along the surface, a laser source which is illuminated on the cantilever and finally a light detector which records the reflection of laser to determine deflection and motion of the cantilever (**Figure** 2.19). The atomic scale interactions between the tip and the sample surface are transduced to changes in motion of the cantilever which is then recorded and reconstructed in the form of a 3D surface profile image with the help of computer software.

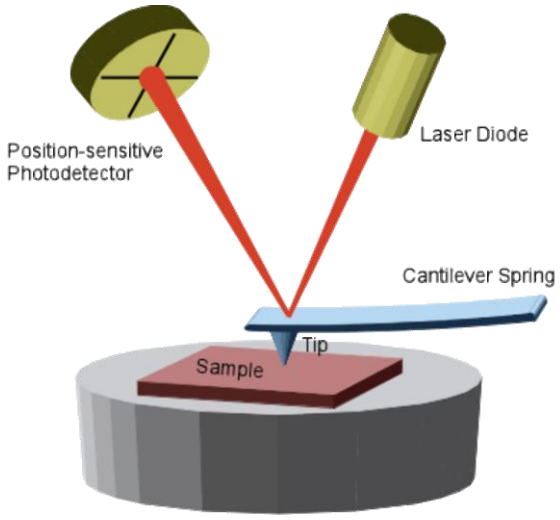

Figure 2.19. Schematic of atomic force microscopy apparatus (adapted from [103]).

2.5.2. Contact angle measurement

Surface wettability is an important parameter affecting the biological response of cells to an artificial surface [104]. It is quantified by the critical surface energy, which is the excess energy that a surface of a material possesses in comparison to the bulk, that balances the intermolecular forces between the solid surface and a fluid (**Figure** 2.20).

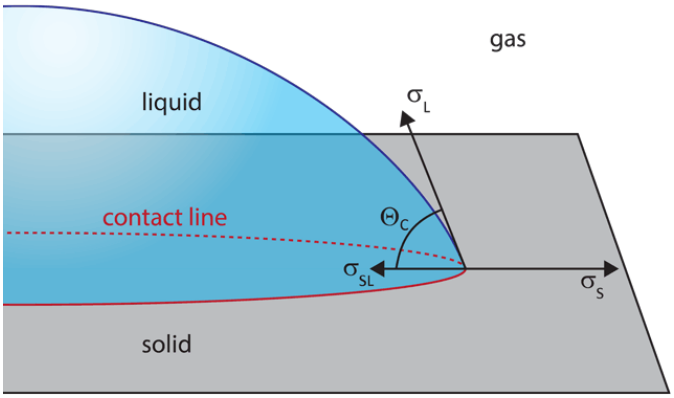

Figure 2.20. Schematic of a fluid drop on a solid surface with a contact angle $\boldsymbol{\theta}$ at the gas, solid and liquid interface (adapted from [105]).

To understand critical surface energy (or surface free energy), the schematic diagram of a fluid drop on surface with a contact angle $\boldsymbol{\theta}_C$ can be considered [105]. There are three interfaces in this illustration: solid-gas ($\boldsymbol{\sigma}_S$ is the interfacial energy of the solid-gas), solid-liquid ($\boldsymbol{\sigma}_{SL}$ is the interfacial energy of the solid-liquid) and liquid-gas ($\boldsymbol{\sigma}_L$ is the interfacial energy of the liquid-gas). In order for the drop to maintain its shape and not collapse, the interfaces should be in wetting equilibrium state i.e., $\boldsymbol{\sigma}_S$ should be equal to $\boldsymbol{\sigma}_{SL}$ and cosine of $\boldsymbol{\sigma}_L$ (**Equation** 2.1).

$$\boldsymbol{\sigma}_S = \boldsymbol{\sigma}_{SL} + \boldsymbol{\sigma}_L.\cos \boldsymbol{\theta}_C \qquad \textbf{Equation } 2.1$$

The contact angle $\boldsymbol{\theta}_C$ determines the shape of the fluid and is a measure of wettability of the surface. If $\boldsymbol{\theta}_C$ is greater than 90 °, the fluid does not wet the surface completely and is characterized as hydrophobic. If $\boldsymbol{\theta}_C$ is less than 90 °, the fluid spreads on the surface and is characterized as hydrophilic. When $\boldsymbol{\theta}_C$ is equal to 0 °, the state is defined as complete wetting and the surface energy $\boldsymbol{\sigma}_{SL}$ measured in such a state is known as critical surface energy or free surface energy. In reality, $\boldsymbol{\theta}_C$ cannot be zero and such a parameter can only be calculated by estimation methods. One such method was proposed by Zisman [106]. In this method, cosine of contact angle of each surface was measured with different fluids and plotted against their respective fluid surface tension. The resulting straight line was extrapolated to point where contact angle is 0 °, which is the critical surface energy.

2.5.3. Electrical impedance spectroscopy

Electrical impedance spectroscopy (EIS) is a versatile tool that provides a quantitative measurement of the electrochemical behavior for surfaces in a fluidic medium. Applications of EIS include bioelectrode characterization, corrosion analysis, DNA biosensing etc. [107-108]. Working principle of EIS is derived from Ohm's law where a sinusoidal voltage signal is applied to a measurement system and complex impedance of the system is measured form the output voltage (**Figure** 2.21). Impedance Z of a system is a function of the radial frequency $\boldsymbol{\omega}$ and is defined in

Equation 2.2, where U_m and I_m are peak current and voltage of sinusoidal signals, respectively and $\boldsymbol{\theta}$ is the phase shift.

$$Z = \frac{U(t)}{I(t)} = \frac{U_m \,.\, \sin(\boldsymbol{\omega} t)}{I_m . \sin(\boldsymbol{\omega} t + \boldsymbol{\theta})}$$ **Equation** 2.2

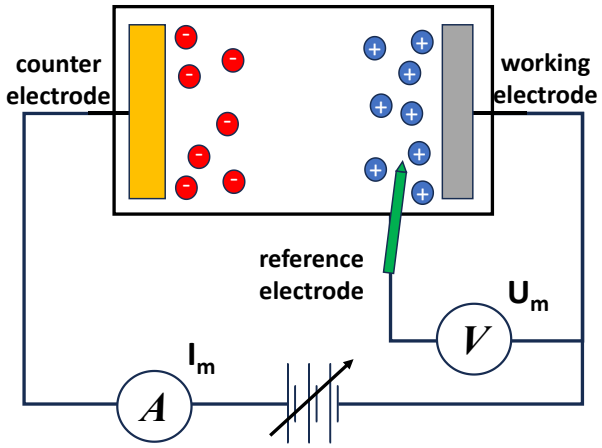

Figure 2.21. Schematic of measurement setup for potentiostatic electrochemical impedance spectroscopy.

EIS can be represented in Bode diagram and Nyquist diagram. Bode diagram is used for analyzing the global impedance contribution of a system at a several frequencies (**Figure** 2.22a), whereas Nyquist diagram is used to correlate the real (resistive) and imaginary (capacitive/inductive) parts of the impedance spectrum (**Figure** 2.22b). The EIS measurements can be fit to an electrical equivalent circuit model to explicitly determine the values of individual electrical components of a system. For example, the EIS data measured of a microelectrode surface in a conductive electrolyte can be fit to a Randal's circuit (**Figure** 2.22c) to determine the values of the electrolyte resistance (R_S), double-layer capacitance (C_{dl}), active charge-transfer resistance (R_{ct}) and Warburg diffusion element W. Electrolyte resistance is a function of ionic mobility, ionic conductivity and the side length of the electrode [109]. Double-layer capacitance is a function of relative dielectric permittivity of the electrolyte, width of the Helmholtz double-layer and effective area of the electrode surface. Charge-transfer resistance is a function of exchange current density (redox reaction) of the electrode material and effective area of the electrode surface [110]. Finally, the Warburg diffusion is a frequency independent component which is function on the ionic concertation at the electrode surface and stirring rate of the electrolyte. It can be noted here that the effective surface area of the electrode does play a large role in its impedance spectroscopy properties. Presence of nanostructures on the electrode surfaces would alter the individual components of the impedance spectrum depending of the height, density and roughness, which could be further evaluated with the electrical equivalent circuit.

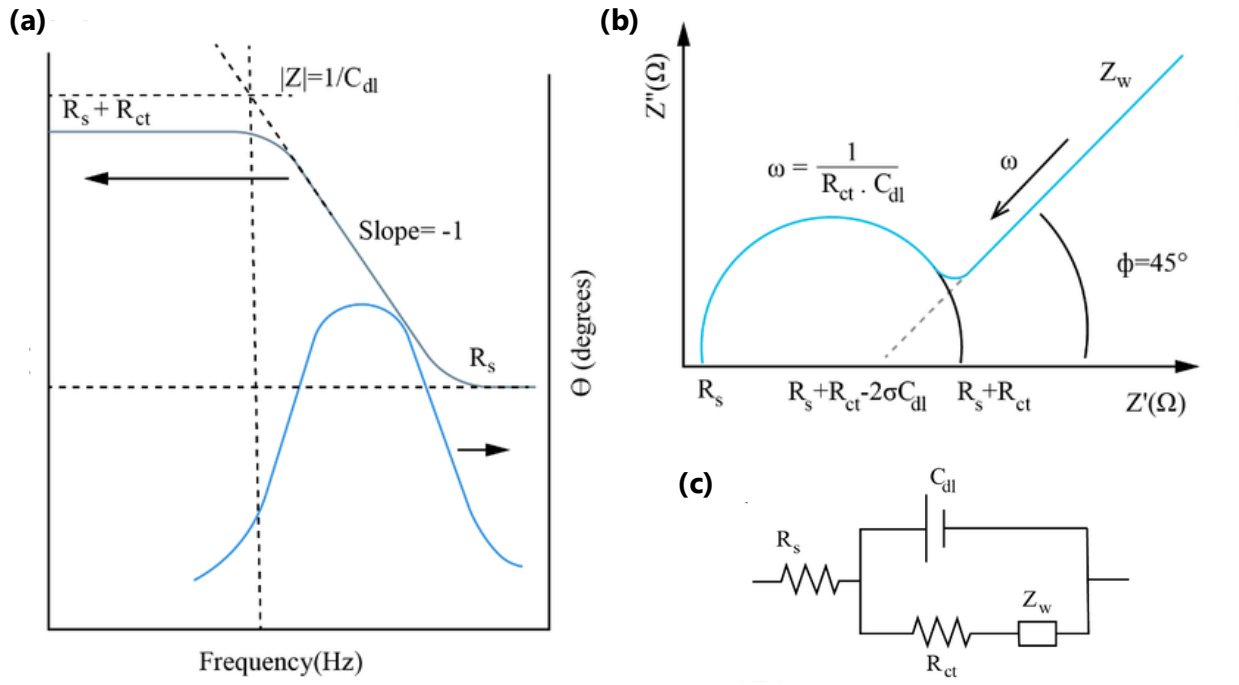

Figure 2.22. Electrochemical impedance spectroscopy illustrated in (a) Bode magnitude and phase diagram and (b) Nyquist diagram (adapted from [111]). (c) Randel's electrical circuit model to represent the information of the impedance spectroscopy diagrams.

2.5.4. Scanning electron microscopy

Scanning electron microscopy (SEM) is one of the most widely used sub-micron range imaging method based on focused beam of high-energy electrons. The information obtained from the SEM can used for the determination of external morphology (texture), chemical composition, crystallinity and orientation of materials [112]. Accelerated electrons possess a significant amount of kinetic energy, which undergoes substantial modifications upon interaction with a solid substrate. The electron-surface interaction leads to a combination of elastic and inelastic scattering effects, which results in the formation of a pear-shaped interaction volume [113]. The main signals obtained from this volume include secondary electrons, backscattered electrons, diffracted backscattered electrons, X-rays, cathodoluminescence and thermal energy, all of which reveal distinctive information about the substrate (**Figure** 2.23).

Key components of an SEM include an electron source (tungsten filament, solid state crystal, field emission gun, etc.), a series of condenser lenses which focuses the electron beam as it moves from the source down the column, a scanning coil for beam deflection and detectors for secondary electrons, backscattered electrons, X-rays etc.

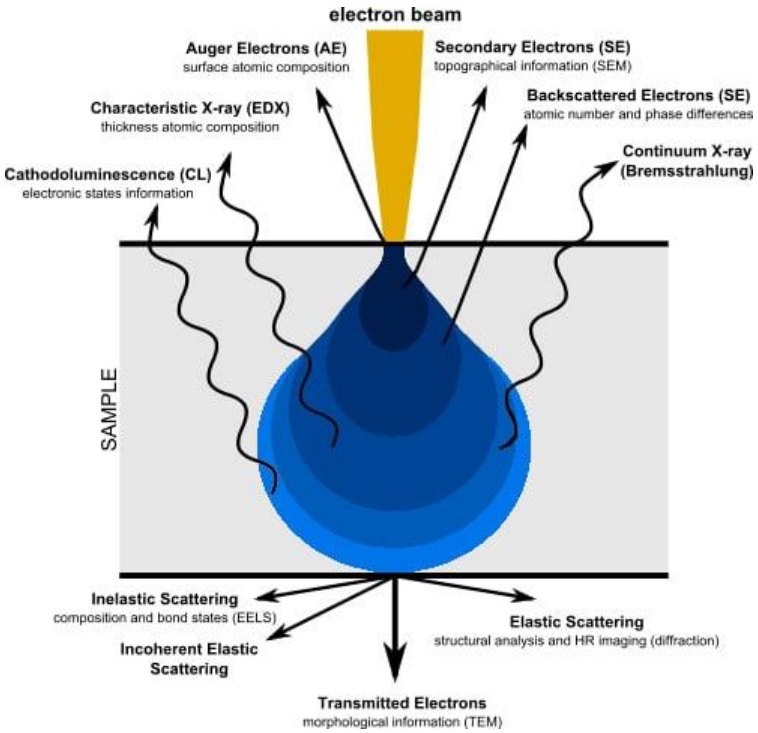

Figure 2.23. Schematic representation of the interaction between the electron beam and the surface (adapted from [113]).

2.6. Fluorescence microscopy for neuron adhesion analysis

Fluorescence microscopy is a specific type of optical microscopy with uses fluorescence properties of the materials to map and image components on a substrate, especially biological samples (**Figure** 2.24). The fluorophore (fluorescent chemical compound that can re-emit light upon light excitation) on the substrate is illuminated with light of a specific wavelength and the emitted light (of a different wavelength) is selectively detected and imaged.

Epifluorescent microscope are the most commonly used fluorescent microscopes, where the excitation of the fluorophore and detection of the fluorescence are done through the same light path. The key components of this setup include an intense near-monochromatic light source (xenon arc lamps, mercury-vapor lamps, light emitting diodes), an excitation filter which permits only excitation photon, a dichroic beam-splitter which selectively permits emission and excitation photons, an objective lens for focusing, an emission filter which only permits emission photons and finally an emission photon detector with an ocular lens. Preparation of biological samples for epifluorescence imaging is done by expression of a fluorescent protein. These are done by the binding of fluorescent protein to a biological molecule such as nucleic acids, drugs, toxins or peptides. Immunostaining is another common preparation technique, where the fluorescent protein is labelled to a highly specific antibody (primary or secondary) binding to an antigen.

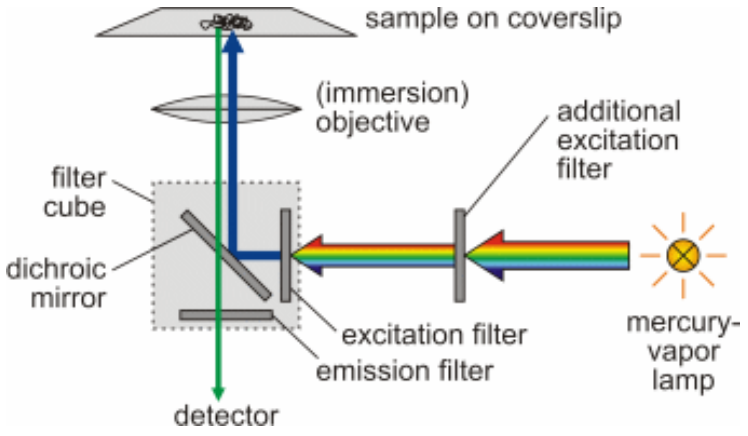

Figure 2.24. Schematic of the immunofluorescence microscopy apparatus (adapted from [114]).

3. Materials and methods

In this chapter, the materials and experimental methods used for the development of biomimetic nanostructured surfaces have been described. Firstly, the detailed description biomimetic nanostructuring process based on nanoimprint lithography has been described and then the fabrication process of microelectrode arrays chips with the biomimetic nanostructures has been presented. Afterwards, measurement apparatus of surface physical and electrochemical characterization of the nanostructures have been explained. Finally, the cell culture procedures used for electrophysiological experiments and fluorescence microscopy have been illustrated.

3.1. Nanostructuring process

Fabrication and nanostructuring of electrode surfaces performed in this study has been divided to four main sub-processes. The first sub-process was the development of the collagen coated silicon wafer used as a master stamp for the nanoimprint lithography process. Second sub-process was the biomimetic nanostructure fabrication with nanoimprint lithography and gold electroplating. The third sub-process was the transfer of biomimetic nanostructures to microelectrode surfaces. The final sub-process was the assembly of the nanostructured microelectrodes from wafer-level to chip-level that were used for impedance measurements and electrophysiology recordings. Standard operating procedures for the nanostructuring processes can be seen in Appendix II.

3.1.1. Fabrication of collagen coated silicon master for nanoimprint lithography

The first step was the formation of dissolved collagen solution to be spin-coated. The second step was the spin-coating of the solution on a silicon wafer. The final step was the patterning of collagen fiber network on the silicon master with photolithography methods.

3.1.1.1. Formation of collagen solution

Collagen type I extracted from bovine Achilles tendon was dissolved and filtered to be used for the spin-coating by the process described by Yang et al [115] (**Figure** 3.1a and section 1 of Appendix II):

1. Bovine Achilles tendon collagen type I powder was dissolved overnight in 0.01 M HCl solution with constant stirring at 4 °C. The optimum concentration of 1 mg/ml (w/v) was used for getting a homogenous high density collagen fiber network. The dissolved solution was homogenized by blending at 9000 RPM for 5 minutes.
2. The blended solution was filtered first with a 100 µm pore width nylon filter and then with 20 µm pore width nylon filter to remove micro-scaled agglomerates. This filtered solution was used for spin-coating process.

3.1.1.2. Spin-coating collagen solution on silicon master

The collagen fibers were uniformly spin-coated on a clean silicon wafer with the solution prepared in the section 3.1.1.1 (**Figure** 3.1b and section 1 of Appendix II).

1. The silicon wafer was cleaned for 20 minutes in piranha solution (H_2SO_4:H_2O_2) at 120 °C and then O_2 plasma treated for 10 minutes to promote collagen adsorption.
2. 1 ml of the collagen solution was spin-coated at 20 RPM for 45 minutes without acceleration on the cleaned silicon surface.

3.1.1.3. Patterning of wafer

The spin-coating method described in section 3.1.1.2 resulted in uniform coating of collagen fibers on the complete surface of the silicon wafer. Such a master stamp could ideally work with the nanoimprint lithography process. But master stamp with defined collagen coated area would make the nanostructure growth with gold electroplating more adaptable. Photolithography and reactive-ion etching has been used to pattern the collagen coated surface (**Figure** 3.1c and section 1 of Appendix II).

1. The collagen coated silicon wafer was spin-coated with image-reversal photoresist for 60 seconds at 3000 RPM and was then post baked at 90 °C for 120 seconds to deposit resist thickness of 2 µm.
2. The wafer was then exposed with 365 nm UV light for 10 seconds at 34 mJ/cm^2 under a bright field mask (mask design **Figure** 1 of Appendix I) containing the rectangular defined surface area and then developed in halogen-based solution to remove unexposed regions of the resist.
3. The collagen fibers on the open regions were then removed by reactive-ion etching with O_2 gas flow of 30 sccm at 13 Pa and 100 W power. Post etching, the resist was stripped with acetone and iso-propyl alcohol to obtain defined areas of collagen coated fibers.
4. The collagen master was spin-coated with a thin layer of anti-sticking layer at 2000 RPM for 30 seconds [116].

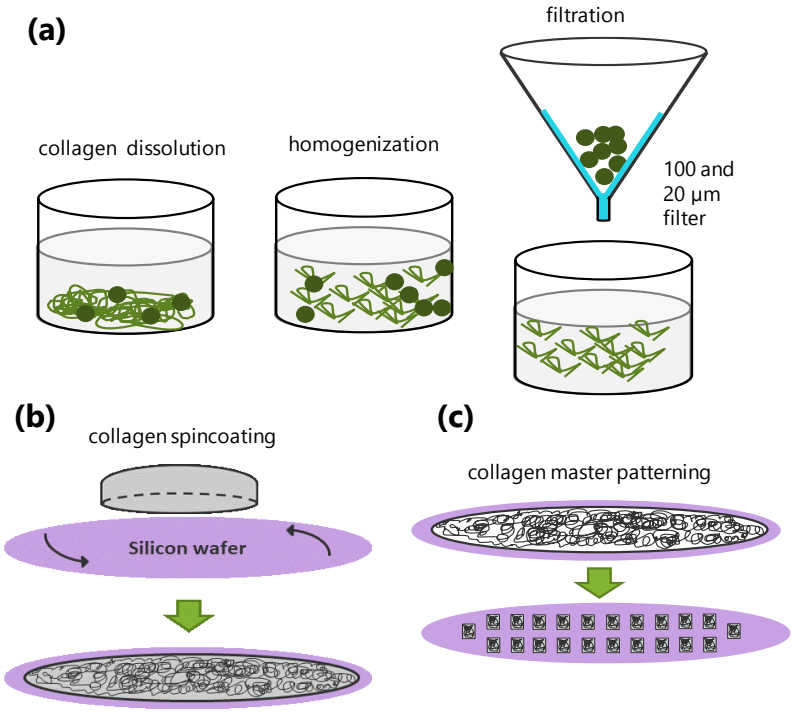

Figure 3.1. Illustration of (a) collagen solution preparation, (b) collagen spin-coating on silicon wafer and (c) patterning with photolithography for nanoimprint lithography master preparation.

3.1.2. Fabrication of biomimetic nanostructures

The collagen coated silicon master was used as a template for the nanoimprint lithography (NIL), which was then processed to fabricate collagen-like gold nanostructures by gold electroplating. The nanostructure fabrication can be divided to five main steps.

3.1.2.1. Substrate preparation

Evaporated gold surface deposited on glass wafer was nanostructured and the developed to form microelectrode arrays (**Figure** 3.2a and section 2 of Appendix II):

1. 20 nm of Ti followed by 200 nm of Au was evaporated on borosilicate glass wafers. The Au acts as a seed layer for the electroplating process and Ti layer promotes adhesion between glass and gold.
2. The substrate gold wafer was spin-coated with thermal nanoimprint resist at 1500 RPM for 30 seconds and then hard baked for 60 seconds at 100 °C to produce a resist thickness of 450 nm.

3.1.2.2. Nanoimprinting process

The NIL resist coated gold wafer described in section 3.1.2.1 was used as the thermoplastic polymer and the collagen coated silicon wafer described in section 3.1.1 was used as a master stamp in the nanoimprint process (**Figure** 3.2b and section 2 of Appendix II):

1. The collagen fibers were nanoimprinted on thermal nanoimprint resist at 160 °C and 40 bar for 5 minutes and the pressure was released at 100 °C, as the glass transition temperature of the resist was 105 °C.
2. The wafer sandwich was then cooled to room temperature and separated (**Figure** 3.2c).

3.1.2.3. Residual layer etching

Following nanoimprinting, a relatively large thickness of residual layer of the nanoimprint resist was left under the imprint, which was etched in a controlled approach with reactive-ion etching (**Figure** 3.2d and section 2 of Appendix II).

The total nanoimprint resist thickness does not change post nanoimprinting and was measured to be 450 nm. The depth of indentations created by imprint was measured to be ranging between 10 nm and 150 nm. Depending on the collagen network density to be replicated into the gold nanostructures, the residual layer to be etched was measured to be 400 nm, which leaves the remaining resist thickness to be 50 nm. The reactive-ion etching was performed with O_2 gas flow of 30 sccm at 13 Pa and 25 W power at a resist etch rate of 3.2 nm/sec.

3.1.2.4. Nanostructure growth

The imprinted cavities on the thermoplastic resist were filled with electroplated gold. The wafer was electroplated in potentiostatic two-electrode setup using a platinum mesh as a counter electrode and a gold sulfite bath as plating electrolyte to fill the open regions of the nanoimprint resist. The electroplating process was based on the **Equation** 3.1a-b (see section 2 of Appendix II):

$$[Au(SO_3)_2]^{3-} \rightarrow [Au(SO_3)]^- + (SO_3)^{2-} \quad \textbf{Equation } 3.1a$$

$$[Au(SO_3)]^- \rightarrow Au^+ + SO_3^{2-} \quad \textbf{Equation } 3.1b$$

The electroplating was performed in a galvanostatic mode and the plating time t (seconds) was calculated from the Faraday's laws of electrolysis (**Equation** 3.2),

$$t = \frac{\boldsymbol{\rho}.d.A.z.F}{M.J} \quad \textbf{Equation } 3.2$$

where $\boldsymbol{\rho}$ the density of gold (19.32 gm/cm^3), d the layer thickness (in nm), z the charge number per ion (1), F the Faraday constant (in 96485 C/mol), M the molar mass of gold (in 198 g/mol) and J the current density (1 mA/cm^2). The layer thickness d was determined by the height of nanoimprint resist layer post residual layer etch (30 - 50 nm).

1. The wafer was housed in a homemade wafer holder designed with PMMA material and electroplating was performed at 60 °C and 7.5 pH. To improve the plating quality, 10 ml of gloss additive was added into the gold electrolyte. The parameters for J and t were set as per the calculations done with the **Equation** 3.2 (**Figure** 3.2e).
2. After electroplating was completed, the wafer was cleaned with distilled water and the nanoimprint resist was stripped with acetone and iso-propyl alcohol leaving behind standalone gold-plated nanostructures on evaporated gold surface (**Figure** 3.2f).

3.1.3. Fabrication of microelectrode arrays with biomimetic nanostructures

The nanostructuring method described in the section 3.1.2 has been used as a substrate layer to develop surface of microelectrodes. The wafer-scale nanostructured MEAs have then been transferred into chip-scale PCB MEAs.

3.1.3.1. Electrode and connection tracks formation

The nanostructured gold wafer (described in section 3.1.2) was processed with photolithography and subsequently the gold tracks were formed by gold etching (**Figure** 3.2g-h and section 3 of Appendix II):

1. The nanostructured gold surface was spin-coated with photoresist for 60 seconds at 8000 RPM and was then post baked for 120 seconds at 90 °C to deposit resist with thickness 1.5 µm.
2. The wafer was then exposed with 365 nm UV light for 8.5 seconds at 34 mJ/cm^2 under a bright field mask containing the MEA design (mask design **Figure** 2 of Appendix I) and

then developed in halogen-based solution to remove unexposed regions of the photoresist. Post-development, photoresist was hard baked for 5 minutes at 110 °C.

3. The removal of excess Au was performed in $KI:I_2:H_20$ (4:1:40) solution for 30 seconds and removal of excess Ti was performed in 5 % HF solution for 30 seconds. The left-over resist was stripped in acetone and then iso-propyl alcohol leaving behind microelectrodes on the wafer.

3.1.3.2. Passivation layer deposition

MEAs were passivated with dielectric material to insulate the microelectrodes from rest of the gold surface (**Figure** 3.2i section 3 of Appendix II). The MEAs fabricated in section 3.1.3.1 were deposited two different passivation layer material in this study. 1 µm of SU-8 epoxy-based polymer was deposited by spin-coating and then to cross-linked by baking at 150 °C for 3 hours. Also, a multilayered stack of alternating silicon oxide and silicon nitride with a cumulative height of 1 µm deposited by plasma-enhanced chemical vapor deposition. Such a combination would provide electrical insulation and compensates for internal stress of the thin films [117].

3.1.3.3. Electrode and connection pad opening

The microelectrodes and the contact pad regions on the passivation layer of the MEAs surface have been opened by using photolithography methods and reactive-ion etching (**Figure** 3.2j and section 3 of Appendix II).

1. The insulated MEA surface described in section 3.1.3.2 was spin-coated with positive photoresist for 60 seconds at 6000 RPM and was then post baked for 120 seconds at 90 °C to deposit resist with thickness 4 µm.
2. The wafer was then exposed with 365 nm UV light for 28.5 seconds at 34 mJ/cm^2 under a dark field mask containing the contact pad design (mask design **Figure** 3 of Appendix I) and then developed in halogen-based solution to remove unexposed regions of the resist. Post development, resist was hard baked for 5 minutes at 110 °C.
3. The unexposed regions were then reactive-ion etched with $CF_4 – O_2$ plasma with gas flow of 25 sccm and 3.1 sccm, respectively at 1.33 Pa and 100 W power to completely remove the passivation layer. Post reactive-ion etching, the resist was stripped with acetone and iso-propyl alcohol to obtain MEAs with passivation opened internal and external contact pads.

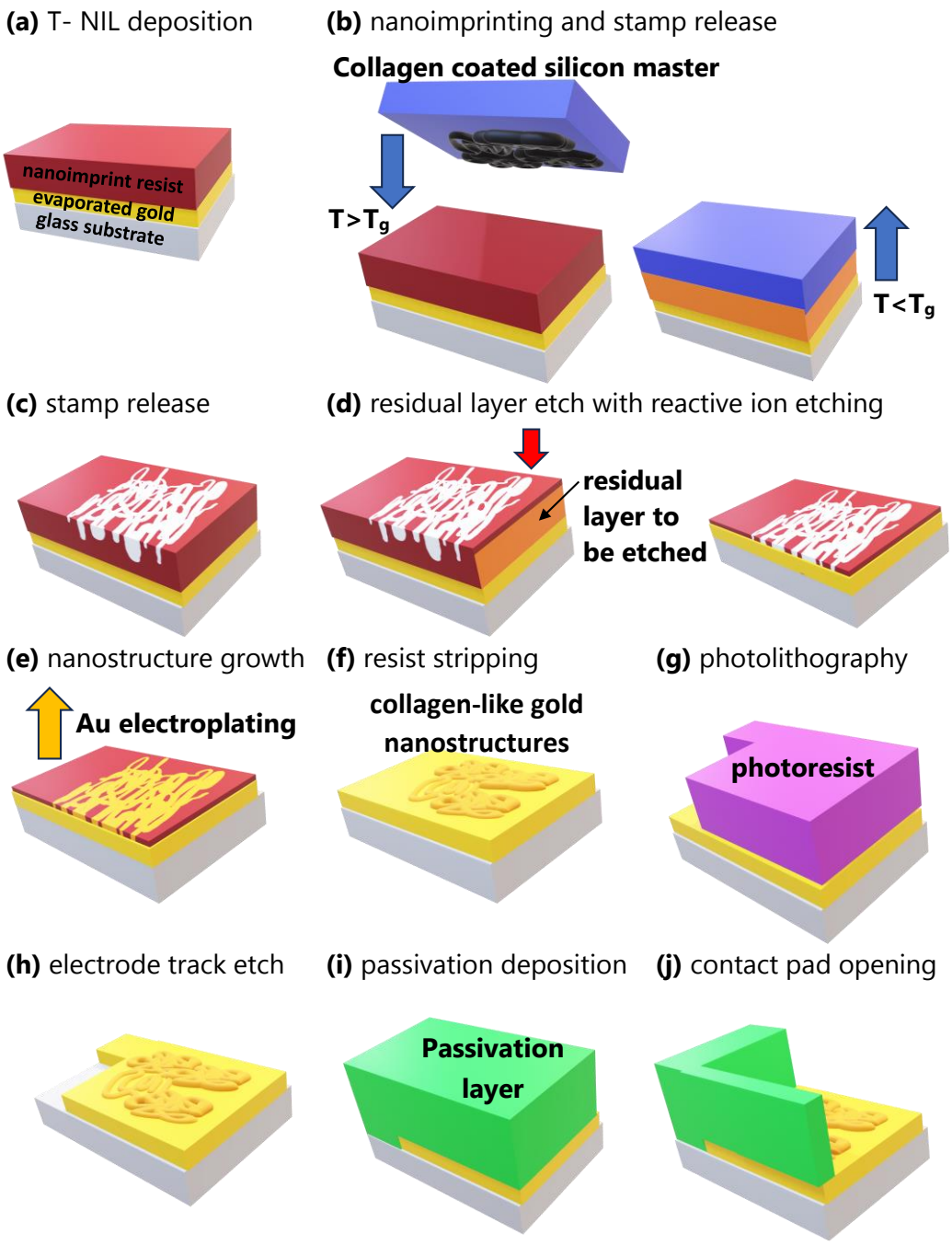

Figure 3.2. Schematic illustration of the microelectrode fabrication process with collagen-like gold nanostructures on a glass wafer (a)-(j) as explained in the text.

3.1.3.4. Wafer-level to chip-level assembly

The MEAs fabricated on the glass wafer have been transferred to chip scale units with flip-chip bonding method and housed with polydimethylsiloxane (PDMS) polymer (see section 4 of Appendix II):

1. With the photolithography masks used in this study, a single processed wafer consisted of 42 MEAs and each MEA consisted of 60 microelectrodes arranged in a square layout (**Figure** 3.3a). The nanostructuring process was designed such that 30 microelectrodes were nanostructured and 30 microelectrodes were unstructured. The MEA had external dimensions of 11 mm x 11 mm, which has been diced with a diamond blade wafer saw.
2. The dies were bonded with a PCB using flip-chip bonding and silver adhesion glue (**Figure** 3.3b and mask design **Figure** 4 of Appendix I). The outer contacts of the MEA die match in position with the internal contact pads of the PCB. Therefore, each microelectrode of the MEA has an external connection on the PCB.
3. The PCB was then isolated with PDMS silicone elastomer and a glass ring was assembled on the top, to create a cavity for cell culture medium. This PCB assembled MEA chip (**Figure** 3.3c) has been used for electrochemical characterization methods and cell culture experiments.

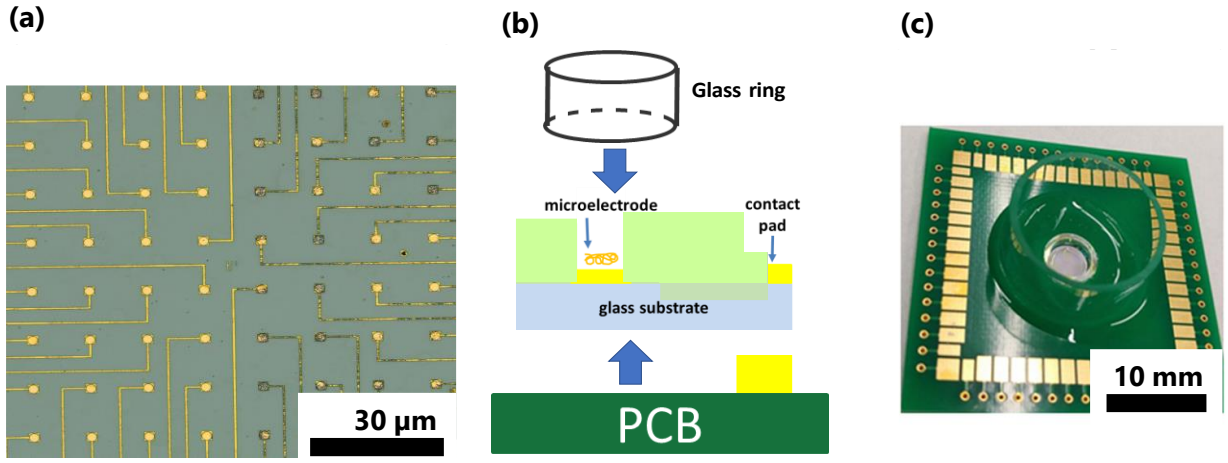

Figure 3.3. (a) Optical microscopy image of nanostructured MEA layout. (b) Schematic illustration of MEA chip assembly with the wafer scale die. (c) Photograph of assembled MEA PCB chip.

3.2. Nanostructure characterization methods

3.2.1. Electrochemical impedance spectroscopy

Electrochemical impedance spectroscopy (EIS) has been used for analysis of changes in impedance properties of the macroelectrodes (nanostructured surface area 20 mm^2) and microelectrodes (nanostructured surface area approx. 756 μm^2). And since the compatibility of the measuring surface area was specific to the input impedances and load currents of the potentiostat [118], the macro- and microelectrode surfaces were measured for the EIS analysis with two different experimental setups. For both measurement apparatus, linearity and stability was controlled with Kramers–Kronig relations and Lissajous figures provided by the potentiostat software.

3.2.1.1. EIS of macroelectrodes (electrode surface area 20 mm^2)

The biomimetic gold nanostructured macroelectrodes (described in section 3.1.2) deposited on the glass wafer were diced to 17.5 mm x 20 mm rectangle shaped die and the active area of measurement was selected to a circular surface with 5 mm diameter. EIS was also measured for unstructured gold surface with same dimensions for comparison (**Figure** 3.4a). The EIS measurements were performed in a three-electrode setup in potentiostatic mode. Impedance measurements of macroelectrodes were performed in the frequency range between 1 Hz and 100 kHz with a 10 mV sinusoidal input signal. Bias voltage of 200 mV was applied for measurement after testing linearity of the potentiostat. The probes were attached to the working electrode of potentiostat with copper adhesive tape (WE). Platinum mesh (10 cm x 10 cm) was used as counter electrode (CE) and 3 M Ag/AgCl electrode was used for reference (RE). Measurements were performed in 0.01 M NaCl solution (w/v) as electrolyte. Mathematical fitting of impedance data to equivalent circuit performed by corresponding potentiostat software.

3.2.1.2. EIS of microelectrodes (electrode surface area approx. 756 μm^2)

The PCB MEA chips fabricated with the process line described in section 3.1.3 have been used for the EIS measurements. The glass ring of MEA chip has been used as compartment to house the electrolyte. The EIS measurements were performed in a three-electrode setup in potentiostatic mode. Impedance measurements of macroelectrodes were performed in the frequency range between 1 Hz and 3 MHz with a 10 mV sinusoidal input signal. Bias voltage of 120 mV was applied for measurement after testing linearity of the potentiostat was tested. The working electrode was connected to the external contact pad of the MEA (WE). Gold electrode with circular surface diameter 1 mm was used as counter electrode (CE) and 3 M Ag/AgCl electrode as reference (RE). Measurements were performed in 0.01 M KCl solution (w/v) as electrolyte (**Figure** 3.4b).

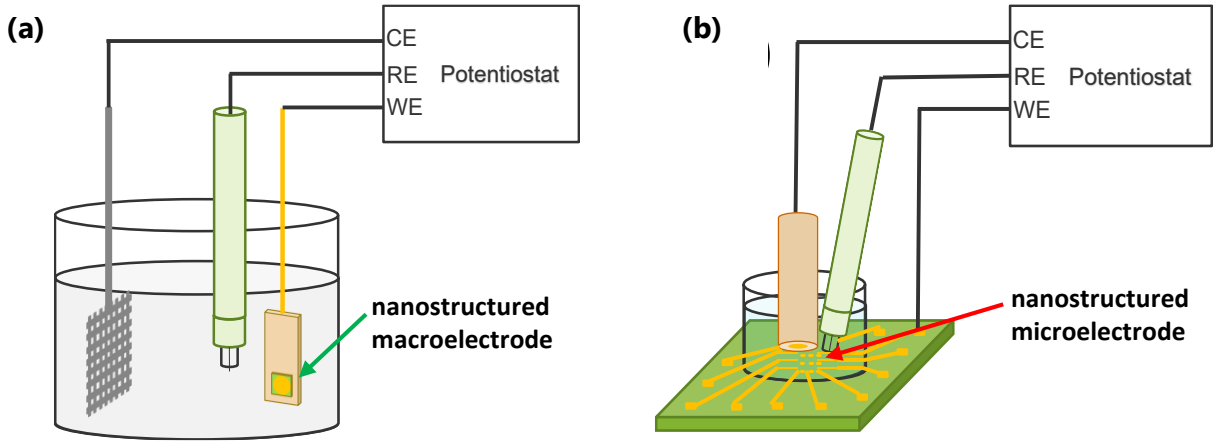

Figure 3.4. Illustration of three-electrode potentiostatic electrical impedance spectroscopy apparatus for (a) macroelectrodes (nanostructured surface area 20 mm^2) and (b) microelectrodes (nanostructured surface area approx. 756 μm^2).

3.2.2. Seal impedance estimation with impedance measurement

Seal impedance of the nanostructured and unstructured microelectrodes were measured at 1 kHz frequency in a two-electrode potentiostatic system with the apparatus MEA-IT60 device (manufactured Multichannel Systems GmbH) (**Figure** 3.5a-b). Enteric neuronal culture described in section 3.3 have been used for the seal impedance analysis and the measurements were performed on the MEAs prior to cell culturing (with DMEM solution as electrolyte) and on DIV 5 of differentiation. Ag/AgCl wire has been used as counter/reference electrode.

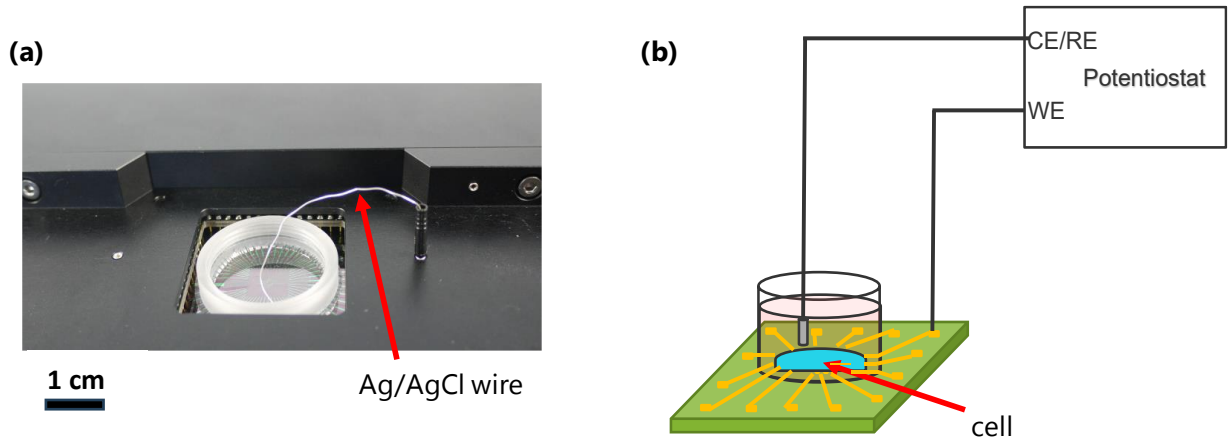

Figure 3.5. (a) MEA-IT device used for two-electrode potentiostatic seal impedance measurements with Ag/AgCl reference electrode. (b) Illustration of seal impedance measurement with cells cultured on microelectrodes.

3.2.3. Surface topographical characterization

3.2.3.1. Atomic force microscopy

Surface profile measurements of the collagen fibers on the silicon wafer and the collagen-like gold nanostructures on gold substrate were performed in tapping mode atomic force microscopy using cantilevers with tip radius 7 nm. Statistical analysis, isolation and segmentation of structural data of the biomimetic nanostructures was done using Gwyddion software.

3.2.3.2. Scanning electron microscopy

Topographical analysis of collagen-like gold nanostructures and collagen fibers coated on silicon wafer was done using scanning electron microscopy. The nanostructured microelectrode surfaces were sputter-coated with 10 nm of gold to prevent charging effects of dielectric passivation material.

Cell fixation and drying: Prior to scanning electron microscopy imaging, the enteric neuronal culture was fixed on DIV 10 with 5 % glutaraldehyde (w/v) solution and the dried in a mixture of diluted ethanol and hexamethyldisilane solutions of varied concentrations in sequential steps. See Table 2 of Appendix III for cell culture drying and fixation steps.

3.2.4. Contact angle measurements

Static surface contact angle was measured for collagen coated silicon, nanostructured gold and unstructured gold surfaces. Along with distilled water, ethylene glycol and glycerol were used as analyte fluid with dispensing volume of 5 µL. 6 surfaces of each type were measured and the cosine of mean contact angle was used to compute the critical surface energy with Zisman method.

3.3. Enteric neuron culture preparation

Enteric neurons for seal impedance measurements, electrophysiological recordings and fluorescence microscopy were isolated from small intestine of post-natal BALB/c mice (P 2–5) described by Grundmann et al [119]. Muscle layer was stripped and digested for 150 minutes in Hank's balanced salt solution, containing collagenase and DNase. Neural networks of myenteric plexus were cleaned and proliferated in culture flasks, to generate neurospheres. After three days, approx. 20 neurospheres were seeded and differentiated on culture surfaces (**Figure** 3.6). See Table 1 of Appendix III for standard operating procedures of neuronal culture isolation and seeding. Prior to seeding of enteric neurospheres, the different substrates and MEA chips were sterilized under UV-light for 20 min and then O_2 plasma-treated with flow of 40 sccm for 1 minute. Collagen coated silicon surfaces were not plasma-treated to prevent destruction of collagen fibers. MEA chips were coated with poly-D-lysine 1:100 (w/v) dilution in DMEM solution for 1 hour prior to cell seeding.

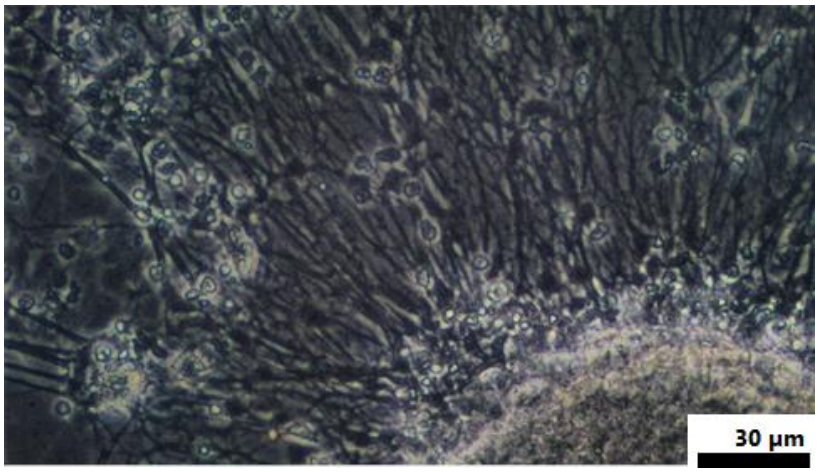

Figure 3.6. Example of enteric neurons differentiating from the neurospheres on a glass slide.

3.4. Extracellular electrophysiology experiments

3.4.1. Measurement setup: MCS MEAmini2100 recording device

Extracellular activity was measured from the enteric neurons (described in section 3.3) on the nanostructured MEA chips (described in section 3.1) on DIV 6–7 with a recording device MCS MEA2100mini (manufactured Multichannel Systems GmbH) (**Figure** 3.7). The MEA PCB chips were fabricated in this study with dimensions and the positioning of the contact pads on the chips to

make them applicable to be used with this device. The usage of this commercial recording device has a major advantage of simultaneous long-term measurements of all 60 electrodes (both nanostructured and unstructured). Also signal processing kits are readily available for the device which makes the spike detection and analysis easier. Since the homemade MEAs were fabricated without an internal reference, the extracellular activity of neurons was measured with an external Ag/AgCl pellet reference electrode in an incubated environment of 37 °C temperature and 5 % CO_2.

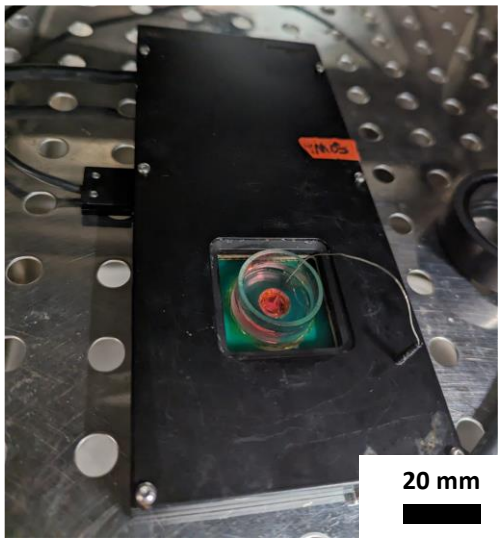

Figure 3.7. MCS MEA2100mini signal recording device with neuronal culture on nanostructured PCB MEA biosensor.

3.4.2. Spike detection and processing

The signals acquired from the nanostructured and unstructured microelectrodes were transmitted from the recording device to the data acquisition computer which were later analyzed for the detected spike activity. The software Multi Channel Experimenter V 2.20.2 was used for spike recording and processing. The raw sampled signals measured by the recording device were processed for the spike detection of individual electrode as illustrated in **Figure** 3.8. The parameters and positioning of the units were selectively chosen in the aforementioned software.

1. High-pass filter: A second order high-pass Butterworth filter with 300 Hz cut-off frequency was used to remove low frequency artefacts such as 50 Hz power line signal.
2. Low-pass filter: A second order low-pass Butterworth filter with 3000 Hz cut-off frequency was used to remove high frequency electromagnetic interference.
3. Spike detector: Extracellular activity in the form of spikes were sorted based on a predefined threshold set by the user. In this study threshold was set between 17 µV and 80 µV depending on the shape of the spike.
4. Spike analyzer: Spikes detected at each electrode were analyzed for the peak-to-peak spike amplitude, spike rate, baseline noise and signal-to-noise ratio.

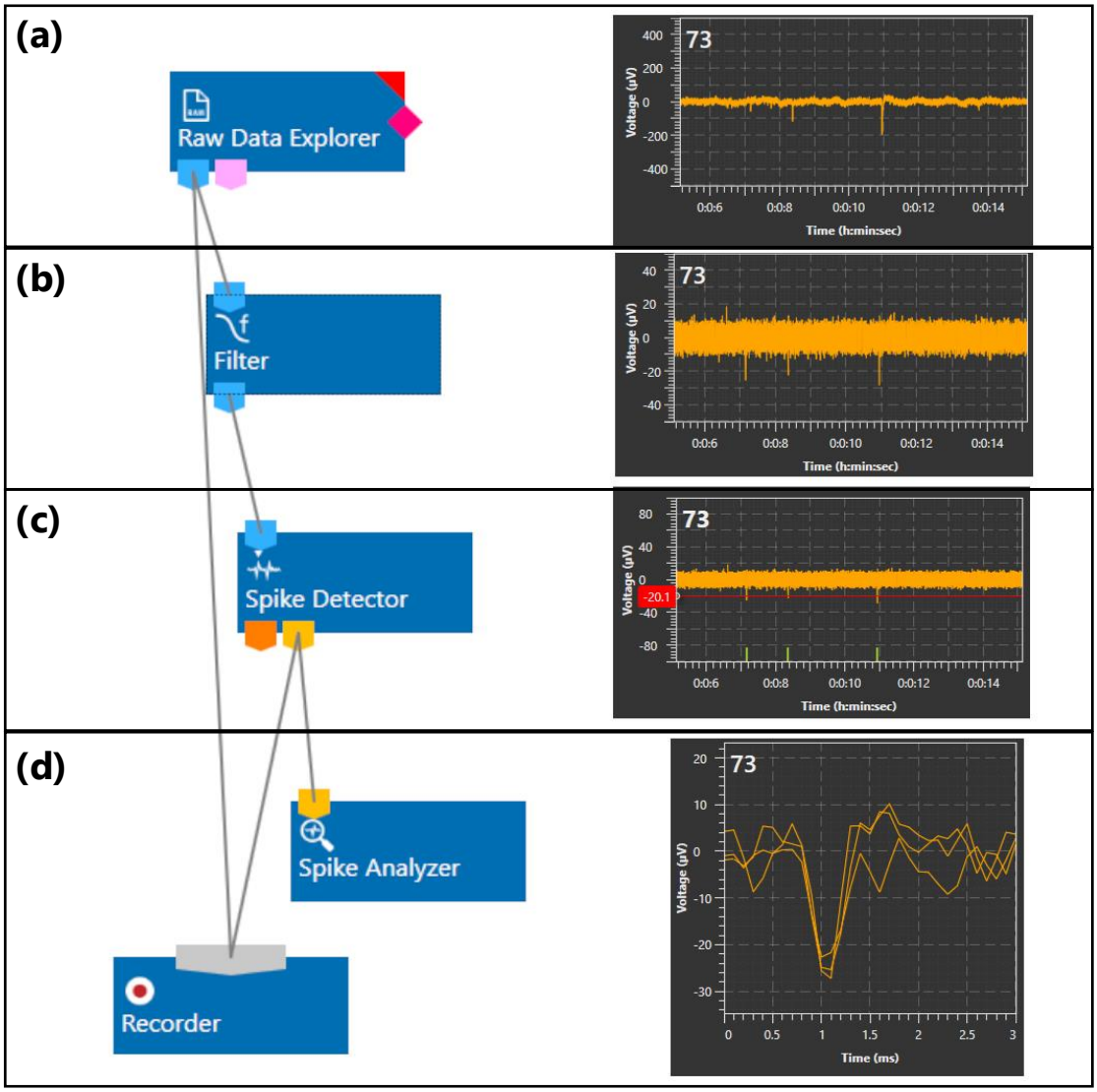

Figure 3.8. Signal processing steps of action potential recordings from the enteric neurons to extract spike properties.

3.4.3. Signal-to-noise ratio measurement with signal generator

To analyze the electronic signal-to-noise ratio of the unstructured and nanostructured electrodes, an external signal generator 60MEA2100-SG (manufactured Multichannel Systems GmbH) simulating the electrogenic activity of hippocampal neurons was used as signal source to record with the same recording device MCS MEA2100mini in DMEM solution (**Figure** 3.9). Ag/AgCl wire has been used as counter/reference electrode.

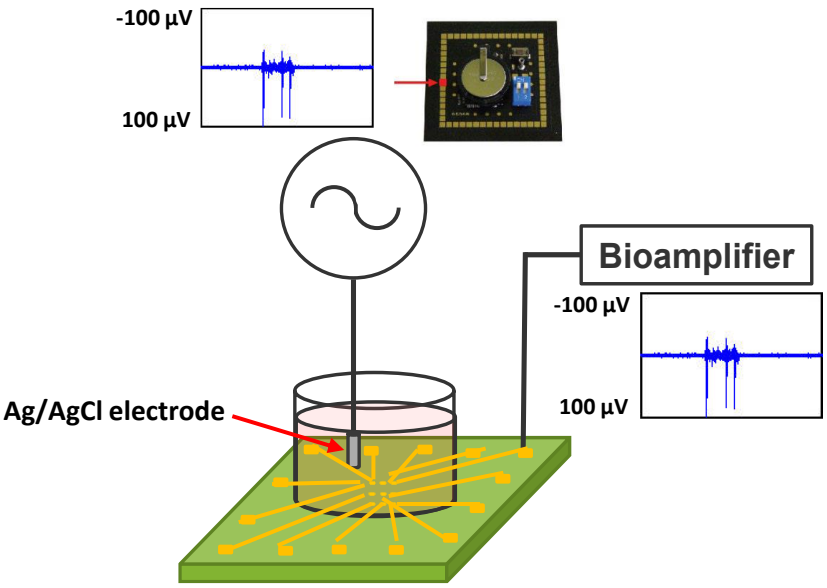

Figure 3.9. Illustration of apparatus used for evaluation of signal-to-noise ratio measurements of the microelectrodes with an external signal generator.

3.5. Fluorescence microscopy

3.5.1. Neuron-astrocyte staining

Enteric neurons were cultured (described in section 3.3) and fixed with 4 % (w/v) formaldehyde solution on DIV 7 on nanostructured gold, unstructured gold and control surfaces. Immunofluorescence staining of neuronal marker was done with Chicken-anti-PGP9.5 and glial marker with Rabbit-anti-S100B. Secondary antibodies Donkey-anti-Chicken 488 and Donkey-anti-Rabbit 594 were used for visualizations. Cell nuclei were stained by DNA intercalating dye 4'6-diamidine-2-phenylindole (DAPI). 10 images of immunofluorescence staining were taken from each surface via reflected light microscopy (**Figure** 3.10a-c). See Appendix IV for standard operating procedure of immunostaining. Total area of PGP9.5 and S100B signals from the different surfaces have been analyzed with ImageJ software and then used to plot raw data, mean values and standard deviation. Analysis of statistical significance of differences was performed via one-way ANOVA with Microsoft Excel software.

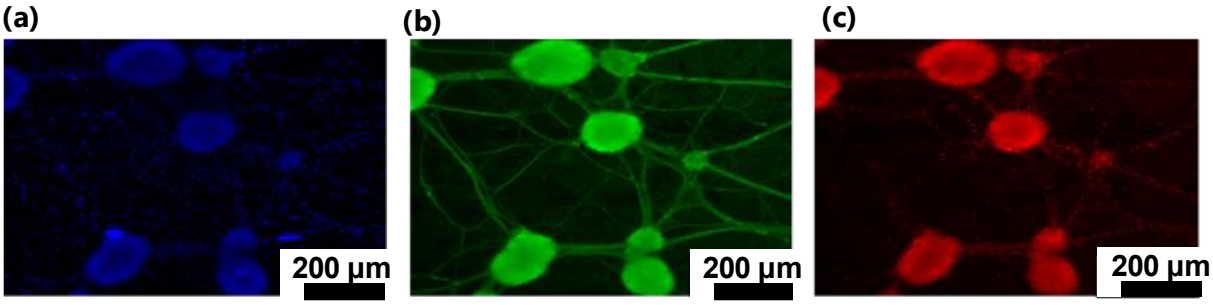

Figure 3.10. Example of immunofluorescence microscopy of (a) cell nuclei marked by DAPI, (b) neurons marked by PGP9.5 antibodies and (c) glial cells marked by S100B antibodies.

3.5.2. Focal adhesion analysis

Focal adhesion analysis of the neurons to the collagen-like gold nanostructured surfaces was done with immunostaining of biomolecules present in the focal adhesion complexes (FACs) and the actin filaments of the cell cytoskeleton. Enteric neuronal culture (described in section 3.3) was seeded on different surfaces and were fixed with 4 % (w/v) formaldehyde solution on DIV 1, 4 and 7. The FACs were stained with primary immunofluorescence marker vinculin monoclonal antibody (purified clone 7F9) and the actin filaments with TRITC-conjugated Phalloidin. Secondary antibodies Donkey-anti-Chicken 488 and Donkey-anti-Rabbit 594 were used for visualization. Cell nuclei were stained by DNA intercalating dye 4'6-diamidine-2-phenylindole. See Appendix IV for standard operating procedure of immunostaining. Over 20 single-cell pictures for each surface and culture period were taken from via reflected light microscopy at 63x magnification and LAS X (**Figure** 3.11a-c).

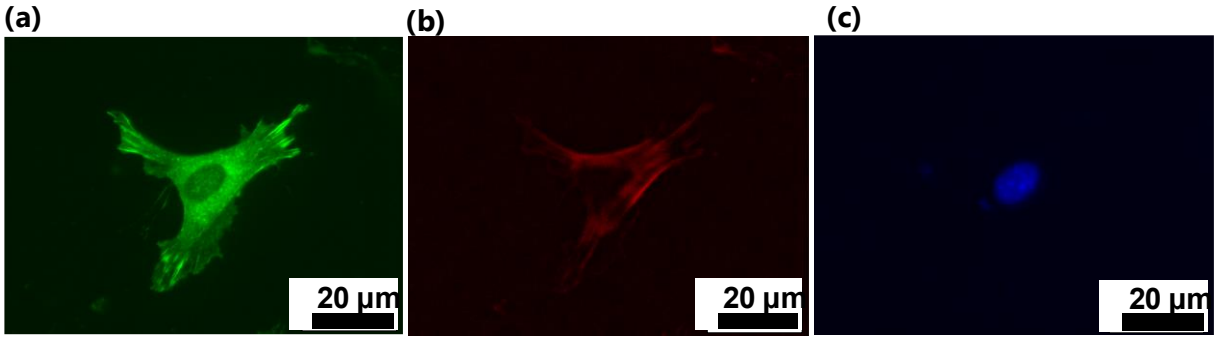

Figure 3.11. Example of immunofluorescence microscopy of (a) FACs marked by anti-vinculin antibodies, (b) actin cytoskeleton marked by phalloidin and (c) cell nuclei marked by DAPI.

The immunofluorescence pictures of the FACs, actin filaments and the nuclei were then processed using ImageJ software. The image processing steps adapted from Horzum et al [120] for the isolation of individual dimension of FACs from the vinculin marked raw image has been described (**Figure** 3.12a-e).

1. For this analysis, the total number of FACs in a unit cell have been segmented and characterized. Therefore, the cell in the raw image was segmented and the background was removed from the image (**Figure** 3.12a).
2. The image was then filtered with Laplacian of Gaussian filter for isolation of the FACs and then with median filter to remove false detection from the cytosol (**Figure** 3.12b).
3. Each isolated FAC was then fitted with and ellipse and a rectangle around its boundary (**Figure** 3.12c-e).
4. The width of smaller axis of the encompassed ellipse (marked by blue circle in **Figure** 3.12e) gave the width of the FAC and the length of the encompassed rectangle (**Figure** 3.12d) gave the length of the FAC.

5. The FACs were then classified based on their longitudinal length in 3 types namely, small (with length below 2 μm), nascent (between length below 2 μm and 6 μm) and mature (with length above 6 μm).

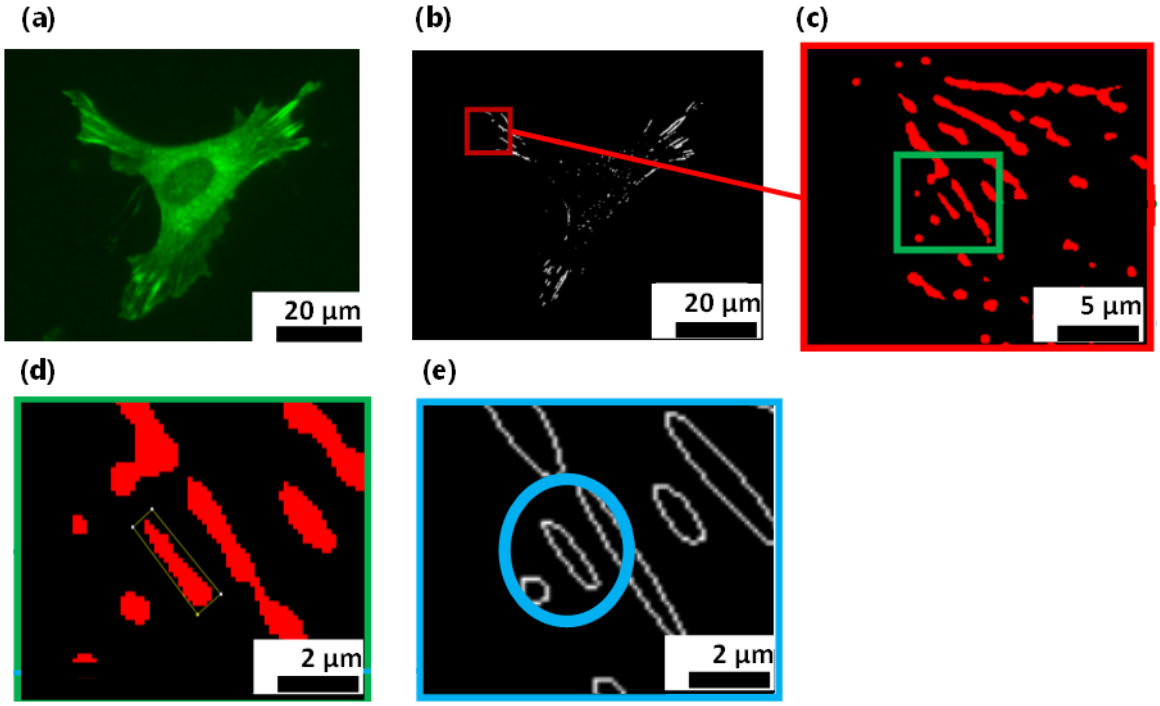

Figure 3.12. (a-e) Image processing steps for extraction of individual FACs from an example of vinculin marked raw microscopy image.

Cell adhesion area of the from phalloidin marked raw image was isolated with the process described by Zonderland et al[121].

1. The phalloidin marked raw microscopy image was first segmented for single cell and removed of the background (**Figure** 3.13a).
2. The cell adhesion area was then isolated with thresholding and binarization methods (**Figure** 3.13b).

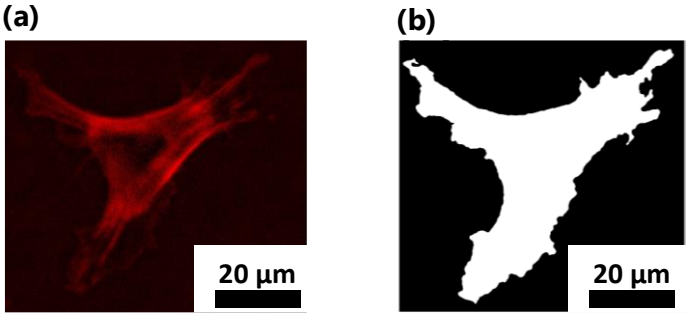

Figure 3.13. (a-b) Image processing steps for extraction of cell adhesion area from an example of actin marked raw microscopy image.

4. Fabrication of biomimetic random nanostructures

In this chapter, fabrication and characterization of biomimetic metallic nanostructures for biosensor functionalization has been presented. Firstly, the randomness pattern of collagen type I fiber network on silicon surface has been evaluated. Afterwards, the dimensional properties of the collagen like-gold nanostructures fabricated from the natural collagen fibers with nanoimprint lithography has been evaluated with surface microscopy methods. Finally, the biomimetic nanostructures were characterized with contact angle measurements and electrochemical impedance spectroscopy.

Results of this chapter selectively published in:
Nowduri, B., Schulte, S., Decker, D., Schäfer, K., & Saumer, M. (2020). Biomimetic Nanostructures Fabricated by Nanoimprint Lithography for Improved Cell-Coupling. Advanced Functional Materials, 30(45), 2004227. https://doi.org/10.1002/adfm.202004227

4.1. Development of silicon master stamp with biological nanostructures for nanoimprint lithography

It has been established in the motivation of the study to use natural biomolecular nanostructures as a template for the replication and fabrication of biomimetic nanostructures, primarily due to their inherent affinity for the growth of cells and secondly due to randomness in their dimensions and organization. Therefore, it is necessary to establish a biomimetic NIL master template with the most feasible biomolecule and its optimum coating density.

4.1.1. Laminin, collagen and other extracellular matrix (ECM) components

Since NIL has been used for this biomimetic replication, the biomolecules are required to be coated on an ultra-planar surface (e.g., silicon wafer, glass wafer, glass slide etc.). Therefore, different biomolecules present in the ECM, as well as the composite mixture, have been coated on silicon wafer with incubation methods. Silicon wafer showed the best biomolecular adsorption and highest surface planarity in comparison to glass and PDMS. Surface profile (100 μm^2) of each incubated surface was measured with AFM. The smallest and largest axial dimension (height) of the biomolecules were measured and summarized in **Table** 4.1.

Laminin (**Figure** 4.1a) and fibronectin (**Figure** 4.1b) incubated surfaces showed nanodimensional features which were very difficult to be measured with AFM and the structures were beyond the limits of nanoimprint-based replication methods. Moreover, the thermal and mechanical properties of the diminished biomolecules have not been documented in literature. Collagen type IV (from bovine calf skin) incubated surfaces on the other hand showed nanostructures with dimensions in the range between 30 and 60 nm (**Figure** 4.1c), but the density of the structures was very small to be replicated into biomimetic nanostructures. This was essential for biosensor application as the density of the nanostructures is directly correlated to the extent of effective surface enhancement. Collagen type I (from bovine Achilles tendon) incubated surfaces solved this issue with distinctive double-helix structures with fiber dimension varying between 10 nm and 2 µm (**Figure** 4.1d). Silicon surface incubated with ECM gel (extracted from mucosal mouse membrane) showed an overall microrough surface profile with RMS roughness to be measured approx. 600 nm due salt deposition from the gel. Hence, isolation of individual nanofeatures would not be possible from the surface profile (**Figure** 4.1e). Considering these factors, collagen type I was selected to be replicated into biomimetic nanostructures. Firstly, the dimensions and organization of collagen fibers showed a 3D random profile, which was the primary goal of this study. Secondly, the features were coated in dimensions that could be replicated with nanoimprint lithography, which was not possible with fibronectin, laminin and ECM composite. Finally, the collagen fibers are well documented for their impeccable strength and temperature tolerance which would be beneficial for nanoimprint lithography [26,27,122]. Moreover, collagen has also been used in literature as a bioink to promote cell adhesion on biosensor surfaces with processes such as inkjet printing and electrospinning [123].

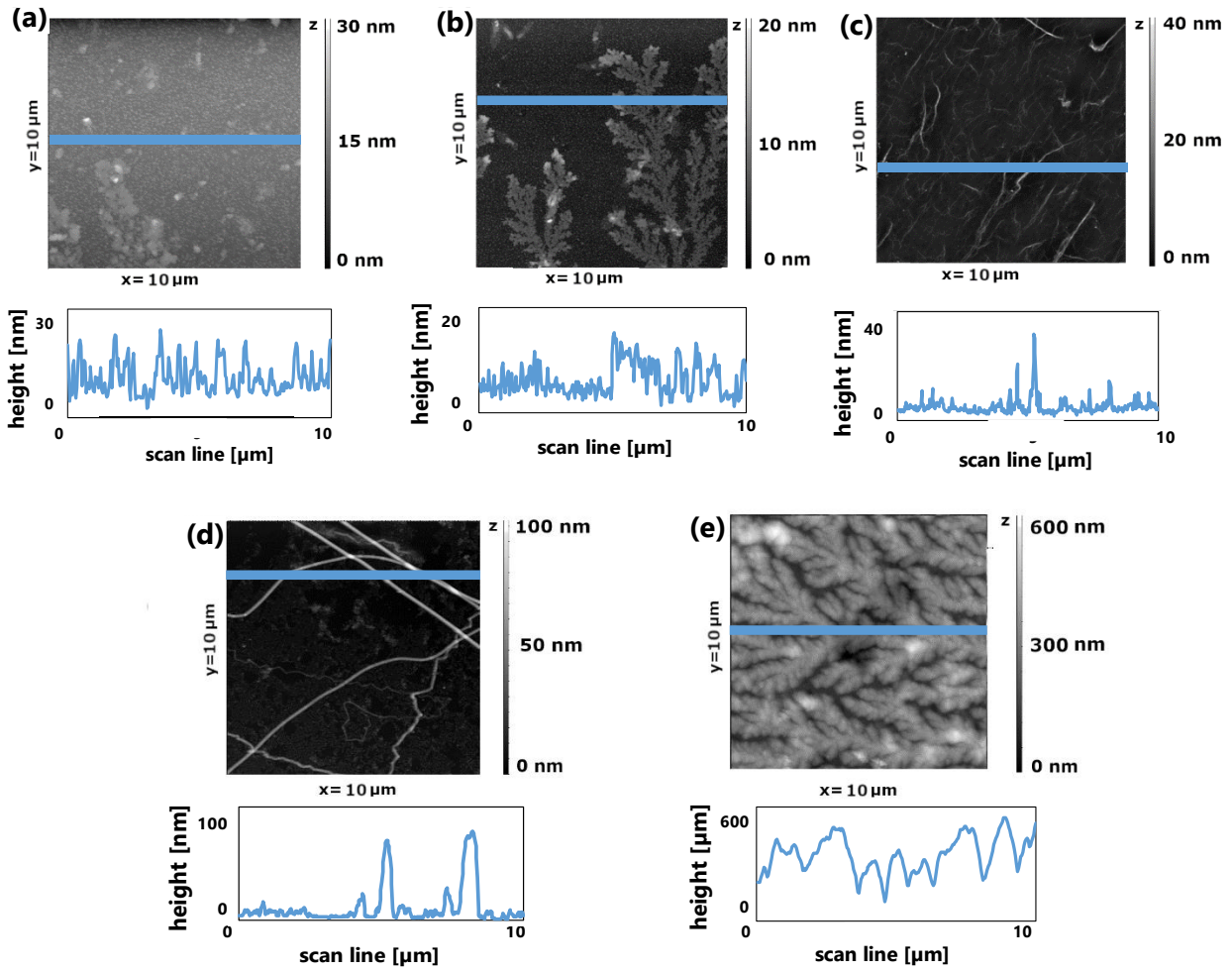

Figure 4.1. Examples of AFM surface profiles of (a) laminin (1:100 mg/ml), (b) fibronectin (1:100 mg/ml), (c) collagen type IV (1:100 mg/ml) (d) collagen type I (1:100 mg/ml) and (e) ECM gel from mucosal mouse membrane (1:100 mg/ml) incubated on silicon wafer.

Table 4.1. Summary of axial dimension (nanostructure height) features of the natural biomolecules present in the extracellular matrix measured with AFM (n = 3).

	Maximum axial dimension (height) [nm]	Minimum axial dimension (height) [nm]
Laminin	28 ± 3.6	4.1 ± 1.8
Fibronectin	17.5 ± 1.3	3.6 ± 0.7
Collagen type IV	37.6 ± 4.8	5.4 ± 4.6
Collagen type I	175 ± 57.7	31.6 ± 8.4
ECM composite gel	585.6 ± 118.2	20.3 ± 12.3

4.1.2. Optimum coating methods of collagen type I for NIL replication

Successful adhesion of collagen type I fibers on to silicon wafer surface has been observed with the incubation process. Even after repeated rinsing with DI water, acetone or isopropanol, the collagen coating was not observed to have lost its structural composition and contact with silicon surface. But the incubation process would be impractical for NIL as the density of the collagen fibers should large enough to be replicated into synthetic metal nanostructures. Therefore, the collagen coating on silicon wafer with other methods such as evaporation in ambient condition has been investigated. The diluted solution of collagen network was placed over the silicon surface and was left to evaporate overnight. Surface profile of collagen fiber network coated on silicon surface with incubation in comparison to evaporation method can be seen in **Figure** 4.2a-b.

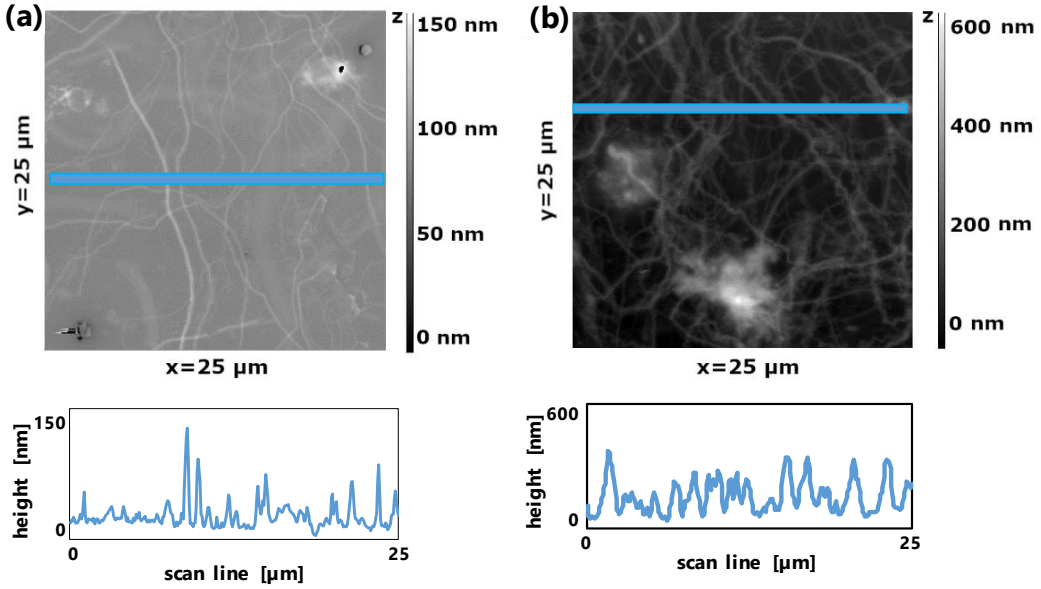

Figure 4.2. Examples of AFM surface profiles of collagen coated silicon wafer with (a) incubation method and (b) evaporation method.

Since all the components in the collagen solution were deposited on the silicon surface, the collagen fiber density was observed to much larger for the evaporated substrate, in comparison to the incubated substrate. Although such a high density of collagen fiber network was desired for the nanostructuring process, the evaporation method failed in homogenous coating of the complete silicon wafer. It was impossible to evaporate the collagen solution on a completely flat surface, which resulted in a flow of solution directed by gravity and one area of the wafer was much densely coated than the other area. Therefore, to incorporate the advantages of incubation and evaporation methods, the collagen solution has been spin-coated on the silicon wafer at a very small angular velocity. This ensured there existed no gravitational flow gradient during the evaporation process and the wafer was homogenously coated with the collagen fibers. Collagen fiber network spin-coated on silicon surface with 100 RPM, 50 RPM and 20 RPM, respectively can be seen in **Figure** 4.3a-c. It is clear that the angular velocity of the spin-coating process is inversely

proportional to the density of the fiber network. Therefore, the silicon wafer spin-coated with collagen solution at 20 RPM angular velocity has been used for nanoimprinting in this study. Density of the collagen fibers was calculated as the ratio of the collagen fiber coverage to the complete measured surface (which for this example was 25 µm x 25 µm). The measured densities of collagen fibers on silicon wafer coated with incubation, evaporation and spin-coating methods can be seen in **Table** 4.2.

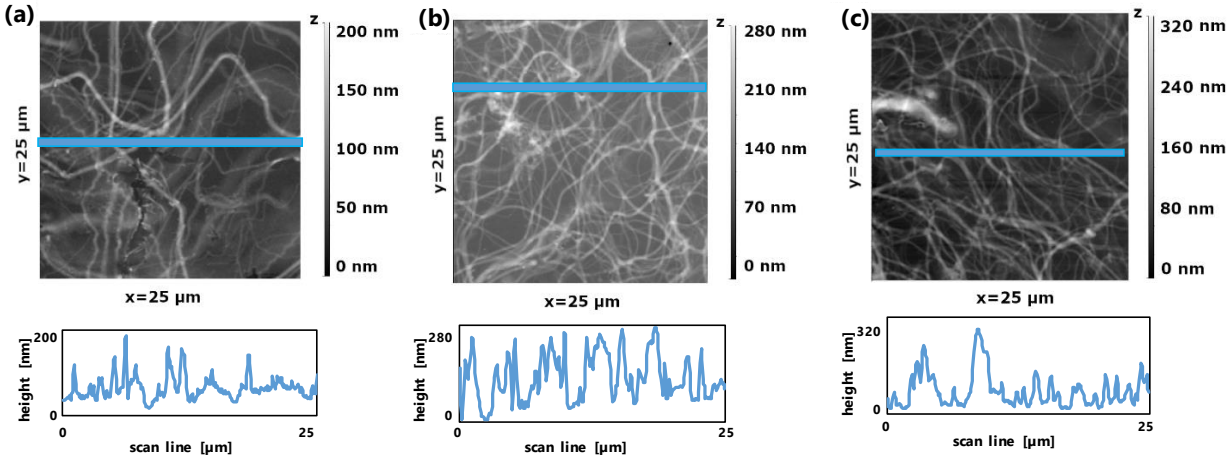

Figure 4.3. Examples of AFM surface profiles of collagen solution spin-coated on silicon wafer with angular velocity (a) 100 RPM, (b) 50 RPM and (c) 20 RPM.

Table 4.2. Dimensional features of collagen type I extracted from bovine Achilles tendon measured with AFM (n = 3).

	Maximum axial dimension (height) [nm]	Minimum axial dimension (height) [nm]	Density of surface coverage [%]
Incubated collagen	149.5 ± 8.2	11.1 ± 1.4	3.4 ± 3.1
Evaporated collagen	561 ± 174.6	10.7 ± 2.8	78.6 ± 12.9
Spin-coated collagen type 100 RPM	187.6 ± 26.4	18.6 ± 2.4	43.1 ± 9.7
Spin-coated collagen type 50 RPM	277.1 ± 38.7	12.4 ± 2.7	52.8 ± 11.1
Spin-coated collagen type 20 RPM	310.2 ± 65.5	183.2 ± 2.2	59.1 ± 9.5

4.1.3. Pattering of collagen coated silicon master

The collagen fibers were coated homogenously on the complete surface of the 4-inch silicon wafer. In principle, this wafer could be used as the master stamp in nanoimprint lithography process. But such a master stamp was impractical for subsequent nanostructure growth. The collagen-like gold

nanostructures were grown by electroplating process which involves estimation of the total structuring area and the charge required to fill the cavities created by nanoimprint lithography. By reducing the collagen coated surface area on the silicon master, the subsequent area for electroplating was also reduced. This was beneficial in improving the control of structure growth and reducing the material required to fill the nanoimprint cavities.

Patterning of collagen fibers on silicon master with photolithography has been done with destructive and non-destructive methods. In destructive pattering process, the silicon wafer was first spin-coated with collagen solution and then photolithography was used to pattern a photoresist on top (**Figure** 4.4a). The open regions of the resist were destructed by oxygen plasma. In non-destructive process, the silicon wafer was first patterned with an image reversal photoresist and then spin-coated with collagen solution (**Figure** 4.4b). The photoresist (along with the collagen fibers on top) was then removed in lift-off process with acetone solution. The collagen coated silicon master has been patterned in this study with destructive process for two reasons. Firstly, due to the hydrophobic nature of the photoresist, spin-coating of collagen fibers on top was very difficult when compared with a hydrophilic silicon surface. Secondly, the edges of the patterned regions were well defined with the plasma etching, which was beneficial in electroplating process.

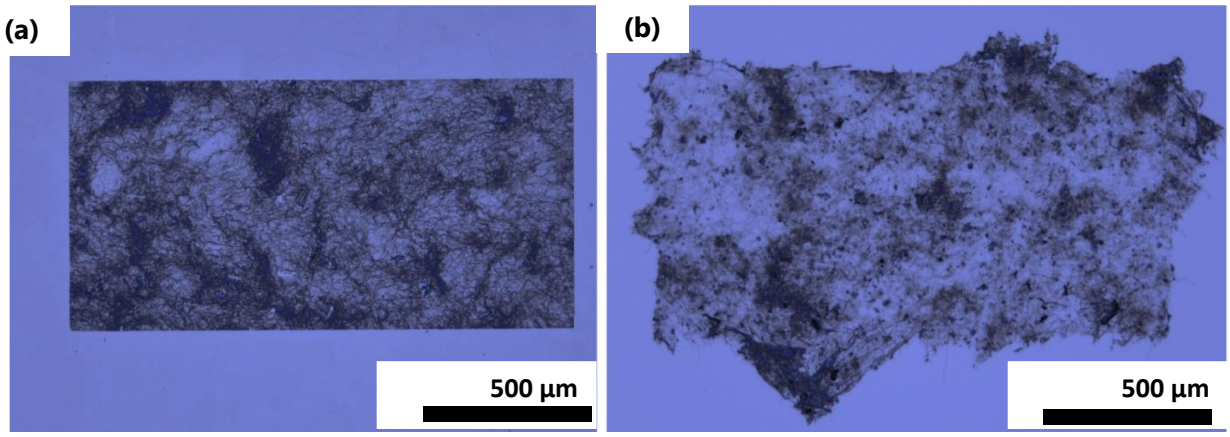

Figure 4.4. Collagen coated silicon master patterned with (a) destructive and (b) non-destructive process.

4.1.4. Collagen coated silicon master for nanoimprint lithography

Collagen fibers, like most natural biomolecules are composed of chains of large hydrocarbons organized in various levels of complexity resulting in formation of matrix of nanofibrils and large fiber bundles [25]. Although collagen fibers possess high degree of mechanical strength and temperature tolerance in comparison to other biomolecules, eventual denaturation and failure is an inevitable process due to its hydrocarbon composition. Thermal nanoimprint lithography (NIL) used in this study for nanostructuring was performed at temperature ranging between 140 °C and 180 °C and at pressure greater than 30 bar. Therefore, the collagen spin-coated silicon master was tested for temperature tolerance by placing the wafer on hotplate with temperature incrementing

from 140 °C to 200 °C for 5 minutes (**Figure** 4.5a-d). No clear evidence of denaturation was observed for collagen fibers up to the temperature of 180 °C. But at 200 °C the fibers were observed to start welting and buckling (**Figure** 4.5d), which was set as the limit of its temperature tolerance.

The pressure tolerance of the collagen coated silicon master was tested in a nanoimprint lithography apparatus, where the master was pressed at room temperature in similar increment steps of 5 minutes ranging from 20 bar to 50 bar against a thermoplastic polymer to counter the local pressure from the collagen fibers (**Figure** 4.5e-h). No evidence of denaturation on the collagen coated silicon master at the highest pressure was observed, which confirms the excellent mechanical strength of the collagen fibers.

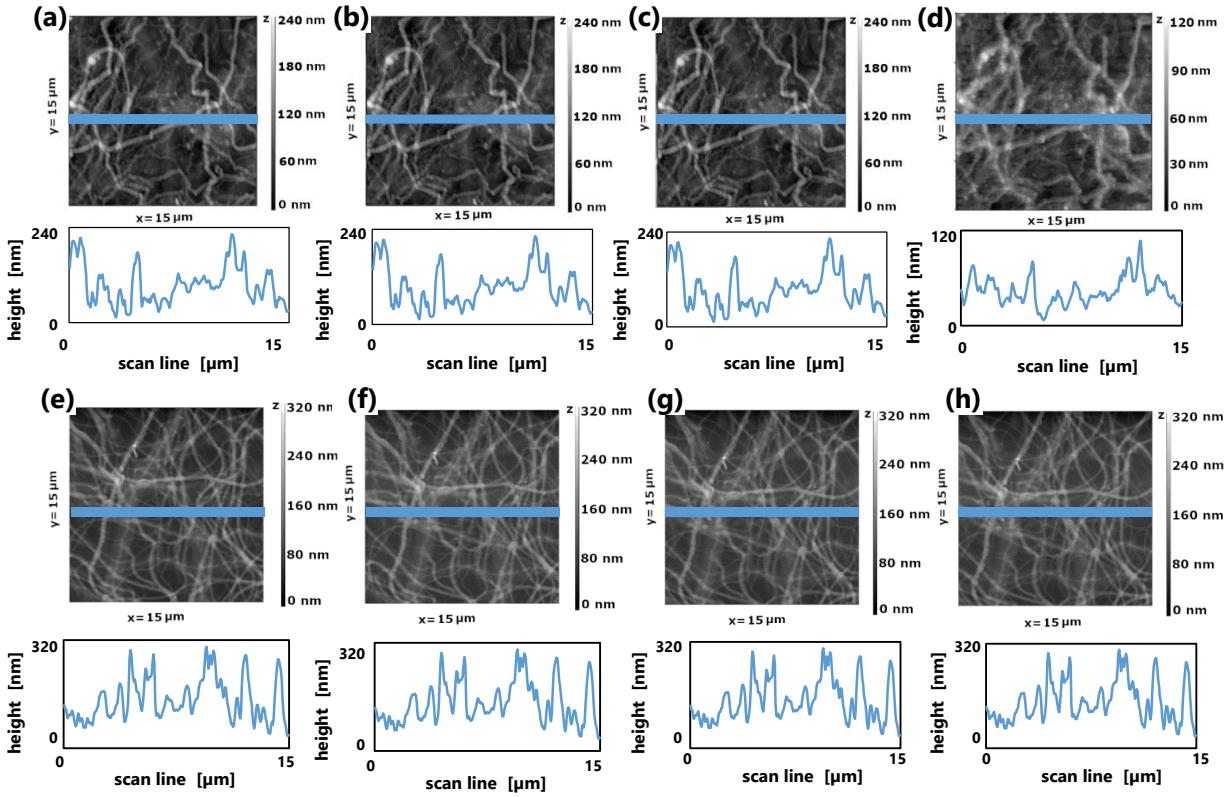

Figure 4.5. AFM surface profiles of collagen coated silicon heated for 5 minutes at (a) 140 °C, (b) 160 °C, (c) 180 °C and (d) 200 °C. AFM surface profiles of collagen coated silicon pressed for 5 minutes at (e) 20 bar, (f) 30 bar, (g) 40 bar and (h) 50 bar in the nanoimprint apparatus.

Finally, the long-term temperature and pressure tolerance of the collagen fibers were evaluated in the NIL apparatus. The collagen coated silicon fibers were imprinted for 5 minutes at 185 °C and 30 bar repetitively for several times, up until of collagen fiber denaturation was observed. The collagen coated silicon master was observed to be stable for 15 nanoimprint processes, after which minor signs of denaturation were visible. Nevertheless, to further improve the lifetime of the

nanostructuring process, intermediate stamps with UV curable polymer stamps can be used for long-term replication.

4.2. Topographical features of collagen-like gold nanostructures (CLGNS)

4.2.1. Replication of smallest reproducible collagen fiber into CLGNS by nanoimprint lithography

It can be observed in **Figure** 4.6a-b that most of collagen fibers on the silicon master were successfully replicated on to evaporated gold in lateral dimensions (width and length), as well as, random orientation. Nevertheless, there are three main challenges with the overall structuring process. Firstly, the collagen fibers with radial dimensions smaller than 40 nm were not replicated into CLGNS on evaporated gold and consequently the density of the CLGNS was smaller as compared to the collagen fiber density on master. Secondly, the larger bundles of the collagen fiber network were composed of striated double-helix profile [124], whereas the CLGNS replicated only the macro-dimension (width and height) for the fiber network. Finally, the collagen fibers present on the silicon master showed random axial dimension (height) varying between 10 nm and 3 µm, but the CLGNS showed uniform height of approx. 40 nm. All these issues are attributed to the fact that growth of CLGNS was a bottom-up fabrication process and the choice of final height of the CLGNS was decided by the smallest reproducible collagen fiber.

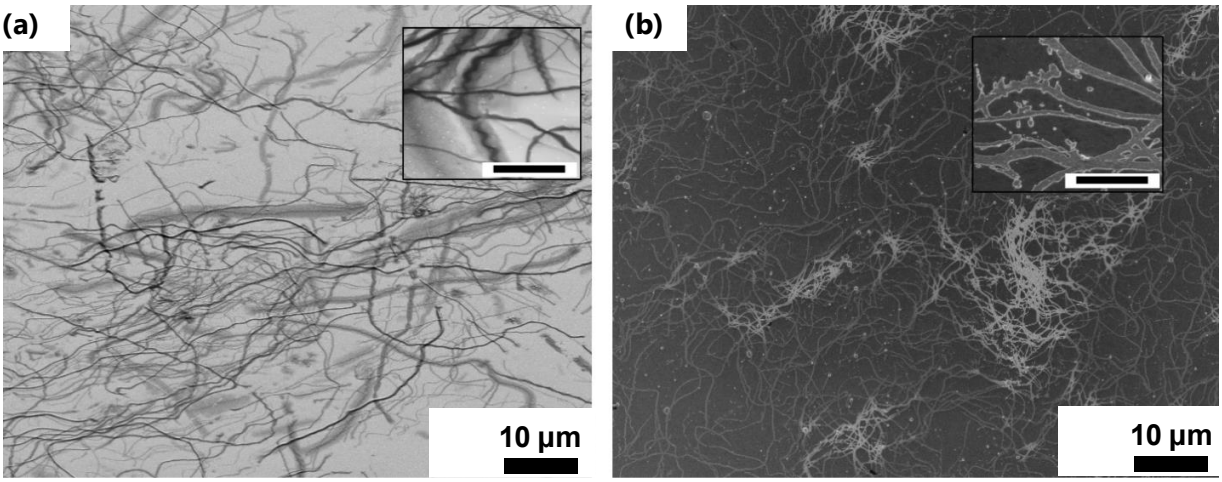

Figure 4.6. SEM images of (a) collagen fibers coated on silicon wafer (inset scale bar 1 µm) and (b) CLGNS developed from the nanoimprint process (inset scale bar 1 µm).

The concept of smallest reproducible collagen fiber has been illustrated in **Figure** 4.7a-c. The initial spin-coated thickness of the NIL resist on the evaporated gold surface was measured to be 450 nm which were optimum for structure transfer and stamp release properties [125]. The cavities created on the nanoimprint resist were measured to have a depth ranging between 10 nm and 230 nm, similar to the dimensions of the collagen fibers on the silicon master (**Figure** 4.7b). For these cavities to be filled with electroplated gold, they should be in contact with the evaporated gold

substrate surface. Therefore, reactive-ion etching was used to gradually remove the residual layer. When 410 nm of the residual layer of NIL resist was etched, the leftover final thickness of the NIL resist is 40 nm. The cavities with depth smaller than 40 nm do not come in contact with the evaporated gold and therefore could not be filled with electroplating (marked by red colored line in **Figure** 4.7b). The information of the collagen fibers with height smaller than 40 nm was not replicated into gold. Therefore, 40 nm is the height of smallest collagen nanofiber which can be replicated into CLGNS (**Figure** 4.7c). The height of the smallest replicable collagen fiber can be set larger than 40 nm in order to increase the CLGNS height (for instance 80 nm as shown in **Figure** 4.7c), but this would lead to further loss of information of the smaller fibers. Also, because of the bottom-up fabrication process, the information at the base of the collagen fiber imprint on NIL resist with double-helix striations were etched with reactive-ion etching. Therefore, the height of the CLGNS is dependent on the two main factors: The electroplating charge per surface area and the thickness of the NIL resist. The surface density of CLGNS was dependent on the density of natural collagen fiber network on the silicon master, as well as, the final thickness of the NIL resist post residual layer etching.

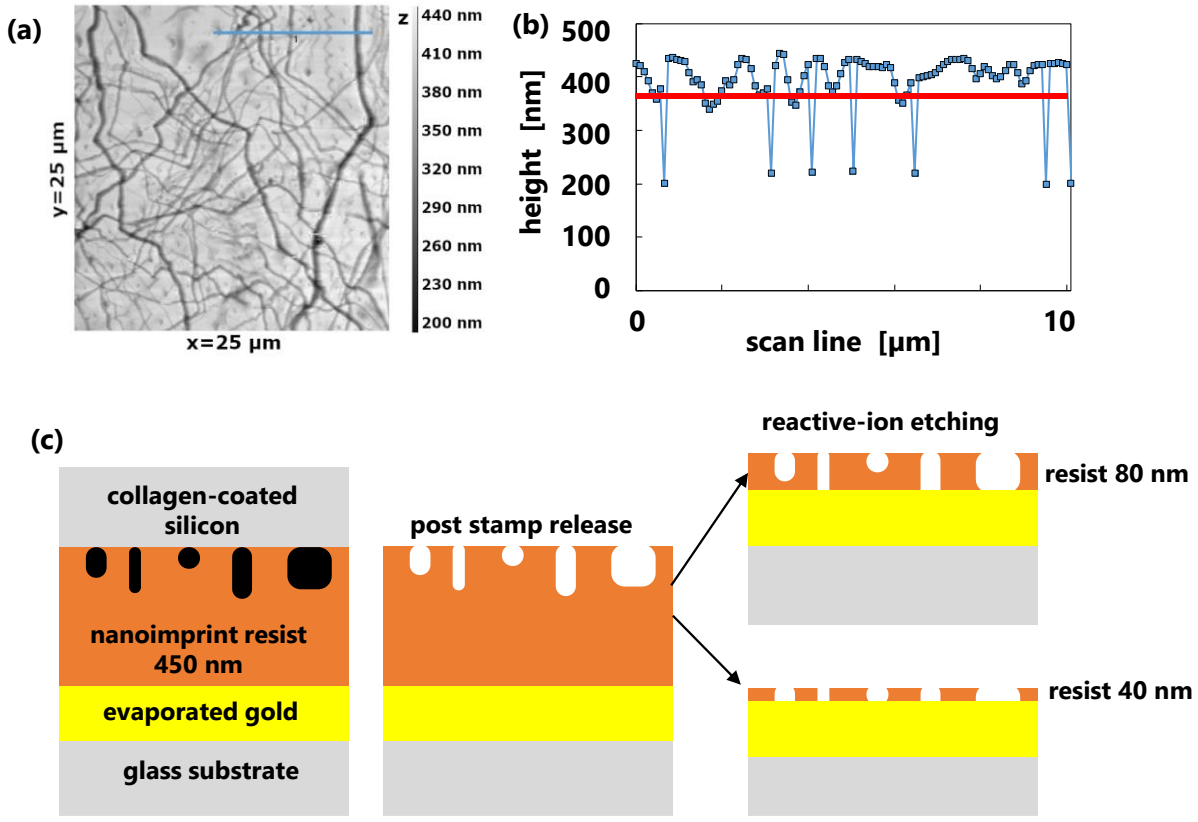

Figure 4.7. (a) AFM profile of nanoimprinted thermoplastic polymer with collagen coated silicon and (b) the scan line (10 µm) of the imprinted surface marked by blue colored line in (a). (c) Illustration of smallest replicable collagen fiber imprinted and subsequently removed of resist residual layer.

4.2.2. Topographical features of CLGNS

AFM measurements of nanostructured gold and collagen coated silicon master surfaces have been used to extract the topographical features such as nanofeature height, width and density. The maximum and minimum dimensions of the fiber structures of the CLGNS on evaporated gold surface and collagen fibers coated on silicon master have been summarized in **Table** 4.3. Initial observations showed successful replication of the collagen fiber random organization into CLGNS. Widths of collagen fibers on silicon vary from 10 nm to 5 µm, whereas the CLGNS have widths varying from 200 nm to 5 µm. To further understand the quality of the biomimetic replication, AFM profile (7 µm x 7 µm) have been analyzed at the exact same location on the collagen master and the nanostructured gold surface (**Figure** 4.8a-b). Dimensions of individual fibers can be compared with the scan lines of the aforementioned AFM profiles at the same starting and ending points (**Figure** 4.8c). For this particular scan line of 4 µm, the measured heights of the collagen fibers were 57 nm, 71 nm and 112 nm. The height of the CLGNS was controlled by the electroplating time and was equal to the height of the smallest reproducible collagen fiber, which was approx. 40 nm and was uniform throughout the entire surface of the substrate evaporated gold surface. The widths of the CLGNS were measured to be almost the same as the collagen fibers on the master stamp (measured at the bottom of the fiber) but marginally wider. This was mainly due to widening of the nanoimprint cavities caused due to the sidewall etching effect during the residual layer removal of the NIL resist [126]. From topographical analysis, the increase in surface area was measured to be 24 % for the nanostructured gold surface in the example of **Figure** 4.8d (20 µm × 20 µm). Total of 10 scans were performed at different locations on the nanostructured gold and collagen coated master to measure a mean increase in the surface area 28 ± 1.7 % and 58 ± 10.4 %, respectively. This increase in surface area is a characteristic of the nanostructuring process with the smallest reproducible collagen fiber to be set as 40 nm. Due to the bottom-up metal deposition (electroplating) approx. 50 % of the collagen fiber information was lost in the NIL-based replication process. It could be resolved if the metal deposition on the NIL resist is done with top-bottom process (e.g. physical vapor deposition) and then separated from the deposited metal.

Table 4.3. Dimensional features of the collagen coated on silicon master and the CLGNS measured with AFM (n =10).

	Maximum lateral dimension (width) [nm]	Minimum lateral (width) dimension [nm]	Maximum axial dimension (height) [nm]	Minimum axial dimension (height) [nm]	Density [%]
Collagen coated silicon master	277.1 ± 38.7	15.6 ± 2.7	254.6 ± 61.7	15.6 ± 2.7	58 ± 10.4
Collagen-like gold nanostructures	1801.1 ± 401.6	95.5 ± 2.7	41.1 ± 1.8	39.4 ± 2.3	28 ± 1.7

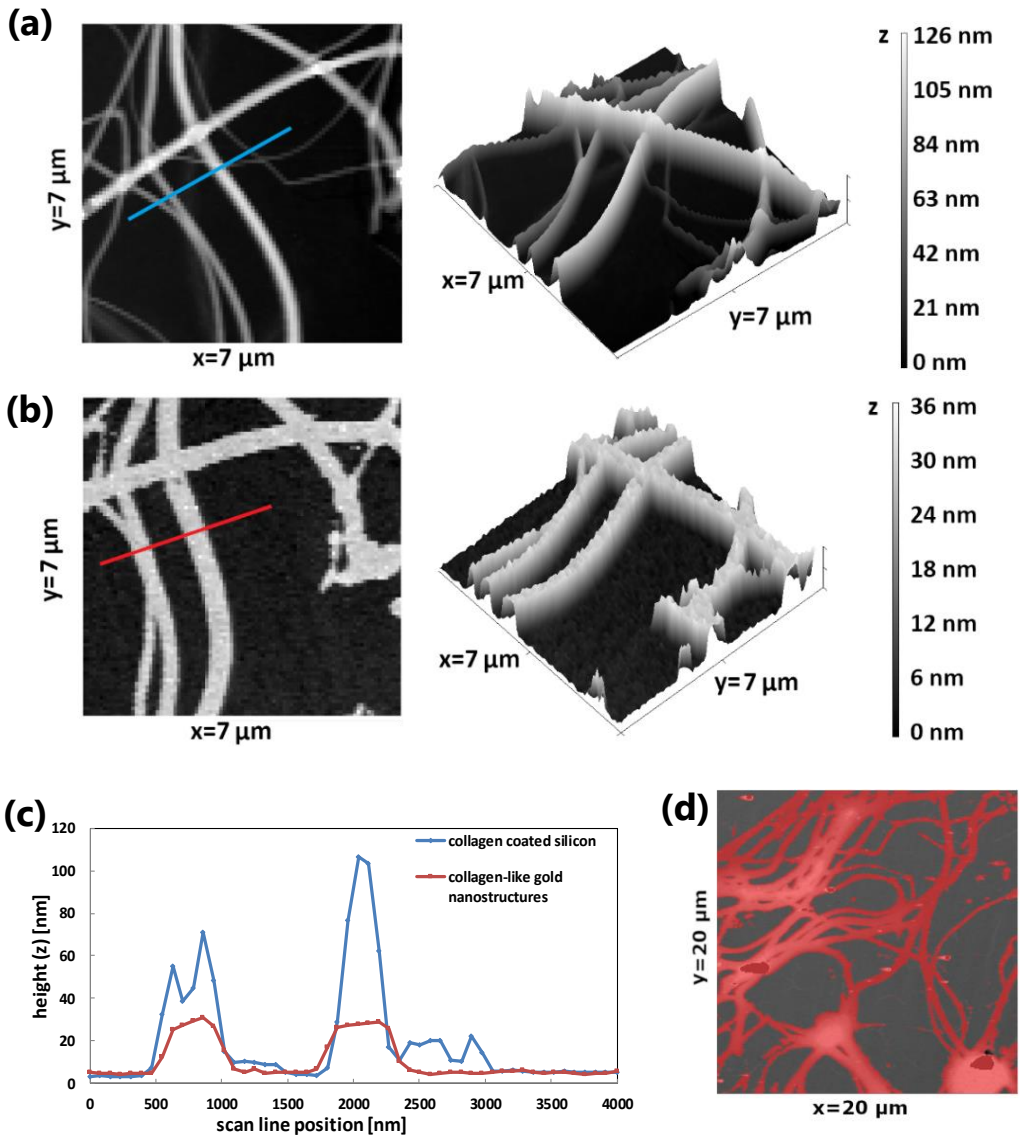

Figure 4.8. AFM surface profile of (a) collagen fibers coated on silicon wafer and (b) CLGNS developed from the nanoimprint process. (c) Comparison of scanned profile line (length 4 µm) from (a,b) marked in their respective colors. (d) Example of surface area marked by thresholding process on the collagen-like gold nanostructured surface.

4.2.3. Randomness analysis of CLGNS

As explained in the Chapter 3, the randomness orientation of the nanostructures can be assigned a profile, i.e., 1D-, 2D- or 3D, depending on number of varying dimensional parameters of the nanostructures. It is clear from the topographical analysis with AFM that the collagen fibers coated on the silicon master vary in height (axial dimension), width (lateral dimension) as well as intrastructural distance and hence they exhibit 3D randomness.

Using a similar bottom-top fabrication nanostructuring approach (with NIL and electroplating), organized symmetric nanostructures have been previous fabricated on gold substrate

(**Figure** 4.9a). The heights of individual nanostructures have a mean of 163.85 nm and the standard deviation was observed to be 1.68 nm, which is 1.2 % of the mean value. The Gaussian distribution of the nanostructure height in this array would show very large probability density function (PDF) (**Figure** 4.9b). The intrastructural distance and the nanostructure width also showed minor variance and this would be a general representation of a symmetric and ordered profile of nanostructures. The same principle has been used for the evaluation of the randomness in CLGNS features from the measured AFM surface profiles.

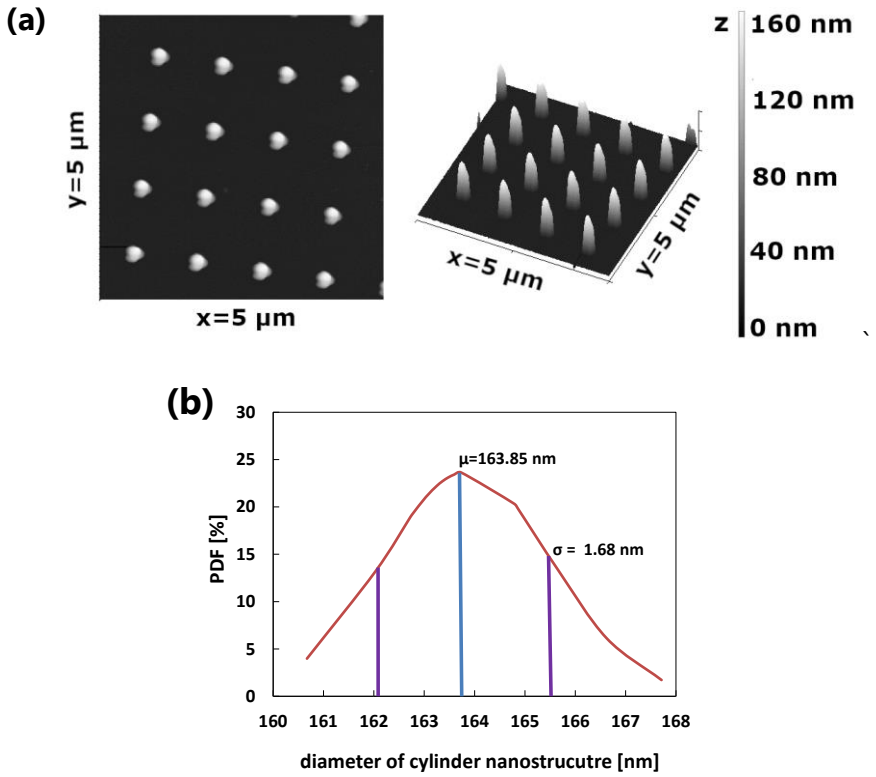

Figure 4.9. (a) AFM image of organized cylindrical gold nanostructures fabricated with nanoimprint lithography. (b) Gaussian distribution (PDF) of the measured lateral dimensions (diameter) of the cylindrical nanostructures with mean **µ** 163.85 nm and standard deviation **σ** 1.63 nm.[†]

Unlike the organized nanostructures, the random biomimetic nanostructures have been segmented and fractionalized with mathematical methods to determine lateral dimension and axial dimension from the AFM profile (**Figure** 4.10a). As the individual fibers were observed to be continuous over the measurement window and isolation of the CLGNS length was not possible.

The aforementioned analysis was performed for a cumulative of 10 AFM surface profiles of CLGNS on evaporated gold, each of measurement area 20 µm x 20 µm. The widths of the CLGNS varied

[†]*Symmetric gold nanostructures fabricated with nanoimprint lithography on gold substrate done by Dominique Decker, University of Applied Sciences Kaiserslautern Germany*.

from a minimum of 220 nm to a maximum of 1800 nm (**Table** 4.3). A total 240 CLGNS units were identified and isolated from the background evaporated gold surface from 20 surface profile measurements. The Gaussian distribution of the CLGNS widths can be seen in **Figure** 4.11a. The mean of the CLGNS width distribution was measured to be 785 nm with a standard deviation of 352 nm. The segmentation method has also been used on SEM image for total area 100 µm x 100 µm (**Figure** 4.10b) with contrast against background as threshold for the nanostructures. A total 3500 CLGNS fibers were identified and isolated from the background evaporated gold surface. Gaussian distribution of the of CLGNS widths can be seen in **Figure** 4.11b. The widths of the CLGNS varied from a minimum of 250 nm to a maximum of 3000 nm. The mean of the CLGNS width distribution was measured to be 826 nm with a standard deviation of 507 nm. For both SEM and AFM CLGNS width distributions, the standard deviation amounted to approx. 40 % of the mean, as compared to 1.2 % in the case of previously mentioned ordered nanostructures. This was definite evidence of the presence of randomness in the dimensions of biomimetic nanostructures. The distribution of CLGNS axial dimension (height) measured for the 240 CLGNS units isolated from the cumulative AFM surface profile measurements can be seen in **Figure** 4.11c. The mean was measured to be 39.87 nm with a standard deviation of 1.36 nm. The standard deviation is measured to be 6 % of the mean, which represented an absence of large randomness in the CLGNS height measurements.

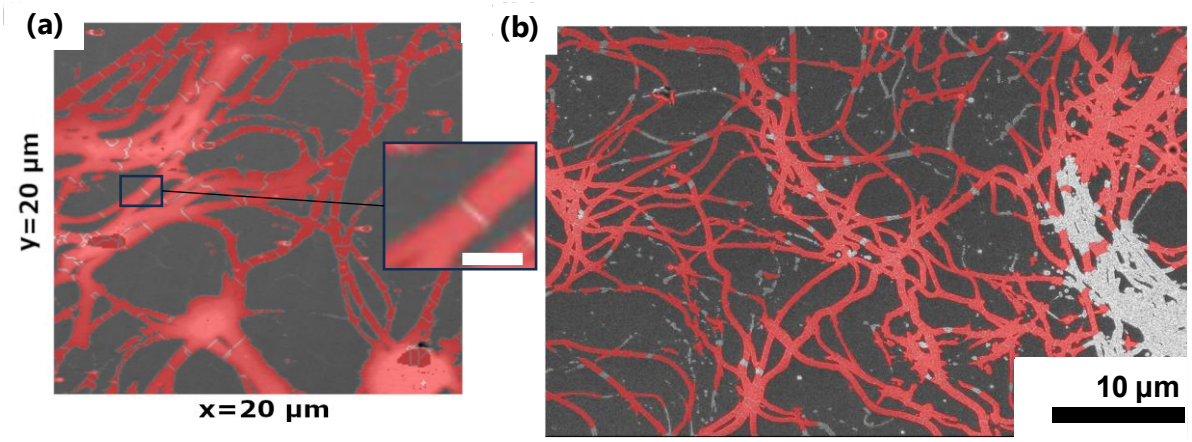

Figure 4.10. (a) AFM (inset scale bar 1 µm) and (b) SEM of CLGNS surface segmented and fractionalized with topographical methods for extraction of CLGNS lateral dimension (width).

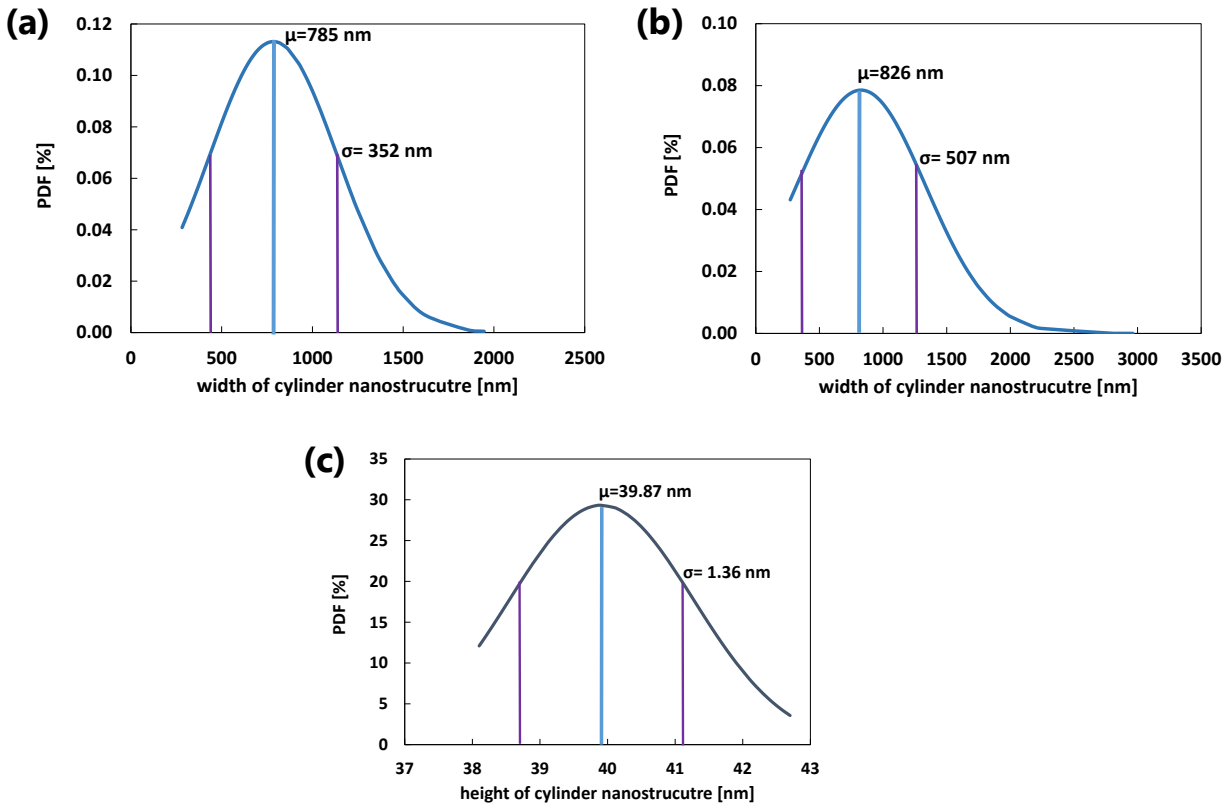

Figure 4.11. Gaussian distribution (PDF) of the measured lateral dimensions (width) of the CLGNS with (a) AFM measurements with mean **μ** 785 nm and standard deviation **σ** 352 nm (n = 240) and (b) SEM measurements with mean **μ** 826 nm and standard deviation **σ** 507 nm (n =3500). (c) Gaussian distribution of the measured axial dimensions (height) of CLGNS with AFM measurements with mean **μ** 39.87 nm and standard deviation **σ** 1.36 nm (n = 240).

4.2.4. Reproducibility of nanostructuring process

Reproducibility is the qualitative property of the nanostructure fabrication process which can be defined by the extent to which the replication of collagen fibers on silicon master to CLGNS changes over several repetitions, whilst keeping the process parameters same. To measure this property, the same collagen coated silicon master was used for making several copies (16) of CLGNS surfaces (on gold evaporated substrates) with NIL and the surface profile of one particular CLGNS fiber at the exact same location was measured for each repetition. AFM cross section of CLGNS for multiple repetitions and the master collagen fiber can be seen in **Figure** 4.12a-b.

As previously explained, the height of collagen on the master fiber is much larger than that of the corresponding CLGNS due to the bottom-up fabrication approach. Nevertheless, the CLGNS height and width of all the subsequent replicated surfaces were measured to have exactly same dimensions. This is a testament to the nanostructuring process which shows a high degree of reproducibility. The collagen coated silicon master was not used for more than 16 imprints, as the

collagen fiber networks started to show signs of denaturation which was already established from the temperature tolerance experiments.

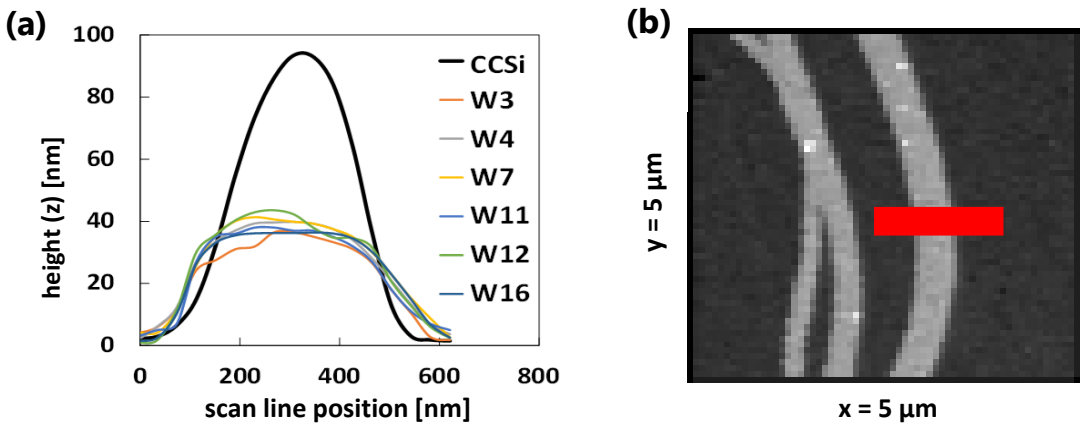

Figure 4.12. (a) Nanostructure profile comparison of a single CLGNS for several copies of nanostructured gold wafers (n = 6) with the replicating (b) collagen fiber measured with AFM. CSSi refers to collagen fiber profile of collagen coated silicon master to be replicated. W3 is the third nanostructured gold wafer fabricated from the process, whereas W16 refers to the 16th nanostructured gold wafer.

4.3. Physicochemical characterization of CLGNS

Presence of nanostructures on a metallic surface has the primary effect of increasing its effective surface area, which has been established in the previous section with surface microscopy methods such as AFM and SEM. In this section, the physical and chemical effects induced by CLGNS biomimetic nanostructures, as well as, their possible implications for biosensor application have been explained in detail.

4.3.1. Surface wetting characterization

The most common method to visualize the wetting ability of surfaces is by sessile drop contact angle measurements. Contact angle (CA) for the substrates is formed at the interface between solid surface (unstructured and nanostructured gold), the analyte fluid (distilled water droplet) and the ambient atmosphere. In principle, smaller the measured CA of the sessile drop, larger is the hydrophilicity and surface wetting. Effect of nanostructures contributing to the hydrophilicity is largely dependent on the regime in which the fluid interacts with the nanostructured surface [127]. For example, a highly dense nanorough topography would push the surface to be hydrophobic and a sparsely dense nanorough surface would make the surface hydrophilic [128]. In this study the CA of nanostructured surface was measured and compared with unstructured gold and collagen coated silicon surface (which used as the master stamp in the NIL process) (**Figure** 4.13a-c).

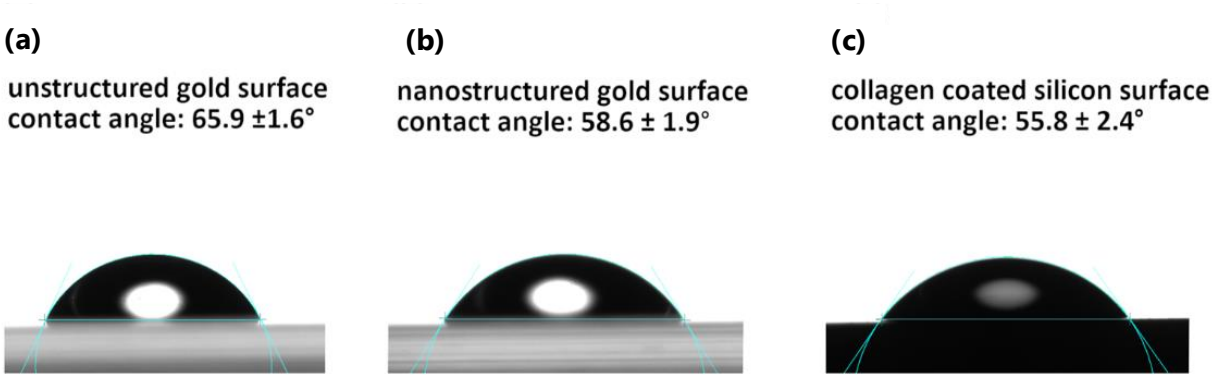

Figure 4.13. Sessile drop contact angle measurement with distilled water droplet (5 µL) on (a) unstructured gold, (b) nanostructured gold and (c) collagen coated silicon surface.

It can be observed that the CA for nanostructured gold was measured to be 15 % lower than that of unstructured gold (n = 6). Collagen coated silicon has an even smaller CA which was the improvement desired. But this is harder to accomplish since the interfacial free energy of silicon is higher than that of gold [129-130]. Moreover, the collagen fibers have an inherent negative surface charge due to their composition, which would further aid in reducing the contact angle measurement [131].

Changes in wettability of the gold surfaces induced by the CLGNS can been evaluated by static CA measurements. But to quantify the surface wettability of the surfaces, critical surface energy (CSE) has been calculated with Zisman method. Contact angles of the surfaces have been measured with fluids of different surface tension and the cosine of the measured values have been extrapolated to 0° to obtain the CSE. Larger CSE indicates overall higher wettability of the surface and vice versa. The measured values of the CA can be seen in **Table** 4.4 and the calculated CSE of the surfaces estimated from the Zisman method can be observed in **Figure** 4.14. As observed with the static CA measurements, enhancement in CSE by 33 % was measured for nanostructured gold in comparison to unstructured gold. Nevertheless, the maximum CSE was observed for collagen coated silicon master, which is the improvement desired for the nanostructured gold. The increase in surface wettability of the nanostructured gold suggests that the CLGNS height and density influences the gold surface to be in Wenzel regime of surface wetting [128]. Increase in surface wetting by synthetic nanostructures have been shown to improve the cell attachment, spreading and cytoskeletal organization in literature [132-133], which could be a major advantage in biosensor application.

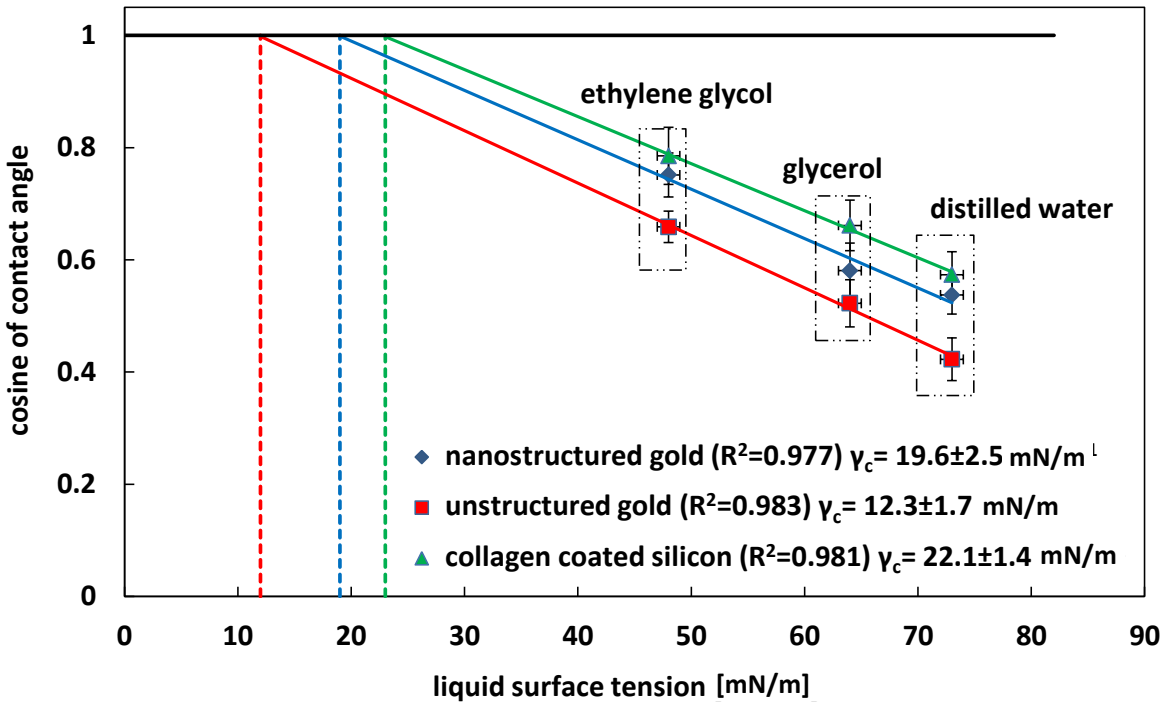

Figure 4.14. Zisman plot and CSE measurement (γ_c) of unstructured gold, nanostructured gold and collagen coated silicon surface measured from contact angle measurements with distilled water (surface tension 72.8 mN/m @ 20 °C), ethylene glycol (surface tension 47.7 mN/m @ 20 °C) and glycerol (surface tension 64 mN/m @ 20 °C)] (n = 6) [134]. The measurement points represent the mean of the cosine of contact angles per fluid and the bars represent the standard deviation. The colored bold lines represent the linear regression and the colored dotted line represent the extrapolation of liquid surface tension to cosine 1 (where contact angle is zero) of each surface. The linear regression for each surface was performed on all measurement points and the error of CSE was calculated by computing the mean absolute error.

Table 4.4. Static contact angle and critical surface energy measured with Zisman method for different surfaces (n = 6).

	Static contact angle with distilled water [°]	Static contact angle with glycerol [°]	Static contact angle with ethylene glycol [°]	Critical surface energy γ_c [mN/m]
Collagen coated silicon master	55.8 ± 2.4	48.5 ± 1.4	38.2 ± 1.4	22.1 ± 1.4
Collagen-like gold nanostructured gold surface	58.6 ± 1.9	56.5 ± 1.3	41.5 ± 1.3	19.6 ± 2.5
unstructured gold surface	65.9 ± 1.6	58.1 ± 1.8	48.8 ± 1.6	12.3 ± 1.7

4.3.2. Electrochemical impedance characterization

Electrochemical impedance spectroscopy presents quantitative information on the electrochemical properties of a conductive surface especially in a fluidic medium, which can be utilized to characterize signal-transfer properties of electrode surfaces of a biosensor. Nanostructured and unstructured macroelectrode surfaces with 20 mm^2 (circle with 5 mm diameter) were both characterized with EIS measurements in a three-electrode potentiostatic setup with 10 mV input voltage in a frequency range between 1 Hz and 100 kHz.

Comparison of impedance magnitude and phase measurements for nanostructured and unstructured macroelectrodes can be observed in **Figure** 4.15a-b. The most significant influence of nanostructures on the gold surface was observed at frequencies below 1 kHz. 54 % reduction in the impedance magnitude (at 1 kHz) was observed for nanostructured gold over unstructured gold. Similarly, the influence of nanostructures on phase shift was observed at frequencies below 1 kHz, which corresponds to higher capacitive contribution in the impedance transfer function.

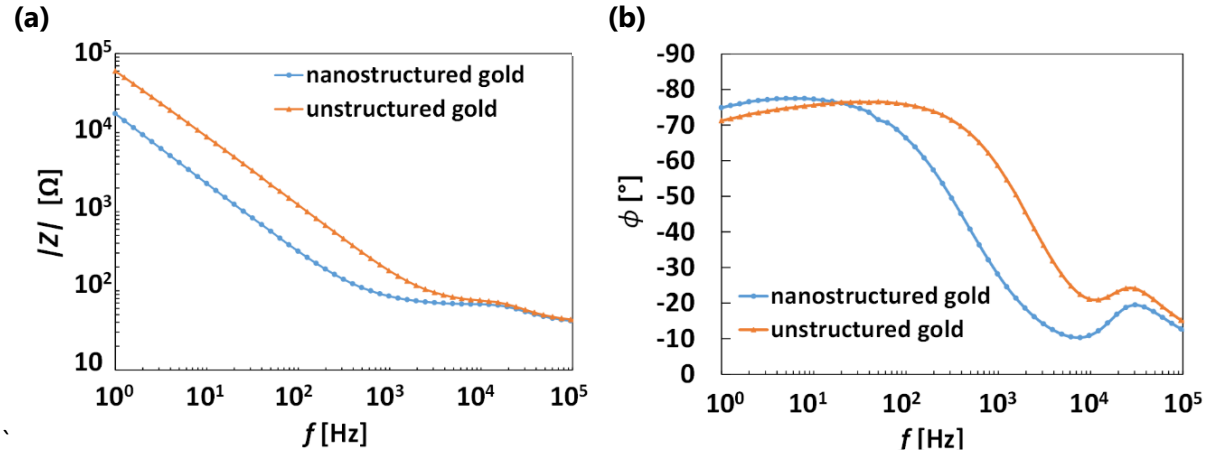

Figure 4.15. Electrochemical impedance spectroscopy of nanostructured and unstructured gold electrodes (w/v) showing (a) the magnitude of the impedance |Z| and (b) the corresponding phase $\boldsymbol{\varphi}$.

The impedance transfer function of the electrode is comprised of electrochemical interactions occurring the interface between electrolyte solution and the electrode surface, which includes double-layer capacitance, charge-transfer resistance and electrolyte resistance. These individual components as well as the global impedance plays a significant role in determining the thermal noise of the microelectrode. The global impedance (Z) is correlated to the baseline thermal noise ($\boldsymbol{v}_{thermal}$) with the **Equation** 4.1, where is the k_B Boltzmann constant, T is the temperature, and Δf is the frequency range [135].

$$\boldsymbol{v}_{thermal}^2 = 4.k_B.T.\Delta f.Z \qquad \textbf{Equation } 4.1$$

Reduced global impedance of the nanostructured surface signifies a smaller noise and consequently enhanced signal-to-noise ratio in biosensor recordings. It is known that the electrophysiological activity from cardiac or neuronal cultures lies in the frequency range between

10 Hz and 2000 Hz [136-138]. Since a significant reduction in impedance magnitude caused by CLGNS was observed in this frequency range, the nanostructuring process would be beneficial for electrophysiological biosensor applications such as microelectrodes, needle electrode etc.

Nyquist representation in the imaginary and real parts of the measured impedance spectrum can be seen in **Figure** 4.16a-b. For easier understanding, the impedance Nyquist spectrum has been divided into high frequency and low frequency regions. The semicircle region in **Figure** 4.16a is a representative of the high frequency measurements (1 kHz-100 kHz), where the charge-transfer processes are dominant [139]. The straight lines in **Figure** 4.16b are a representative of the low frequency measurements (1 Hz-1 kHz) where the diffusion processes are dominant [139].

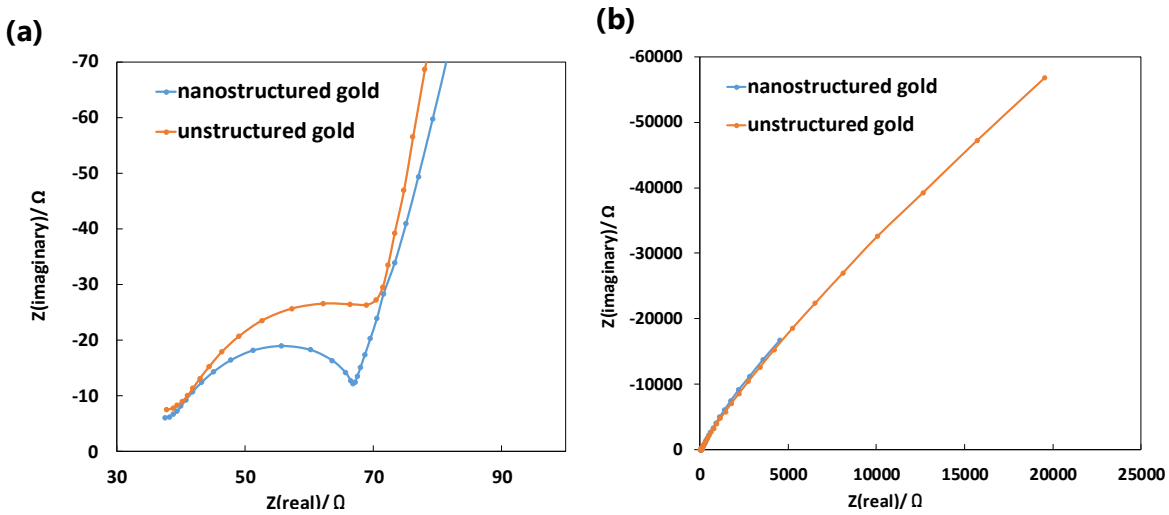

Figure 4.16. Nyquist representation of impedance spectroscopy measured for nanostructured and unstructured gold (a) in high frequency range 1 kHz-100 kHz and (b) in low frequency range 1 Hz-1 kHz.

To further evaluate the individual resistive and capacitive components of the Nyquist impedance spectrum, the measurements have been mathematically fit into an electrode equivalent circuit representing charge-transfer mechanisms occurring at the electrode-electrolyte interface (**Figure** 4.17a-b). The equivalent circuit (**Figure** 4.17c) consists of the previously mentioned double-layer capacitance (C_{dl}), charge-transfer resistance (R_{ct}), electrolyte spreading resistance (R_s), Warburg diffusion (W) and the capacitance-resistance (C_{ref}-R_{ref}) pair contributed by the reference electrode. As expected, the most predominant effect of the CLGNS was observed with the increase in double-layer capacitance with minor reduction in charge-transfer resistance. The impact of the CLGNS on other components (W, R_s and C_{ref}-R_{ref}) was negligible as they are a function of the measurement apparatus rather than the electrode surface. Results of impedance spectroscopy measurements and fitted equivalent circuit calculations have been summarized in **Table** 4.5.

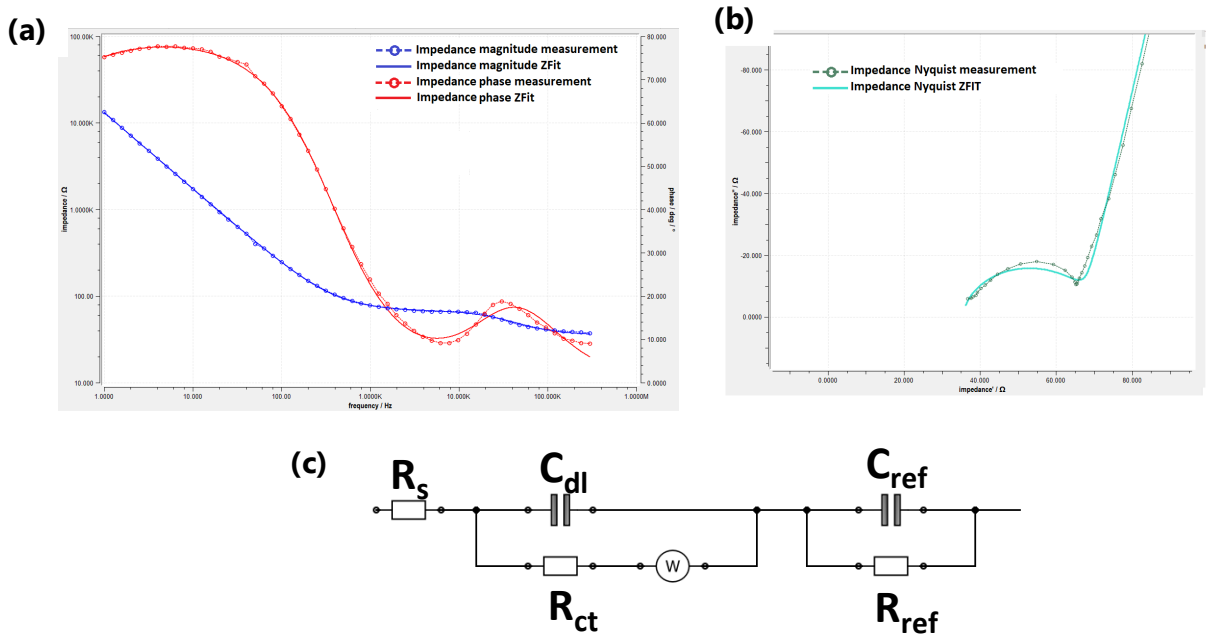

Figure 4.17. (a) Impedance magnitude-phase and (b) Nyquist plot fitted with the electrical equivalent circuit (c) depicting the nanostructured electrode surface.

The double-layer capacitance at the electrode-electrolyte interface is formed by the inner Helmholtz plane consisting of the adsorbed water molecules on the electrode surface and the outer Helmholtz plane consisting of the hydrated counter ions attracted by the applied electric field [70]. CLGNS on the microelectrode surface effectively enlarged the area of the Helmholtz planes and simultaneously reduced the distance between the planes, which eventually leads to enlargement of the double-layer capacitance. Nanostructures also raise the active sites for chemical reaction across the electrode causing a decrease in charge-transfer resistance [75].

Table 4.5. Electrochemical impedance spectroscopy measurements performed for collagen-like gold nanostructured surface and unstructured gold surface (n = 12).

	Impedance magnitude at 1 kHz [kΩ]	Impedance phase at 1 kHz [°]	Double-layer capacitance calculated from equivalent circuit [nF]	Charge-transfer resistance calculated from equivalent circuit [kΩ]
Collagen-like gold nanostructured gold surface	85 ± 6.3	-27 ± 2.5	60 ± 12.7	2.03 ± 0.49
unstructured gold surface	180 ± 19.8	-61 ± 2.1	32 ± 16.9	2.77 ± 0.61

4.4. Summary and outlook

In this chapter, the fabrication process of biomimetic nanostructures developed with electroplated gold with nanoimprint lithography has been presented. There have been studies illustrating the biomimetic nanostructures with soft lithography methods with biocompatible polymers such as PDMS [28]. But the non-conductive nature of the polymer would be impractical for metallic biosensor surfaces. There have also been other studies where nanoimprint lithography has been used for fabrication of organized nanostructures on metallic surfaces [41]. But since randomness in the nanostructures is the key requirement for the replication of natural nanorough environment, the biomimetic nanostructuring method described in this study is one of the pioneers in the fabrication of truly random nanostructures. AFM and SEM measurements have shown the 2D randomness in spatial organization and lateral dimension of the CLGNS. The reproducibility of the process has also been observed over 15 repetitions of nanostructuring process with the same collagen coated silicon master stamp. This was a compelling result of the nanostructuring process, as lack of high reproducibility is one of the major drawbacks of natural nanostructuring methods (such as ECM and collagen coatings). Surface wetting analysis with contact angle measurements showed an increased hydrophilicity induced by the CLGNS. Increased hydrophilicity has shown to be beneficial for cell surface adhesion by multiple studies [104,132-133]. Impedance measurements have shown reduced impedance magnitude for the nanostructured gold surfaces which would eventually result in superior charge-transfer properties, especially for biosensing application. Along with surface characterization, cell culture experiments to evaluate the cell growth, proliferation and adhesion would be further beneficial for biosensing application, which has been presented in detail in Chapter 6.

Despite successful replication of the collagen fibers network to random biomimetic nanostructures with superior surface properties, the fabrication process suffered from certain major limitations. Firstly, the loss of axial randomness information from the natural collagen network. The nanostructuring process described in this chapter has bottom-up structure growth fabrication, which resulted in the CLGNS to have fairly uniform height. Also, the striated topography of the larger collagen fibers could not be replicated due to the same reason. Therefore, the CLGNS exhibit 2D randomness profile as compared to the true form of 3D randomness existing in collagen fiber network on silicon master. Secondly, artefacts of gold electroplating arising due to a very small thickness of the NIL resist could also be observed on the nanostructured surface. Nevertheless, the increase in overall effective surface area due to these artefacts do not significantly contribute to the overall surface or electrochemical properties of the nanostructured gold surfaces.

Despite its limitations a major advantage of the nanostructuring process was its versatility and it could be used for several metallic biosensor applications. **Figure** 4.18a-b shows examples of two such applications, where the CLGNS have been structured on the surface of microelectrodes and micro-heater meander pattern, respectively. Microelectrode arrays are biosensor devices used for the measurement of electrophysiological activity from neurons and cardiomyocytes. Structuring

of microelectrodes with CLGNS would enhance the neuronal adhesion due to its biomimetic topographical features. CLGNS would also improve signal transmission by boosting the signal-to-noise ratio as suggested by reduction in global impedance of the microelectrodes. Similarly, nanostructured meander pattern could be used to guide cells on a biosensor surface for drug delivery application [140].

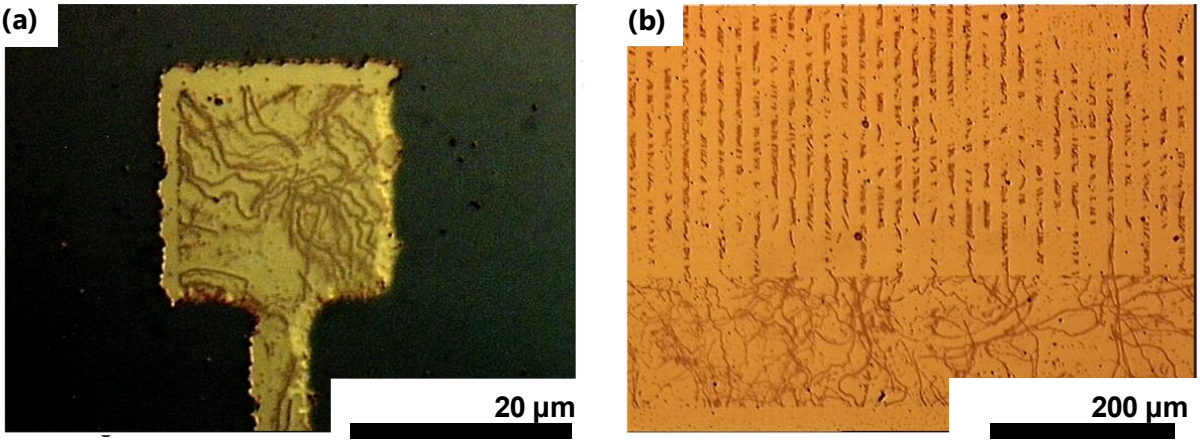

Figure 4.18. Application of CLGNS nanostructuring process on (a) microelectrode array surface and (b) micro-heater meander pattern.

5. Biomimetic nanostructured microelectrode arrays: Characterization and application

The enlarged effective surface area of the collagen-like gold nanostructures had resulted in a stark increase in surface wetting, as well as, reduction in global impedance. In this chapter, the application of the biomimetic nanostructures on microelectrode surfaces has been presented and then electrochemical and physical modifications induced by the nanostructures have been characterized. Afterwards, the modifications induced by the nanostructures on extracellular activity recordings and seal impedance measurements from neuronal cells have been illustrated.

Results of this chapter selectively published in:
Nowduri, B., Schulte, S., Jolfaei, N. A., Decker, D., Rabe, H., Schäfer, K., & Saumer, M. (2023). Advanced Biomimetic Nanostructured Microelectrode Arrays for Enhanced Extracellular Recordings of Enteric Neurons. Advanced Materials Interfaces, 10(16). https://doi.org/10.1002/admi.202300023.

5.1. Fabrication of biomimetic nanostructured microelectrode arrays

Fabrication of functional microelectrode array (MEA) biosensors for electrophysiological application would necessitate optimum charge transfer properties at wafer scale. Therefore, gold lithography methods, electrode spacing and dimensions, biosensor assembly and selection of passivation layer have been briefly discussed here.

The nanostructured microelectrode arrays (MEAs) in this study were fabricated on glass substrate wafers evaporated with gold as electrode layer. The nanostructured gold wafer has been converted to MEA patterned wafer with microelectrode surfaces, external contact pads and connection tracks with photolithography process. This has been done by gold-etching method and metal lift-off process. Lift-off has been done prior to gold electrode layer evaporation on substrate glass wafer (**Figure** 5.1a), whereas gold-etching process has been done post nanostructuring step (**Figure** 5.1b). Although both methods resulted in functional MEAs, the latter has been used for the fabrication of the biomimetic nanostructured MEA biosensors, primarily to prevent alignment-based artifacts. Moreover, lift-off resist had resulted in a step on the gold seed layer post electroplating, which resulted in metal layer stripping during nanoimprinting.

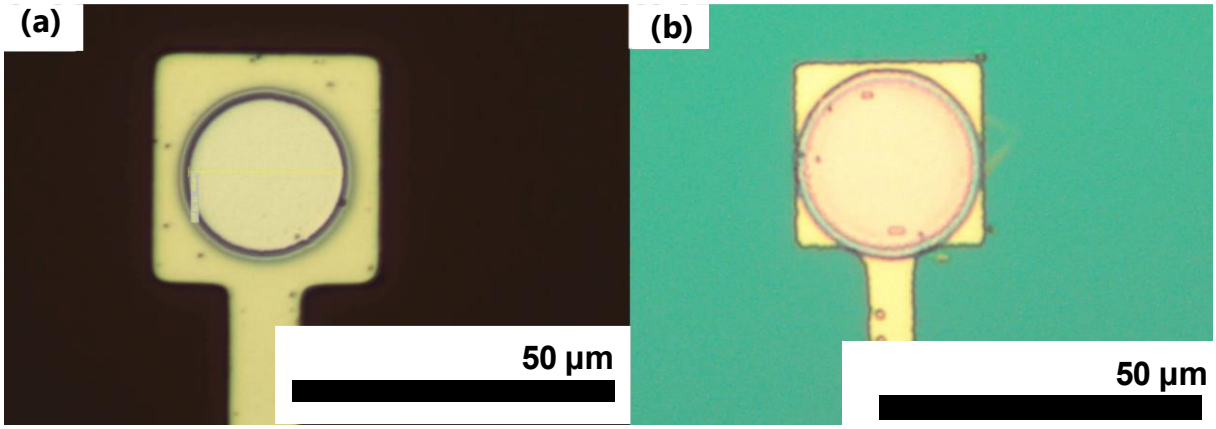

Figure 5.1. Microscopy image of the gold microelectrodes fabricated with (a) lift-off process and (b) gold etching process.

Nanostructured microelectrodes were fabricated with electrode diameters 25 µm and 30 µm; and with interelectrode distances 100 µm and 500 µm. The four MEA configurations of different diameters and interelectrode distances can be seen in **Figure** 5.2a-d and the impedance measured for the 4 configurations of microelectrodes at 1 kHz can be seen in **Figure** 5.2e. The impedance for microelectrodes with 25 µm diameter was measured to be twice the value of the impedance measured for microelectrodes with 30 µm diameter. Interestingly, the interelectrode distance did not alter the impedance measured for the same electrode diameter, which implies the passivation layer prevents the presence of parasitic capacitances between microelectrodes. In order to maintain consistency in surface characterization methods and cell culture experiments, only MEAs

with 30 µm diameter configuration have been used for electrochemical characterization and electrophysiological application.

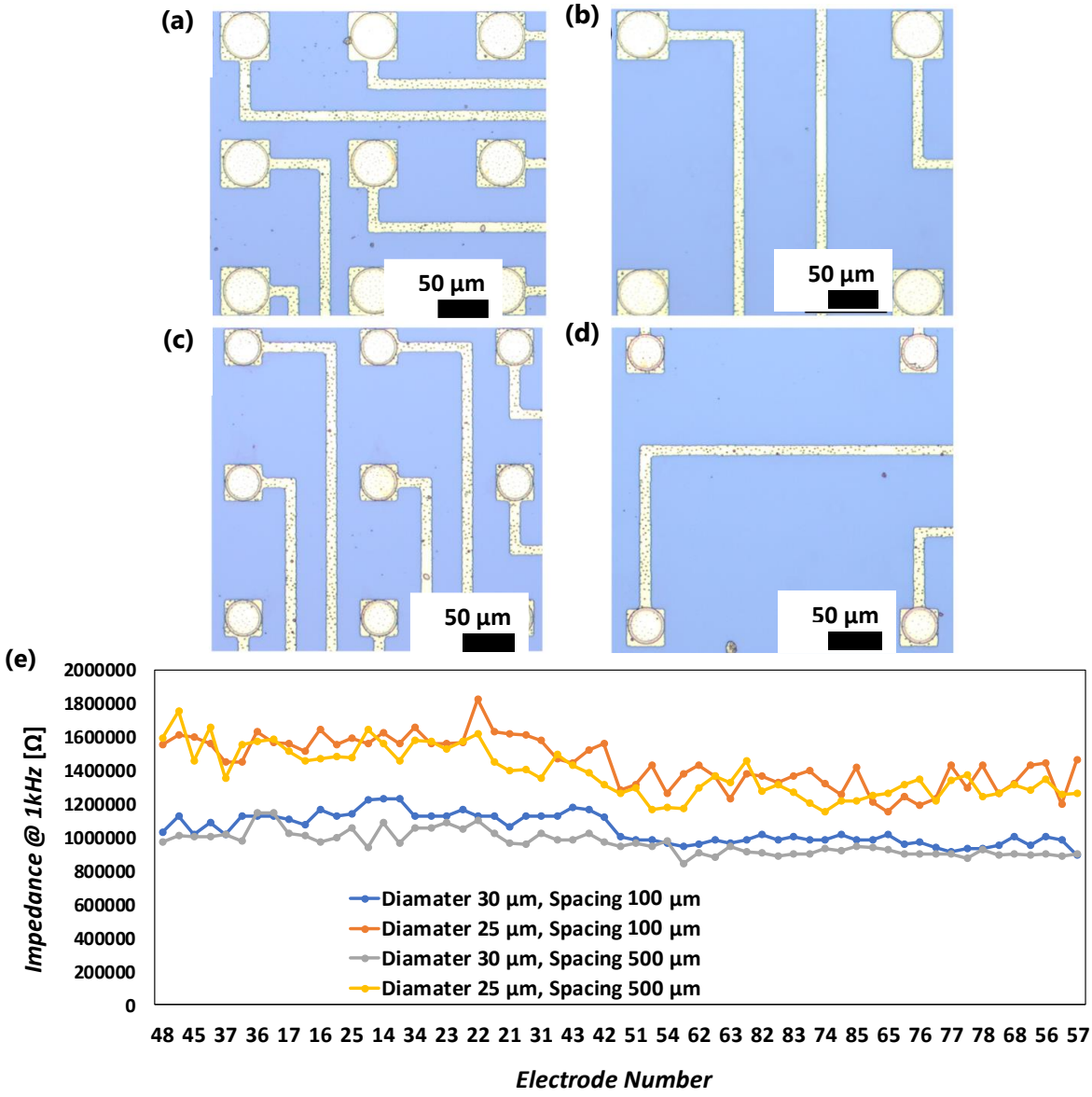

Figure 5.2. Optical microscopy image of microelectrodes with different geometrical configurations: (a) diameter 30 µm and spacing 100 µm, (b) diameter 30 µm and spacing 500 µm, (c) diameter 25 µm and spacing 100 µm and (d) diameter 25 µm and spacing 500 µm. (e) Impedance measured for the microelectrodes with different geometrical configurations at 1 kHz frequency.

Throughput of the MEA chip assembly is necessary to evaluate the cost of fabrication as well as cell culture experiments. The nanostructured MEAs fabricated on glass substrate wafer in this study were developed into fully functional biosensor chips for extracellular activity recordings from electrogenic cells such as neurons and cardiomyocytes. This has been done as monolithic

biosensors (**Figure** 5.3a) and flip-chip bonded printed circuit board (PCB) biosensors (**Figure** 5.3b). In monolithic MEAs, the microelectrode array, external contacts for signal recorder and connection tracks were all fabricated on a single substrate glass wafer. Therefore, a single 4-inch wafer can be used to fabricate only 2 nanostructured MEAs. To increase the throughput of the nanostructured MEA fabrication process, the MEA wafers have been diced into smaller units and were assembled into a PCB with flip-chip bonding and a silver adhesive. By doing so, several MEA biosensors were fabricated from a single 4-inch wafer. Since no significant differences in the signal transmission properties were observed between the two types of MEAs, the flip-chip bonded PCB MEAs have been preferred for the surface characterization methods and cell culture experiments.

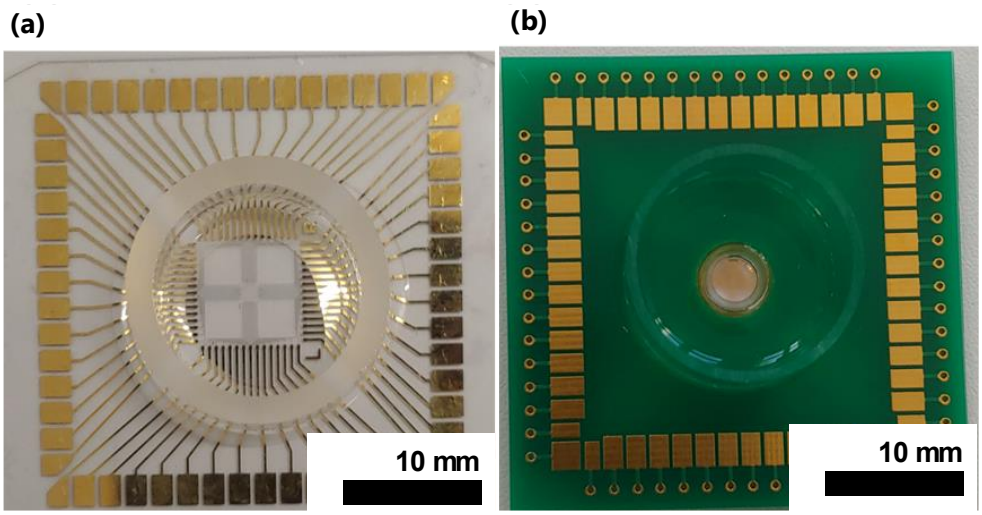

Figure 5.3. Nanostructured MEAs fabricated on glass substrate wafer assembled into (a) monolithic chips and into (b) flip-chip bonded PCB chips.

Passivation of MEA wafer was done to isolate the microelectrode regions to cellular interface. In this study, two passivation layer materials have been tested for optimum signal transmission and prevention of parasitic capacitances. Firstly, a multilayered stack of alternating silicon oxide and silicon nitride with a cumulative height of 1 µm was deposited by plasma-enhanced chemical vapor deposition. Secondly, 1 µm of SU-8 epoxy-based polymer was deposited with spin-coating process and cross-linked at high temperature. Silicon nitride-silicon oxide stack is more stable as a passivation layer as it is not largely affected by oxygen plasma cleaning process (surface profile in **Figure** 5.4a). In contrast, SU-8 spin-coating was observed to be very homogenous due to the chemical development of photoactive regions (surface profile in **Figure** 5.4b), thus preventing a step in the profile of the cell culture surface. For the fabrication of the nanostructured MEAs in this study, both SU-8 polymer layer and silicon nitride-silicon oxide stack have been used as a passivation layers. No significant differences were observed in the electrode impedance properties between the MEAs fabricated with the two different passivation layers and both were successful in preventing parasitic capacitances (**Figure** 5.4c).

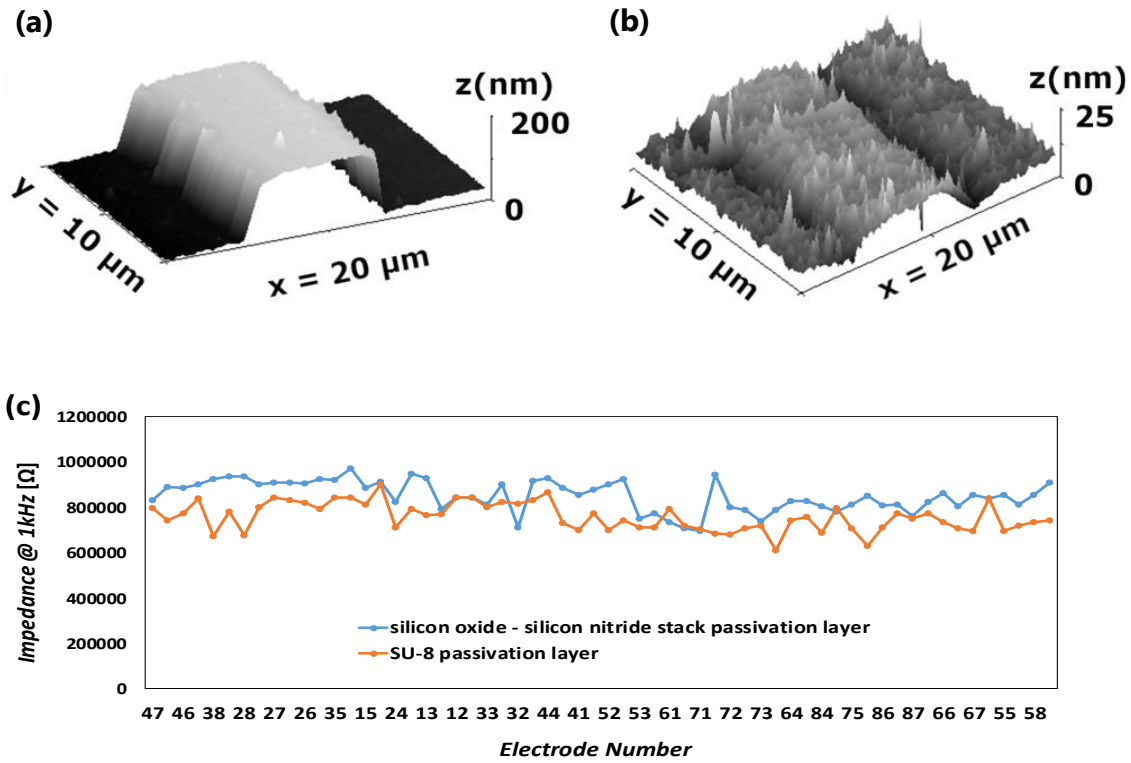

Figure 5.4. Surface profile of passivation layer deposited on the microelectrode array connection track measured with AFM: (a) multilayered stack of alternating silicon oxide and silicon nitride and (b) spin-coated SU-8 polymer. (c) Comparison of impedance properties of the two passivation layers deposited on MEA wafers.

5.2. Topographical analysis of collagen-like gold nanostructured microelectrodes (CLGNS MEAs)

5.2.1. Comparison of nanostructured macro- and microelectrode surfaces

In the previous chapter, the nanostructuring process has been used on macroelectrode surfaces, i.e., circular surface areas with diameter 5 mm (overall surface area 20 mm^2) (**Figure** 5.5a). In this chapter, nanostructured microelectrode surfaces have been fabricated with diameter 30 µm (approx. surface area 756 μm^2). For the larger surface areas, the increase in the CLGNS surface area was measured to be approx. 28 % and due to the uniform density of the collagen fibers on the master stamp, this result was replicated for several structured surfaces of a same substrate wafer. But the microelectrodes have approx. 167 times smaller diameter and hence the individual microelectrodes in a MEA are expected to have different nanostructure coverage densities and subsequently different increase in surface areas. The dimensions (length and width) of the nanostructures were closer to the microelectrode diameter making it critical to evaluate the surface parameters of each microelectrode individually (**Figure** 5.5b).

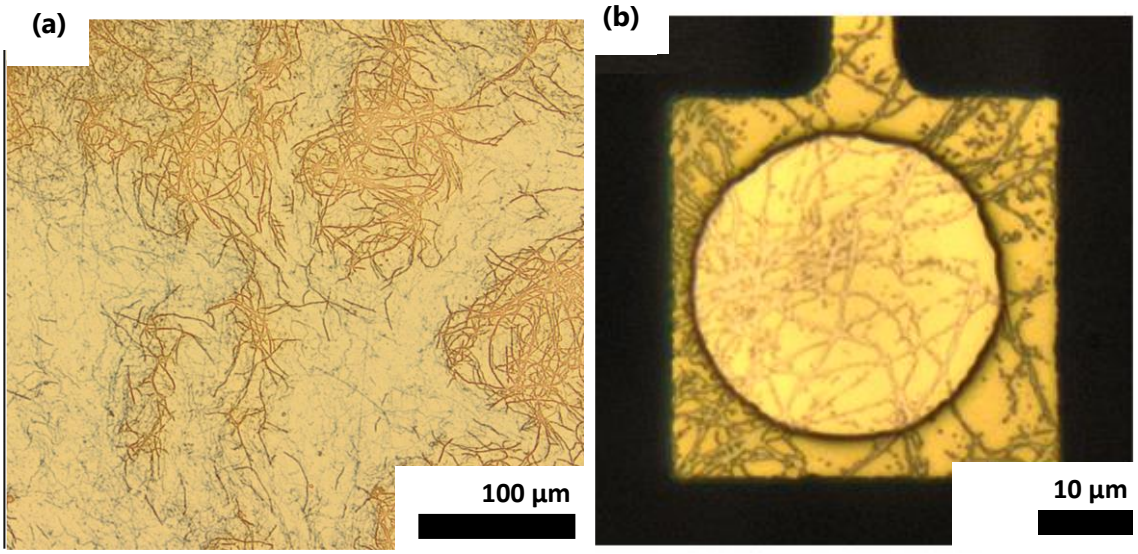

Figure 5.5. Optical microscopy images of the electroplated CLGNS on (a) macroelectrode with 5 mm diameter and (b) microelectrode with 30 µm diameter.

5.2.2. Classification of microelectrodes as a function of CLGNS height and density

In literature, certain studies recommend 50 nm as the optimum nanostructure height to promote neuronal network communication, primarily due to the replication of natural cell environment [141-142]. It has been established in the previous chapter that the height of the nanostructures can be determined by modulating the electroplating time through which the open cavities in the nanoimprint resist are filled. The density of nanostructures on the microelectrode was a function of the height of least reproducible collagen fiber present on the NIL master, which is also the thickness of nanoimprint resist that was left post residual layer removal. It is important to note that the density of CLGNS is not dependent on the electroplating time. In contrast to Chapter 4 where 40 nm was selected to the be the smallest reproducible fiber height to be replicated to CLGNS, 50 nm was selected in this chapter to fabricate CLGNS MEAs with two different heights. By doing so the effect of nanostructure height (keeping density constant) was evaluated with topographical analysis and impedance spectroscopy. By using different electroplating periods (t) in the **Equation** 5.1, nanostructured MEAs have been fabricated with two different heights: 30 nm and 50 nm.

$$t = \frac{\boldsymbol{\rho} \cdot h \cdot z \cdot F}{M \cdot J} \qquad \textbf{Equation } 5.1$$

h is the height of the nanostructures to be grown (i.e. 30 nm and 50 nm) on the imprinted NIL resist (with height 50 nm), $\boldsymbol{\rho}$ the density of gold (19.32 gm/cm^3), J is the electroplating density (1 mA/cm), F is Faraday's constant (96485 C/mol), M is molar mass of gold (198 g/mol) and z is 1 for gold to deposited. The CLGNS microelectrodes with axial dimension (height) 30 nm were denoted H1 and with height 50 nm were denoted as H2. Lateral dimension (width) of the

CLGNS was measured to be in the range between 100 nm and 3 µm for both H1 and H2 MEAs. The longitudinal dimension (length) was measured to be in the range between 50 nm and 30 µm (which is the diameter of the microelectrode). Surface profiles of 30 H1 CLGNS microelectrodes and 30 H2 CLGNS microelectrodes were measured with AFM and the nanostructure density was extracted with threshold-based topographical methods. As expected, the overall increase in surface area (nanostructure density) was measured to be in the range between 20 % and 68 % for H1 and H2 CLGNS MEAs. Due to the presence of such a large variation in the CLGNS density, the nanostructured MEAs were further classified to low density (20 % - 40 %) and high density (40 % - 68 %). For easier understanding, low density CLGNS microelectrodes were denoted as D1 and high density CLGNS microelectrodes were denoted as D2. Hence, the topographical effects of the biomimetic nanostructures have been evaluated in this study from four groups of CLGNS microelectrodes namely, H1D1, H1D2, H2D1 and H2D2. Examples of surface profiles of the 4 groups of CLGNS microelectrodes can be seen in **Figure** 5.6a-d. Distribution of number, height and percentage of nanostructuring density can be seen in **Table** 5.1. The randomness in organization and dimensions of the CLGNS within the microelectrodes of the array could be clearly seen for both H1 and H2 MEAs from this analysis. It is important to note that this distribution is only a function of the nanostructuring process with least reproducible collagen fiber height 50 nm. The distribution would significantly change for a different height of least reproducible collagen fiber (see **Figure** 4.7c).

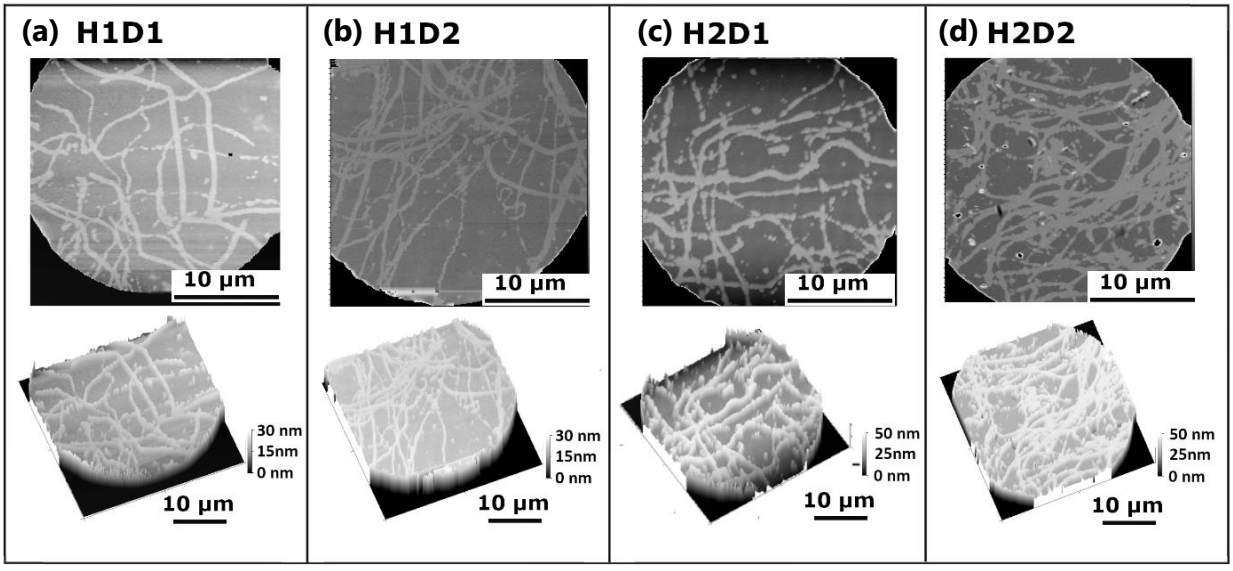

Figure 5.6. Examples of (a) H1D1, (b) H1D2, (c) H2D1 and (d) H2D2 nanostructured microelectrode surface profiles measured with AFM. See Appendix VI for 2D AFM profiles of all the measured CLGNS microelectrodes.

The scanning electron microscopy images of H1 (**Figure** 5.7a) and H2 nanostructured microelectrode (**Figure** 5.7b) surface illustrates the relative heights of passivation layer and the CLGNS. As mentioned in the previous chapter, the collagen fiber network coated on the silicon master stamp demonstrates 3D randomness, whereas the CLGNS demonstrate 2D randomness. The information of randomness in the height of CLGNS could not replicated due the bottom-up nature of the fabrication process (as explained in section 4.2.2).

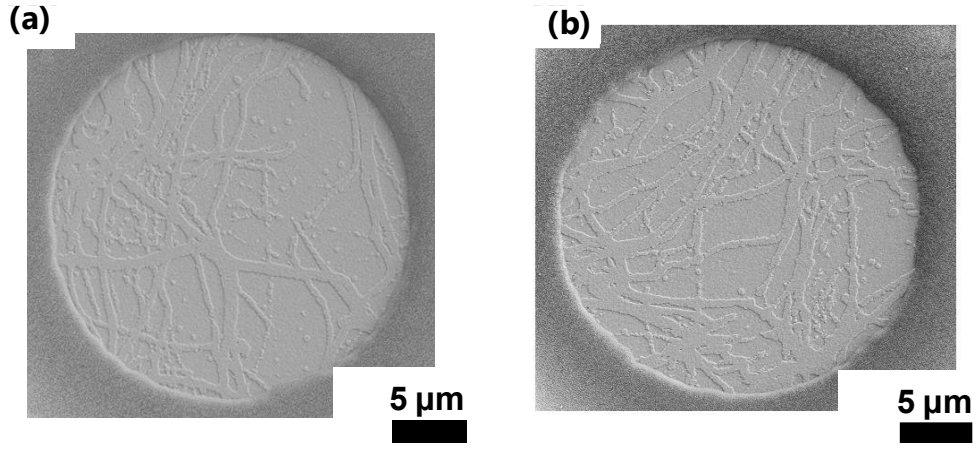

Figure 5.7. SEM images of microelectrode structured with CLGNS with height (a) 30 nm and (b) 50 nm.

Table 5.1. Distribution of different types of CLGNS microelectrodes and unstructured microelectrodes for the smallest reproducible collagen fiber height of 50 nm. See Appendix VI for 2D AFM profiles of all the measured CLGNS microelectrodes.

Type of microelectrode	Percentage of nanostructure coverage on microelectrode surface [%]	Height of nanostructures [nm]	Number of measurements
Unstructured	-	-	60
H1D1 nanostructured	20-40	30	8
H1D2 nanostructured	40-68	30	22
H2D1 nanostructured	20-40	50	6
H2D2 nanostructured	40-68	50	24

5.2.3. Nanostructured microelectrode interface with cell culture

Enteric neurons cultured from postnatal mice were dried and fixed on DIV 10 to observe the adhesion interface and growth pattern of neurons on nanostructured gold microelectrodes (**Figure** 5.8a). The images are representative to the neuronal cultures seeded on the MEAs during extracellular activity measurements. The cells spread along the surface of passivation layer and adhere to the nanostructured gold microelectrode. The membrane of the neuronal processes are in close contact with the metallic microelectrode and reduction of seal gap due to the nanostructures would help in efficient transmission of extracellular activity. At higher magnification it can be seen that some of the neurites originating from the cell body are directed by the features of CLGNS (**Figure** 5.8b). This was particularly interesting as the directionality in neurite growth is predominantly observed with natural collagen fibers present in ECM network [143-144]. This suggests that the directionality in neurite growth was not only a feature of the chemical composition of the natural collagen fiber, but also topographical features of the synthetic CLGNS. The biomimetic replication of functionality of natural biomolecules along with topographical features is indeed an interesting development which could be utilized for several biosensor applications. At lower magnification, it can be observed that the passivation layer constituted more than 99 % of microelectrode region, where most of the neural network has spread (**Figure** 5.8c). This is quite unfortunate as the nanostructures are present only on the gold microelectrodes and not on the passivation layer. Therefore, to observe a larger effect of CLGNS on the microelectrodes, it is essential to nanostructure the complete MEA cell culture area i.e., including the passivation region. Cross sectional SEM with focused ion beam and critical point drying has been used in literature to observe the nanoscaled interaction of cell membrane proteins with synthetic nanostructures [88]. In this study, analytical methods such as seal impedance measurements and fluorescence microscopy has been used to further evaluate the adhesion of neurons to the biomimetic nanostructures.

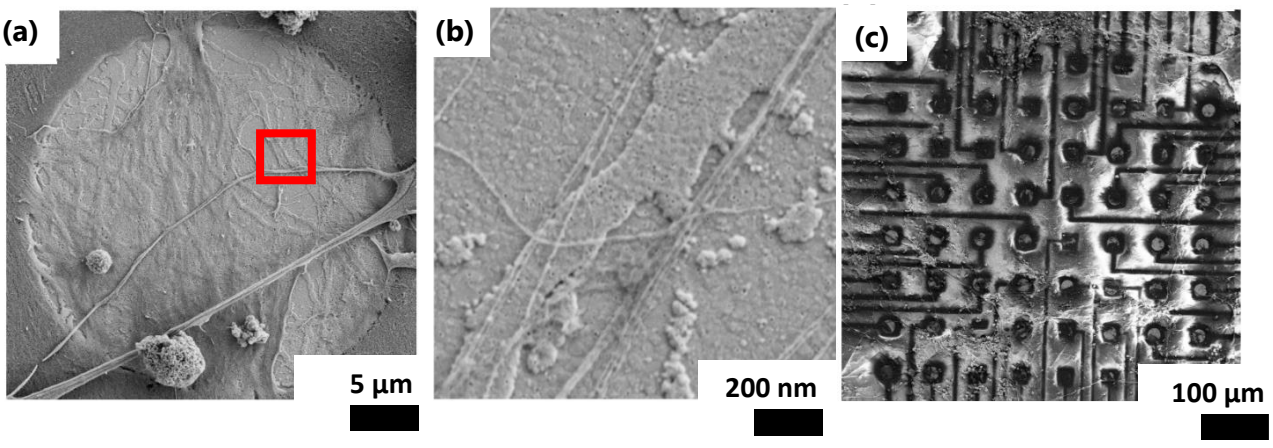

Figure 5.8. SEM images of enteric neurons cultured on H2 CLGNS microelectrodes at (a) 2500x magnification, (b) 20000x magnification (part marked in red box in (a)) and (c) 100x magnification. Substrates sputtered with 10 nm of Au prior to imaging.

5.3. Impedance spectroscopy of CLGNS microelectrodes

Electrochemical impedance spectroscopy of microelectrodes for electrophysiological application is commonly used to evaluate its charge transfer properties. Impedance spectroscopy measurements for the nanostructured gold macroelectrodes described in Chapter 4 illustrated a stark reduction in impedance magnitude at frequencies less than 1 kHz. The same measurement parameters cannot be used for the microelectrodes analyzed in this chapter (which are 167 times smaller than the macroelectrodes). Firstly, the diffusion and reaction kinetics of the ionic species with the nanostructured electrodes are largely altered for microscale surfaces [145]. Secondly, the lateral dimension of the CLGNS is closer to the lateral dimension of the active microelectrode surface. Therefore, the density of the nanostructures on the surface varies largely between microelectrodes of the array. In the previous section, the classification of nanostructured microelectrodes based on the structure height and density of the CLGNS has been presented (H1D1, H1D2, H2D1 and H2D2). Therefore, the same classification of nanostructured gold microelectrodes along with unstructured planar microelectrode have been analyzed with impedance spectroscopy measurements. The impedance spectroscopy measurements have been carried out in the frequency range from 1 Hz to 3 MHz with an input voltage of 10 mV and a DC bias of 120 mV in 0.01 M KCl solution. The recorded data has been represented in Bode magnitude and phase diagrams, as well as, Nyquist diagram.

As explained previously, the increase in surface area as a fraction of overall electrode surface area is much smaller for the microelectrodes when compared to macroelectrodes (approx. 167 times). Therefore, the differences in the impedance spectra between the nanostructured and unstructured microelectrodes would be much harder to visualize. Nevertheless, reduced impedance magnitude was observed for all the nanostructured microelectrodes in comparison to unstructured microelectrodes, especially in the frequency range between 1 Hz and 10 kHz (**Figure** 5.9a). At frequencies larger than 10 kHz the reduction in impedance magnitude becomes less significant. To further visualize the effect of CLGNS, impedance magnitude measured for different microelectrodes at 1 kHz has been presented in the inset of **Figure** 5.9a and **Table** 5.2. The largest effect of CLGNS was observed for H2D2 microelectrodes where 41.3 % reduction in impedance magnitude observed. H2D1, H1D2 and H1D1 subsequently showed reduction in impedance magnitude of 30.1 %, 28.3 % and 22.7 %, respectively. It can be observed that both density (surface coverage) and height of the CLGNS contribute to reduction of microelectrode impedance, with the former playing a more significant role. In contrast, the predominant effect of CLGNS on microelectrode impedance phase spectrum can be observed at 100 kHz frequency (**Figure** 5.9b and **Table** 5.2). This behavior of the impedance phase is a characteristic of the constant phase element in the impedance transfer function, which in literature has been correlated to double-layer capacitance [70]. Similar to impedance magnitude spectra, H2D2 CLGNS microelectrodes showed

the maximum phase shift, followed by H2D1, H1D2, H1D1 and finally unstructured microelectrodes.

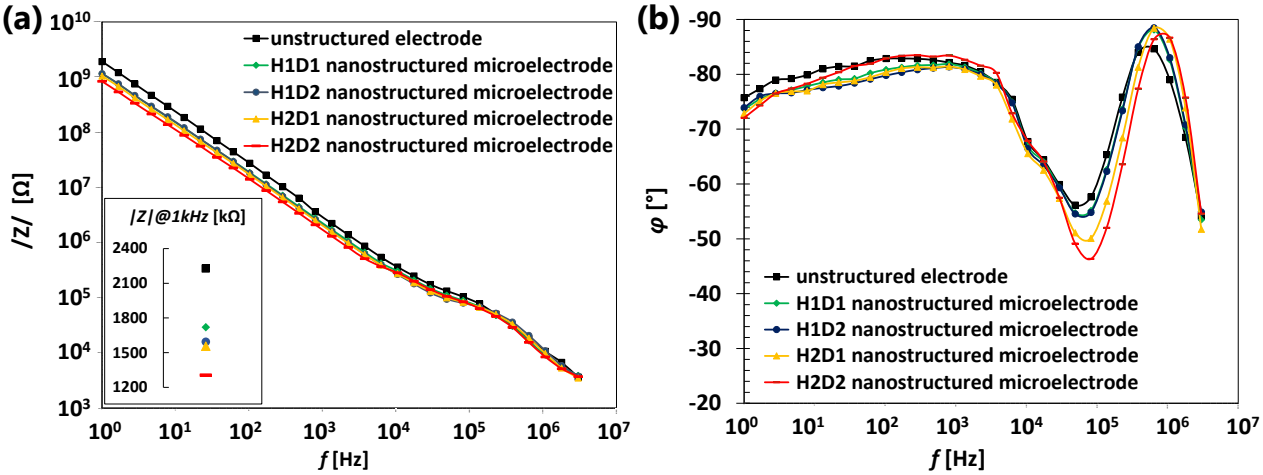

Figure 5.9. Electrochemical impedance spectroscopy of H1D1, H1D2, H2D1, H2D2 nanostructured and unstructured gold microelectrodes (a) impedance magnitude |Z| spectrum (inset impedance of the microelectrodes at 1 kHz) and (b) impedance phase ***φ*** spectrum.

The Nyquist diagram of the imaginary and real impedance of the different groups of nanostructured microelectrodes and unstructured planar microelectrodes can be seen in **Figure** 5.10a-b. At higher frequencies (**Figure** 5.10a), the unstructured microelectrodes showed larger impedance contributed by the charge transmission components followed by H1D1, H1D2, H2D1 and H2D2 showing the smallest impedance. At lower frequencies (**Figure** 5.10b), the impedance contribution by diffusive components followed a similar pattern with highest diffusion impedance observed for unstructured microelectrodes. Impedance spectrum of microelectrodes contributed by diffusion components was much harder to interpret than charge-transfer components, as the complex diffusion profile and the boundary conditions at microelectrode surface needs to be precisely determined. Therefore, an accurate equivalent circuit for the nanostructured microelectrodes could not be developed in this study to be used for the mathematical fitting and extraction of individual impedance components of the spectrum. Nevertheless, insights from the mathematical fitting of electrical equivalent circuit components of the nanostructured macroelectrodes performed in Chapter 4 could be referred for getting a brief outlook. The reduction in the impedance could be attributed to enhanced double-layer capacitance and diminished charge-transfer resistance. Cyclic voltammetry measurements have been performed on electroplated nanostructured gold microelectrodes in literature which have shown enhanced charge injection capacity related to increased double-layer capacitance and reduced charge-transfer resistance as well [39,41,146].

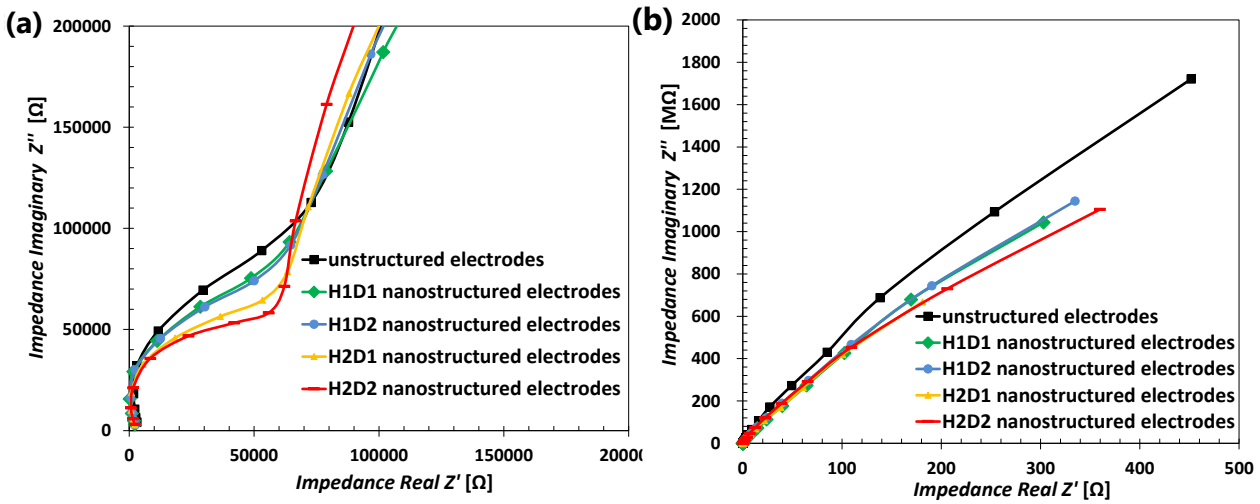

Figure 5.10. Nyquist representation of the impedance measurements performed for microelectrode arrays with different nanostructure height and density: (a) high frequency range (100 kHz-3 MHz) and (b) low frequency range (1 Hz-100 kHz).

Table 5.2. Electrochemical impedance spectroscopy measurements for different types of nanostructured microelectrodes and unstructured microelectrodes.

Type of microelectrode	Impedance magnitude at 1 kHz [kΩ]	Reduction in impedance magnitude at 1 kHz as compared to unstructured electrodes [%]	Impedance phase at 100 kHz [°]
Unstructured	2227 ± 137	-	-57.9 ± 1.6
H1D1 nanostructured	1721 ± 134	22.7	-54.5 ± 3.4
H1D2 nanostructured	1595 ± 79	28.3	-54.6 ± 2.6
H2D1 nanostructured	1556 ± 86	30.1	-50.4 ± 1.8
H2D2 nanostructured	1305 ± 72	41.3	-45.7 ± 3.1

5.4. Characterization of cell adhesion with seal impedance

Adhesion of cells on culture surface is one of the major foundations for a confluent cell growth, differentiation and proliferation [77]. It is especially important for neurons to form robust neurite network, which then promote intra- and extracellular signaling [81,147-148]. For enhanced extracellular activity to be recorded from the microelectrodes, it is beneficial for the neurons to adhere tightly to the biomimetic nanostructures. Considering the topographical and electrochemical measurements performed in this chapter, H2 CLGNS MEAs have been exclusively used for seal impedance analysis. The interface between the nanostructured microelectrode and the electrogenic neuronal cell has been presented in an electrical equivalent circuit (**Figure** 5.11a). The charge-transfer components of the cell membrane (extra- and intracellular ion channels) and the nanostructured microelectrode (charge-transfer and diffusion elements) are shunted by the seal impedance (Z_{Seal}) which is directly proportional to the distance between the two surfaces at the junction [41,89]. A smaller seal gap between the interfaces would result in larger Z_{seal} and tighter adhesion. Since the frequency range of the electrogenic activity measured from neurons is primarily around 1 kHz (spikes, bursts, post synaptic potentials), the seal impedance measurements were performed at the same frequency [136-138]. Nevertheless, other works in literature have performed seal impedance spectroscopy over a large frequency range on non-electrogenic cells for comprehensive adhesion analysis [149]. Measurement of seal impedance spectroscopy for a neuronal culture on the microelectrode would necessitate the potentiostat being used for several minutes (especially for low frequency signals). This could lead to thermal effects that be detrimental to cell membrane such as ablation and electroporation [150].

Non-electrogenic cells were preferred to the cell adhesion evaluation with seal impedance measurements in literature, as there exists no electronic interference from ion channels present in the cell membrane [41]. But it also important to note that the adhesion mechanics of cells differ vastly based on their type and morphology [151]. And since enteric neurons have been used for electrophysiological application of the nanostructured microelectrodes in this study, the same cells were used for cell adhesion analysis as well. The sinusoidal signal from the potentiostat measuring seal impedance has an amplitude of 10 mV, whereas the extracellular action potential signal from neurons is measured in the range of 100 µV [152]. Therefore, the electrogenic activity of the neurons would be minimally interfering with the seal impedance measurements from the potentiostatic apparatus. Despite the minimal interference, application of enteric neuronal culture is more appropriate for characterization of the cell adhesion to nanostructured MEAs. It is also important to have high confluency of cells on the microelectrode surface to have accurate seal impedance measurements [41]. Presence of open gaps on the culture surface would result in the measurement potential to be detected by the microelectrode without interacting with the cell membrane. The high confluency of the neuronal cell culture on the microelectrodes can be observed in **Figure** 5.11b with optical microscopy prior to seal impedance measurements.

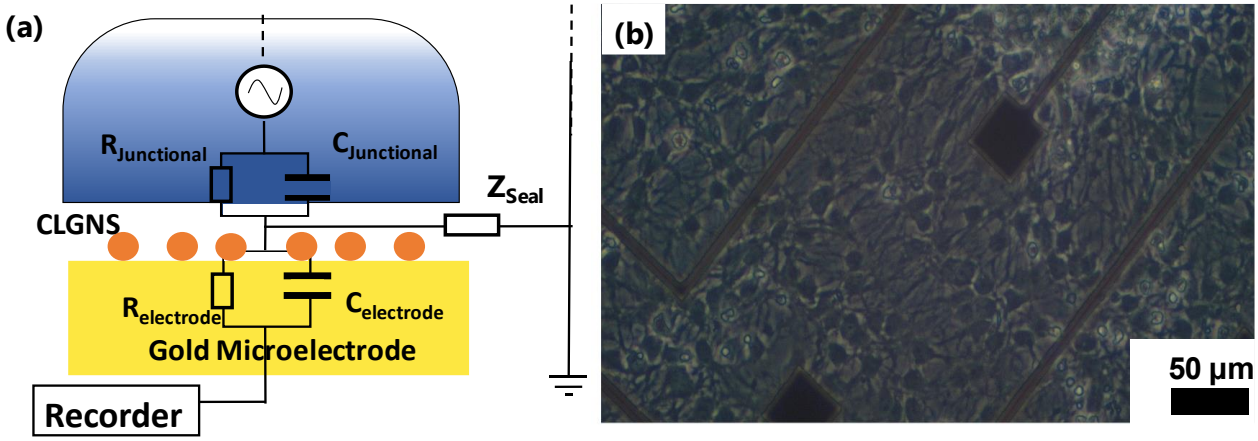

Figure 5.11. (a) Schematic of electrical circuit analogue for the characterization of seal impedance (Z_{Seal}) between the CLGNS nanostructured microelectrode and the adhered neuron. (b) Optical microscopy of the enteric neuron cultured on nanostructured microelectrode illustrating complete confluency for the seal impedance measurements.[†]

Comparison of measured impedances without cell culture and with enteric neurons differentiated on DIV 5 for 30 unstructured and 30 H2 nanostructured electrodes shows significant differences (**Figure** 5.12). Seal impedances were measured for three different H2 nanostructured MEAs with same measurement parameters and the data is summarized in **Table** 5.3. The nanostructured microelectrodes show marginally smaller impedance measurements compared to unstructured microelectrodes without cells, which correlates to the EIS measurements presented in section 5.3. Whereas, the seal impedance measured with enteric neurons for the exact same electrodes shows significant amplification of 340 %. This implies that the seal gap between the microelectrode and the enteric neurons is reduced by the protruding CLGNS and hence promoting the cell adhesion. It is interesting to observe that the standard deviation of seal impedances measured for microelectrodes are much higher than the impedance measurements without cells. As previously explained, the seal between the electrode surface and cell membrane not only dependent on the type of cell, but also the part of the cell adhering to it (e.g., dendrite, axon, soma etc.) [150] leading to significant deviation. Moreover, the ion channels of the neuronal membrane could interfere with the measuring potential. Nevertheless, even with the minimal interference on impedance measurements, it can be inferred that CLGNS do indeed promote the cell-surface coupling on the microelectrodes, which would subsequently improve the neuronal signal transmission.

[†] *Cell cultures on MEAs performed by Negin Adavoudi Jolfaei (master student), Technical University of Kaiserslautern Germany*

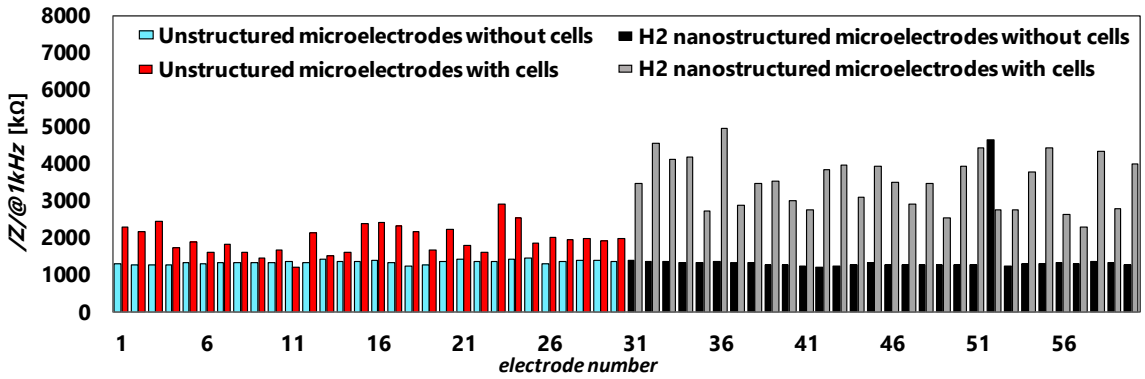

Figure 5.12. Impedance measurements of unstructured microelectrodes (electrode number 1-30) and H2 nanostructured microelectrodes (electrode number 31-60) at 1 kHz frequency with and without enteric neurons cultured on the surface.

Table 5.3. Impedance measurements to evaluate seal of H2 nanostructured microelectrodes with enteric neurons (n = 3).

Type of microelectrode	Impedance at 1 kHz without cells [kΩ]	Impedance at 1 kHz with cells [kΩ]
Unstructured	1340 ± 49	1985 ± 346
H2 nanostructured	1293 ± 48	3497 ± 696

5.5. Electrophysiological measurements of CLGNS MEAs

5.5.1. Configuration of extracellular activity measured from enteric neuronal culture

Reduction in impedance magnitude revealed from the impedance spectroscopy measurements and a tighter surface coupling revealed from the seal impedance analysis suggests superior charge-transfer properties and higher signal-to-noise ratio (SNR) for the cell culture recordings from the CLGNS microelectrodes. Therefore, signal recording properties of the nanostructured microelectrodes have been evaluated by culturing neurospheres from the myenteric plexus of post-natal mice on the MEA surfaces, which were later proliferated as enteric neurons. Differentiation and proliferation of neurospheres resulted in excellent neuronal network on the MEAs [119]. Since the recorded extracellular neuronal activity of the cell culture is in a range within a single millivolt [152], it could be superposed in electronic noise, which could lead to false interpretation of action potential spikes. Standard procedure to evaluate the validity of spike detection is through stimulating the neuronal culture with neurotransmitters such as acetyl choline and glutamate, which would amplify the spike rate as well as spike amplitude [153-154]. But for the evaluation of electronic charge transfer properties of nanostructured microelectrodes, it is practical to record and evaluate spontaneous activity where the effect of nanostructures on the

cell culture exclusively modulates the detected spike properties. Spontaneous extracellular recordings were processed with appropriate filters and the validity of the action potential spikes was checked by comparing the shape with standard spike templates. Depending upon the shape of the action potential spikes, they have been classified into two main forms. A negatively unipolar spike with peak-to-peak amplitude not exceeding 40 µV (**Figure** 5.13a) and a bipolar spike with peak-to-peak amplitude larger than 80 µV (**Figure** 5.13b). Differentiation of cell culture from the neurospheres result in neurons of varied morphology which generate and transmit extracellular signals of different shapes [155]. Since the signal-to-noise ratio of the bipolar spikes is very large in comparison to the unipolar signals, they have been analyzed separately for the signal and noise properties. Several cell culture experiments with the nanostructured MEAs have been performed to achieve a valid number of active channels measuring signals for microelectrode characterization. In total, unipolar spike data from 24 H2 nanostructured microelectrodes and 12 unstructured microelectrodes have been analyzed. It is important to note here that the detection of bipolar spikes is extremely rare (2 H2 nanostructured microelectrodes and 2 unstructured microelectrodes), in comparison to the unipolar spikes. The detected spikes have been analyzed in section 5.5.5 to characterize the changes induced by the biomimetic nanostructures on the microelectrodes.

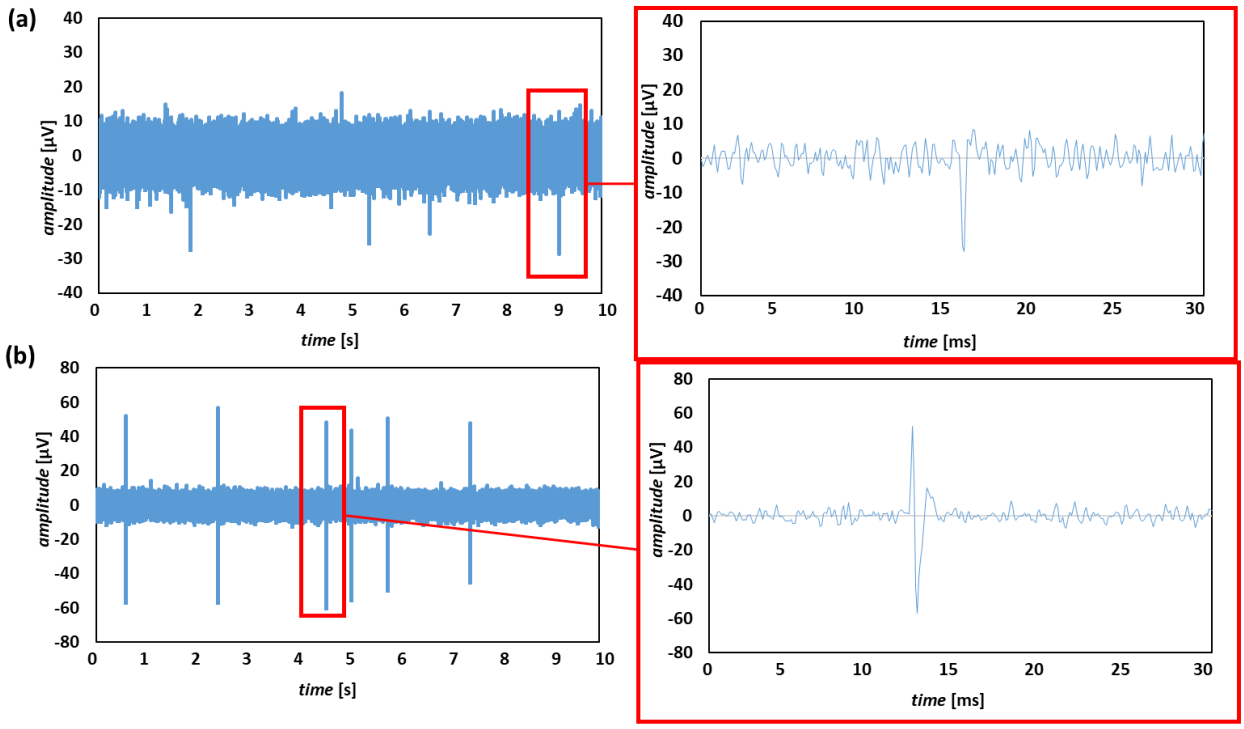

Figure 5.13. Examples of action potential spikes detected from the extracellular recordings of enteric neuron culture by nanostructured MEAs: (a) unipolar spikes and (b) bipolar spikes.[†]

[†]*Cell cultures on MEAs and recordings performed by Negin Adavoudi Jolfaei (master student), Technical University of Kaiserslautern Germany and Steven Schulte, University of Applied Sciences Kaiserslautern Germany.*

5.5.2. Baseline noise characterization of the microelectrode recordings

Prior to analyzing the spike properties from the recordings, it is essential to understand the properties of the baseline noise. Thermal noise in microelectronics is a quantitative extent of the electromagnetic interference present in the measurement apparatus [156]. It is also largely dependent on the global impedance of the measuring electrode. The H2 CLGNS present on the microelectrodes have been responsible for the reduction the global impedance of the measuring microelectrode, which in turn could result in the reduction of thermal noise (see **Equation** 4.1 in section 4.3.2). This reduction is valid for enhancing electronic performance of the microelectrodes in a controlled electrochemical system with a constant measuring potential and electrolyte resistance. In electrophysiological recordings, the baseline noise is complex and is a function of cell-surface coupling [157-158]. Interestingly, a significant improvement in the seal impedance has been observed with H2 nanostructured microelectrodes, which has been electronically correlated to reduced seal gap between cell membrane and microelectrode surface. Unfortunately, this enhancement could lead to a larger baseline seal noise for H2 nanostructured microelectrodes and hence be detrimental to the detection of weaker action potential signals. The RMS baseline thermal noise was measured to be 3 times smaller than the RMS baseline seal noise for the same microelectrode (**Figure** 5.14). And baseline seal noise varies across the electrodes depending on the presence of neuron cell body, axons or dendrites [159]. Therefore, apart from measuring the spike properties of the neuronal signals, the baseline seal noise of the recordings has also been evaluated, which was then used to calculate the signal-to-noise ratio of the microelectrodes with the respective spike measurements.

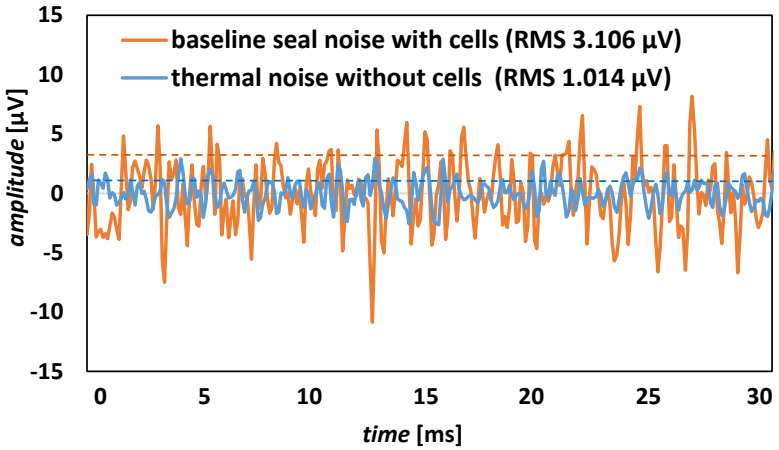

Figure 5.14. Comparison of thermal noise without cells and baseline seal noise with cells measured on the nanostructured microelectrode (RMS value of noise marked as dotted line).

5.5.3. Signal-to-noise ratio characterization with external signal generator

As established in the previous section, the spike amplitude and the baseline noise of the extracellular activity is a function of the morphology of neuron coupled to the microelectrode, as

well as, the seal gap between the neuron and the microelectrode surface. Therefore, to evaluate the impact of the CLGNS eliminating the cell-surface coupling effect, SNR of the microelectrodes has been calculated by recording spikes from a constant signal generator (measurement setup described in section 3.4.3). The signal generator produces signals simulating the amplitude, time period and shape of action potential spikes and bursts generated by hippocampal neurons. The waveform of the original signal generated from the signal generator and the recorded signals from the H2 nanostructured and unstructured microelectrodes can be seen in **Figure** 5.15. The measured peak-to-peak of spike amplitudes ($V_{s,p2p}$) and root-mean-square of baseline noise ($V_{n,RMS}$) of H2 nanostructured and unstructured microelectrodes of have been summarized in **Table** 5.4. The recorded data from the microelectrodes was not processed with any filters. The overall impact of the increased effective surface area by CLGNS on microelectrodes can be observed predominantly in the reduction of baseline noise by 47 %, whereas the impact is minimal for spike peak-to-peak amplitude. Nevertheless, the SNR (ratio of spike amplitude and baseline noise) is significantly amplified by 30 %, which reaffirms the enhanced electrical properties measured with impedance spectroscopy of the H2 nanostructured microelectrodes.

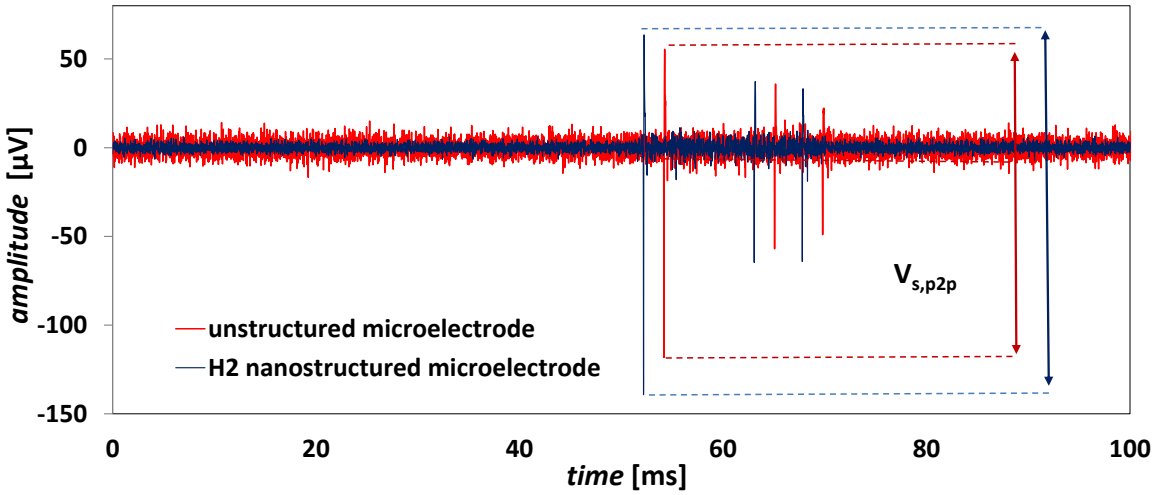

Figure 5.15. Signal recordings of simulated action potentials produced by constant signal generator on H2 nanostructured and unstructured microelectrodes.

Table 5.4. Summary of signal-to-noise ratio measured for H2 nanostructured and unstructured microelectrodes with constant signal generator (n = 60).

Type of microelectrode	$V_{s,p2p}$ [µV]	$V_{n,RMS}$ [µV]	Signal-to-noise ratio $V_{s,p2p}/V_{n,RMS}$
Unstructured	168.12 ± 18.3	10.49 ± 2.2	16.02
H2 nanostructured	171.45 ± 16.1	6.24 ± 1.9	27.7

5.5.4. Detection of action potential spikes from enteric neuronal extracellular recordings

The spikes were detected from the filtered signal by amplitude thresholding method based on the standard deviation of the baseline seal noise. Waveforms of the detected unipolar and bipolar action potential spikes recorded from the enteric neuron culture on H2 nanostructured and unstructured microelectrodes on DIV 6–7 can be seen in **Figure** 5.16a-d. The detected spikes provide a vast variety of dynamic information from the neural network (such as activity score, plasticity, etc.) and it was essential to choose the information that was required to characterize the effect of the nanostructures. Reduced global impedance would alter the peak-to-peak voltage of the detected spike, whereas enhanced neural network dynamics would result in altered number of spikes and reduced seal gap would reduce spike transmission losses. Therefore, in a constant active recording period (30 seconds in this study), properties such as spike rate, the peak-to-peak of the largest and smallest detected spikes, the mean peak-to-peak amplitude of all the detected spikes, the baseline noise and the signal-to-noise ratio have been calculated. The number of total active channels has not been used for the microelectrode characterization, as it was a function of the cell culturing process and not microelectrode quality.

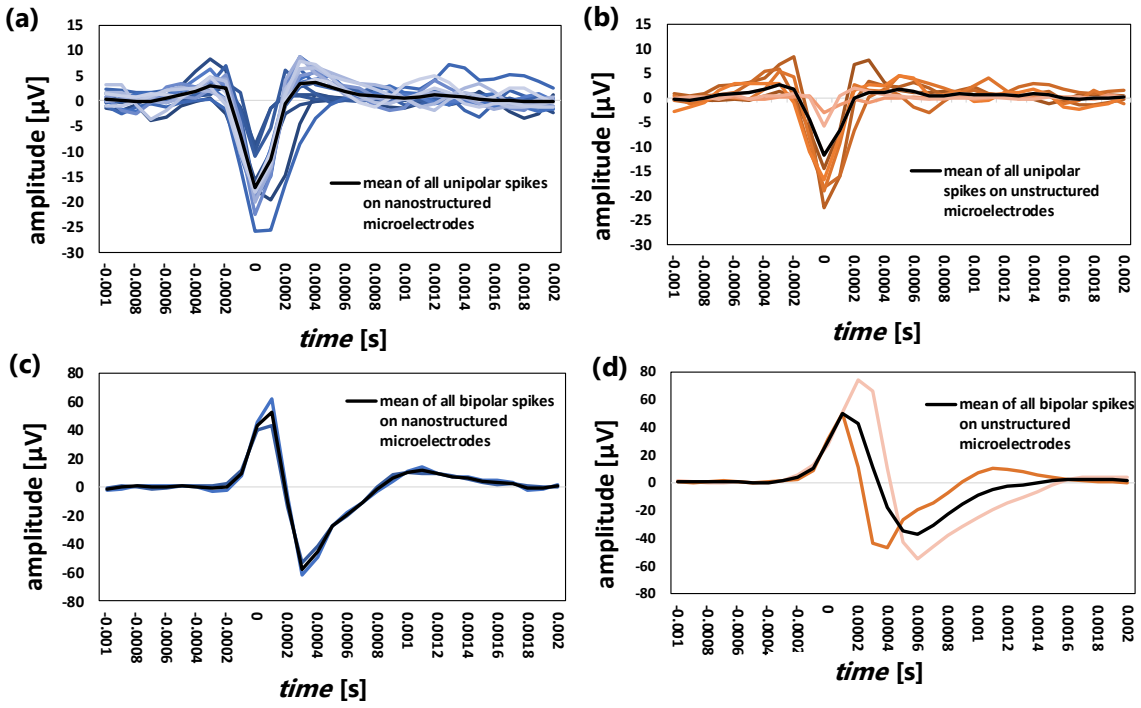

Figure 5.16. Waveforms of the detected action potential spikes measured from the enteric neuron culture on DIV 6–7: (a) Unipolar spikes from H2 nanostructured microelectrodes (n = 24), (b) unipolar spikes from unstructured microelectrodes (n = 12), (c) bipolar spikes from H2 nanostructured microelectrodes (n = 2) and (d) bipolar spikes from unstructured microelectrodes (n = 2). Each line represents the mean waveform of all spikes measured per channel and the black colored line represents the mean cutout of all measured channels.

5.5.5. Evaluation of spike properties recorded from CLGNS MEAs

Unipolar and Bipolar spike properties measured for H2 nanostructured and unstructured microelectrodes have been summarized in **Table** 5.5. Comparison of the detected spike rate (number of unipolar and bipolar spikes detected in 30 seconds) for H2 nanostructured microelectrodes and unstructured microelectrodes can be seen in **Figure** 5.17a. The nanostructures were expected to promote the neuronal adhesion by providing topographical cues and thus enhancing the intra- and extracellular signaling. This subsequently would then correspond to higher signal spike rate measured by the microelectrode. Nevertheless, no significant difference was observed between the two sets of microelectrodes for both unipolar and bipolar spikes. This was perhaps because the effect of nanostructuring was only confined to the microelectrodes and the rest of the cell culture was grown on unstructured passivation layer. And the spike rate was proportional to not just the cell dynamics of the neuron under the microelectrode, but the complete neuron network in the vicinity of the microelectrode, which is comprised of the aforementioned unstructured passivation layer.

The comparison of the baseline seal noise ($V_{n,RMS}$) measured for the H2 nanostructured and unstructured microelectrodes (only in the channels where the spikes were detected) can be seen in **Figure** 15.17b. In contrast to the thermal noise measured with the external signal generator in section 5.5.3, significant increase in the baseline seal noise was observed for both unipolar spikes. This result verifies the seal impedance measurements described in section 5.4. As explained in section 5.4, a larger seal noise signifies a tighter adhesion of cells to the surfaces. Therefore, the probability of electrical signal transmission being attenuated by ohmic loss should be lower for the H2 nanostructured microelectrodes, as compared to unstructured microelectrodes. Nevertheless, amplified baseline noise leads to spikes of smaller amplitude to be not detected by the recording device. Therefore, tighter coupling of the neurons to the microelectrodes by the biomimetic nanostructures provides advantages, as well as, disadvantages to the extracellular activity recordings from electrogenic cells. To solve this issue, needle shaped microelectrodes (of height approx. 500 µm) have been fabricated in literature, which would penetrate the seal gap completely resulting in measurement of a combination of extra- and intracellular action potentials with minimal baseline noise [160].

In this study, the largest spike detected in the 30 second measurement period on the microelectrode channel is denoted as maximum peak-to-peak amplitude ($V_{s,p2p}$ max) and the smallest detected spike as minimum peak-to-peak amplitude ($V_{s,p2p}$ min). Mean of all spikes detected in the 30 second measurement period is denoted as mean peak-to-peak amplitude ($V_{s,p2p}$ mean). In comparison to unstructured microelectrodes, H2 nanostructured microelectrodes have shown noteworthy enhancement in $V_{s,p2p}$ max, $V_{s,p2p}$ min and $V_{s,p2p}$ mean for the detected unipolar spikes (**Figure** 15.17c-e). 51 % amplification in $V_{s,p2p}$ min was measured for the nanostructured microelectrodes, which is significant for the detection of diminished action

potential signals that are superposed by the baseline seal noise. Likewise, 70 % amplification was observed for $V_{s,p2p}$ max, which can be attributed to reduction in transmission losses due to reduced seal gap. Finally, 55 % amplification was observed for $V_{s,p2p}$ mean, which is an indicator for overall enhancement of the nanostructures on the microelectrodes. As explained in section 5.5.2, baseline noise of each recording channel is characterized by the seal between the microelectrode and the cell. Therefore, the ratio of $V_{s,p2p}$ mean and $V_{n,RMS}$ was calculated for the H2 nanostructured and unstructured microelectrodes (**Figure** 15.17f). Improvement of the signal-to-noise ratio by 35 % for the unipolar spikes confirms the cumulative electronic and biological impact of the biomimetic nanostructures on the microelectrodes used for electrophysiological application. Unfortunately, no significant results could be derived from the bipolar spikes as the detection of these signals are extremely rare (n = 2). Nevertheless, it is important to present the information here, as the spikes were detected from the same cell culture as the unipolar spikes.

In literature, nanostructured microelectrodes have been fabricated with much higher enhancement in SNR of extracellular recordings [161]. But such an improvement could be due application of novel ultra-high conductive nanostructured material (e.g. graphene) on metallic electrode. Since both unstructured and nanostructured microelectrode evaluated in this study are composed of gold, a diminished enhancement in electrophysiological properties is understandable. Moreover, the primary objective of this study is to interface neurons randomly organized nanostructures, which has been successfully accomplished.

Table 5.5. Summary of unipolar and bipolar spike properties measured from the extracellular activity recordings of enteric neurons from with H2 nanostructured microelectrodes and unstructured microelectrodes.

Type of microelectrode	Spike morphology	Spike number	V_{p2p} min [µV]	V_{p2p} mean [µV]	V_{p2p} max [µV]	Baseline seal noise RMS [µV]	Signal-to-noise ratio
H2 nanostructured (n = 24)	Unipolar	25.95 ± 8.1	21.76 ± 5.7	28.87 ± 7.8	39.14 ± 13.9	3.19 ± 0.9	11.21 ± 1.7
Unstructured (n = 12)	Unipolar	24.22 ± 6.8	14.66 ± 5.6	18.38 ± 6.8	23.66 ± 14.4	2.15 ± 0.38	8.71 ± 2.0
H2 nanostructured (n = 2)	Bipolar	30.26 ± 8.8	93.01 ± 39.13	105.75 ± 37.8	118.5 ± 35.3	3.47 ± 0.65	30.26 ± 10.4
Unstructured (n = 2)	Bipolar	29.26 ± 5.0	47.75 ± 20.5	123.74 ± 26.9	151.5 ± 36.6	2.46 ± 0.46	29.53 ± 2.7

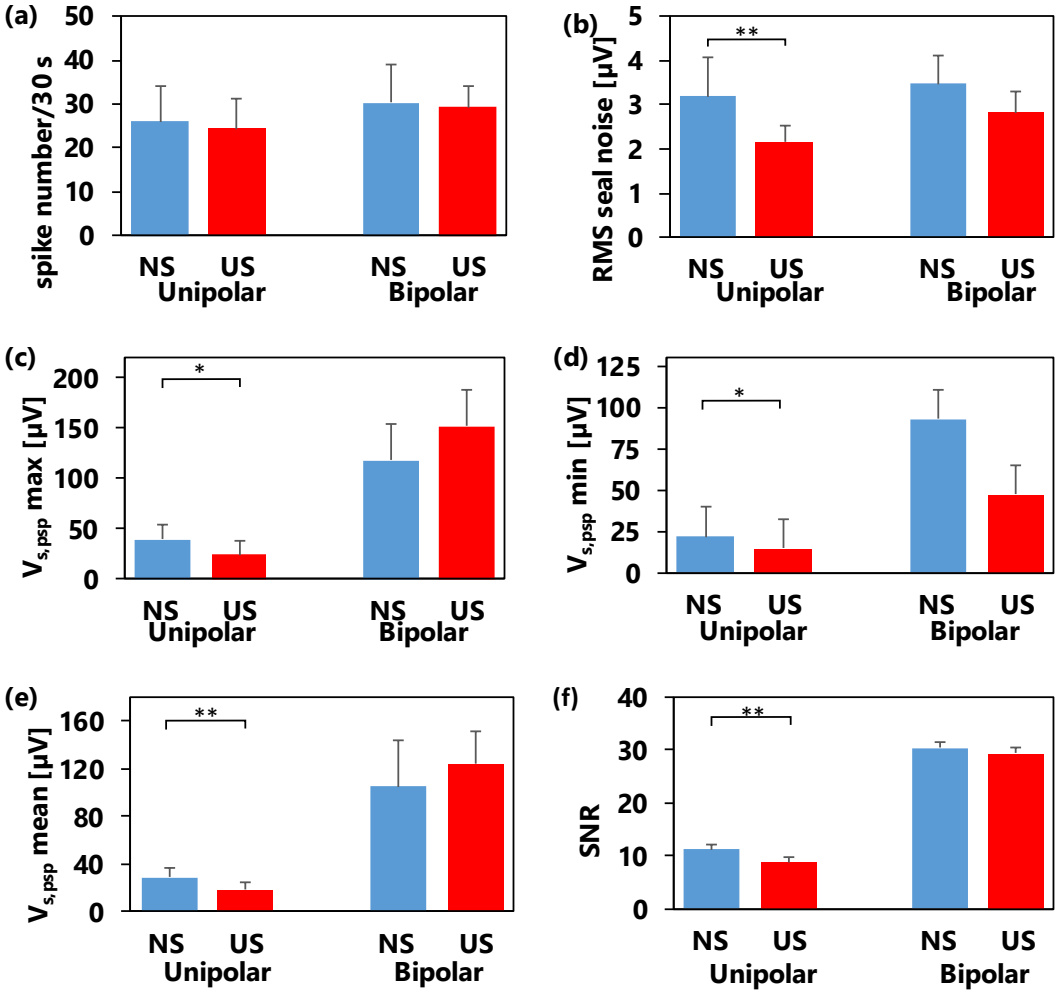

Figure 5.17. Unipolar and bipolar spike properties for nanostructured (NS) and unstructured microelectrode (US) channels: (a) total number of spikes measured in the measurement period of 30 seconds, (b) RMS of seal noise measured for the active channels where the spikes were recorded, (c) maximum peak-to-peak amplitude ($V_{s,p2p}$ max) of spikes measured by a channel in 30 second measurement period, (d) minimum peak-to-peak amplitude ($V_{s,p2p}$ min) of spikes measured by a channel in 30 second measurement period, (e) mean peak-to-peak amplitude ($V_{s,p2p}$ mean) of all spikes measured by a channel in 30 second measurement period and (f) signal-to-noise ratio SNR (ratio of $V_{s,p2p}$ mean and RMS seal noise of the corresponding channel). Analysis of statistical significance by one-way ANOVA (*$p < 0.05$, **$p < 0.01$, n (H2 nanostructured microelectrodes) = 24, n (unstructured microelectrodes) = 12).

5.6. Summary and outlook

In this chapter, the application of the biomimetic nanostructuring process on the surface of microelectrodes have been presented, which then have been used for recording extracellular activity from electrogenic cell cultures. MEAs fabricated with uniform organized nanostructures have shown several beneficial effects for biosensing application. Unfortunately, the natural

adhesion of surface of the cells is hardly uniform. Therefore, randomly organized nanostructures on microelectrodes offer a new perspective in understanding the cell-surface coupling, as well as extracellular signaling. Topographical characterization of the CLGNS biomimetic nanostructures showed randomness not only within a microelectrode surface, but also across all microelectrodes in the array. MEAs were fabricated with nanostructures of two different heights by adjusting the electroplating time and each were classified to high-density and low density depending upon the nanostructure coverage. Surface characterization with impedance spectroscopy showed the maximum reduction in impedance by densely nanostructured microelectrodes with larger height, which have been exclusively used for cell culture experiments. From the seal impedance measurements, it was observed that the CLGNS biomimetic nanostructures provided considerably tighter coupling compared to unstructured microelectrodes. Finally, electrophysiological experiments showed improved signal-to-noise ratio, as well as, superior action potential spike detection properties for the nanostructured microelectrodes. All of these findings suggest that the nanostructuring process to be versatile not only for the microelectrodes, but also for other biosensor surfaces.

Enhancement of microelectrode electrophysiological application by the CLGNS can be illustrated with three major perspectives (**Figure** 5.18). Firstly, the reduction of global impedance of the microelectrodes by enlarging the effective surface area has resulted in reduced thermal baseline noise (marked by 1 in **Figure** 5.18). Secondly, the protruding nanostructures have diminished the seal gap distance between the neuronal membrane and the microelectrode surface. Therefore, attenuation of extracellular activity due to ohmic losses through the seal gap has also been reduced, leading to enhanced SNR (marked by 2 in **Figure** 5.18). Finally, the nanostructures mimic the natural adhesion surface of the neuron which is composed of extracellular matrix biomolecules. The neurons bind firmly onto the nanostructures during their growth process with the help of focal adhesion complexes, which helps in formation of stronger cytoskeleton structure [97]. Stable cytoskeleton in turn regulates robust intra- and extracellular signaling in neural network [81] (marked by 3 in **Figure** 5.18).

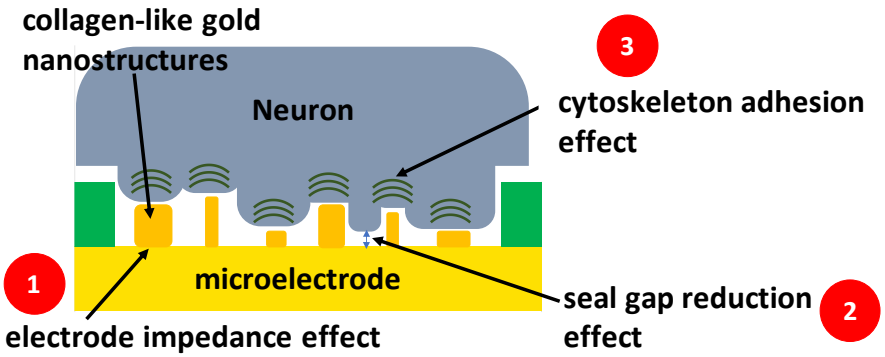

Figure 5.18. Illustration of the CLGNS biomimetic nanostructure effects on the microelectrodes and neurons for the improvement of electrophysiological experiments.

In this study, microelectrode arrays have been used for the acquisition of extracellular activity from the enteric neurons of mammalian myenteric plexus. Profound analysis of this information can help investigate cross-talk between immune system and enteric nervous system, which in turn helps in prediction of inflammatory bowel diseases [162]. In literature, MEAs have been used extensively with electrogenic neurons found in several organs of both central nervous and peripheral nervous system. For instance, human-derived induced pluripotent stem cells have been used for the prediction and treatment of central nervous system disorders such as epilepsy and Alzheimer's syndrome [163]. In other example, hippocampal slice cultures have been used with MEAs for studies of brain damage, neuronal protection and neuronal repair [164]. Therefore, the biomimetic nanostructured microelectrodes fabricated in this study were also briefly tested to record extracellular activity from other types of electrogenic cells. The extracellular activity measured with the CLGNS microelectrodes from Neuro2A mouse neuroblastoma cell line can be seen in **Figure** 5.19a and the activity measured from mouse enteric smooth muscle cells can be seen in **Figure** 5.19b. Effects of biomimetic nanostructures on the electrical spike properties, such as signal-to-noise ratio, have not been evaluated for these recordings, as extensive analysis of cell adhesion with seal impedance measurements and fluorescence microscopy experiments was done only for enteric neurons in this study. Nevertheless, it is proof-of-concept for the extension of biomimetic nanostructured microelectrodes application to other types of electrogenic cells.

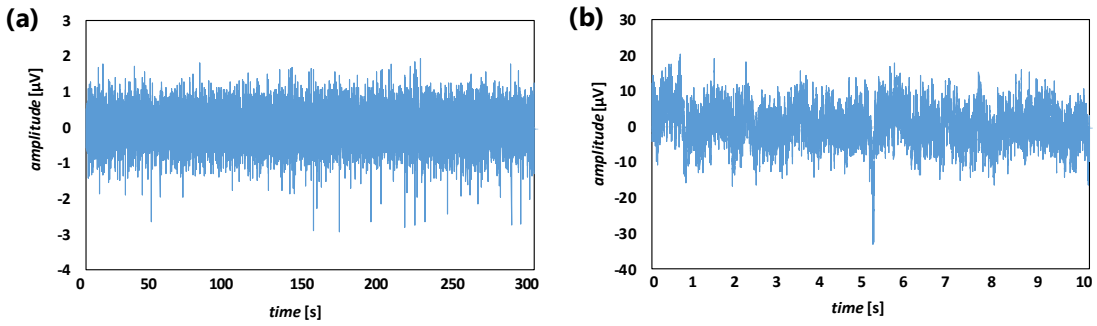

Figure 5.19. Action potential signals measured on CLGNS biomimetic nanostructured microelectrodes from (a) Neuro2A mouse neuroblastoma cell line and (b) mouse enteric smooth muscle tissue.[†]

Despite showing evidence in the enhancement of the surface, electrochemical and cell adhesion properties by the CLGNS on the MEAs, the findings could be further improved in future to substantially assert its application. Firstly, the best impedance reduction was observed with H2 microelectrodes with larger nanostructure height. This height cannot be larger than 50 nm due to the bottom-up nanostructure growth with electroplating process. Therefore, modifications could

[†]*Neuro2A mouse neuroblastoma culture on nanostructured MEAs done by Sophie Mannschatz, University of Applied Sciences Kaiserslautern Germany. Mouse enteric smooth muscle cells on nanostructured MEAs done by Anne Christmann, University of Applied Sciences Kaiserslautern Germany.*

be implemented in the biomimetic process to develop larger nanostructures without compromising the nanostructure density, which would definitely further improve the impedance properties of the microelectrodes. Secondly, the seal impedance was measured at 1 kHz based on the findings in the literature [41]. It would be insightful to safely measure the seal impedance over a complete frequency spectrum and extract useful information on cell-surface coupling. This would necessitate the potentiostatic measurements to be done in an incubated environment, which could be logistically difficult. The enhancement in some spike properties (such as spike rate) could not be observed. This was because only the electrode surfaces are nanostructured, the passivation layer (which encompasses more than 99 % of the culture surface) is planar unstructured. Therefore, to truly understand the effect of biomimetic nanostructures on the extracellular signaling of the neurons, the complete cell culture surface of the microelectrode array must be nanostructured.

6. Cell adhesion investigation on collagen-like gold nanostructures

In the previous chapter, superior extracellular signal recording was measured for microelectrodes structured with collagen-like gold nanostructures, which was attributed to the reduction in seal impedance and subsequently improved cell-surface coupling. In this chapter, the enhanced cellular interaction to the biomimetic nanostructures has been investigated with fluorescence microscopy.

Results of this chapter selectively published in:

1: Nowduri, B., Schulte, S., Decker, D., Schäfer, K., & Saumer, M. (2020). Biomimetic Nanostructures Fabricated by Nanoimprint Lithography for Improved Cell-Coupling. Advanced Functional Materials, 30(45), 2004227. https://doi.org/10.1002/adfm.202004227.

2: Nowduri, B., Schulte, S., Decker, D., Schäfer, K., & Saumer, M. (September 19-23 2022, Leuven Belgium). Fabrication of metal and polymer biomimetic nanostructures replicating extracellular matrix biomolecules with nanoimprint lithography, 48th international conference on Micro and Nano Engineering - Eurosensors (MNE-ES).

The primary objective of the microelectrode surface functionalization with biomimetic synthetic nanostructures in this study was to improve the neuronal adhesion by reduce the seal gap with neuronal membrane. Improved adhesion would eventually result in promotion of neuronal growth and formation of robust neuronal networks, thus ensuring superior electrogenic activity recordings [81,148]. In the previous chapter, improved adhesion as well as enhanced charge transfer properties were indeed observed for enteric neurons cultured on biomimetic nanostructured MEAs. Apart from electronic optimization, the biomimetic nanostructures could also influence the adhesion and growth of the cells by providing topographical cues to the cell membrane, which in turn modulates the structure of cell cytoskeleton [165] and focal adhesion complexes (FACs) [166]. Therefore, proteins in the cytoskeleton and cell membrane have been stained with appropriate fluorescence markers in this chapter and their respective significance in the growth and adhesion process of cells to the biomimetic nanostructures have been summarized in **Table** 6.1.

Table 6.1. Overview of fluorescence microscopy methods presented in this chapter with appropriate markers and their significance in neuronal growth and adhesion to the biomimetic nanostructured surfaces.

Analysis method	Marker	Measured quantity	Significance
Cell growth assay	Chicken-anti-PGP9.5	Density of neuronal structures	Growth of neurons compared for different surfaces
	Rabbit-anti-S100B	Density of glial structures	Growth of glial cells compared for different surfaces
Focal adhesion analysis	Vinculin Monoclonal antibody	Distribution of FAC network	Larger number of FACs per unit cell was correlated to improved adhesion [167-168]
	TRITC-conjugated phalloidin	Actin cytoskeleton structure	Cell spread area was extracted for the actin fiber network and compared for different surfaces
		FAC surface coverage	Area of individual FACs calculated as a function of complete cell spread area and compared for different surfaces

6.1. Neuron-glial cells growth assay on biomimetic nanostructures

Confluent growth of neurons and glial cells on the biomimetic nanostructured surface is essential for the robust transmission of electrogenic activity from the cell body to the biosensor. Neuron and glial cells have been stained and the microscopy images have been evaluated for percentage area of cells covered on the biomimetic nanostructured surfaces, as well as, control surfaces.

6.1.1. Fluorescence microscopy with neuronal and glial cell markers

The neuron-glial cell growth assay has been performed on CLGNS surfaces (height 40 nm) and unstructured planar gold surfaces with area approx. 20 mm^2. This was the surface area of cell culture on the flip-chip bonded PCB MEAs used in this study (see **Figure** 4.1) and the results from these experiments can be projected to the microelectrode surfaces. Moreover, the microelectrodes (with diameter 30 µm) account to less than 1 % of the total cell culture area on the MEA chip, making the staining and microscopy process impractical for individual microelectrode evaluation. Comparison for primary cell culture is extremely difficult due to their high dependency on surface properties and culture pH value [169]. Therefore, enteric neuronal cells were used for assessing the influences on growth of networks. Collagen coated silicon wafer and laminin coated glass were used as positive controls for the cell cultures, along with the nanostructured and unstructured gold surfaces. Examples of fluorescence staining of enteric neural networks cultured on the aforementioned surfaces on DIV 7 can be seen in **Figure** 6.1. Differences in the density of neuronal and glial structures between the gold surfaces can be noticed from the immunofluorescence staining. Also, cells cluster aggregation could be observed on the nanostructured surfaces i.e., CLGNS gold and collagen coated silicon, which was absent on unstructured gold and glass.

6.1.2. Comparison of cell density on culture surfaces

Comparison of neuronal and glial structure areas to the whole picture area section showed significant differences in growth networks (**Figure** 6.2a-b and Table 1 of Appendix V). The density of neuronal and glial structures on nanostructured gold surface was significantly higher compared to unstructured gold, showing that the biomimetic nanostructuring process immensely improved growth and proliferation of cells on the conductive metal. Approx. 3-fold increase in density has been observed in the neuronal structures, whereas an improvement of factor of 1.8 has been observed for the glial structures. Collagen coated silicon was also used in this analysis, as it is the analogous to the CLGNS, which indeed showed the highest density of both neurons and glial structures. This result was expected, as the collagen interaction with the cells was improved by both topographical, as well as, biochemical effects of the hydrocarbon structures of the individual fibers [170]. Moreover, the collagen fibers possess 3D randomness which further contributed to the adhesion of cells to the surface. In contrast, the CLGNS only showed 2D randomness and the adhesion was improved only by topographical effects. Nevertheless, the application of the biomimetic nanostructures in this study is dedicated to biosensor surface functionalization. Therefore, the enhancement in the cell growth behavior on metallic nanostructured surface in comparison to unstructured surface is noteworthy. In literature, similar promising results were observed when nanostructured gold surfaces were cultivated with neuronal cells [171-172]. Unfortunately, enhanced neuronal-glial growth induced by the biomimetic nanostructures are only limited to the microelectrode surfaces and not the complete cell culture surface of the MEA.

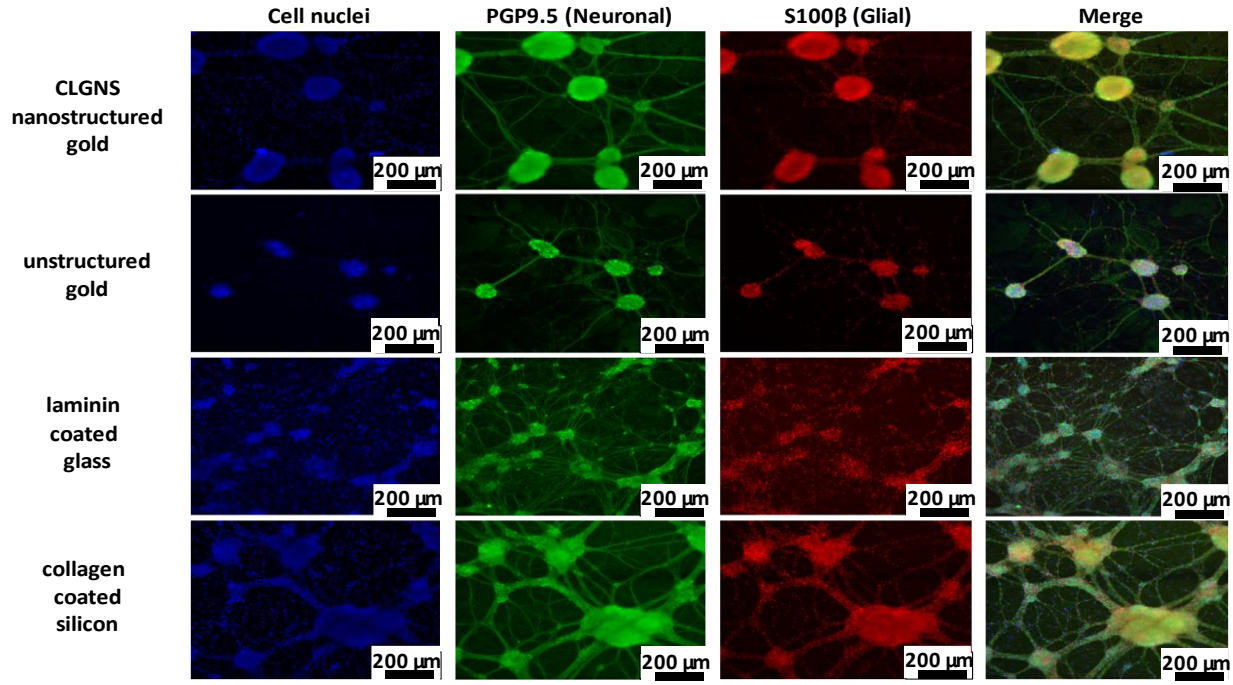

Figure 6.1. Immunofluorescence staining microscopy images of enteric neuronal culture on CLGNS nanostructured gold and control surfaces. Neuronal marker PGP9.5 (green), glial marker S100B (red) and cell nuclei (DAPI, blue).

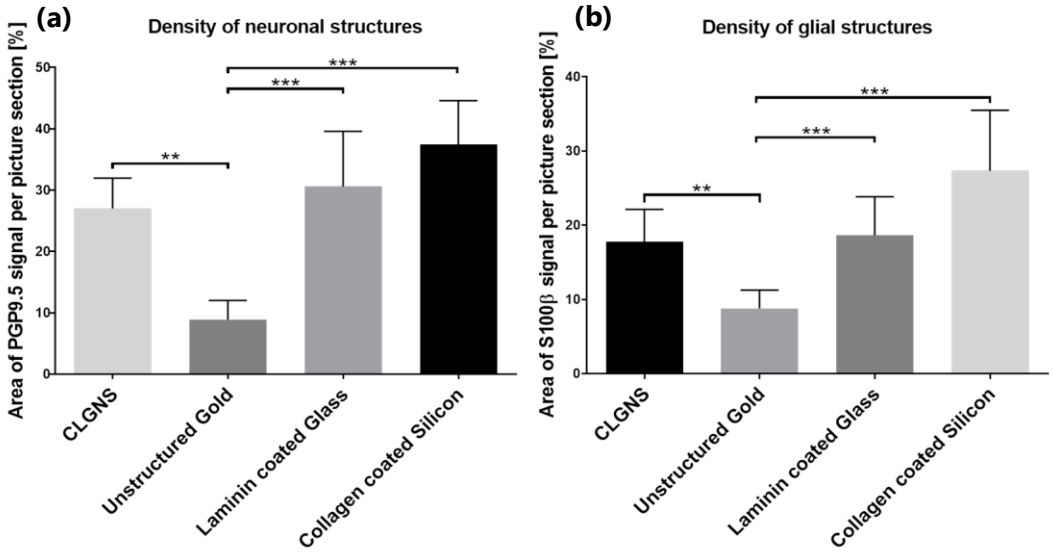

Figure 6.2. Comparison of (a) neuronal cells (PGP9.5 area to whole picture section) and (b) glial cells (S100B area to whole picture section) on CLGNS nanostructured gold and control surfaces. Mean values and standard deviation from raw data, analysis of statistical significance by one-way ANOVA (**p < 0.01, ***p < 0.005, n = 4).[†]

[†]*Cell culture, microscopy and image analysis on surfaces done by Steven Schulte, University of Applied Sciences Kaiserslautern Germany.*

6.2. Investigation of FAC growth and maturation

6.2.1. Fluorescence microscopy of FACs and actin cytoskeleton

The focal adhesion analysis of the neurons was performed with on CLGNS nanostructured (height 40 nm) and unstructured planar gold macroelectrode surfaces with surface area approx. 20 mm^2. Planar glass surface has been used as a positive control. As explained in the previous section, it was impossible to map the microelectrode surface on the MEA culture surface for the fluorescence microscopy. Therefore, macroelectrode surfaces were used for the focal adhesion analysis instead of microelectrode surfaces. Enteric neurons extracted from post-natal mice were cultured on the aforementioned surfaces and fixed on DIV 1 (**Figure** 6.3a), DIV 4 (**Figure** 6.3b) and DIV 7 (**Figure** 6.3c). Stronger adhesion of cells to the nanostructured surface can be effectively characterized by number, shape, size and orientation of the FACs formed at the interface [167-168]. The FACs have been imaged by marking vinculin protein present in its composition. Similarly, actin cytoskeleton has also been marked for the same microcopy images to evaluate the shape of the cells adhering to the culture surface.

A timeline of focal adhesion analysis is performed in this study to understand the progress of FAC formation and maturation on the cell culture surfaces. Dormant FACs are minute and circular in dimensions and upon cell growth and differentiation, the FACs mature in size as well as aspect ratio [77]. Larger number of FACs with higher aspect ratio would eventually result in stronger adhesion of the cells to the culture surface [168,173]. Apart from vinculin staining presented in this study, other proteins present in the FAC such as talin, kindlin and paxillin have been used for fluorescence microscopy and subsequent adhesion analysis in literature [174-175].

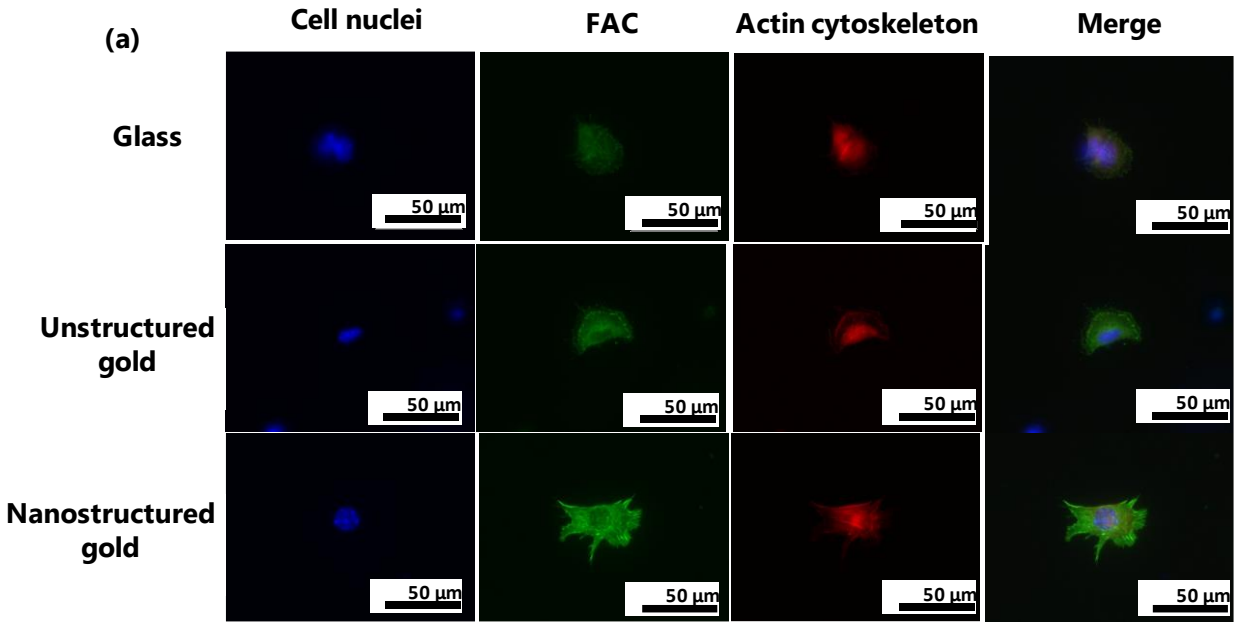

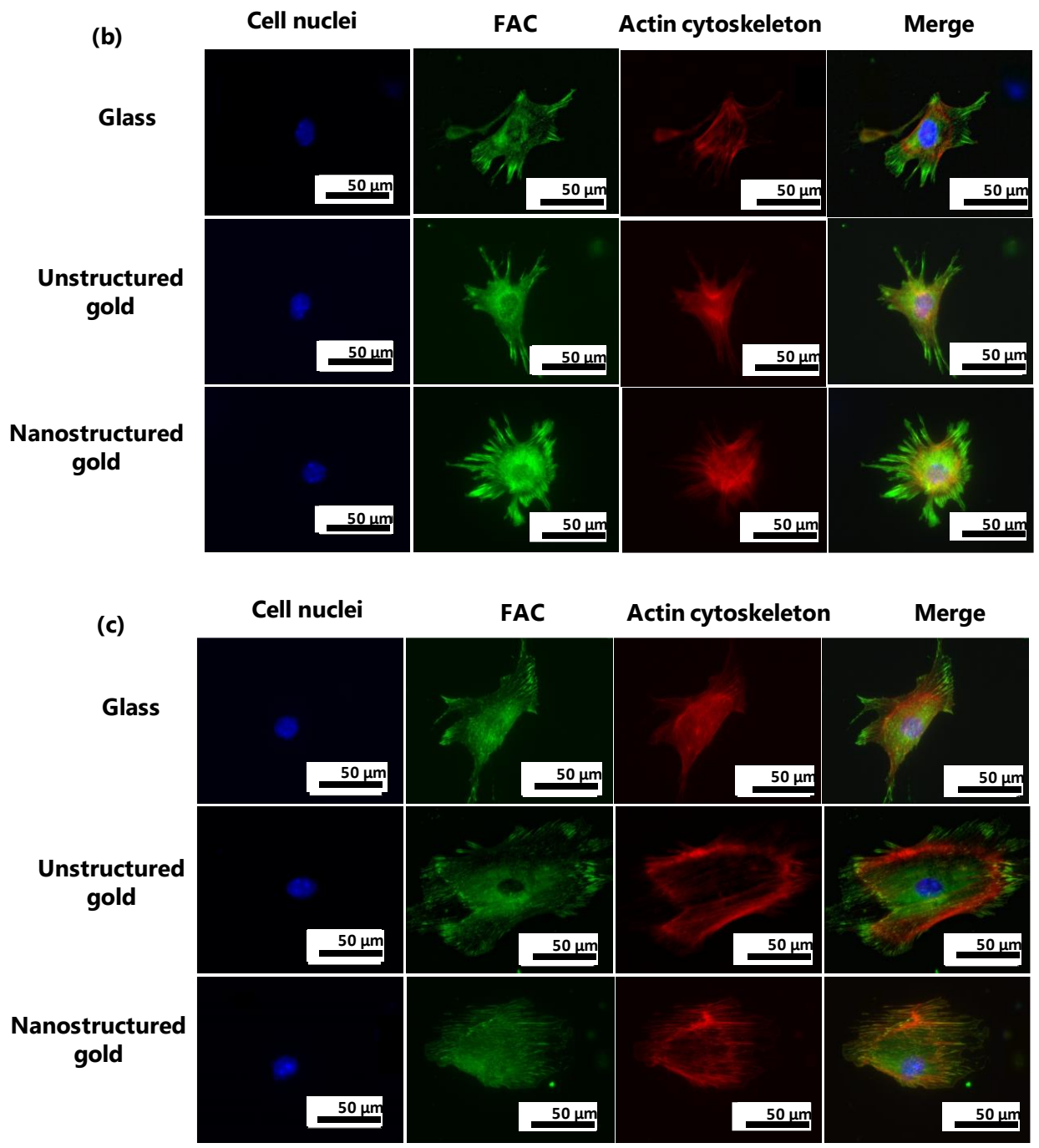

Figure 6.3. Formation and maturation of FACs and actin filaments for enteric neuronal culture on CLGNS nanostructured gold and control surfaces. Immunofluorescence staining of FAC marked by vinculin monoclonal antibody (green), actin cytoskeleton marked by TRITC conjugated phalloidin (red) and cell nuclei with DAPI (blue) fixed and imaged on (a) DIV 1, (b) DIV 4 and (c) DIV 7.[†]

[†]*Cell culture and microscopy on surfaces done by Negin Adavoudi Jolfaei, Technical University of Kaiserslautern Germany.*

The FACs were classified based on its longitudinal length namely, small (length smaller than 2 µm), nascent (length larger than 2 µm and smaller than 6 µm) and mature (length larger than 6 µm). The length-based classification of FACs has been performed in literature to characterize cell adhesion to nanostructured surfaces and it has been applied to this study as well [176]. It can be observed in **Figure** 6.3a that the cell size on the DIV 1 on all three surfaces was uniformly diminished and the population of the FACs was predominantly small. In contrast, cells with larger dimensions fixed on DIV 4 (**Figure** 6.3b) showed a distinctive distribution of small, nascent and mature FACs. The first differences in the FAC shape, size and density between the nanostructured and unstructured gold surfaces were also observed here. No significant differences in the actin cytoskeleton structure was observed between surfaces on DIV 4, suggesting minimal impact on the cell shape. On DIV 7, the fully differentiated cells showed profound differences for the different types of FACs, especially at the periphery of the cell cytoskeleton (**Figure** 6.3c). From the raw fluorescence microscopy images of FACs and actin cytoskeleton, diverse information could be extracted to characterize the cell-surface coupling. Dimensional parameters of individual FACs such as longitudinal length, lateral width and surface area of coverage were calculated from the vinculin stained images (see Section 3.5.2). Similarly, the surface adhesion area of unit cell spread on the different surfaces has been extracted from the actin cytoskeleton staining images (see Section 3.5.2). Number of cells in the microscopy image was determined with the nuclei staining, which was essential for unit-cell focal adhesion analysis.

6.2.2. Comparison of number of FACs per unit cell formed on culture surfaces

The distribution of different types of FACs and total number measured on DIV 1, DIV 4 and DIV 7 per unit cell on culture surfaces can be seen in **Figure** 6.4a-d (see Table 2 of Appendix V). As observed in the microscopy images, the total number of FACs on all types of surfaces increases gradually with prolonged cell cultures.

On DIV 1, more than 75 % of the total number was consisted of the small FACs, whereas the contribution of the nascent FACs was minute and mature FACs was negligible. Interestingly, it can be observed that planar glass surface enabled the dormant neurons to form marginally larger number of small and nascent FACs, in comparison to the gold surfaces. This can be the attributed to the superior adsorption properties of the borosilicate material, which plays the preliminary role in cell attachment to the surface while seeding. Absence of large differences between nanostructured gold and unstructured gold on DIV 1 suggests that the nanotopography of the surface does not significantly influence the onset of FAC formation. On DIV 4, first differences in the total number of FACs between the surfaces could be observed. The nanostructured gold surfaces show relatively larger number of total FACs in comparison to unstructured gold and glass. Interestingly, no significant difference in small FACs could be observed between the three surfaces, while nascent and mature FACs are higher in number for the nanostructured surfaces.

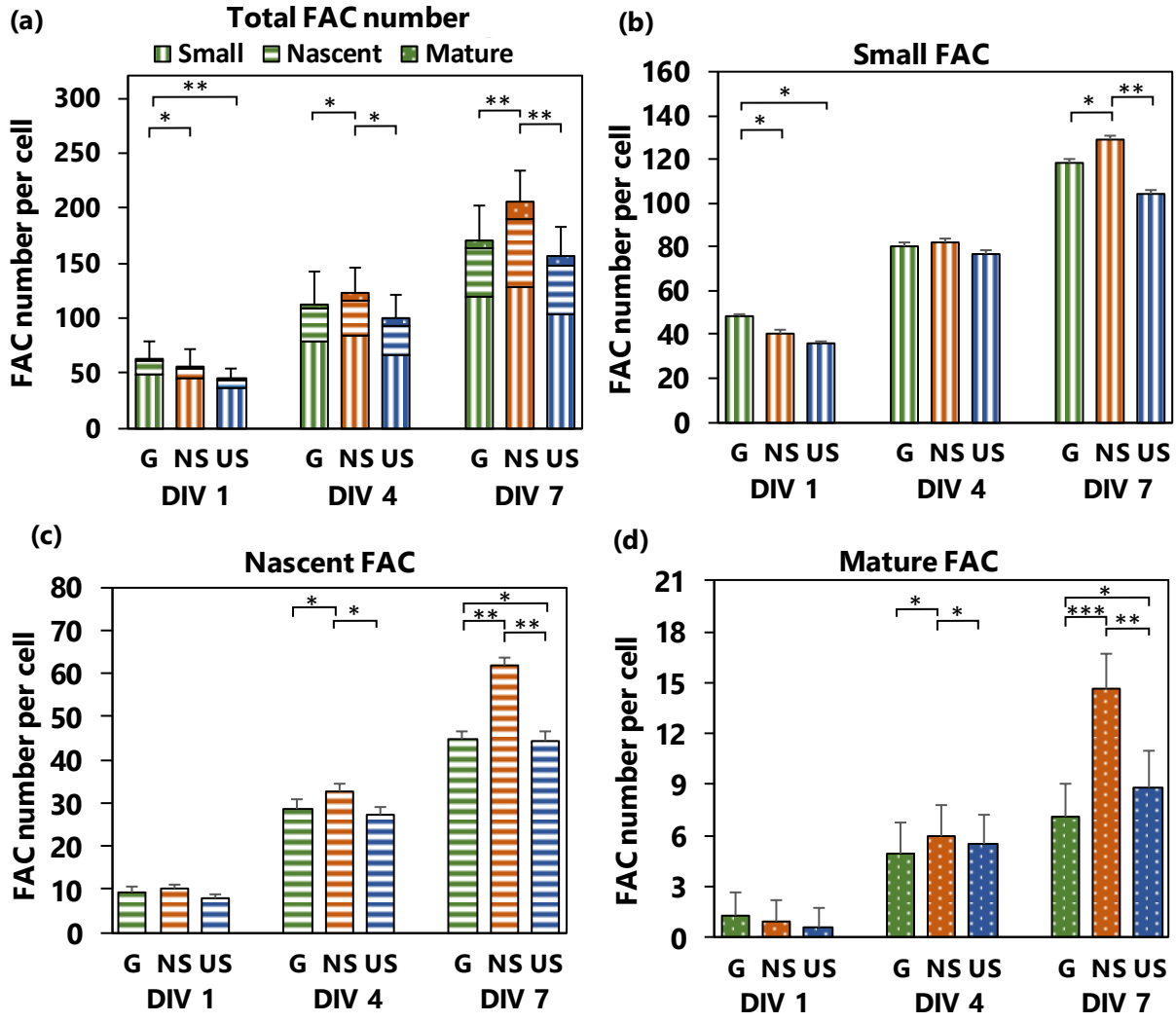

Figure 6.4. Relation of number of FACs measured by fluorescence imaging of vinculin for nanostructured gold (NS), unstructured gold (US) and glass (G) surfaces. The FAC were classified into small (length smaller than 2 μm), nascent (length between 2 μm and 6 μm) and mature (length longer than 6 μm). The measurements were performed with neurons fixed on DIV 1, DIV 4 and DIV 7. Mean values and standard deviation from raw data, analysis of statistical significance by one-way ANOVA (*p < 0.05, **p < 0.01, ***p < 0.005, n = 10).

As observed in the microscopy images, the full extent of FAC distribution for the gold and glass surfaces was seen on DIV 7. In comparison to unstructured surfaces, the nanostructured gold shows significant enhancement in total number, as well as, small, nascent and mature FACs. The nanostructured gold surfaces possess approx. twice the number of mature FACs, as compared to unstructured gold and glass surface. Minimal difference in the FAC number was observed between the unstructured glass and unstructured gold surfaces, which suggested that FAC maturation is significantly promoted by the nanotopography of the surface. And as the cell grows and spreads across the nanostructured gold, several new small and nascent FACs are formed, which further

contributed to the increase in total FACs. The FACs act as an anchor for the cells to the surface of adhesion and strength of cell adhesion is directly proportional to the total number, as well as, its dimensions [167-168,173]. Therefore, it can be inferred here that the nanotopography of the gold surface would activate the cells develop larger number of mature FACs during its growth, which in turn promotes the adhesion.

6.2.3. Comparison of adhesion area of cell

The area of cell spread on the adhesion surface has been calculated by segmentation of actin cytoskeleton marked by phalloidin in fluorescence microscopy images. Actin fibers are bound to the FACs of the cells at the periphery of the cell-surface interface and the boundaries of cells are marked by the phalloidin staining [121]. The overview of the adhesion surface area measured for enteric neuronal tissue on nanostructured gold, unstructured gold and planar glass surfaces fixed on DIV 1, DIV 4 and DIV 7 can be seen in **Figure** 6.5 (see Table 3 of Appendix V). On DIV 1, the glass surface showed slightly larger cell adhesion area in comparison to gold surfaces, which was similar to the trend observed for total FAC number in section 6.2.2. This could be material surface effect rather than a topographical effect, as the superior surface adsorption properties of glass helped in initial spreading of cells. On DIV 4, no significant difference in the cell adhesion area among the gold and glass surfaces was measured, which was clearly observed on DIV 1. Similarly, no significant differences between the nanostructured and unstructured gold were observed on DIV 7. It is evident from these observations that the topographical effects of the nanostructures improved the neuronal adhesion by the formation of larger number of FACs, without significantly increasing the cell adhesion area.

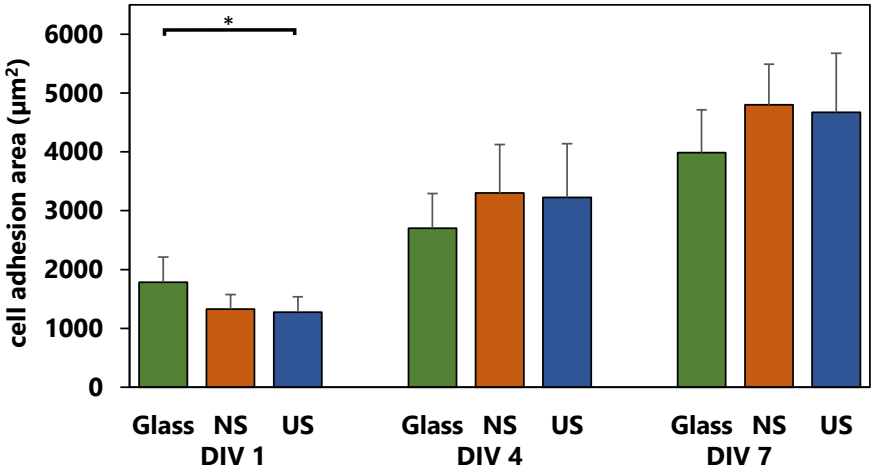

Figure 6.5. Relation of cell adhesion area measured by fluorescence imaging of actin cytoskeleton for nanostructured gold (NS), unstructured gold (US) and glass surfaces. The measurements were performed on neurons fixed on DIV 1, DIV 4 and DIV 7. Mean values and standard deviation from raw data, analysis of statistical significance by one-way ANOVA (*$p < 0.05$ $n = 10$).

6.2.4. Comparison of coverage area of FACs by unit cell

The nanostructured surfaces showed a significantly higher number of FACs, especially as the cell culture proliferates on DIV 7. Enhanced surface interaction of cells is not only function of total number of FACs, but also the proportion of cell adhesion area covered by the FACs. Therefore, the area covered by each type of FAC, as well as, the total FAC area has been calculated from vinculin marked microscopy images and phalloidin-marked microscopy images (see section 3.5.2). The FAC surface coverage area on nanostructured gold, unstructured gold and glass surfaces have been calculated on DIV 1, DIV 4 and DIV 7 can be seen in **Figure** 6.6a-d (see Table 4 of Appendix V).

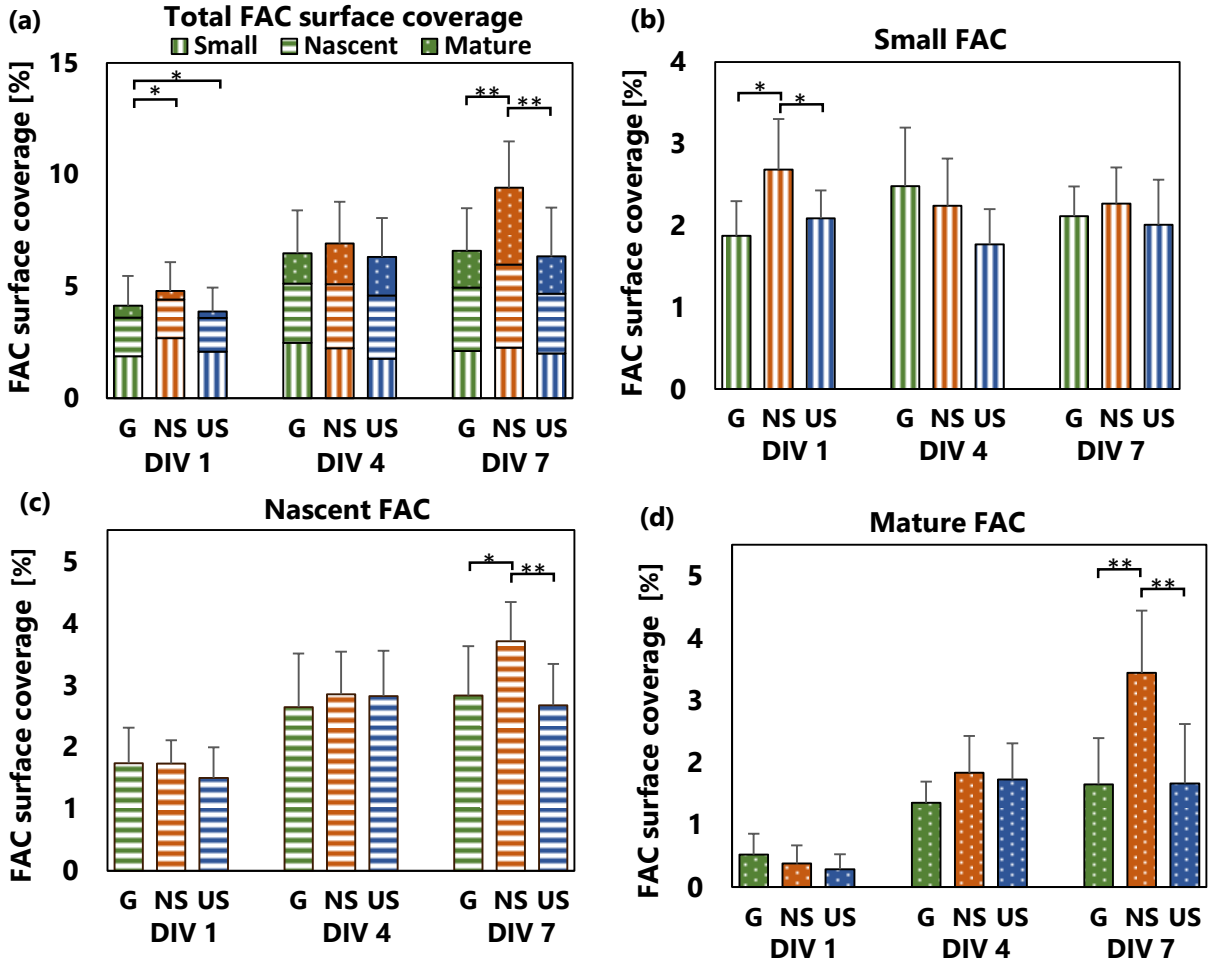

Figure 6.6. Relation of surface area covered by FACs measured by correlating vinculin marked surface to actin marked cell adhesion area for nanostructured gold (NS), unstructured gold (US) and glass (G) surfaces. The focal adhesion surface coverage measurements were classified into small (length smaller than 2 μm), nascent (length between 2 μm and 6 μm) and mature (length longer than 6 μm). The measurements were performed on neurons fixed on DIV 1, DIV 4 and DIV 7. Mean values and standard deviation from raw data, analysis of statistical significance by one-way ANOVA (*$p < 0.05$, **$p < 0.01$, $n = 10$).

On DIV 1, it can be observed that the total FAC surface coverage and the surface coverage of small FACs was larger for nanostructured gold in comparison to both unstructured gold and unstructured glass surfaces. This was in contrast to the result observed with the number of FACs measured in section 6.2.2, where glass surfaces showed maximum number of total and small FACs. This suggested that despite of having relatively smaller number, the nanostructured gold enabled the neurons to develop FACs with higher aspect ratio on the surface from the early stages of development. Similarly, nascent FACs contributed significantly to the total area of focal adhesion coverage of each surface, despite having a relatively smaller number. Therefore, the classification of the FACs based on the longitudinal length was extremely important here to understand the progress of its growth and maturation. On DIV 4, no significant difference in any of the FAC surface coverage area between different surfaces was observed. This was an unexpected result as significant differences on DIV 4 were observed for the number of nascent and mature FACs between nanostructured and unstructured surfaces in section 6.3.2.

On DIV 7, the most substantial differences in FAC surface coverage were observed between nanostructured and unstructured surfaces, as the cells have completely proliferated. In comparison to unstructured gold, 50 % increase in the total FAC coverage, 37 % increase in nascent FAC coverage and 70 % in mature FAC coverage has been observed for the nanostructured gold. Similar to the number of FACs measured in section 6.2.2, the unstructured glass and unstructured gold showed similar FAC surface coverage. The mature FACs contributed the highest in the total FAC coverage, that is despite having lesser number, which showed the importance of FAC maturation during the cell growth and its significance in enhancement of cell interaction to the culture surface.

6.3. Summary and outlook

The main objective of this chapter was to understand and analyze the topographical advantages provided by CLGNS biomimetic nanostructures on the biomechanics of cell culture adhesion. From the cell growth assay, significantly larger networks of the neurons and glial cells were observed for the nanostructured surfaces (natural collagen and CLGNS) in comparison to planar unstructured surfaces (glass and gold). This result could be correlated with the enhancement in surface wetting induced by the synthetic and natural nanostructures. Cell-surface interaction is also modulated by the formation and maturation of FACs consisting of membrane proteins, cytoskeletal components and functional groups present on the culture surface [77,167-168,173]. From the focal adhesion analysis, significant enhancement in FAC population was observed for nanostructured surfaces, especially on DIV 7. Moreover, the coverage of the mature FACs was also enhanced by biomimetic nanostructures as the cell culture proliferated on DIV 7.

Functionalization of biosensor surfaces with synthetic nanostructures in literature has shown immense beneficial effects in enhancement of cell surface coupling. But the molecular–level understanding behind this enhancement has not yet been properly established. Combination of

high-resolution electron microscopy with focused ion beam technique has been previously used to visualize the junction between the cell membrane with the nanostructures [88], but not the individual FACs. Therefore, to precisely characterize the cell adhesion with nanostructures, a combination of ultra-high magnification electron microscopy with fluorescence markers would help visualize the morphology, shape and orientation of individual FACs. In case of neurons, it would also be interesting to observe the combination of focal adhesion analysis with fluorescence microscopy of calcium transients propagated across the cell membrane on the nanostructured surfaces, which would extend the understanding of the relation between cell adhesion and extracellular signaling.

It has been observed with the surface wetting measurements in Chapter 4, as well as, in neuronal growth assay in this chapter that the CLGNS indeed enhance the cell spreading properties of the gold surface. But in both the experiments, the optimum surface properties were observed for natural collagen fibers coated on silicon surface. The topographical properties of the nanostructures play a crucial role in surface spreading of cells, but in order to attain the best cell adhesion properties, it is essential to mimic the biomolecular structure of the natural collagen. Hence mimicking of the 3D randomness in the natural collagen nanostructures is very essential to best reproduce the adhesion properties on the culture surface. Nevertheless, the findings in this chapter provide a brief outlook on the timeline of FAC formation and maturation on the biomimetic nanostructures. And by correlating with the seal impedance measurements and electrophysiological measurements in Chapter 5, it could be established that biomimetic nanostructures on the metal surface do indeed enhance cell-surface interaction which eventually would be significantly beneficial for biosensor functionalization.

7. Discussion and future advancements

Randomly organized biomimetic metal nanostructures inspired from the organization and dimensions of natural collagen have been successfully fabricated in this study. Electrochemical, physical and biological characterization have shown significant improvement in performance of the biomimetic nanostructured microelectrodes. Despite excellent reproducibility of the nanostructuring process, there are important discussion points to be addressed, which could not only help improve the nanostructuring process, but also efficient application of the nanostructures to biosensors and tissue engineering.

7.1. Comparison of biomimetic nanostructuring process to state-of-the-art research

In this study, a novel biomimetic nanostructuring method has been described with natural nanostructures present in the extracellular matrix used as a template. In literature, biomimetic nanostructures have been fabricated with several natural templates such as shark skin [177], moth eye [178], lotus leaf [179], cicada wing [180] etc. Interestingly, biomimetic nanostructures have shown to replicate the functional property of the natural nanostructures along with the topographical features. For instance, ceramic nanostructures have reproduced the antireflection surface property that was a characteristic of the moth eye template (**Figure** 7.1a) [179]. Similarly, polymeric nanostructures have shown to reproduce superhydrophobicity which existed in the lotus leaf surface template (**Figure** 7.1b) [178]. The biomimetic nanostructuring presented in this study is dedicated exclusively for biosensor functionalization (e.g., microelectrode surfaces). Therefore, the cell adhesion properties associated with natural nanostructures have been replicated with the CLGNS. Moreover, it can be seen in **Figure** 7.1a-b that the state-of-the-art biomimetic nanostructured surfaces do not exhibit substantial randomness in its nanofeatures. Whereas the CLGNS fabricated in this study exhibit randomness in dimensions, as well as, structure orientation.

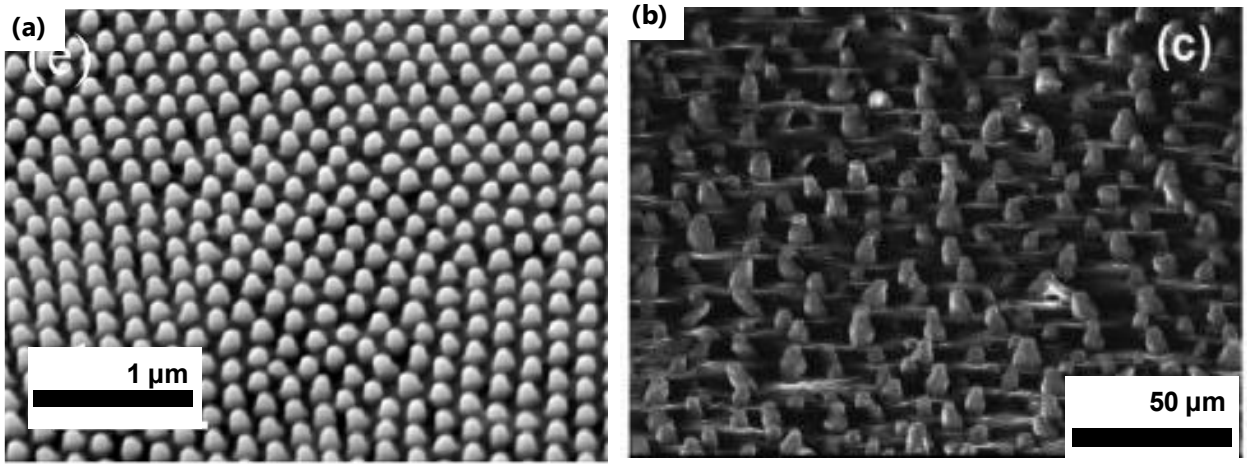

Figure 7.1. (a) SEM of moth eye inspired nanostructures (adapted from [178]) and (b) SEM of lotus leaf inspired nanostructures (adapted from [179]).

Apart from the randomness in the nanostructures, it is also important to compare the biomimetic nanostructured microelectrodes developed in this study with examples of other state-of-the-art nanostructured gold microelectrodes used for neural interfaces. For instance, **Figure** 7.2a shows the impedance spectra measured with wire-like gold nanostructured microelectrode fabricated with anodized alumina template [181] and **Figure** 7.2b shows mushroom shaped gold nanostructured microelectrodes fabricated with nanoimprint lithography [41]. It could be observed that the relative reduction in impedance magnitude (in comparison to unstructured microelectrode) is relatable to the impedance reduction induced by the CLGNS presented in this study. It is important to point out that there have also been other studies with nanostructured

gold microelectrodes with impedance reduction in much larger magnitude as compared to biomimetic nanostructures fabricated in this study. Gold nanoflake structured microelectrodes developed with electrodeposition showed 44x reduction in impedance magnitude at 1 kHz [182] (**Figure** 7.2c), which is desired for the biomimetic nanostructuring. Nevertheless, CLGNS possess the additional advantage of directly replicating the topography of natural cell adhesion surfaces, which have helped the promotion of neuron life cycle events such as growth, differentiation and proliferation.

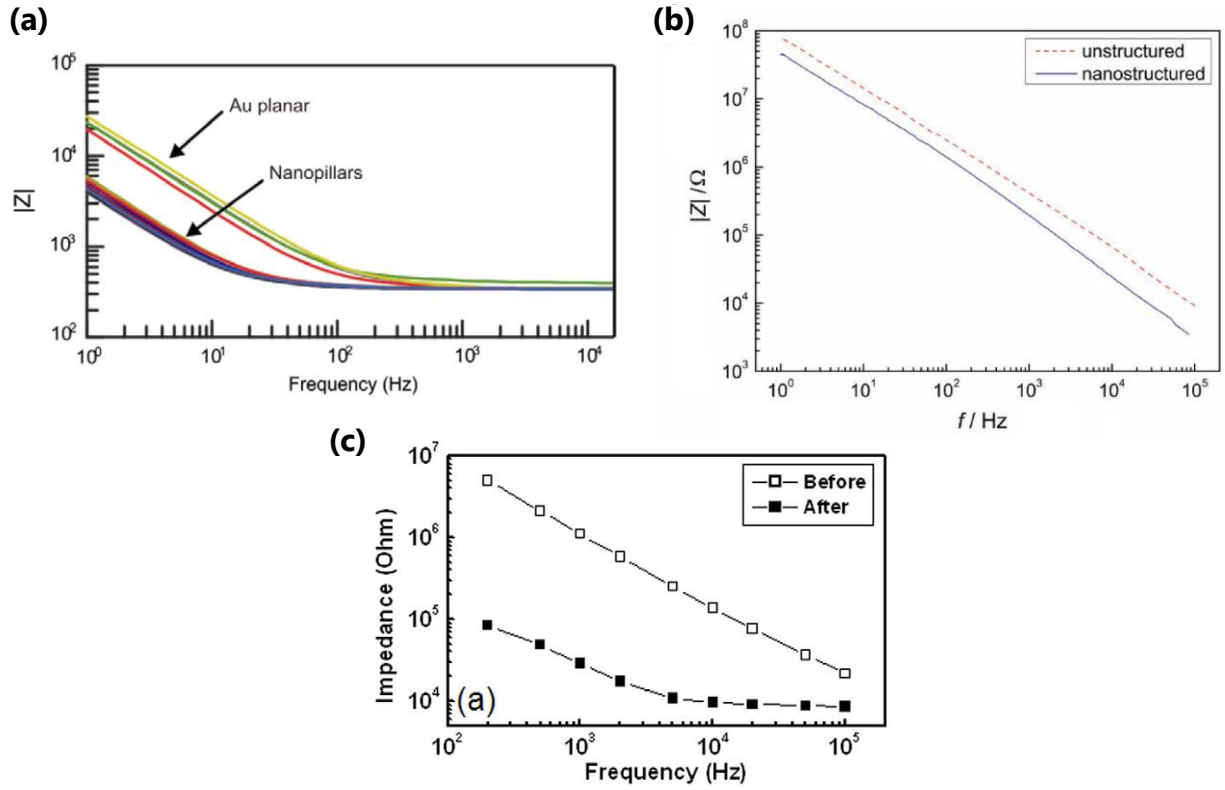

Figure 7.2. Impedance magnitude reduction measured for gold nanostructured microelectrodes in comparison to planar gold microelectrodes: (a) gold nanopillars developed with anodic alumina template (adapted from [181]), (b) mushroom-shaped gold structures developed with nanoimprint lithography (adapted from [41]) and (c) flake nanostructured gold structures developed with electrodeposition, before deposition in white and after deposition in black (adapted from [182]).

7.2. 3D Random collagen-like gold nanostructures

It has been mentioned in several sections of this study that the CLGNS fabricated with thermal nanoimprint lithography and gold electroplating exhibit 2D randomness profile. This is because of the bottom-up nanostructure fabrication process which results is excellent covalent adhesion to the underlying substrate gold layer. Nevertheless, surface wetting measurements in Chapter 4, as well as, neuronal growth assay in Chapter 6 have shown that the 3D randomness exhibited by natural collagen showed the best surface enhancement. Therefore, novel approaches to fabricate the 3D random CLGNS that do not use the bottom-up nanostructure growth have been discussed

here. Deposition of metal on the nanoimprinted resist can be done with physical vapor deposition methods such as evaporation [33] and with chemical methods such as electrodeposition [34]. And in Chapter 4, it was shown that the cavities on the imprinted surface did indeed exhibit a 3D randomness profile. Therefore, deposited metal will be expected to fill all the imprinted cavities and hence forming a nanostructure pattern which also exhibits 3D randomness profile. The challenge here was to extract the top-bottom deposited nanostructured gold on to another substrate such as glass or silicon wafer. The thermal nanoimprint resist used for the fabrication of 2D random CLGNS was a thermoplastic polymer with a glass transition temperature of 105 °C, which makes it vulnerable to structural disintegration when used in high temperature physical vapor deposition methods (such as metal evaporation). Instead, a thermosetting polymer was used as a nanoimprint resist, where the polymer was irreversibly cross-linked during the imprint process giving it high thermal stability. Post imprint, the metal layers (200 nm Au as nanostructure layer and 20 nm Ti as sticking layer) were evaporated into the nanoimprint cavities. In literature, the exaction of top-bottom deposited layers onto another substrate wafers have been done with methods such as compression bonding [183], adhesive bonding [184] etc. Compression bonding has the disadvantage of using extremely high temperature and pressure conditions which could lead to unnecessary structural damage (such as peeling and bucking), which makes adhesive bonding easier to use. Biocompatible and optically transparent polymer OrmoComp® has been used as the adhesion layer. And by subsequent UV curing and thermal crosslinking, the nanostructure layer and substrate wafer were firmly bound and then separated from nanoimprint resist surface giving standalone nanostructured gold surface. AFM scanned profile of the natural collagen fibers on NIL master, 2D randomness CLGNS fabricated in this study and 3D randomness CLGNS fabricated with the aforementioned process line with evaporation and adhesive bonding can be seen in **Figure** 7.3a-c. The smaller CLGNS shows a height of 32 nm (marked by red line **Figure** 7.3c), the larger nanostructure shows a height of 177 nm (marked by blue line **Figure** 7.3c) and the wider nanostructure shows a width of 2 µm (marked by yellow line **Figure** 7.3c). Unfortunately, the double-helix hydrocarbon structure of the natural collagen fibers (with microfibrils of dimensions under 1 nm) could not be observed on the 3D random CLGNS surface. This is a proof-of-concept for the fabrication of 3D random CLGNS and they are expected to show superior surface wetting and cell growth, compared to the 2D random CLGNS.

The 2D CLGNS fabricated with electroplating are adhered to the substrate surface with extremely strong metallic bonds, whereas the 3D CLGNS fabricated by evaporation and adhesive bonding are bound by an external polymer layer. Therefore, long-term stability of the structures to the substrate wafer has to be tested. Moreover, the presence of a dielectric polymer medium in the wafer stack could be disadvantageous for electric signal conduction, which could be subsequently detrimental to biosensor application. Several characterization tests have to be performed to compare the advantages (as well as disadvantages) of 3D random CLGNS over 2D random CLGNS.

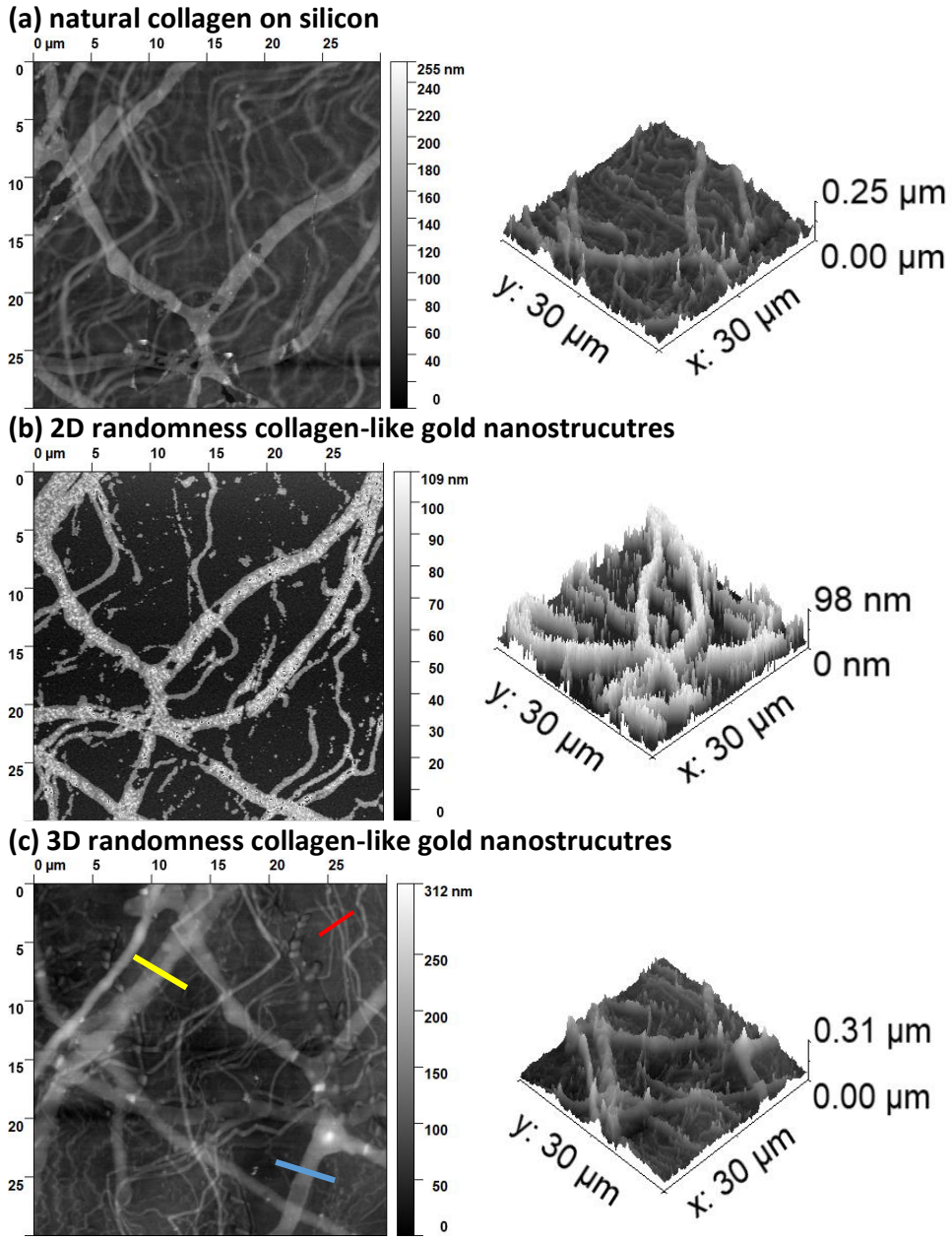

Figure 7.3. (a) Collagen fiber network spin-coated on silicon and used as master stamp for nanoimprint-based replication methods. (b) CLGNS fabricated with thermal nanoimprint lithography and subsequent electroplating depicting 2D randomness in the structural orientation. (c) CLGNS fabricated with UV nanoimprint lithography and subsequent physical vapor deposition depicting 3D randomness in the structural orientation (adapted from [185]).

7.3. Whole-surface-nanostructured microelectrodes

The nanostructured microelectrode arrays in this study have showed significant improvement in signal-to-noise ratio by reducing the global impedance and improved the coupling between cells and the electrode surface. For the extracellular activity measurements, approx. 200 000 cells were

plated on each MEA chip, which encompasses a culture surface of approx. 20 mm^2. The MEA with 60 electrodes (each of surface diameter of 30 µm) encompasses approx. 1 % of the total culture surface area. As only the electrode surfaces were nanostructured, the passivation layer which encompasses more than 99 % of the culture surface was planar unstructured. Therefore, it is essential for the complete cell culture surface including the passivation layer to be structured with biomimetic nanostructures to obtain optimum neuronal growth and network formation. SU-8 epoxy-based polymer has been used as the passivation layer for the microelectrodes due to its supreme biocompatibility and electrical insulation properties [186]. Unfortunately, SU-8 as an insulating polymer layer cannot be nanostructured with the nanoimprint lithography. For this application, nanoimprintable insulating polymer is required that can be cured at a temperature lower than 200 °C, so as to not destroy the information of the collagen fibers on the master stamp. OrmoComp® has been used for this application, which is a UV-curable, optically transparent, biocompatible polymer with electrical permittivity in the range similar to SU-8 polymer [187]. OrmoComp® can be used as a complete dielectric passivation on top of glass substrate or in combination with an auxiliary SU-8 layer. The nanostructured MEAs post patterning with lithography and gold etch for contact pads and connection tracks was spin-coated with 1 µm of OrmoComp® polymer and then imprinted with an intermediate IPS foil (with a negative tone of the collagen coated silicon master) and then cured with UV light and finally cross-linked at 150 °C to form dielectric passivation layer. This passivation layer is then processed with photolithography to open microelectrode contact pads. AFM profile and SEM image of the whole-surface nanostructured MEAs can be seen in **Figure** 7.4a-b. It can be observed that the nanostructured passivation layer exhibits 3D randomness profile where anisotropy was observed in lateral dimensions, axial dimensions and structural organization. Upon further inspection, the collagen-like polymer nanostructures (CLPNS) with larger width replicated the nano-fibril double-helix organization which was observed in the natural collagen fiber network on silicon master. Therefore, the CLPNS indeed exhibited the truest from of 3D randomness replication which was absent in collagen-like metal nanostructures. Early biocompatibility tests with enteric neurons on the nanostructured OrmoComp® surfaces showed excellent results, with a large proportion of live cells even after DIV 7.

In literature, polymers such as SU-8, parylene C and polyimide have been used for passivation of microelectrode which exhibit excellent dielectric and structural stability for long term electrophysiological application. But OrmoComp® is a relatively novel polymer and no substantial literature exists elucidating its long term structural and electrical stability. A comprehensive characterization of physical, optical, electrical and biological properties is essential to truly understand the potential of the 3D random nanostructured passivation layer for biosensor application. Subsequently a combination of 3D randomness in CLGNS and CLPNS passivation layer would eventually result in the fabrication of a completely 3D random nanostructured microelectrode array.

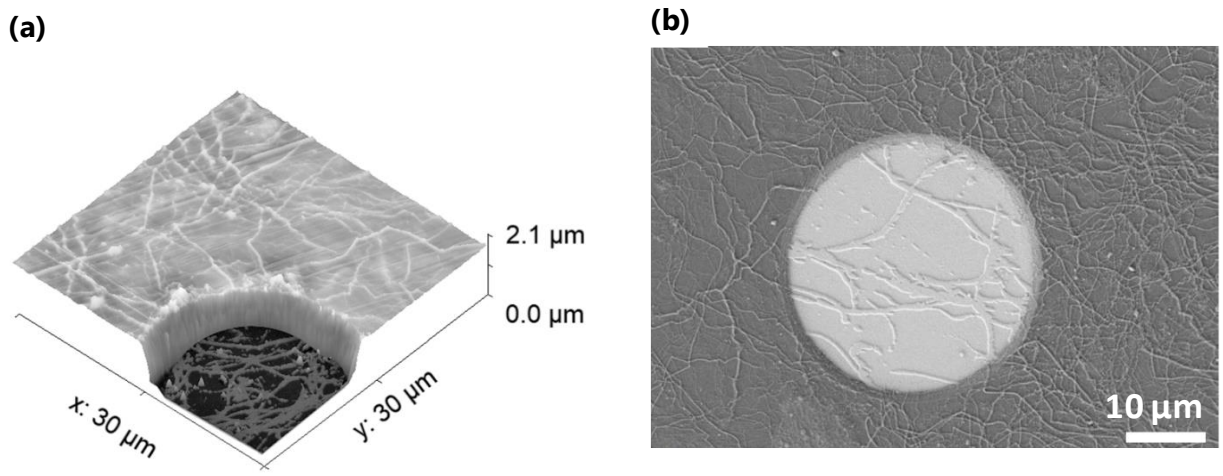

Figure 7.4. (a) AFM surface profile and (b) scanning electron microscopy image of whole-surface-nanostructured microelectrodes where the passivation layer surface (OrmoComp® material) is nanostructured with UV nanoimprint lithography and the electrode surface is nanostructured with thermal nanoimprint lithography (adapted from [185]).

7.4. Biomimetic nanostructures replicating extracellular matrix composite

During the initial stages of randomly organized nanostructures fabrication process, inspiration was derived from the natural adhesion surface of the mammalian basement membrane which consists of a complex network of ECM biomolecules such as collagen, fibrin, laminin etc. Collagen is the most predominant component of the ECM network and its thermal and mechanical stability made it applicable to be used in nanoimprint lithography for the fabrication of randomly organized biomimetic nanostructures. During the process of the biomimetic collagen nanostructure fabrication with NIL and natural collagen fibers, novel techniques with versatile materials were discovered that negated the necessity of thermal and mechanical stability for the structures on the master stamp. This essentially allowed the extension of the biomimetic synthetic nanostructure fabrication process to other sensitive biomolecules of ECM, as well as, the complete ECM composite network. This would be the next step of the biomimetic nanostructuring process, as the beneficial effects of composite ECM coatings are documented to be superior in comparison to collagen coatings for cell culture experiments [188].

The first step in the replication process of the ECM network was the fabrication of the master stamp for the NIL environment and this in itself has been the biggest challenge. In contrary to collagen coatings, there exists very limited literature on established methods for reproducible coatings of composite ECM network on flat surfaces such as glass or silicon. Moreover, it was also challenging to image the ECM coat with surface scanning methods or electron microscopy, especially without fixation with organic aldehydes. The ECM gel commonly used for cell surface

coating (extracted from mucosal mouse membrane) is diluted in culture medium solution. The culture medium solution consists of a high proportion of dissolved salts (eg. sodium bicarbonate, sodium chloride, etc.) which are deposited on the silicon surface when incubated or spin-coated. Therefore, it could not be used for NIL master preparation. Alternate approach was to individually spin coat the biomolecules present in the ECM complex in a sequential order. Therefore, collagen type I (1:100 mg/ml), collagen type IV (1:100 mg/ml), fibronectin (1:100 mg/ml) and laminin (1:100 mg/ml) were spin-coated in succession on the same silicon wafer with the method described in Chapter 3 (**Figure** 7.5). It could be observed that the collagen fibers were dominating the surface profile due to their larger dimension and the other biomolecules could be sparsely derived from the surface profile. This pseudo-ECM NIL master could be used for biomimetic replication, but it is not the truest representation of ECM composite consisting of several other biomolecules.

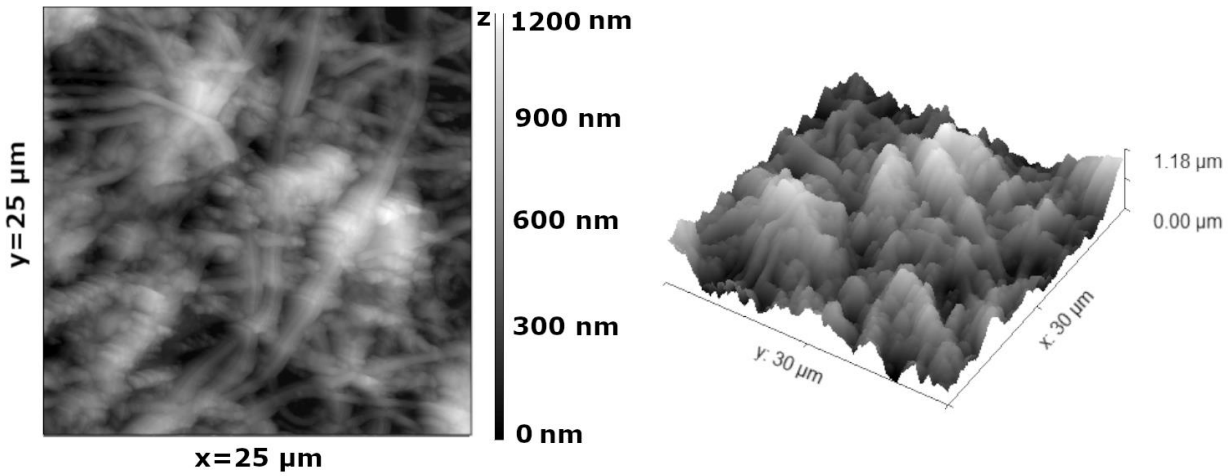

Figure 7.5. AFM surface profile of pseudo-ECM NIL master developed by sequential spin-coating of collagen type I, collagen type IV, fibronectin and laminin on silicon wafer with the process used in this study for collagen solution.

Other ECM composites such as Matrigel® and Maxgel®, which have been successfully isolated on glass and silicon surfaces in literature [21] could be used for the development of biomimetic master stamp. SEM and AFM of ECM composite Matrigel® resembling the anterior corneal basement membrane can be seen in **Figure** 7.6a-b [21]. The features show a 3D randomness profile, but the mechanical stability could not be reproduced in this study.

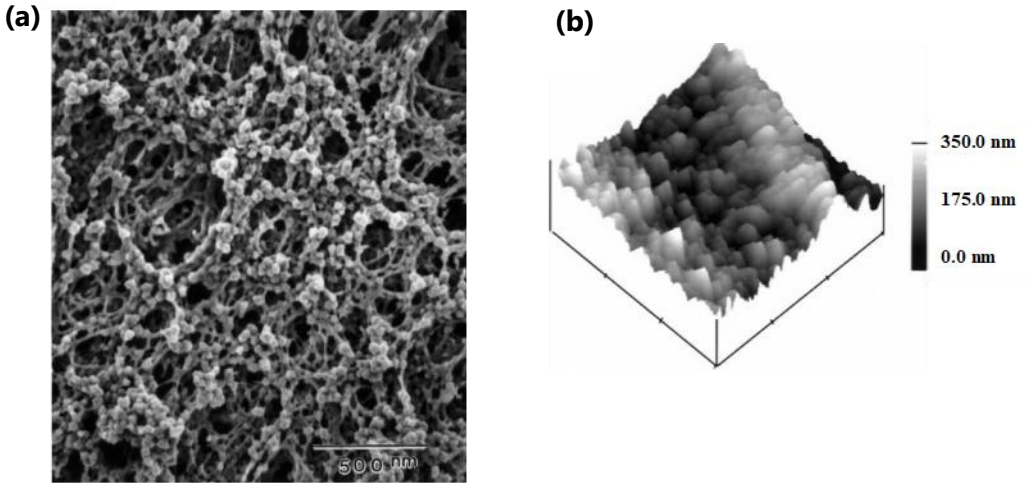

Figure 7.6. (a) SEM and (b) AFM 3D profile of Matrigel® ECM (adapted from [21]).

Unfortunately, a master stamp with the composite ECM network of molecules for replication and nanostructure fabrication could be not developed. Nevertheless, if a master stamp could be successfully coated with ECM composite, they could be replicated with soft nanoimprint lithography [28]. In soft NIL, the thermosetting polymer (such as polydimethylsiloxane) can be deposited on the ECM coated master and with the help of a chemical curing agent, the polymer can be fixed and cross-linked at room temperature for an extended time period. This negative tone of the ECM composite network on the thermosetting polymer can be then replicated into the biomimetic polymer and metal nanostructures with the processes described in this study. Application of synthetic ECM-mimicking nanostructures could be extremely beneficial to the functionalization of metal and polymer surfaces for biosensor application, as well as, tissue engineering.

7.5. Application of biomimetic nanostructures to other biosensors

Biomimetic synthetic nanostructures have been applied on the surface of microelectrodes and a significant improvement was observed in electrophysiology measurements. The synthetic nanostructures can also be used for other applications in biosensors and tissue engineering, where cell-coupling plays an important role. An overview of alternate applications of the biomimetic nanostructures in biomedical technology and tissue engineering can be seen in **Figure** 7.7.

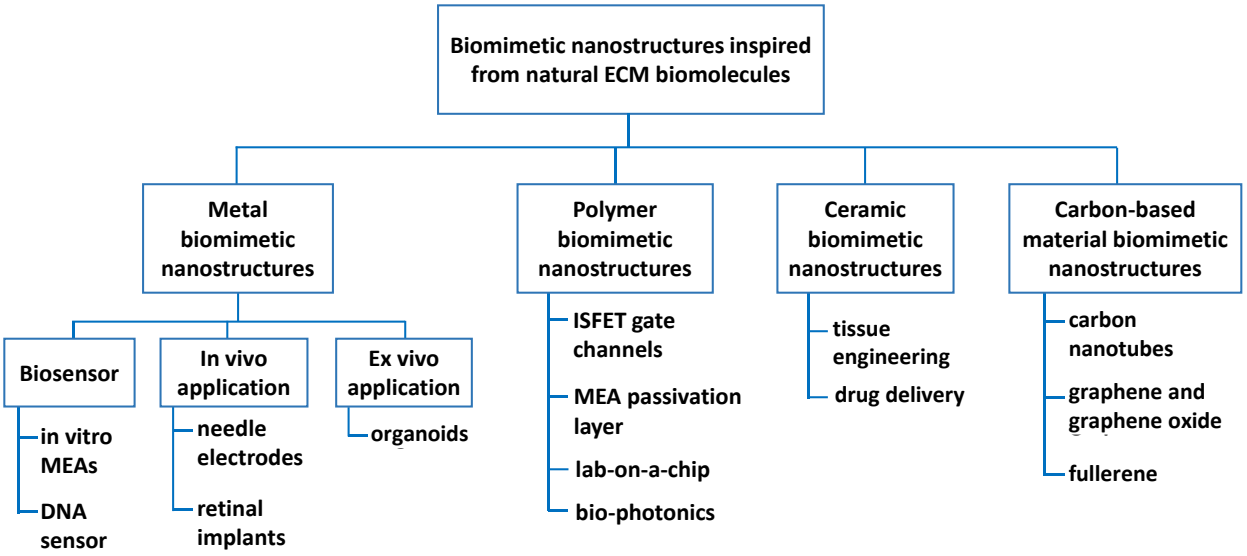

Figure 7.7. Illustration of possible biosensor applications of biomimetic synthetic nanostructures classified based on material and cell environment.

7.5.1. Biosensors

The metallic biomimetic nanostructures can find a profound application in the functionalization of the metal surfaces for biomolecular sensors such as DNA sensors, bacterial sensors etc. The larger active sensor surface area with the biomimetic nanostructuring would promote the adhesion of proteins and cellular components and at the same time would reduce the impedance. The biomimetic nanostructured patterned surfaces could provide topographical cues for cells which can eventually be applied for targeted drug delivery [189]. Also, the biomimetic nanostructures could be fabricated replicating the functional shape of biomolecule receptors (such as enzymes, aptamers, etc. [190-191]) which would be extremely beneficial in biomolecular sensing. Polymer nanostructures can find an important application where biocompatible dielectric surfaces are in contact with the cells, one of which is the passivation layer for microelectrodes that has been discussed in this section 7.2. Another example is the gate channels of ion-sensitive field effect transistor (ISFET). Since the dielectric gate channels are the active sensor surface of the ISFETs, the nanostructuring could significantly promote adhesion and consequently signal acquisition [192]. OrmoComp® polymer described in section 7.2 for the polymer nanostructuring has been successfully used in development of active lenses in industry, which could open the door for the application in bio-photonics as well [193].

7.5.2. In vivo and ex vivo application

In vivo microelectrodes (e.g., needle biosensor) are used for the extraction of extracellular activity from neuronal organs such as brain and spinal cord, where the electrodes are placed within the organism [194-195]. The most critical factor for successful implantation of in vivo electrodes is the formation of scar tissue. Presence of nanostructures on the electrode surface mimics the natural

basement membrane environment and subsequently reduces the scar tissue formation [196]. For ex vivo application, the organs and organoids are extracted from the organism and are cultured in the artificial environment where they are measured for extra- and intracellular activity. Scar tissue formation is a major issue here as well which could be alleviated with nanostructured microelectrode surface. Moreover, the penetration of the organoid epithelium is a requirement for the efficient recordings which could be accomplished by the 3D nanostructures.

7.5.3. Carbon-based materials and ceramics

In this study, the biomimetic nanostructuring process has been presented for metal biosensor surfaces and for polymer dielectric surfaces. Ideally, it could be extended for other materials used in biosensor application and tissue engineering, most prominently for carbon-based materials and ceramics. Carbon-based materials such as graphene and carbon nanotubes are known for their excellent mechanical strength, biocompatibility and electrical conductivity which make them great substrate materials for biosensor application [197-198]. Graphene and CNTs are most commonly deposited by wet chemical methods and chemical vapor deposition [199-200], which makes them applicable to be used in nanoimprint lithography and subsequently for biomimetic nanostructuring. Ceramics such as TiN, ITO and IrO have been commonly used as the electrode material for MEAs due to their excellent conductivity and nanorough columnar structure [68,201-202]. These ceramics can be further optimized with the biomimetic nanostructuring, as the most common methods of deposition include physical vapor deposition and atomic layer deposition. Other ceramics such as hydroxyapatite and forsterite which are extensively used in tissue engineering can also be functionalized with the biomimetic nanostructuring for bone tissue engineering and targeted drug delivery [203-205].

Conclusion

This study presents an advanced biomimetic nanostructuring technique inspired from the biological nanostructures present in the natural adhesion surface of cells. The nanostructures have been fabricated inspired from the randomness pattern of natural collagen fibers present in the extracellular matrix. The collagen fibers were replicated in to gold nanostructures with nanoimprint lithography and electroplating. Subsequently, they were applied to the surface of microelectrode arrays that were used in electrophysiological recordings.

The primary requirement of the biomimetic nanostructures was to possess a high degree of randomness in their organization and dimensions. Collagen fibers are one the most prominent ECM biomolecules and by spin-coating the fibers onto a flat silicon surface, the structural randomness was successfully transferred to collagen-like gold nanostructures (CLGNS). The CLGNS macroelectrode surfaces (20 mm^2) were then characterized with topographical measurements, surface wetting measurements and electrochemical impedance spectroscopy. The lateral dimensions (width) of the CLGNS measured with AFM was found to be in the range between 95 nm and 1800 nm, which was similar to the natural collagen fibers, whereas the axial dimension was measured to be uniform across the entire surface. Depending upon the electroplating time for nanostructure growth and the height of the smallest reproducible collagen fiber, the CLGNS on macroelectrode surfaces was measured to have an axial dimension of 40 nm. For CLGNS with 40 nm height, the overall increase in the surface area measured to be approx. 28 %. The surface wetting of the CLGNS macroelectrode surfaces was evaluated with contact angle measurements and an increase of 33 % in the critical surface energy was measured in comparison to unstructured surfaces. Impedance spectroscopy on the CLGNS macroelectrode surfaces showed 54 % reduction in impedance magnitude at 1 kHz in comparison to unstructured surfaces.

The CLGNS were used for the functionalization of microelectrode arrays to promote the adhesion of neuronal culture to the electrode surfaces and hence improve the quality of extracellular recordings. To have a better understanding of the effect of nanostructure on the electronic properties of the microelectrodes, the CLGNS were fabricated with two heights: 30 nm and 50 nm. The nanostructure densities were measured to be in range between 20 % and 68 % on microelectrodes. From impedance spectroscopy measurements, the largest decrease in impedance magnitude was observed for nanostructures with higher density and larger height, whereas the electrodes with smaller height showed very minimal reduction in impedance. Cell adhesion analysis on microelectrode was performed by measuring the seal impedance at cell-microelectrode junction and observed 3-fold amplification of the seal impedance for CLGNS microelectrode (with 50 nm height). This could be directly correlated to a smaller seal gap between the neuronal culture and the microelectrode resulting in tighter cell-surface coupling. Finally, electrophysiological measurements showed 35 % increase in signal-to-noise ratio for the CLGNS microelectrode (with 50 nm height), in comparison to unstructured microelectrodes.

Along with the biosensor surface characterization, the cellular focal adhesion and growth effects of the CLGNS have also been analyzed in this study with immunofluorescence microscopy. Neuron-glial growth assay showed approx. 270 % improvement in the neuronal surface coverage and 180 % in glial surface coverage for the nanostructured macroelectrode surfaces. Afterwards, comprehensive analysis of growth and maturation of focal adhesion complexes (FACs) on nanostructured macroelectrode surfaces was performed. 50 % increase in the total FAC coverage, 37 % increase in nascent FAC coverage and 70 % increase in mature FAC coverage was observed for the nanostructured gold on day 7 of differentiation. The increase in number of the FACs and presence of larger proportion of the FACs with higher aspect ratio was attributed to be the reason for the stronger adhesion of cells to the CLGNS surfaces, which eventually resulted in enhancement in microelectrode electrophysiological properties.

The enhancement in the electrophysiological properties of the microelectrode induced by the biomimetic nanostructures enables the opportunities to be applied for the in vivo and ex vivo applications. The extension of biomimetic nanostructuring process with other materials such as polymers, ceramics, carbon-based materials would further expand its versatility which eventually would lead to multifold applications in biosensor technology, tissue engineering and drug delivery.

References

[1] Clark, L. C., Wolf, R., Granger, D., & Taylor, Z. (1953). Continuous Recording of Blood Oxygen Tensions by Polarography. Journal of Applied Physiology, 6(3), 189–193. https://doi.org/10.1152/jappl.1953.6.3.189

[2] Ferreira, G. N. M., da-Silva, A.-C., & Tomé, B. (2009). Acoustic wave biosensors: physical models and biological applications of quartz crystal microbalance. Trends in Biotechnology, 27(12), 689–697. https://doi.org/10.1016/j.tibtech.2009.09.003

[3] Owicki, J. C., & Wallace Parce, J. (1992). Biosensors based on the energy metabolism of living cells: The physical chemistry and cell biology of extracellular acidification. Biosensors and Bioelectronics, 7(4), 255–272. https://doi.org/10.1016/0956-5663(92)87004-9

[4] Narayanaswamy, R. (1991). Current developments in optical biochemical sensors. Biosensors and Bioelectronics, 6(6), 467–475. https://doi.org/10.1016/0956-5663(91)85044-W

[5] Rotthier, A., Eeckhout, M., Gryson, N., Dewettinck, K., & Messens, K. (2007). Protein-Based Detection of GM Ingredients. In Advances in Food Diagnostics (pp. 199–210). https://doi.org/https://doi.org/10.1002/9780470277805.ch10

[6] Damborský, P., Švitel, J., & Katrlík, J. (2016). Optical biosensors. Essays in Biochemistry, 60(1), 91–100. https://doi.org/10.1042/EBC20150010

[7] Cooper, M. A. (2002). Optical biosensors in drug discovery. Nature Reviews Drug Discovery, 1(7), 515–528. https://doi.org/10.1038/nrd838

[8] Wise, K. D., Angell, J. B., & Starr, A. (1970). An Integrated-Circuit Approach to Extracellular Microelectrodes. IEEE Transactions on Biomedical Engineering, BME-17(3), 238–247. https://doi.org/10.1109/TBME.1970.4502738

[9] Ermis, M., Antmen, E., & Hasirci, V. (2018). Micro and Nanofabrication methods to control cell-substrate interactions and cell behavior: A review from the tissue engineering perspective. Bioactive Materials, 3(3), 355–369. https://doi.org/10.1016/j.bioactmat.2018.05.005

[10] Stratakis, E., Ranella, A., & Fotakis, C. (2011). Biomimetic micro/nanostructured functional surfaces for microfluidic and tissue engineering applications. Biomicrofluidics, 5(1). https://doi.org/10.1063/1.3553235

[11] Bandzerewicz, A., & Gadomska-Gajadhur, A. (2022). Into the Tissues: Extracellular Matrix and Its Artificial Substitutes: Cell Signalling Mechanisms. Cells, 11(5), 914. https://doi.org/10.3390/cells11050914

[12] Politi, S., Carotenuto, F., Rinaldi, A., di Nardo, P., Manzari, V., Albertini, M. C., Araneo, R., Ramakrishna, S., & Teodori, L. (2020). Smart ECM-Based Electrospun Biomaterials for

Skeletal Muscle Regeneration. Nanomaterials, 10(9), 1781. https://doi.org/10.3390/nano10091781

[13] Joddar, B., & Ito, Y. (2011). Biological modifications of materials surfaces with proteins for regenerative medicine. Journal of Materials Chemistry, 21(36), 13737. https://doi.org/10.1039/c1jm10984g

[14] Veis, A., & Cohen, J. (1955). The Degradation of Collagen. II. The Solubilization Process in the Acid pH Range. Journal of the American Chemical Society, 77(9), 2364–2368. https://doi.org/10.1021/ja01614a003

[15] Hayashi, T., & Nagai, Y. (1973). Effect of pH on the Stability of Collagen Molecule in Solution. The Journal of Biochemistry, 73(5), 999–1006. https://doi.org/10.1093/oxfordjournals.jbchem.a130184

[16] Altug, H., Oh, S.-H., Maier, S. A., & Homola, J. (2022). Advances and applications of nanophotonic biosensors. Nature Nanotechnology, 17(1), 5–16. https://doi.org/10.1038/s41565-021-01045-5

[17] Yeom, S.-H. (2011). Nanostructures in Biosensor-A Review. Frontiers in Bioscience, 16(1), 997. https://doi.org/10.2741/3731

[18] Banerjee, A., Maity, S., & Mastrangelo, C. H. (2021). Nanostructures for Biosensing, with a Brief Overview on Cancer Detection, IoT, and the Role of Machine Learning in Smart Biosensors. Sensors, 21(4), 1253. https://doi.org/10.3390/s21041253

[19] Mulchandani, A., & Myung, N. V. (2011). Conducting polymer nanowires-based label-free biosensors. Current Opinion in Biotechnology, 22(4), 502–508. https://doi.org/10.1016/j.copbio.2011.05.508

[20] Nazari-Vanani, R., Sattarahmady, N., Yadegari, H., & Heli, H. (2018). A novel and ultrasensitive electrochemical DNA biosensor based on an ice crystals-like gold nanostructure for the detection of Enterococcus faecalis gene sequence. Colloids and Surfaces B: Biointerfaces, 166, 245–253. https://doi.org/10.1016/j.colsurfb.2018.03.025

[21] Abrams, G. A., Goodman, S. L., Nealey, P. F., Franco, M., & Murphy, C. J. (2000). Nanoscale topography of the basement membrane underlying the corneal epithelium of the rhesus macaque. Cell and Tissue Research, 299(1), 39–46. https://doi.org/10.1007/s004419900074

[22] Abrams, G. A., Schaus, S. S., Goodman, S. L., Nealey, P. F., & Murphy, C. J. (2000). Nanoscale Topography of the Corneal Epithelial Basement Membrane and Descemet's Membrane of the Human. Cornea, 19(1), 57–64. https://doi.org/10.1097/00003226-200001000-00012

[23] Zhang, Y., Zhang, Z., Yang, J., Yue, Y., & Zhang, H. (2022). Fabrication of superhydrophobic surface on stainless steel by two-step chemical etching. Chemical Physics Letters, 797, 139567. https://doi.org/10.1016/j.cplett.2022.139567

[24] Frantz, C., Stewart, K. M., & Weaver, V. M. (2010). The extracellular matrix at a glance. Journal of Cell Science, 123(24), 4195–4200. https://doi.org/10.1242/jcs.023820

[25] Silver, F. H., Freeman, J. W., & Seehra, G. P. (2003). Collagen self-assembly and the development of tendon mechanical properties. Journal of Biomechanics, 36(10), 1529–1553. https://doi.org/10.1016/S0021-9290(03)00135-0

[26] Yang, L., Fitié, C. F. C., van der Werf, K. O., Bennink, M. L., Dijkstra, P. J., & Feijen, J. (2008). Mechanical properties of single electrospun collagen type I fibers. Biomaterials, 29(8), 955–962. https://doi.org/10.1016/j.biomaterials.2007.10.058

[27] Bozec, L., & Odlyha, M. (2011). Thermal Denaturation Studies of Collagen by Microthermal Analysis and Atomic Force Microscopy. Biophysical Journal, 101(1), 228–236. https://doi.org/10.1016/j.bpj.2011.04.033

[28] Dai, X., & Xu, Q. (2011). Nanostructured substrate fabricated by sectioning tendon using a microtome for tissue engineering. Nanotechnology, 22(49), 494008. https://doi.org/10.1088/0957-4484/22/49/494008

[29] Dede Eren, A., Vasilevich, A., Eren, E. D., Sudarsanam, P., Tuvshindorj, U., de Boer, J., & Foolen, J. (2021). Tendon-Derived Biomimetic Surface Topographies Induce Phenotypic Maintenance of Tenocytes In Vitro. Tissue Engineering Part A, 27(15–16), 1023–1036. https://doi.org/10.1089/ten.tea.2020.0249

[30] Austin, M. D., Ge, H., Wu, W., Li, M., Yu, Z., Wasserman, D., Lyon, S. A., & Chou, S. Y. (2004). Fabrication of 5nm linewidth and 14nm pitch features by nanoimprint lithography. Applied Physics Letters, 84(26), 5299–5301. https://doi.org/10.1063/1.1766071

[31] Chou, S. Y., & Krauss, P. R. (1997). Imprint lithography with sub-10 nm feature size and high throughput. Microelectronic Engineering, 35(1–4), 237–240. https://doi.org/10.1016/S0167-9317(96)00097-4

[32] Watanabe, K., Morita, T., Kometani, R., Hoshino, T., Kondo, K., Kanda, K., Haruyama, Y., Kaito, T., Fujita, J., Ishida, M., Ochiai, Y., Tajima, T., & Matsui, S. (2004). Nanoimprint using three-dimensional microlens mold made by focused-ion-beam chemical vapor deposition. Journal of Vacuum Science & Technology B: Microelectronics and Nanometer Structures, 22(1), 22. https://doi.org/10.1116/1.1633281

[33] Contreras, A. M., Grunes, J., Yan, X.-M., Liddle, A., & Somorjai, G. A. (2005). Fabrication of platinum nanoparticles and nanowires by electron beam lithography (EBL) and nanoimprint lithography (NIL): comparison of ethylene hydrogenation kinetics. Catalysis Letters, 100(3–4), 115–124. https://doi.org/10.1007/s10562-004-3436-7

[34] Li, M., Luo, W., Chen, Y., & Cheng, X. (2021). Nickel micro-pillar mold produced by pulse and pulse-reverse current electrodeposition for nanoimprint lithography. Materials Letters, 301, 130310. https://doi.org/10.1016/j.matlet.2021.130310

[35] Hussein, L., Urban, G., & Krüger, M. (2011). Fabrication and characterization of bucky paper-based nanostructured electrodes as a novel material for biofuel cell applications. Physical Chemistry Chemical Physics, 13(13), 5831. https://doi.org/10.1039/c0cp02254c

[36] Huang, Y., Ho, C. T., Lin, Y., Lee, C., Ho, S., Li, M., & Hwang, E. (2018). Nanoimprinted Anisotropic Topography Preferentially Guides Axons and Enhances Nerve Regeneration. Macromolecular Bioscience, 18(12), 1800335. https://doi.org/10.1002/mabi.201800335

[37] Higashiki, T. (2011). Nanoimprint lithography and future patterning for semiconductor devices. Journal of Micro/Nanolithography, MEMS, and MOEMS, 10(4), 043008. https://doi.org/10.1117/1.3658024

[38] Patel, B. A. (2020). Chapter 04 - Microelectrodes and nanoelectrodes. In B. Patel (Ed.), Electrochemistry for Bioanalysis (pp. 51–72). Elsevier. https://10.1016/B978-0-12-821203-5.00007-5

[39] Boehler, C., Stieglitz, T., & Asplund, M. (2015). Nanostructured platinum grass enables superior impedance reduction for neural microelectrodes. Biomaterials, 67, 346–353. https://doi.org/10.1016/j.biomaterials.2015.07.036

[40] Kim, J.-H., Kang, G., Nam, Y., & Choi, Y.-K. (2010). Surface-modified microelectrode array with flake nanostructure for neural recording and stimulation. Nanotechnology, 21(8), 085303. https://doi.org/10.1088/0957-4484/21/8/085303

[41] Decker, D., Hempelmann, R., Natter, H., Pirrung, M., Rabe, H., Schäfer, K. H., & Saumer, M. (2019). 3D Nanostructured Multielectrode Arrays: Fabrication, Electrochemical Characterization, and Evaluation of Cell-Electrode Adhesion. Advanced Materials Technologies, 4(2), 1800436. https://doi.org/10.1002/admt.201800436

[42] Buitenweg, J. R., Rutten, W. L. C., Marani, E., Polman, S. K. L., & Ursum, J. (2002). Extracellular detection of active membrane currents in the neuron–electrode interface. Journal of Neuroscience Methods, 115(2), 211–221. https://doi.org/10.1016/S0165-0270(02)00021-3

[43] Kulangara, K., & Leong, K. W. (2009). Substrate topography shapes cell function. Soft Matter, 5(21), 4072. https://doi.org/10.1039/b910132m

[44] Anselme, K., Ploux, L., & Ponche, A. (2010). Cell/Material Interfaces: Influence of Surface Chemistry and Surface Topography on Cell Adhesion. Journal of Adhesion Science and Technology, 24(5), 831–852. https://doi.org/10.1163/016942409X12598231568186

[45] Yang, K., Jung, K., Ko, E., Kim, J., Park, K. I., Kim, J., & Cho, S.-W. (2013). Nanotopographical Manipulation of Focal Adhesion Formation for Enhanced Differentiation of Human Neural Stem Cells. ACS Applied Materials & Interfaces, 5(21), 10529–10540. https://doi.org/10.1021/am402156f

[46] Belu, A., Schnitker, J., Bertazzo, S., Neumann, E., Mayer, D., Offenhäuser, A., & Santoto, F. (2016). Ultra-thin resin embedding method for scanning electron microscopy of

individual cells on high and low aspect ratio 3D nanostructures. Journal of Microscopy, 263(1), 78–86. https://doi.org/10.1111/jmi.12378

[47] Noback, C. R. (1983). Principles of Neuroanatomy. Jay B. Angevine, Jr., Carl W. Cotman. The Quarterly Review of Biology, 58(1), 122–122. https://doi.org/10.1086/413172

[48] Marieb, E. N., & Hoehn, K. (2007). Chapter 11 – Fundamentals of the Nervous System and Nervous Tissue. In Marieb, E. N., & Hoehn, K., Human anatomy & physiology 7th edition (pp. 387–429). Pearson Benjamin Cummings. ISBN 0805359095, 9780805359091

[49] Pivovarov, A. S., Calahorro, F., & Walker, R. J. (2019). Na^+/K^+-pump and neurotransmitter membrane receptors. Invertebrate Neuroscience,19 (1), 1. https://doi.org/10.1007/s10158-018-0221-7

[50] Pereda, A. E. (2014). Electrical synapses and their functional interactions with chemical synapses. Nature Reviews Neuroscience, 15(4), 250–263. https://doi.org/10.1038/nrn3708

[51] Jäckel, D., Bakkum, D. J., Russell, T. L., Müller, J., Radivojevic, M., Frey, U., Franke, F., & Hierlemann, A. (2017). Combination of High-density Microelectrode Array and Patch Clamp Recordings to Enable Studies of Multisynaptic Integration. Scientific Reports, 7(1), 978. https://doi.org/10.1038/s41598-017-00981-4

[52] Nordhausen, C. T., Maynard, E. M., & Normann, R. A. (1996). Single unit recording capabilities of a 100 microelectrode array. Brain Research, 726(1–2), 129–140. https://doi.org/10.1016/0006-8993(96)00321-6

[53] Hofmann, F., & Bading, H. (2006). Long term recordings with microelectrode arrays: Studies of transcription-dependent neuronal plasticity and axonal regeneration. Journal of Physiology-Paris, 99(2–3), 125–132. https://doi.org/10.1016/j.jphysparis.2005.12.005

[54] Chiappalone, M., Vato, A., Tedesco, M. (B.), Marcoli, M., Davide, F., & Martinoia, S. (2003). Networks of neurons coupled to microelectrode arrays: a neuronal sensory system for pharmacological applications. Biosensors and Bioelectronics, 18(5–6), 627–634. https://doi.org/10.1016/S0956-5663(03)00041-1

[55] Morin, F. O., Takamura, Y., & Tamiya, E. (2005). Investigating neuronal activity with planar microelectrode arrays: achievements and new perspectives. Journal of Bioscience and Bioengineering, 100(2), 131–143. https://doi.org/10.1263/jbb.100.131

[56] Neher, E., & Sakamann, B. (1976). Single-channel currents recorded from membrane of denervated frog muscle fibres. Nature, 260(5554), 799–802. https://doi.org/10.1038/260799a0

[57] Priel, A., Gil, Z., Moy, V. T., Magleby, K. L., & Silberberg, S. D. (2007). Ionic Requirements for Membrane-Glass Adhesion and Giga Seal Formation in Patch-Clamp Recording. Biophysical Journal, 92(11), 3893–3900. https://doi.org/10.1529/biophysj.106.099119

[58] Ding, S., Matta, S. G., & Zhou, F.-M. (2011). Kv3-Like Potassium Channels Are Required for Sustained High-Frequency Firing in Basal Ganglia Output Neurons. Journal of Neurophysiology, 105(2), 554–570. https://doi.org/10.1152/jn.00707.2010

[59] What is the Patch-Clamp Technique? Patch-clamp configurations, https://www.leica-microsystems.com/science-lab/life-science/the-patch-clamp-technique/, Accessed 01 March 2023

[60] Hammond, C. (2015). Chapter 04 - The voltage-gated channels of Na+ action potentials. In Hammond, C., Cellular and Molecular Neurophysiology 4th edition (pp. 51–72). Elsevier. https://10.1016/B978-0-12-821203-5.00007-5

[61] Kelly, M. L., & Woodbury, D. J. (2003). Chapter 25 - Advantages and disadvantages of patch clamping versus using BLM. In Tien, H.T., & Ottova-Leitmannova, A., Membrane Science and Technology Volume 7 (pp. 699-721). Elsevier. https://doi.org/10.1016/S0927-5193(03)80049-9

[62] Tabata, M., Khamhanglit, C., Kotaki, S., & Miyahara, Y. (2022). Detection of cell membrane proteins using ion-sensitive field effect transistors combined with chemical signal amplification. Chemical Communications, 58(53), 7368–7371. https://doi.org/10.1039/D2CC02159E

[63] Struijk, J. J. (1997). The extracellular potential of a myelinated nerve fiber in an unbounded medium and in nerve cuff models. Biophysical Journal, 72(6), 2457–2469. https://doi.org/10.1016/S0006-3495(97)78890-8

[64] Viswam, V., Obien, M. E. J., Franke, F., Frey, U., & Hierlemann, A. (2019). Optimal Electrode Size for Multi-Scale Extracellular-Potential Recording From Neuronal Assemblies. Frontiers in Neuroscience, 13. https://doi.org/10.3389/fnins.2019.00385

[65] Mao, G., Kilani, M., & Ahmed, M. (2022). Review—Micro/Nanoelectrodes and Their Use in Electrocrystallization: Historical Perspective and Current Trends. Journal of The Electrochemical Society, 169(2), 022505. https://doi.org/10.1149/1945-7111/ac51a0

[66] Naturwissenschaftliches und Medizinisches Institut Germany, Microelectrode Array, https://www.nmi-tt.de/microdevices/meas/, Accessed 01 March 2024

[67] Thomas, Jr., C., Springer, P., Loeb, G., Berwaldnetter, Y., & Okun, L. (1972). A miniature microelectrode array to monitor the bioelectric activity of cultured cells. Experimental Cell Research, 74(1), 61–66. https://doi.org/10.1016/0014-4827(72)90481-8

[68] Janders, M., Egert, U., Stelzle, M., & Nisch, W. (1996) Novel thin film titanium nitride micro-electrodes with excellent charge transfer capability for cell stimulation and sensing applications. Proceedings of 18th Annual International Conference of the IEEE Engineering in Medicine and Biology Society, 245–247(1). https://doi.org/10.1109/IEMBS.1996.656936

[69] Lopez, C. M., Chun, H. S., Wang, S., Berti, L., Putzeys, J., van den Bulcke, C., Weijers, J.-W., Firrincieli, A., Reumers, V., Braeken, D., & van Helleputte, N. (2018). A Multimodal CMOS MEA for High-Throughput Intracellular Action Potential Measurements and Impedance Spectroscopy in Drug-Screening Applications. IEEE Journal of Solid-State Circuits, 53(11), 3076–3086. https://doi.org/10.1109/JSSC.2018.2863952

[70] Kovacs, G. T. A. (1994). Chapter 07 - Introduction to the Theory, Design, and Modeling of Thin-Film Microelectrodes for Neural Interfaces, In Stenger, D.A. & McKenna T. M., Enabling Technologies for Cultured Neural Networks (pp. 121-166). Academic Press. ISBN13: 9780126659702

[71] Randles, J. E. B. (1947). Kinetics of rapid electrode reactions. Discussions of the Faraday Society, 1, 11-19. https://doi.org/10.1039/df9470100011

[72] Muralidharan, V. S. (1997). Warburg impedance - basics revisited. Anti-Corrosion Methods and Materials, 44(1), 26–29. https://doi.org/10.1108/00035599710157387

[73] Hughes, M. P., Bustamante, K., Banks, D. J., & Ewins, D. J. (n.d.). Effects of electrode size on the performance of neural recording microelectrodes. 1st Annual International IEEE-EMBS Special Topic Conference on Microtechnologies in Medicine and Biology. Proceedings (Cat. No.00EX451), 220–223. https://doi.org/10.1109/MMB.2000.893776

[74] Zeng, Q., Yu, S., Fan, Z., Huang, Y., Song, B., & Zhou, T. (2022). Nanocone-Array-Based Platinum-Iridium Oxide Neural Microelectrodes: Structure, Electrochemistry, Durability and Biocompatibility Study. Nanomaterials, 12(19), 3445. https://doi.org/10.3390/nano12193445

[75] Bandaru, P. R., Yamada, H., Narayanan, R., & Hoefer, M. (2017). The role of defects and dimensionality in influencing the charge, capacitance, and energy storage of graphene and 2D materials. Nanotechnology Reviews, 6(5), 421–433. https://doi.org/10.1515/ntrev-2016-0099

[76] Heuschkel, M. O. (2001). Fabrication of multi-electrode array devices for electrophysiological monitoring of in-vitro cell/tissue cultures, Diploma thesis, École Polytechnique Fédérale de Lausanne. https://doi.org/10.5075/epfl-thesis-2370

[77] Khalili, A., & Ahmad, M. (2015). A Review of Cell Adhesion Studies for Biomedical and Biological Applications. International Journal of Molecular Sciences, 16(8), 18149–18184. https://doi.org/10.3390/ijms160818149

[78] Gingell, D., & Fornes, J. A. (1975). Demonstration of intermolecular forces in cell adhesion using a new electrochemical technique. Nature, 256(5514), 210–211. https://doi.org/10.1038/256210a0

[79] Alberts, B., Johnson, A., Lewis, J., Raff, M., Roberts, K., & Walter, P. (2002). Chapter 19 - Cell Junctions, Cell Adhesion, and the Extracellular Matrix. In Alberts, B., Johnson, A., Lewis, J., Raff, M., Roberts, K., & Walter, P. Molecular Biology of the Cell (pp. 1155–1228). Garland Science. ISBN10: 0815340729University of Reading,

[80] Cell Migration lab - role of nitric oxide, http://www.reading.ac.uk/nitricoxide/intro/migration/adhesion.htm, Accessed 01 March 2023

[81] Blau, A. (2013). Cell adhesion promotion strategies for signal transduction enhancement in microelectrode array in vitro electrophysiology: An introductory overview and critical

discussion. Current Opinion in Colloid & Interface Science, 18(5), 481–492. https://doi.org/10.1016/j.cocis.2013.07.005

[82] Martino, F., Perestrelo, A. R., Vinarský, V., Pagliari, S., & Forte, G. (2018). Cellular Mechanotransduction: From Tension to Function. Frontiers in Physiology, 9. https://doi.org/10.3389/fphys.2018.00824

[83] Kim, M.-H., Park, M., Kang, K., & Choi, I. S. (2014). Neurons on nanometric topographies: insights into neuronal behaviors in vitro. Biomaterial Science, 2(2), 148–155. https://doi.org/10.1039/C3BM60255A

[84] Hwang, C., Kim, H. W., Yoon, H., & Kim, D. S. (2020). Promoted migration of fibroblast cells on low aspect ratio isotropic nanopore surface by reduced maturation of focal adhesion at peripheral region. Colloids and Surfaces B: Biointerfaces, 195, 111229. https://doi.org/10.1016/j.colsurfb.2020.111229

[85] de Beer, A. G. F., Cavalcanti-Adam, E. A., Majer, G., Lopez-García, M., Kessler, H., & Spatz, J. P. (2010). Force-induced destabilization of focal adhesions at defined integrin spacings on nanostructured surfaces. Physical Review E, 81(5), 051914. https://doi.org/10.1103/PhysRevE.81.051914

[86] Ferrari, A., Cecchini, M., Serresi, M., Faraci, P., Pisignano, D., & Beltram, F. (2010). Neuronal polarity selection by topography-induced focal adhesion control. Biomaterials, 31(17), 4682–4694. https://doi.org/10.1016/j.biomaterials.2010.02.032

[87] Santoro, F., Schnitker, J., Panaitov, G., & Offenhäusser, A. (2013). On Chip Guidance and Recording of Cardiomyocytes with 3D Mushroom-Shaped Electrodes. Nano Letters, 13(11), 5379–5384. https://doi.org/10.1021/nl402901y

[88] Santoro, F., Dasgupta, S., Schnitker, J., Auth, T., Neumann, E., Panaitov, G., Gompper, G., & Offenhäusser, A. (2014). Interfacing Electrogenic Cells with 3D Nanoelectrodes: Position, Shape, and Size Matter. ACS Nano, 8(7), 6713–6723. https://doi.org/10.1021/nn500393p

[89] Spira, M. E., & Hai, A. (2013). Multi-electrode array technologies for neuroscience and cardiology. Nature Nanotechnology, 8(2), 83–94. https://doi.org/10.1038/nnano.2012.265

[90] Buitenweg, J. R., Rutten, W. L. C., Willems, W. P. A., & van Nieuwkasteele, J. W. (1998). Measurement of sealing resistance of cell-electrode interfaces in neuronal cultures using impedance spectroscopy. Medical and Biological Engineering and Computing, 36(5), 630–637. https://doi.org/10.1007/BF02524436

[91] Glinsner, T., & Kreindl, G. (2010). Chapter 24 - Nanoimprint Lithography. In Wang, M., Lithography (pp. 495–516). Intech. https://doi.org/10.5772/8190

[92] Kang, Y., Omoto, S., Nakai, Y., Okada, M., Kanda, K., Haruyama, Y., & Matsui, S. (2011). Nanoimprint replication of nonplanar nanostructure fabricated by focused-ion-beam chemical vapor deposition. Journal of Vacuum Science & Technology B, 29(1), 011005. https://doi.org/10.1116/1.3524289

[93] Alvarez-Puebla, R., Cui, B., Bravo-Vasquez, J.-P., Veres, T., & Fenniri, H. (2007). Nanoimprinted SERS-Active Substrates with Tunable Surface Plasmon Resonances. The Journal of Physical Chemistry C, 111(18), 6720–6723. https://doi.org/10.1021/jp070906s

[94] Nagai, N., Ono, H., Sakuma, K., Saito, M., Mizuno, J., & Shoji, S. (2009). Copper Multilayer Interconnection Using Ultravaiolet Nanoimprint Lithography with a Double-Deck Mold and Electroplating. Japanese Journal of Applied Physics, 48(11), 115001. https://doi.org/10.1143/JJAP.48.115001

[95] Park, S.-M., Liang, X., Harteneck, B. D., Pick, T. E., Hiroshiba, N., Wu, Y., Helms, B. A., & Olynick, D. L. (2011). Sub-10 nm Nanofabrication via Nanoimprint Directed Self-Assembly of Block Copolymers. ACS Nano, 5(11), 8523–8531. https://doi.org/10.1021/nn201391d

[96] Fruncillo, S., Su, X., Liu, H., & Wong, L. S. (2021). Lithographic Processes for the Scalable Fabrication of Micro- and Nanostructures for Biochips and Biosensors. ACS Sensors, 6(6), 2002–2024. https://doi.org/10.1021/acssensors.0c02704

[97] Milos, F., Belu, A., Mayer, D., Maybeck, V., & Offenhäusser, A. (2021). Polymer Nanopillars Induce Increased Paxillin Adhesion Assembly and Promote Axon Growth in Primary Cortical Neurons. Advanced Biology, 5(2), 2000248. https://doi.org/10.1002/adbi.202000248

[98] Kooy, N., Mohamed, K., Pin, L. T., & Guan, O. S. (2014). A review of roll-to-roll nanoimprint lithography. Nanoscale Research Letters, 9(1), 320. https://doi.org/10.1186/1556-276X-9-320

[99] Siddique, R. H., Gomard, G., & Hölscher, H. (2015). The role of random nanostructures for the omnidirectional anti-reflection properties of the glasswing butterfly. Nature Communications, 6(1), 6909. https://doi.org/10.1038/ncomms7909

[100] Fuhrmann, B., Leipner, H. S., Höche, H.-R., Schubert, L., Werner, P., & Gösele, U. (2005). Ordered Arrays of Silicon Nanowires Produced by Nanosphere Lithography and Molecular Beam Epitaxy. Nano Letters, 5(12), 2524–2527. https://doi.org/10.1021/nl051856a

[101] Ji, W., Zhang, S., Filonenko, G. A., Li, G., Sasaki, T., Feng, C., & Zhang, Y. (2017). Co-organizing synthesis of heterogeneous nanostructures through the photo-cleavage of pre-stabilized self-assemblies. Chemical Communications, 53(34), 4702–4705. https://doi.org/10.1039/C7CC01912B

[102] Shin, J.-W., Cho, D.-H., Moon, J., Joo, C. W., Lee, J., Huh, J. W., Park, S. K., Han, J.-H., Cho, N. S., Hwang, J., Chu, H. Y., & Lee, J.-I. (2014). Random nanostructure scattering layer for suppression of microcavity effect and light extraction in OLEDs. Optics Letters, 39(12), 3527. https://doi.org/10.1364/OL.39.003527

[103] AFM (Atomic Force Microscope) Universität Greifswald, www.physik.uni-greifswald.de/en/research-groups/soft-matter-and-biophysics-prof-christiane-helm/methods/afm-atomic-force-microscope, Accessed 01 March 2023

[104] Menzies, K. L., & Jones, L. (2010). The Impact of Contact Angle on the Biocompatibility of Biomaterials. Optometry and Vision Science, 87(6), 387–399. https://doi.org/10.1097/OPX.0b013e3181da863e

[105] Huhtamäki, T., Tian, X., Korhonen, J. T., & Ras, R. H. A. (2018). Surface-wetting characterization using contact-angle measurements. Nature Protocols, 13(7), 1521–1538. https://doi.org/10.1038/s41596-018-0003-z

[106] Zisman, W. A. (1964). Chapter 01 - Relation of the Equilibrium Contact Angle to Liquid and Solid Constitution. In Fowkes, F.M., Contact Angle, Wettability, and Adhesion Volume 43 (pp. 1-51). American Chemical Society. https://doi.org/10.1021/ba-1964-0043.ch001

[107] MacKay, S., Hermansen, P., Wishart, D., & Chen, J. (2015). Simulations of Interdigitated Electrode Interactions with Gold Nanoparticles for Impedance-Based Biosensing Applications. Sensors, 15(9), 22192–22208. https://doi.org/10.3390/s150922192

[108] Xu, Y., Ye, X., Yang, L., He, P., & Fang, Y. (2006). Impedance DNA Biosensor Using Electropolymerized Polypyrrole/Multiwalled Carbon Nanotubes Modified Electrode. Electroanalysis, 18(15), 1471–1478. https://doi.org/10.1002/elan.200603544

[109] Jones, G., & Bollinger, D. M. (1935). The Measurement of the Conductance of Electrolytes. VII. On Platinization. Journal of the American Chemical Society, 57(2), 280–284. https://doi.org/10.1021/ja01305a016

[110] Newbery, E. (1925). Overvoltage and transfer resistance. Proceedings of the Royal Society of London. Series A. 107(743), 486–495. https://doi.org/10.1098/rspa.1925.0037

[111] Yavarinasab, A., Abedini, M., Tahmooressi, H., Janfaza, S., Tasnim, N., & Hoorfar, M. (2021). Potentiodynamic Electrochemical Impedance Spectroscopy of Polyaniline-Modified Pencil Graphite Electrodes for Selective Detection of Biochemical Trace Elements. Polymers, 14(1), 31. https://doi.org/10.3390/polym14010031

[112] How does Scanning Electron Microscopy (SEM) work? ATRIA Innovation, https://www.leica-microsystems.com/science-lab/life-science/the-patch-clamp-technique, Accessed 01 March 2023

[113] Mandal, S., Mukherjee, A., & Ghosh, G. (2018). Scanning Electron Microscope and its Application. Proceedings of National Conference on Frontier Areas of Research and Applications using Electron Microscopy, https://doi.org/10.13140/RG.2.2.18678.42569

[114] Pawlizak, S. (2009). Mechanosensitive behaviour of neuronal growth cones, Diploma thesis, University of Leipzig, Leipzig.

[115] Yang, L., van der Werf, K. O., Fitié, C. F. C., Bennink, M. L., Dijkstra, P. J., & Feijen, J. (2008). Mechanical Properties of Native and Cross-linked Type I Collagen Fibrils. Biophysical Journal, 94(6), 2204–2211. https://doi.org/10.1529/biophysj.107.111013

[116] Beck, M., Graczyk, M., Maximov, I., Sarwe, E.-L., Ling, T. G. I., Keil, M., & Montelius, L. (2002). Improving stamps for 10 nm level wafer scale nanoimprint lithography. Microelectronic Engineering, 61–62, 441–448. https://doi.org/10.1016/S0167-9317(02)00464-1

[117] Schmitt, G., Schultze, J.-W., Faßbender, F., Buß, G., Lüth, H., & Schöning, M. J. (1999). Passivation and corrosion of microelectrode arrays. Electrochimica Acta, 44(21–22), 3865–3883. https://doi.org/10.1016/S0013-4686(99)00094-8

[118] Understanding the Specifications of your Potentiostat. Gamry Instruments Inc., www.gamry.com/application-notes/instrumentation/understanding-specs-of-potentiostat/, Accessed 01 March 2023

[119] Grundmann, D., Klotz, M., Rabe, H., Glanemann, M., & Schäfer, K.-H. (2015). Isolation of high-purity myenteric plexus from adult human and mouse gastrointestinal tract. Scientific Reports, 5(1), 9226. https://doi.org/10.1038/srep09226

[120] Horzum, U., Ozdil, B., & Pesen-Okvur, D. (2014). Step-by-step quantitative analysis of focal adhesions. MethodsX, 1, 56–59. https://doi.org/10.1016/j.mex.2014.06.004

[121] Zonderland, J., Wieringa, P., & Moroni, L. (2019). A quantitative method to analyse F-actin distribution in cells. MethodsX, 6, 2562–2569. https://doi.org/10.1016/j.mex.2019.10.018

[122] Eyre, D. R., & Wu, J.-J. (2005). Chapter - Collagen Cross-Links. In Brinckmann, J., Notbohm, H. & Müller, P.K., Collagen (pp. 207–229). Springer. https://doi.org/10.1007/b103828

[123] Olegovich Osidak, E., Igorevich Kozhukhov, V., Sergeevna Osidak, M., & Petrovich Domogatskiy, S. (2020). Collagen as Bioink for Bioprinting: A Comprehensive Review. International Journal of Bioprinting, 6(3). https://doi.org/10.18063/ijb.v6i3.270

[124] Orgel, J. P. R. O., Irving, T. C., Miller, A., & Wess, T. J. (2006). Microfibrillar structure of type I collagen in situ. Proceedings of the National Academy of Sciences, 103(24), 9001–9005. https://doi.org/10.1073/pnas.0502718103

[125] Schift, H. (2008). Nanoimprint lithography: An old story in modern times? A review. Journal of Vacuum Science & Technology B: Microelectronics and Nanometer Structures, 26(2), 458. https://doi.org/10.1116/1.2890972

[126] Oehrlein, G. S., Rembetski, J. F., & Payne, E. H. (1990). Study of sidewall passivation and microscopic silicon roughness phenomena in chlorine-based reactive ion etching of silicon trenches. Journal of Vacuum Science & Technology B: Microelectronics Processing and Phenomena, 8(6), 1199–1211. https://doi.org/10.1116/1.584896

[127] Duta, L., Popescu, A. C., Zgura, I., Preda, N., & Mihailescu, I. N. (2015). Chapter 8 - Wettability of Nanostructured Surfaces. In Aliofkhazraei, M., Wetting and Wettability (pp. 207–252). Intech. https://doi.org/10.5772/60808

[128] Parvate, S., Dixit, P., & Chattopadhyay, S. (2020). Superhydrophobic Surfaces: Insights from Theory and Experiment. The Journal of Physical Chemistry B, 124(8), 1323–1360. https://doi.org/10.1021/acs.jpcb.9b08567

[129] Barisik, M., & Beskok, A. (2013). Wetting characterisation of silicon (1,0,0) surface. Molecular Simulation, 39(9), 700–709. https://doi.org/10.1080/08927022.2012.758854

[130] Ricci, E., & Novakovic, R. (2001). Wetting and surface tension measurements on gold alloys. Gold Bulletin, 34(2), 41–49. https://doi.org/10.1007/BF03214811

[131] Chen, G., Wang, Y., Wang, Y., Xiao, H., Huang, X., & Shi, B. (2020). Collagen fibers with tuned wetting properties for dual separation of oil-in-water and water-in-oil emulsion. Journal of Materials Chemistry A, 8(46), 24388–24392. https://doi.org/10.1039/D0TA06625G

[132] Li, P., & Ducheyne, P. (1998). Quasi-biological apatite film induced by titanium in a simulated body fluid. Journal of Biomedical Materials Research, 41(3), 341–348. https://doi.org/10.1002/(SICI)1097-4636(19980905)41:3<341::AID-JBM1>3.0.CO;2-C

[133] Lim, J. Y., Shaughnessy, M. C., Zhou, Z., Noh, H., Vogler, E. A., & Donahue, H. J. (2008). Surface energy effects on osteoblast spatial growth and mineralization. Biomaterials, 29(12), 1776–1784. https://doi.org/10.1016/j.biomaterials.2007.12.026

[134] Roe, R.-J. (1968). Surface tension of polymer liquids. The Journal of Physical Chemistry, 72(6), 2013–2017. https://doi.org/10.1021/j100852a025

[135] Johnson, J. B. (1928). Thermal Agitation of Electricity in Conductors. Physical Review, 32(1), 97–109. https://doi.org/10.1103/PhysRev.32.97

[136] Lodha, N., & Christou, E. A. (2017). Low-Frequency Oscillations and Control of the Motor Output. Frontiers in Physiology, 8(78). https://doi.org/10.3389/fphys.2017.00078

[137] de Kock, C. P. J., & Sakmann, B. (2008). High frequency action potential bursts (≥ 100 Hz) in L2/3 and L5B thick tufted neurons in anaesthetized and awake rat primary somatosensory cortex. The Journal of Physiology, 586(14), 3353–3364. https://doi.org/10.1113/jphysiol.2008.155580

[138] Tereshchenko, L. G., & Josephson, M. E. (2015). Frequency content and characteristics of ventricular conduction. Journal of Electrocardiology, 48(6), 933–937. https://doi.org/10.1016/j.jelectrocard.2015.08.034

[139] Hamann, C. H., Hamnett, A., Vielstich, W. (2007). Chapter 5 – Methods for the study of the Electrode/Electrolyte Interface. In Hamann, C. H., Hamnett, A., Vielstich, W., Electrochemistry 2nd edition (pp. 251–338). Wiley-VCH. ISBN: 978-3-527-31069-2

[140] Baranes, K., Chejanovsky, N., Alon, N., Sharoni, A., & Shefi, O. (2012). Topographic cues of nano-scale height direct neuronal growth pattern. Biotechnology and Bioengineering, 109(7), 1791–1797. https://doi.org/10.1002/bit.24444

[141] Peltola, E. (2019). Hybrid Carbon Nanostructures for Direct Neuronal Interfacing. Frontiers in Materials, 6. https://doi.org/10.3389/fmats.2019.00202

[142] Onesto, V., Cancedda, L., Coluccio, M. L., Nanni, M., Pesce, M., Malara, N., Cesarelli, M., di Fabrizio, E., Amato, F., & Gentile, F. (2017). Nano-topography Enhances Communication in Neural Cells Networks. Scientific Reports, 7(1), 9841. https://doi.org/10.1038/s41598-017-09741-w

[143] Antonova, O. Y., Kochetkova, O. Y., & Shlyapnikov, Y. M. (2021). ECM-Mimetic Nylon Nanofiber Scaffolds for Neurite Growth Guidance. Nanomaterials, 11(2), 516. https://doi.org/10.3390/nano11020516

[144] Yasodharababu, M., & Nair, A. K. (2022). Predicting neurite extension for varying extracellular matrix stiffness and topography. Journal of Biomechanics, 131, 110897. https://doi.org/10.1016/j.jbiomech.2021.110897

[145] Leong, I. W., Kishimoto, S., Tsutsui, M., & Taniguchi, M. (2022). Interference of electrochemical ion diffusion in nanopore sensing. IScience, 25(10), 105073. https://doi.org/10.1016/j.isci.2022.105073

[146] Piret, G., Hébert, C., Mazellier, J.-P., Rousseau, L., Scorsone, E., Cottance, M., Lissorgues, G., Heuschkel, M. O., Picaud, S., Bergonzo, P., & Yvert, B. (2015). 3D-nanostructured boron-doped diamond for microelectrode array neural interfacing. Biomaterials, 53, 173–183. https://doi.org/10.1016/j.biomaterials.2015.02.021

[147] Povlsen, G. K., Ditlevsen, D. K., Berezin, V., & Bock, E. (2003). Intracellular Signaling by the Neural Cell Adhesion Molecule. Neurochemical Research, 28(1), 127–141. https://doi.org/10.1023/A:1021660531484

[148] Sheng, L., Leshchyns'ka, I., & Sytnyk, V. (2013). Cell adhesion and intracellular calcium signaling in neurons. Cell Communication and Signaling, 11(1), 94. https://doi.org/10.1186/1478-811X-11-94

[149] Bayoudh, S., Othmane, A., Ponsonnet, L., & ben Ouada, H. (2008). Electrical detection and characterization of bacterial adhesion using electrochemical impedance spectroscopy-based flow chamber. Colloids and Surfaces A: Physicochemical and Engineering Aspects, 318(1–3), 291–300. https://doi.org/10.1016/j.colsurfa.2008.01.005

[150] Avazzadeh, S., O'Brien, B., Coffey, K., O'Halloran, M., Keane, D., & Quinlan, L. R. (2021). Establishing Irreversible Electroporation Electric Field Potential Threshold in A Suspension In Vitro Model for Cardiac and Neuronal Cells. Journal of Clinical Medicine, 10(22), 5443. https://doi.org/10.3390/jcm10225443

[151] Gumbiner, B. M. (1996). Cell Adhesion: The Molecular Basis of Tissue Architecture and Morphogenesis. Cell, 84(3), 345–357. https://doi.org/10.1016/S0092-8674(00)81279-9

[152] Schulte, S., Gries, M., Christmann, A., & Schäfer, K.-H. (2021). Using multielectrode arrays to investigate neurodegenerative effects of the amyloid-beta peptide. Bioelectronic Medicine, 7(1), 15. https://doi.org/10.1186/s42234-021-00078-4

[153] Delvalle, N. M., Fried, D. E., Rivera-Lopez, G., Gaudette, L., & Gulbransen, B. D. (2018). Cholinergic activation of enteric glia is a physiological mechanism that contributes to the regulation of gastrointestinal motility. American Journal of Physiology-Gastrointestinal and Liver Physiology, 315(4), G473–G483. https://doi.org/10.1152/ajpgi.00155.2018

[154] Wang, G.-D., Wang, X.-Y., Xia, Y., & Wood, J. D. (2014). Dietary Glutamate: Interactions With the Enteric Nervous System. Journal of Neurogastroenterology and Motility, 20(1), 41–53. https://doi.org/10.5056/jnm.2014.20.1.41

[155] Hawkins, E. G., Dewey, W. L., Anitha, M., Srinivasan, S., Grider, J. R., & Akbarali, H. I. (2013). Electrophysiological Characteristics of Enteric Neurons Isolated from the Immortomouse. Digestive Diseases and Sciences, 58(6), 1516–1527. https://doi.org/10.1007/s10620-013-2557-5

[156] Landauer, R. (1989). Johnson-Nyquist noise derived from quantum mechanical transmission. Physica D: Nonlinear Phenomena, 38(1–3), 226–229. https://doi.org/10.1016/0167-2789(89)90197-8

[157] Gomes, J.-M., Bédard, C., Valtcheva, S., Nelson, M., Khokhlova, V., Pouget, P., Venance, L., Bal, T., & Destexhe, A. (2016). Intracellular Impedance Measurements Reveal Non-ohmic Properties of the Extracellular Medium around Neurons. Biophysical Journal, 110(1), 234–246. https://doi.org/10.1016/j.bpj.2015.11.019

[158] Maïno, N., Bertsch, A., & Renaud, P. (2023). Impedance spectroscopy of the cell/nanovolcano interface enables optimization for electrophysiology. Microsystems & Nanoengineering, 9(1), 62. https://doi.org/10.1038/s41378-023-00533-z

[159] Massobrio, P., Massobrio, G., & Martinoia, S. (2016). Interfacing Cultured Neurons to Microtransducers Arrays: A Review of the Neuro-Electronic Junction Models. Frontiers in Neuroscience, 10. https://doi.org/10.3389/fnins.2016.00282

[160] Shokoohimehr, P., Cepkenovic, B., Milos, F., Bednár, J., Hassani, H., Maybeck, V., & Offenhäusser, A. (2022). High-Aspect-Ratio Nanoelectrodes Enable Long-Term Recordings of Neuronal Signals with Subthreshold Resolution. Small, 18(22), 2200053. https://doi.org/10.1002/smll.202200053

[161] Woo, H., Kim, S., Nam, H., Choi, W., Shin, K., Kim, K., Yoon, S., Kim, G. H., Kim, J., & Lim, G. (2021). Au Hierarchical Nanostructure-Based Surface Modification of Microelectrodes for Improved Neural Signal Recording. Analytical Chemistry, 93(34), 11765–11774. https://doi.org/10.1021/acs.analchem.1c02168

[162] Margolis, K. G., Stevanovic, K., Karamooz, N., Li, Z. S., Ahuja, A., D'Autréaux, F., Saurman, V., Chalazonitis, A., & Gershon, M. D. (2011). Enteric Neuronal Density Contributes to the Severity of Intestinal Inflammation. Gastroenterology, 141(2), 588-598.e2. https://doi.org/10.1053/j.gastro.2011.04.047

[163] Pelkonen, A., Pistono, C., Klecki, P., Gómez-Budia, M., Dougalis, A., Konttinen, H., Stanová, I., Fagerlund, I., Leinonen, V., Korhonen, P., & Malm, T. (2021). Functional Characterization of Human Pluripotent Stem Cell-Derived Models of the Brain with Microelectrode Arrays. Cells, 11(1), 106. https://doi.org/10.3390/cells11010106

[164] Noraberg, J., Poulsen, F., Blaabjerg, M., Kristensen, B., Bonde, C., Montero, M., Meyer, M., Gramsbergen, J., & Zimmer, J. (2005). Organotypic Hippocampal Slice Cultures for

Studies of Brain Damage, Neuroprotection and Neurorepair. Current Drug Target -CNS & Neurological Disorders, 4(4), 435–452. https://doi.org/10.2174/1568007054546108

[165] Qin, H., Zhu, C., An, Z., Jiang, Y., Zhao, Y., Wang, J., Liu, X., Hui, B., Zhang, X., & Wang, Y. (2014). Silver nanoparticles promote osteogenic differentiation of human urine-derived stem cells at noncytotoxic concentrations. International Journal of Nanomedicine, 9, 2469-2478. https://doi.org/10.2147/IJN.S59753

[166] Kulkarni, M., Mazare, A., Gongadze, E., Perutkova, Š., Kralj-Iglič, V., Milošev, I., Schmuki, P., A Iglič, & Mozetič, M. (2015). Titanium nanostructures for biomedical applications. Nanotechnology, 26(6), 062002. https://doi.org/10.1088/0957-4484/26/6/062002

[167] Galbraith, C. G., Yamada, K. M., & Sheetz, M. P. (2002). The relationship between force and focal complex development. Journal of Cell Biology, 159(4), 695–705. https://doi.org/10.1083/jcb.200204153

[168] Kim, D., & Wirtz, D. (2013). Focal adhesion size uniquely predicts cell migration. The FASEB Journal, 27(4), 1351–1361. https://doi.org/10.1096/fj.12-220160

[169] Willard, A. L., & Nishi, R. (1985). Neurons dissociated from rat myenteric plexus retain differentiated properties when grown in cell culture. Neuroscience, 16(1), 201–211. https://doi.org/10.1016/0306-4522(85)90057-0

[170] Moxon, S. R., Corbett, N. J., Fisher, K., Potjewyd, G., Domingos, M., & Hooper, N. M. (2019). Blended alginate/collagen hydrogels promote neurogenesis and neuronal maturation. Materials Science and Engineering: C, 104, 109904. https://doi.org/10.1016/j.msec.2019.109904

[171] Chapman, C. A. R., Wang, L., Chen, H., Garrison, J., Lein, P. J., & Seker, E. (2017). Nanoporous Gold Biointerfaces: Modifying Nanostructure to Control Neural Cell Coverage and Enhance Electrophysiological Recording Performance. Advanced Functional Materials, 27(3), 1604631. https://doi.org/10.1002/adfm.201604631

[172] Gilles, S., Winter, S., Michael, K. E., Meffert, S. H., Li, P., Greben, K., Simon, U., Offenhäusser, A., & Mayer, D. (2012). Control of Cell Adhesion and Neurite Outgrowth by Patterned Gold Nanoparticles with Tunable Attractive or Repulsive Surface Properties. Small, 8(21), 3357–3367. https://doi.org/10.1002/smll.201200465

[173] Gallant, N. D., Michael, K. E., & García, A. J. (2005). Cell Adhesion Strengthening: Contributions of Adhesive Area, Integrin Binding, and Focal Adhesion Assembly. Molecular Biology of the Cell, 16(9), 4329–4340. https://doi.org/10.1091/mbc.e05-02-0170

[174] Zhu, L., Plow, E. F., & Qin, J. (2021). Initiation of focal adhesion assembly by talin and kindlin: A dynamic view. Protein Science, 30(3), 531–542. https://doi.org/10.1002/pro.4014

[175] Hu, Y.-L., Lu, S., Szeto, K. W., Sun, J., Wang, Y., Lasheras, J. C., & Chien, S. (2014). FAK and paxillin dynamics at focal adhesions in the protrusions of migrating cells. Scientific Reports, 4(1), 6024. https://doi.org/10.1038/srep06024

[176] Buskermolen, A. B. C., Kurniawan, N. A., & Bouten, C. V. C. (2018). An automated quantitative analysis of cell, nucleus and focal adhesion morphology. PLOS ONE, 13(3), e0195201. https://doi.org/10.1371/journal.pone.0195201

[177] Baum, M. J., Heepe, L., Fadeeva, E., & Gorb, S. N. (2014). Dry friction of microstructured polymer surfaces inspired by snake skin. Beilstein Journal of Nanotechnology, 5, 1091–1103. https://doi.org/10.3762/bjnano.5.122

[178] Li, J., Zhu, J., & Gao, X. (2014). Bio-Inspired High-Performance Antireflection and Antifogging Polymer Films. Small, 10(13), 2578–2582. https://doi.org/10.1002/smll.201303910

[179] Saison, T., Peroz, C., Chauveau, V., Berthier, S., Sondergard, E., & Arribart, H. (2008). Replication of butterfly wing and natural lotus leaf structures by nanoimprint on silica sol–gel films. Bioinspiration & Biomimetics, 3(4), 046004. https://doi.org/10.1088/1748-3182/3/4/046004

[180] Reid, G., McCormack, J. C., Habimana, O., Bayer, F., Goromonzi, C., Casey, E., Cowley, A., & Kelleher, S. M. (2021). Biomimetic Polymer Surfaces by High Resolution Molding of the Wings of Different Cicadas. Materials, 14(8), 1910. https://doi.org/10.3390/ma14081910

[181] Brüggemann, D., Wolfrum, B., Maybeck, V., Mourzina, Y., Jansen, M., & Offenhäusser, A. (2011). Nanostructured gold microelectrodes for extracellular recording from electrogenic cells. Nanotechnology, 22(26), 265104. https://doi.org/10.1088/0957-4484/22/26/265104

[182] Kim, R., Hong, N., & Nam, Y. (2013). Gold nanograin microelectrodes for neuroelectronic interfaces. Biotechnology Journal, 8(2), 206–214. https://doi.org/10.1002/biot.201200219

[183] Matsumae, T., Kariya, S., Kurashima, Y., Thu, L. H. H., Higurashi, E., Hayase, M., & Takagi, H. (2022). Wafer-Scale Room-Temperature Bonding of Smooth Au/Ti-Based Getter Layer for Vacuum Packaging. Sensors, 22(21), 8144. https://doi.org/10.3390/s22218144

[184] Niklaus, F., Decharat, A., Forsberg, F., Roxhed, N., Lapisa, M., Populin, M., Zimmer, F., Lemm, J., & Stemme, G. (2009). Wafer bonding with nano-imprint resists as sacrificial adhesive for fabrication of silicon-on-integrated-circuit (SOIC) wafers in 3D integration of MEMS and ICs. Sensors and Actuators A: Physical, 154(1), 180–186. https://doi.org/10.1016/j.sna.2009.07.009

[185] Nowduri, B., Britz-Grell, A., Saumer, M., & Decker, D. (2023). Nanoimprint lithography-based replication techniques for fabrication of metal and polymer biomimetic nanostructures for biosensor surface functionalization. Nanotechnology, 34(16), 165301. https://doi.org/10.1088/1361-6528/acb35b

[186] Chen, Z., & Lee, J.-B. (2021). Biocompatibility of SU-8 and Its Biomedical Device Applications. Micromachines, 12(7), 794. https://doi.org/10.3390/mi12070794

[187] Schizas, C., & Karalekas, D. (2011). Mechanical characteristics of an Ormocomp® biocompatible hybrid photopolymer. Journal of the Mechanical Behavior of Biomedical Materials, 4(1), 99–106. https://doi.org/10.1016/j.jmbbm.2010.09.010

[188] Clause, K. C., & Barker, T. H. (2013). Extracellular matrix signaling in morphogenesis and repair. Current Opinion in Biotechnology, 24(5), 830–833. https://doi.org/10.1016/j.copbio.2013.04.011

[189] Goldberg, M., Langer, R., & Jia, X. (2007). Nanostructured materials for applications in drug delivery and tissue engineering. Journal of Biomaterials Science, Polymer Edition, 18(3), 241–268. https://doi.org/10.1163/156856207779996931

[190] Ravalli, A., Voccia, D., Palchetti, I., & Marrazza, G. (2016). Electrochemical, Electrochemiluminescence, and Photoelectrochemical Aptamer-Based Nanostructured Sensors for Biomarker Analysis. Biosensors, 6(3), 39. https://doi.org/10.3390/bios6030039

[191] Xie, Y., Liu, T., Chu, Z., & Jin, W. (2021). Recent advances in electrochemical enzymatic biosensors based on regular nanostructured materials. Journal of Electroanalytical Chemistry, 893, 115328. https://doi.org/10.1016/j.jelechem.2021.115328

[192] Kiani, M. J., Abadi, M. H. S., Rahmani, M., Ahmadi, M. T., Harun, F. K. C., Hedayat, S. N., & Yaghoobian, S. H. (2017). Chapter 13 – Carbon Materials Based Ion Sensitive Field Effect Transistor (ISFET): The Emerging Potentials of Nanostructured Carbon-Based ISFET with High Sensitivity. In Ahmadi, M., Ismail, R. & Anwar, S., Handbook of Research on Nanoelectronic Sensor Modeling and Applications (pp. 334–360). IGI Global. https://doi.org/10.4018/978-1-5225-0736-9.ch013

[193] Sikanen, T., Aura, S., Heikkilä, L., Kotiaho, T., Franssila, S., & Kostiainen, R. (2010). Hybrid Ceramic Polymers: New, Nonbiofouling, and Optically Transparent Materials for Microfluidics. Analytical Chemistry, 82(9), 3874–3882. https://doi.org/10.1021/ac1004053

[194] Vieira, D., McEachern, F., Filippelli, R., Dimentberg, E., Harvey, E. J., & Merle, G. (2020). Microelectrochemical Smart Needle for Real Time Minimally Invasive Oximetry. Biosensors, 10(11), 157. https://doi.org/10.3390/bios10110157

[195] Chatard, C., Sabac, A., Moreno-Velasquez, L., Meiller, A., & Marinesco, S. (2018). Minimally Invasive Microelectrode Biosensors Based on Platinized Carbon Fibers for in Vivo Brain Monitoring. ACS Central Science, 4(12), 1751–1760. https://doi.org/10.1021/acscentsci.8b00797

[196] Chapman, C. A. R., Chen, H., Stamou, M., Biener, J., Biener, M. M., Lein, P. J., & Seker, E. (2015). Nanoporous Gold as a Neural Interface Coating: Effects of Topography, Surface Chemistry, and Feature Size. ACS Applied Materials & Interfaces, 7(13), 7093–7100. https://doi.org/10.1021/acsami.5b00410

[197] Dubey, N., Bentini, R., Islam, I., Cao, T., Castro Neto, A. H., & Rosa, V. (2015). Graphene: A Versatile Carbon-Based Material for Bone Tissue Engineering. Stem Cells International, 2015, 1–12. https://doi.org/10.1155/2015/804213

[198] Ku, S. H., Lee, M., & Park, C. B. (2013). Carbon-Based Nanomaterials for Tissue Engineering. Advanced Healthcare Materials, 2(2), 244–260. https://doi.org/10.1002/adhm.201200307

[199] Kumar, M., & Ando, Y. (2010). Chemical Vapor Deposition of Carbon Nanotubes: A Review on Growth Mechanism and Mass Production. Journal of Nanoscience and Nanotechnology, 10(6), 3739–3758. https://doi.org/10.1166/jnn.2010.2939

[200] Rudrapati, R. (2020). Chapter 2 - Graphene: Fabrication Methods, Properties, and Applications in Modern Industries. In Ameen, S., Shaheer Akhtar, M., & Shin, H.-S., Graphene Production and Application (pp. 9-22). Intech. https://doi.org/10.5772/intechopen.92258

[201] Eick, S. (2009). Iridium oxide microelectrode arrays for in-vitro stimulation of individual rat neurons from dissociated cultures. Frontiers in Neuroengineering, 2(16). https://doi.org/10.3389/neuro.16.016.2009

[202] Gross, G. W., Wen, W. Y., & Lin, J. W. (1985). Transparent indium-tin oxide electrode patterns for extracellular, multisite recording in neuronal cultures. Journal of Neuroscience Methods, 15(3), 243–252. https://doi.org/10.1016/0165-0270(85)90105-0

[203] Mondal, S., Dorozhkin, S. v., & Pal, U. (2018). Recent progress on fabrication and drug delivery applications of nanostructured hydroxyapatite. WIREs Nanomedicine and Nanobiotechnology, 10(4). https://doi.org/10.1002/wnan.1504

[204] Hassanzadeh-Tabrizi, S. A., Bigham, A., & Rafienia, M. (2016). Surfactant-assisted sol–gel synthesis of forsterite nanoparticles as a novel drug delivery system. Materials Science and Engineering: C, 58, 737–741. https://doi.org/10.1016/j.msec.2015.09.020

[205] Li, X., Wang, L., Fan, Y., Feng, Q., Cui, F.-Z., & Watari, F. (2013). Nanostructured scaffolds for bone tissue engineering. Journal of Biomedical Materials Research Part A, 101 (8), 2424–2435. https://doi.org/10.1002/jbm.a.34539

Appendix I. Photolithography mask designs

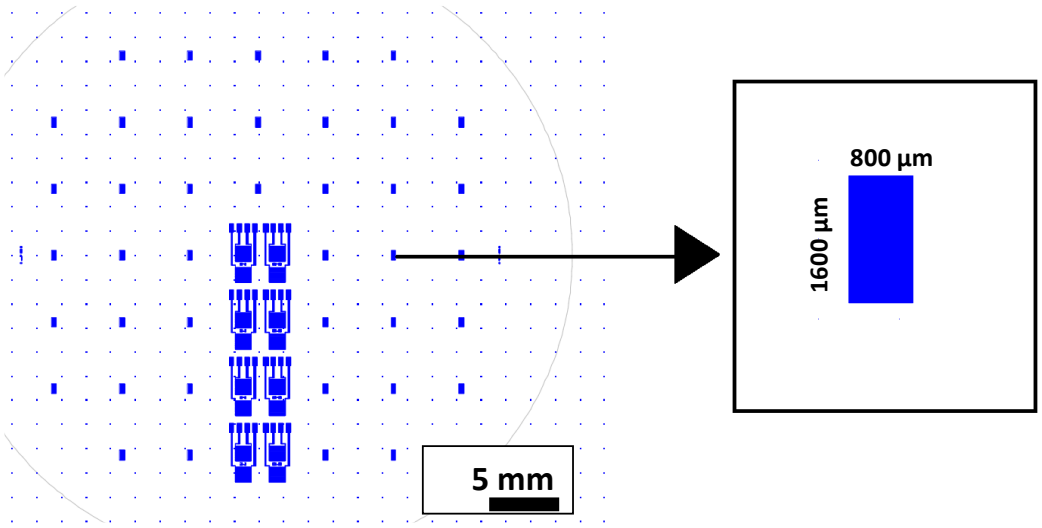

Figure 1. Lithography mask design used for patterning natural collagen fiber network on silicon surface, which was subsequently used as a master template for thermal nanoimprint lithography process. Inset shows the dimensions used for nanostructuring area for each MEA chip.

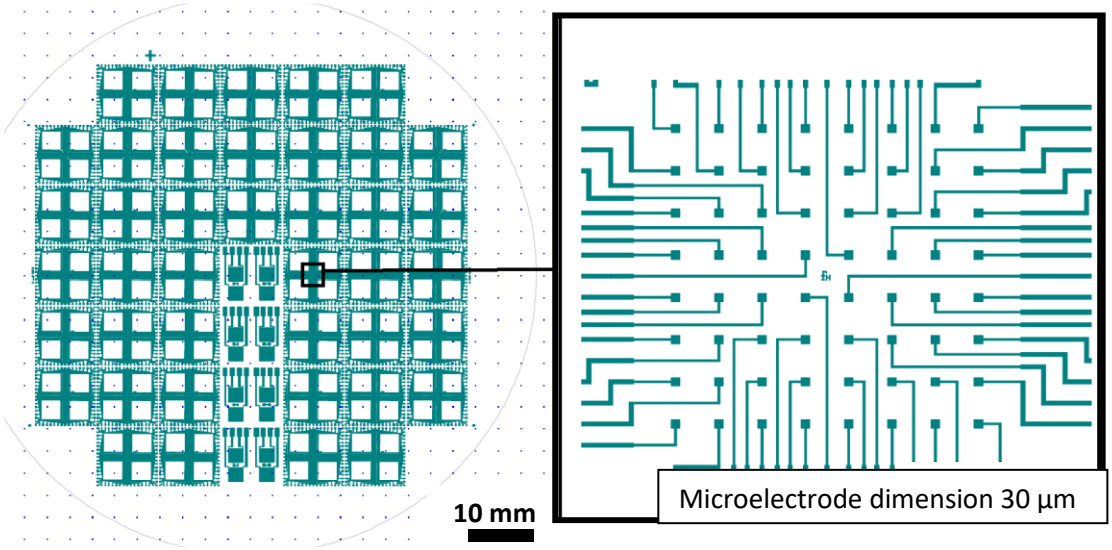

Figure 2. Lithography mask design used for patterning internal contact pads, external contact pads and connection lines on gold substrate surface. Inset shows layout of 60 internal contact pads in the MEA chip.

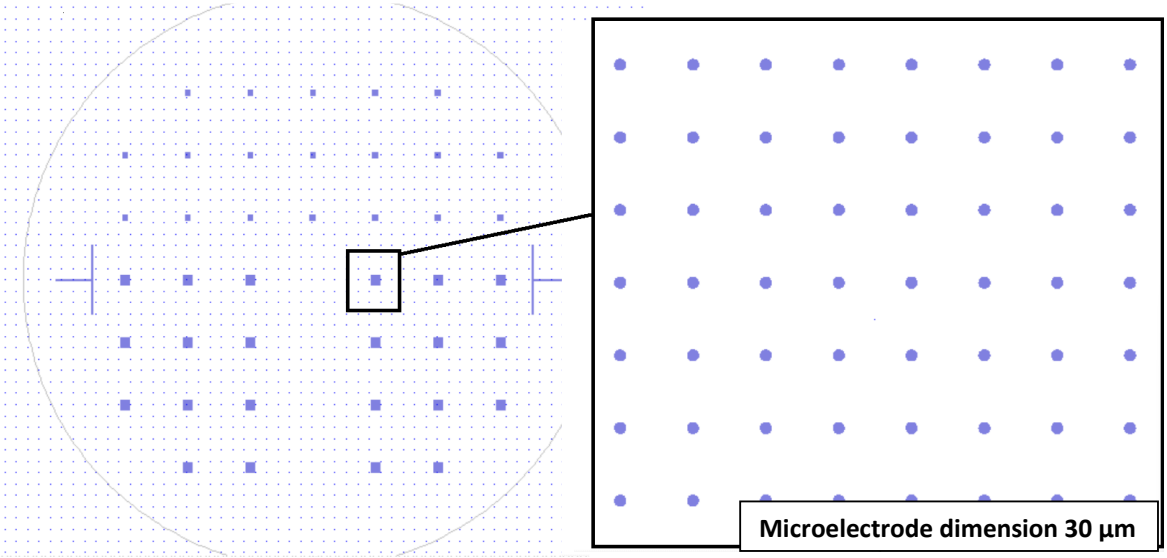

Figure 3. Lithography mask design used for patterning microelectrode openings on the metal contact pads, where the passivation layer is subsequently removed. Inset shows layout of 60 microelectrodes in the MEA chip.

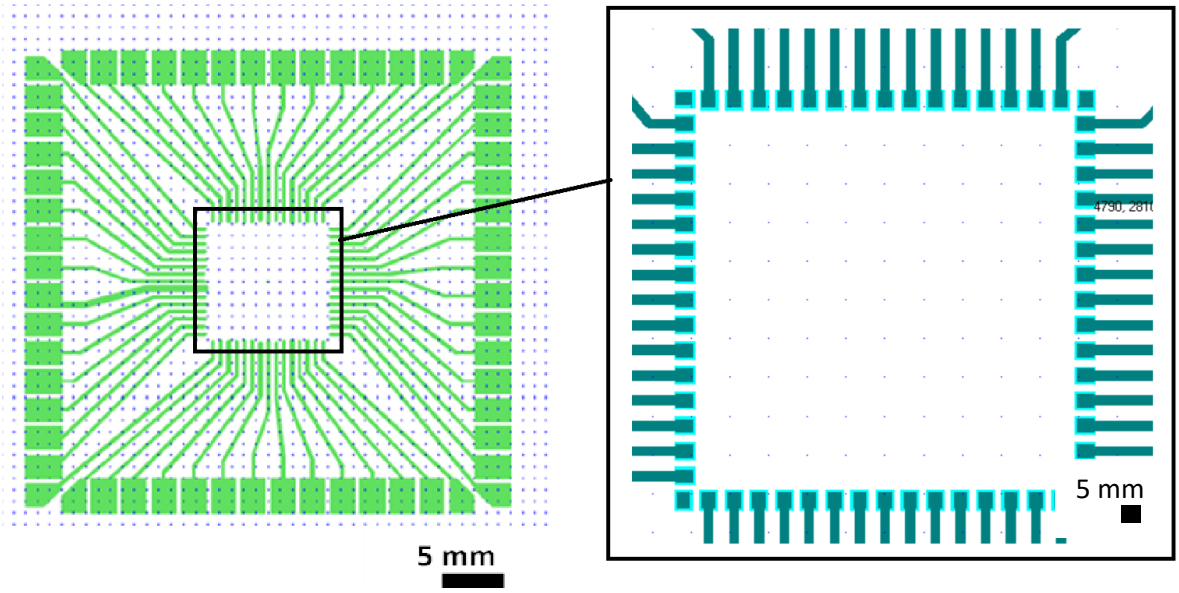

Figure 4. Printed circuit board layout for flip-chip bonding. The external contact pads of the wafer-scale MEA chip fabricated in clean rooms is bonded with the internal contacts of the PCB chip marked in inset to produce fully functional biosensor device.

Appendix II. Cleanroom standard operating procedure

Table 1. Fabrication of collagen coated silicon master

Step	Apparatus/Materials	Process parameters
1. Collagen solution preparation	Bovine Achilles tendon collagen type I	1. Collagen powder 1 mg/ml (w/v) dissolved in 0.01 M HCl at 4 °C overnight with constant stirring 2. Solution mixed at 9000 RPM for 5 minutes 3. Filtered with 100 µm and then 20 µm pore width nylon filter. Filtrate used for spin-coating
2. Collagen spin-coating	Spin-coater	1. Silicon wafer cleaned for 10 minutes in piranha solution and then O_2 plasma treated 2. 1 ml collagen filtrate spin-coated at 20 RPM for 45 minutes
3. Patterning of collagen wafer	Lithography and reactive-ion etching	1. 2 µm image-reversal photoresist AR-U 4030 for 60 seconds at 3000 RPM with acceleration 10 seconds 2. Post-baked 90 °C for 120 seconds 3. 365 nm UV light bright field exposure 10 seconds at 34 mJ/cm^2 4. Developed with AR 300-26 developer for 10 seconds 5. Open regions etched with reactive-ion etching in 30 sccm O_2 gas flow 100 W power and 13 Pa
4. Anti-sticking layer	Spin-coater	1. Anti-sticking layer (BGL-GZ-83) at 2000 RPM for 30 seconds with acceleration 5 seconds

Table 2. Fabrication of collagen-like gold nanostructures

Step	Apparatus/Materials	Process parameters
1. Substrate layer deposition	Physical vapor deposition evaporation apparatus	1. Borosilicate glass wafers cleaned in piranha solution for 10 minutes in piranha solution and then O_2 plasma 2. 20 nm Ti and 200 nm of Au evaporated on glass surface 3. 450 nm thermal NIL resist mr-I8000R spin-coated for 30 seconds at 1500 RPM with acceleration 10 seconds 4. Post-baked 100 °C for 60 seconds
2. Nanoimprinting collagen coated silicon master on thermal NIL resist	Nanoimprint lithography apparatus	1. Collagen coated silicon and resist mr-I8000R imprinted at 160 °C and 40 bar for 5 minutes 2. Stamp released the at 100 °C
3. Residual layer etching	Reactive-ion etching	1. 400 nm of thermal NIL resist residual layer etched with O_2 gas flow of 30 sccm at 13 Pa and 25 W power for 220 seconds
4. Nanostructure growth	Gold electroplating	1. Open cavities of the T-NIL resist filled with gold at plating density 1 mA/cm^2 for time calculated for required nanostructure height in gold-sulfite bath 2. Nanoimprint resist is stripped with acetone and iso-propyl alcohol

Table 3. Fabrication of microelectrode arrays with biomimetic nanostructures

Step	Apparatus/Materials	Process parameters
1.Electrode and connection tracks formation	Lithography and Wet chemical etching	1. 1.5 µm positive photoresist AR-P 5910 (diluted 100:40 in AR 300-12) for 60 seconds at 8000 RPM with acceleration 10 seconds 2. Post-baked 90 °C for 120 seconds 3. 365 nm UV bright field exposure 8.5 seconds at 34 mJ/cm^2 4. Developed with AR 300-26 developer for 60 seconds 5. Hard-baked 110 °C for 5 minutes 6. Open gold regions etched in KI:I_2:$H_2$0 (4:1:40) for 30 seconds 7. Open titanium regions etched in 5 % buffered HF solution for 30 seconds 8. Photoresist is stripped with acetone and iso-propyl alcohol
2. Passivation layer deposition	plasma enhanced chemical vapor deposition	1. SiO_2 and Si_3N_4 deposited with SiH_4 (20 sccm) and N_2O (20 sccm) as alternating layers to form 1 µm of passivation layer
	Spin-coated SU-8 epoxy-based polymer	1. 1 µm photoresist SU-8 2010 (diluted 1:3 in PGMEA) (w/v) for 30 seconds at 3000 RPM with acceleration 10 seconds 2. Soft-baked 90 °C for 60 seconds 3. Flood exposure 10 seconds at 340 mJ/cm^2 4. Post exposure baked 90 °C for 60 seconds 5. Hard baked 150 °C for 180 minutes
3. Inner and outer contact pad opening	Reactive-ion etching	1. 4 µm positive photoresist AR-P 5910 for 60 seconds at 6000 RPM with acceleration 10 seconds 2. Post-baked 90 °C for 120 seconds 3. Dark field exposure 28.5 seconds at 34 mJ/cm^2 4. Developed with AR 300-26 developer for 75 seconds and cleaned 5. Hard-baked 110 °C for 300 seconds 6. Open resist regions etched with CF4-O_2 gas flow of 25 sccm-3.1 sccm respectively at 1.33 Pa and 100 W power for 10 minutes 7. Photoresist is stripped with acetone and iso-propyl alcohol

Table 4. MEA wafer-level to chip-level assembly

Step	Apparatus/Materials	Process parameters
1. Dicing	Wafer Dicer	1. 4-inch nanostructured wafer consists of 42 dies, each diced with diamond saw at 5 mm/sec dice rate
2. PCB chip bonding	Flip-chip bonder	1. Silver glue transferred to the inner contact pads of the PCB chip with a squeegee 2. The diced nanostructured MEA wafer (11 mm x 11 mm) is pick-and-placed on the flipped PCB with the silver glue 3. Baked at 120 °C for 60 minutes
3. PCB passivation		1. PCB passivated with polydimethylsiloxane and a borosilicate glass ring of height 5 mm height and 22 mm diameter 2. Baked for 120 °C for 60 minutes

Appendix III. Enteric neuron culture preparation

Table 1. Fixation and drying of cells on the MEA wafer for SEM imaging

Step	Process parameters
1. Neuron Isolation	1. Post-natal C57BL6J mice (p 2-5) killed without anesthesia 2. Neurons extracted from myenteric plexus of small intestine where the muscle layer was stripped and digested for 150 minutes in Hank's balanced salt solution (H6648, Sigma-Aldrich Corporation), containing collagenase and DNAs. 3. Neural networks of myenteric plexus were cleaned and proliferated in culture flasks to generate neurospheres
2. MEA preparation and cell seeding	1. MEA surface was activated in O_2 plasma 40 sccm gas glow for 1 minute 2. Poly-d-lysine diluted in PBS 1:100 (w/v) coated on MEAs for 1 hour 3. 24 hours for proliferation and then approx. 20 neurospheres (resulting in 200 000 neurons) seeded
3. Culture maintenance	1. Cultured networks maintained in MEM supplemented with horse serum, L-glutamate, glucose, gentamicin at 37 °C and 5 % CO_2 2. Differentiation medium is replaced on DIV 4 after seeding and then subsequently after every 2 days.

Table 2. Fixation and drying of cells on the MEA wafer for SEM imaging

Drying solution	Time
1. Culture medium removed and rinsed in 1x in PBS	10 minutes
2. Cells fixed in 5 % glutaraldehyde	3x 10 minutes
3. 70 % ethanol	30 minutes
4. 80 % ethanol	30 minutes
5. 90 % ethanol	30 minutes
6. 96 % ethanol	30 minutes
7. Absolute ethanol / Hexamethyldisilazane (≥ 99 %) 1:1	30 minutes
8. Hexamethyldisilazane (≥ 99 %), 2nd time left to evaporate	2x 30 minutes
9. MEA wafers performed as soon as possible to avoid rehydration	

Appendix IV. Fluorescence microscopy

Table 1. Neuron-astrocyte growth

Step	Process parameters
1. Staining cells	1. Neuronal networks cultured on nanostructured surfaces fixed in 4 % formaldehyde (w/v) solution on DIV 7 and then washed 3 times with PBS solution 2. Stained with neuronal marker Chicken-anti-PGP9.5 and glial marker Rabbit-anti-S100B for 1 hour and washed with PBS 3. Stained with Secondary antibodies Donkey-anti-Chicken 488 and Donkey-anti-Rabbit 594 for 1 hour and washed with PBS 4. Stained with 6 µl of DAPI
2. Fluorescence microscopy	1. Neurons are imaged at 465 nm emission wavelength; Glial cells are imaged at 565 nm emission wavelength light and nuclei at 605 nm emission wavelength

Table 2. Focal adhesion analysis

Step	Process parameters
1. Staining cells	1. Neuronal networks cultured on nanostructured surfaces fixed in 4 % formalin (w/v) solution on DIV 1 or DIV 3 or DIV 7 and then washed 3 times with PBS solution 2. Cell membrane permeabilized with 0.2 % Triton X100 (w/v) for 10 minutes and washed with PBS 3. Stained with TRITC-conjugated phalloidin (diluted in methanol) for 1 hour and washed with PBS 4. Stained with anti-Vinculin monoclonal antibodies (purified clone 7F9) for 1 hour and washed with PBS 5. Stained with Secondary antibodies Donkey-anti-Chicken 488 and Donkey-anti-Rabbit 594 for 1 hour and washed with PBS 6. Fixed with 6 µl of DAPI
2. Fluorescence microscopy	1. Focal adhesion complexes (Vinculin) are imaged at 465 nm emission wavelength; actin filaments are imaged at 565 nm emission wavelength light and nuclei at 605 nm emission wavelength

Appendix V. Cell adhesion analysis on collagen-like gold nanostructures

Table 1. Relation of (a) PGP9.5 and (b) S100B signal to whole picture area as a measure of the amount of neuronal and glial cells on different structures (n = 4).

Type of microelectrode	Density of neurons measured with PGP9.5 signal	Density of glial cells measured with S100B signal
Planar glass	31.4 ± 9.3	19.3 ± 6.6
Collagen coated silicon	37.1 ± 8.1	26.3 ± 9.5
nanostructured gold	28.1 ± 6.4	18.9 ± 5.4
unstructured gold	9.7 ± 4.2	8.7 ± 4.1

Table 2. Relation of number of focal adhesion complexes measured by fluorescence imaging of vinculin for different structures (n = 10): Glass (G), unstructured (US) and nanostructured glass (NS).

Type of focal adhesion complex	G	NS	US	G	NS	US	G	NS	US
	DIV1	DIV1	DIV1	DIV4	DIV4	DIV4	DIV7	DIV7	DIV7
Small (length smaller than 2 μm)	43.3 ± 11.9	44.8 ± 13.2	36.2 ± 8.1	80.1 ± 10.3	81.6 ± 11.1	77.5 ± 15.8	118.5 ± 22.7	128.8 ± 22.1	104.2 ± 21.5
Nascent (length between 2 μm and 6 μm)	9.31 ± 3.46	9.99 ± 3.54	7.75 ± 2.54	28.8 ± 11.1	33.5 ± 13.2	27.1 ± 7.51	44.6 ± 15.4	61.7 ± 18.3	44.2 ± 14.8
Mature (length longer than 6 μm)	1.33 ± 1.41	0.89 ± 1.28	0.61 ± 1.05	4.87 ± 1.07	5.91 ± 1.47	5.46 ± 2.19	7.13 ± 3.35	14.6 ± 5.24	8.37 ± 2.52
Total	62.9 ± 16.5	55.6 ± 15.3	44.3 ± 10.1	122.8 ± 29.2	119.3 ± 23.7	89.1 ± 22.2	170.2 ± 39.9	198.1 ± 27.8	157.1 ± 29.5

Table 3. Relation of cell adhesion area measured by fluorescence imaging of actin cytoskeleton for different structures (n = 10): Glass (G), unstructured (US) and nanostructured glass (NS).

	G [μm^2]	NS [μm^2]	US [μm^2]	G [μm^2]	NS [μm^2]	US [μm^2]	G [μm^2]	NS [μm^2]	US [μm^2]
	DIV1	DIV1	DIV1	DIV4	DIV4	DIV4	DIV7	DIV7	DIV7
Cell adhesion area	1784 ± 425	1327 ± 246	1275 ± 262	2701 ± 589	3300 ± 824	3226 ± 914	3989 ± 728	4801 ± 689	4670 ± 1005

Table 4. Relation of surface area covered by focal adhesion complexes measured by correlating vinculin marked surface to actin marked cell area for different structures (n = 10): Glass (G), unstructured (US) and nanostructured glass (NS).

Type of focal adhesion complex	G [%]	NS [%]	US [%]	G [%]	NS [%]	US [%]	G [%]	NS [%]	US [%]
	DIV1	DIV1	DIV1	DIV4	DIV4	DIV4	DIV7	DIV7	DIV7
Small (length smaller than 2 µm)	1.87 ± 0.57	2.68 ± 0.61	2.08 ± 0.34	2.47 ± 0.71	2.24 ± 0.57	1.77 ± 0.42	2.11 ± 0.36	2.26 ± 0.44	2.01 ± 0.55
Nascent (length between 2 µm and 6 µm)	1.73 ± 0.33	1.73 ± 0.35	1.49 ± 0.43	2.64 ± 0.86	2.85 ± 0.68	2.82 ± 0.73	2.83 ± 0.79	3.71 ± 0.63	2.67 ± 0.67
Mature (length longer than 6 µm)	0.52 ± 0.42	0.37 ± 0.27	0.28 ± 0.24	1.35 ± 0.34	1.83 ± 0.59	1.72 ± 0.58	1.64 ± 0.74	3.44 ± 0.99	1.66 ± 0.95
Total	4.13 ± 1.32	4.79 ± 1.28	3.87 ± 1.07	6.48 ± 1.92	6.62 ± 1.85	6.42 ± 1.74	6.59 ± 1.91	9.41 ± 2.07	6.34 ± 2.17

Appendix VI. Surface profiles of CLGNS microelectrodes

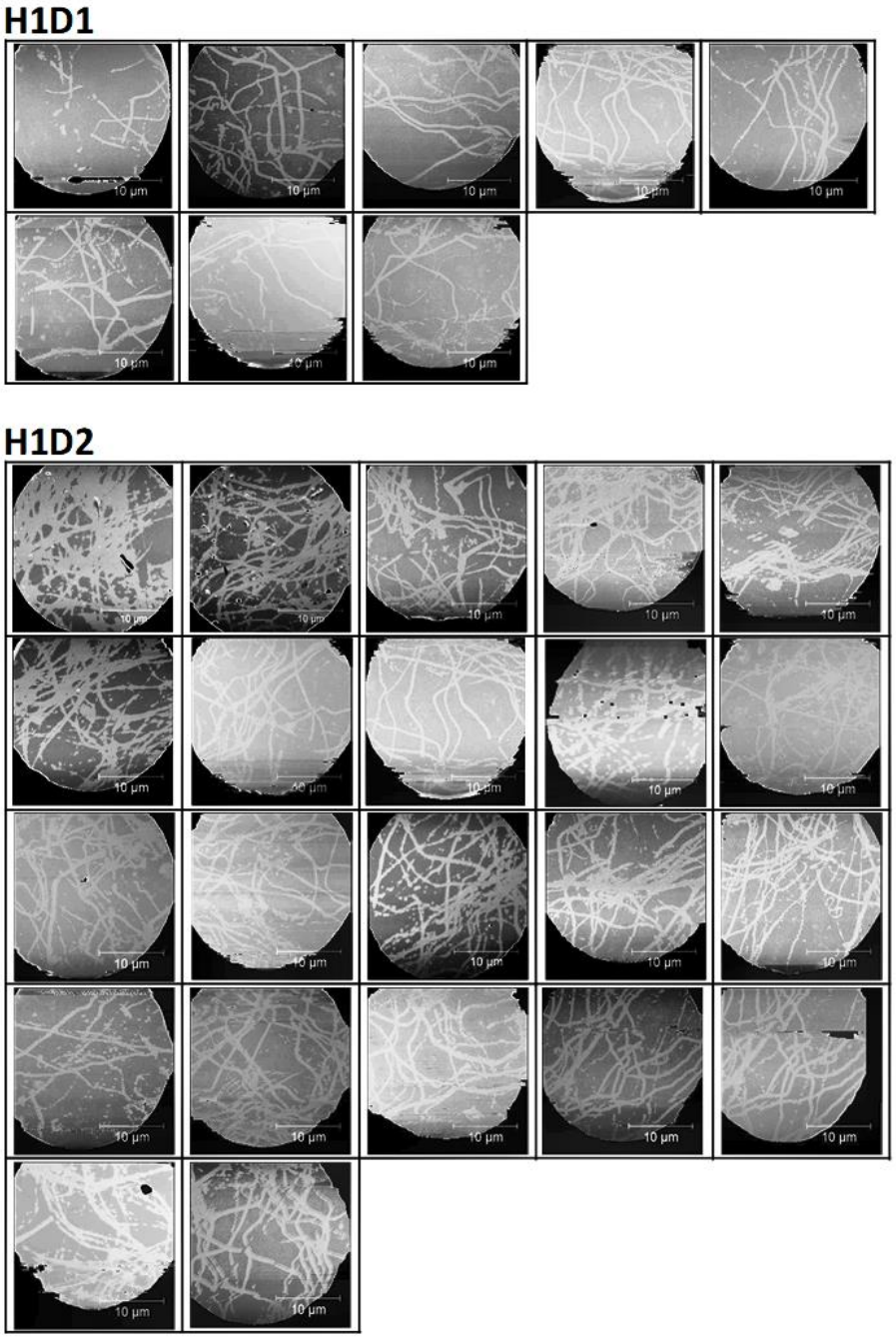

Figure 1. 2D AFM surface profiles of H1D1 and H1D2 CLGNS microelectrodes used for nanostructure coverage and impedance spectroscopy measurements. Height scale similar to the Figure 5.6a-b.

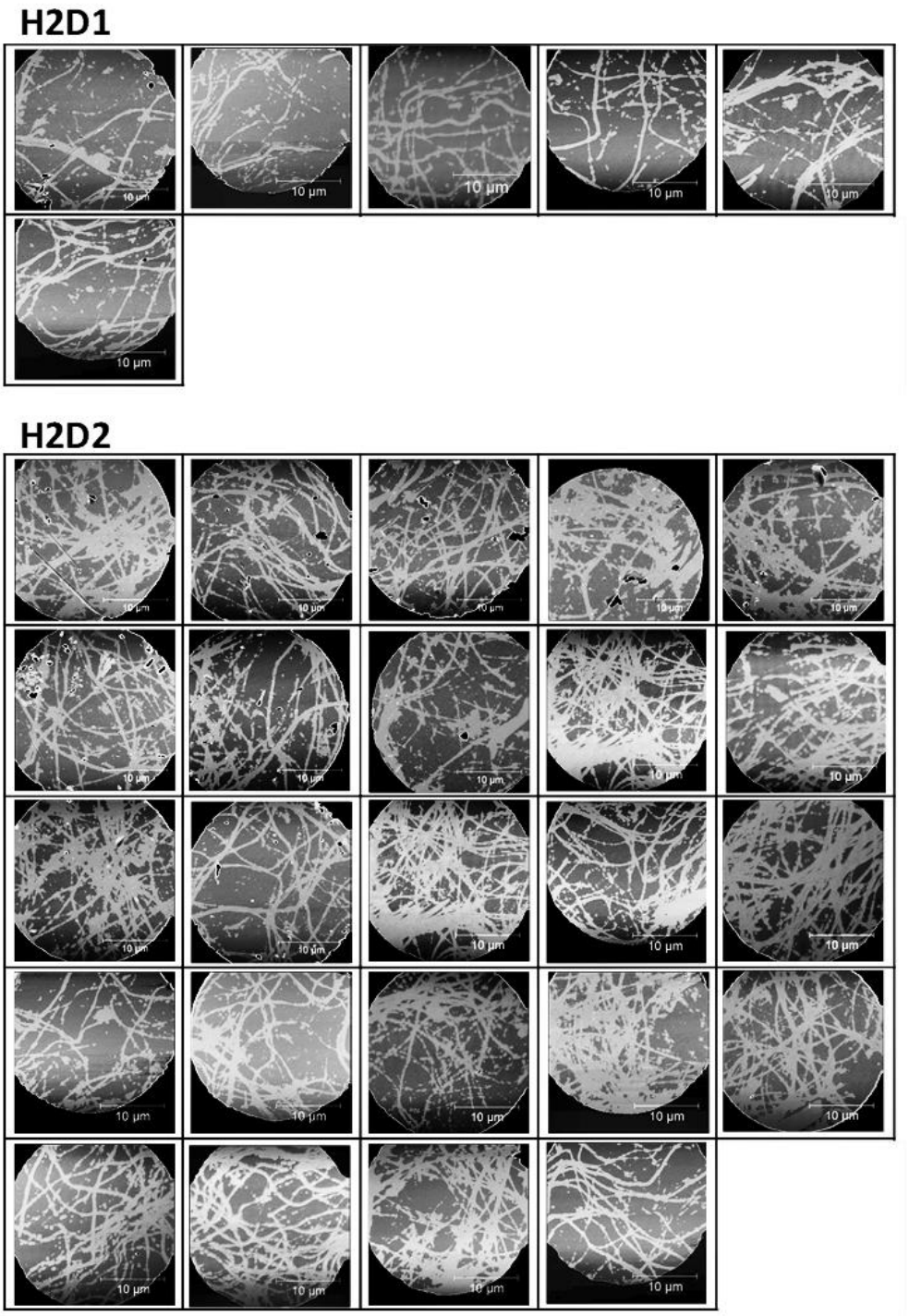

Figure 2. 2D AFM surface profiles of H2D1 and H2D2 CLGNS microelectrodes used for nanostructure coverage and impedance spectroscopy measurements. Height scale similar to the Figure 5.6c-d.

Appendix VII. List of equipment

Name of equipment	Equipment model	Manufacturer
Atomic force microscopy	Dimension IKON	Bruker Corporation
Contact angle measurement	OCA 15	DataPhysics GmbH
Flip chip bonder	T3002-M	Dr. Tresky AG
Fluorescence microscope	DM6 FS	Leica Microsystems Gmbh
Fluorescence microscope	AXIO OBSERVER Z1	Carl Zeiss AG
Hotplate	HP 150	RRT Lanz AG
Impedance tester	MEA-IT60 device	Multichannel Systems GmbH
Mask Aligner	MA/BA 6	Süss Microtec AG
MEA signal recording device	MCS MEAmini2100	Multichannel Systems GmbH
Metal-evaporator	BAK-500	Balzers- Evatec AG
MEA signal generator	60MEA2100-SG	Multichannel Systems GmbH
Nanoimprint Lithography	Eitre 6	Obducat AB
optical microscope	SZH10	Olympus K.K
Oxygen Plasma	Plasma treatment Nano	Diener Plasma GmbH
PECVD	Plasmalab 133	Oxford Instruments PLC
potentiostat	SP200	Biologic SAS
potentiostat	Zennium-X	ZAHNER-Elektrik GmbH & Co. KG
Reactive-ion etching	SI 591 M	SENTECH Instruments GmbH
SEM	Supra 40 Gemini	Carl Zeiss AG
Signal generator	60MEA2100-SG	Multichannel Systems GmbH
Spin-coater	Labspin 8	Süss Microtec AG
wafer Dicer	DAD-2H/6T	Disco Corporation
SEM sputter machine	108 Auto Sputter Coater	Cressington gmbh

Appendix VIII. List of chemicals and materials

Name of equipment	Description/CAS	Manufacturer
3 M Ag/AgCl electrode	6.0733.100	Metroohm GmbH
2'diamidinephenylindole	90229	Merck, S.A. de C.V.
Acetone	67-64-1	Carl Roth Gmbh & Co. Kg
Ag/AgCl pellet electrode	Hybrid Ag-AgCl	Multichannel Systems GmbH
Anti-sticking layer	BGL-GZ-83	PROFACTOR GmbH
Borosilicate glass wafers	Borofloat 33	Siegert Wafer GmbH
Cantilevers AFM	AC240TS-R3	Asylum Research Corporation
Chicken-anti-PGP9.5	ab72910	Abcam PLC
Collagen type I	9007-34-5	Sigma-Aldrich Corporation
Collagenase	5 401 151 001	Roche Holding AG
Diamond blade wafer saw	Nbc-zh 2050	Disco Corporation
DNase	11 284 932 001	Roche Holding AG
Donkey-anti-Chicken 488	703-545-155	Jackson ImmunoResearch
Donkey-anti-Rabbit 594	A-21207	Thermo Fisher Scientific Inc.
Cell culture medium	31331-028	gibco Inc
ECM Gel	E6909	Sigma-Aldrich Corporation
Ethanol	64-17-5	Carl Roth Gmbh & Co. Kg
Ethylene glycol	107-21-1	Carl Roth Gmbh & Co. Kg
Fibronectin	289-149-2	Sigma-Aldrich Corporation
Glutaraldehyde	50-00-0	Carl Roth Gmbh & Co. Kg
Glial marker S100B	ab52642	Abcam PLC
Gloss additive	Glanzzusatz Goldbad SF	Metakem GmbH
Glutaraldehyde	111-30-8	Carl Roth Gmbh & Co. Kg
Glycerol	56-81-5	Carl Roth Gmbh & Co. Kg
Gold electrode	Gold disk Platinum ring	Metroohm GmbH
Gold electrolyte	Goldbad SF	Metakem GmbH
Hydrogen peroxide	7722-84-1	Th. Geyer GmbH & Co. KG.

Hank's balanced salt	(P04-33500	PAN Biotech GmbH
Hexamethyldisilazane	999-97-3	Carl Roth Gmbh & Co. Kg
Hydrochloric acid	7647-01-0	Sigma-Aldrich Corporation
Hydrofluoric acid	7664-39-3	Microchemicals GmbH
Iodine	7553-56-2	Carl Roth Gmbh & Co. Kg
Iso-propyl alcohol	67-63-0	Carl Roth Gmbh & Co. Kg
Laminin	114956-81-9	Sigma-Aldrich Corporation
Nylon filter	Siebgewebe Nylon	Meerwassershop
Phosphate based buffer	7 0011044	Thermo Fisher Scientific Inc.
Poly-D-lysine	27964-99-4	Sigma-Aldrich Corporation
Polydimethylsiloxane	Sylgard 187	Dow Corning Corporation,
Potassium chloride	7447-40-7	Th. Geyer GmbH & Co. KG.
Photoresist	AR-U 4000	Allresist GmbH
Photoresist	AR-P 5910	Allresist GmbH
Photoresist developer	AR 300-26	Allresist GmbH
Photoresist dilutor	AR 300-12	Allresist GmbH
Platinum mesh electrode	929883	Sigma-Aldrich Corporation
Propylene glycol methyl ether acetate (PGMEA)	108-65-6	Sigma-Aldrich Corporation
Silicon wafer	SSP 100	Siegert Wafer GmbH
Silver adhesion glue	H20E-PFC 1OZ	Epoxy Technology, Inc.
Sodium chloride	7647-14-5	Th. Geyer GmbH & Co. KG.
Sulfuric acid	7664-93-9	AppliChem GmbH
Static polymer foil	SoftPress®	Obducat AB
Thermoplastic resist	mR-I 8030 R®	microresist technology GmbH
Thermosetting resist	mR-I 9030 R®	microresist technology GmbH
TRITC-conjugated Phalloidin	90228	Merck, S.A. de C.V.
UV nanoimprint resist	OrmoComp®	microresist technology GmbH
Vinculin monoclonal antibody	90227	Merck, S.A. de C.V.

Appendix IX. List of software

List of software	Name/Version	Manufacturer
Potentiostat software	ThalesXt	ZAHNER-Elektrik GmbH
Potentiostat software	EC-Lab v11.43	Biologic SAS
MEA Impedance tester	MEA-IT V 1.4.18	Multichannel Systems GmbH
AFM data analyzer	Gwyddion V2.55	Czech Metrology Institute
Contact angle measurement	dpiMAX	DataPhysics Instruments GmbH
MEA signal recording	MCS Experimenter V 2.20.0	Multichannel Systems GmbH
MEA signal analyzing software	Multi Channel Analyzer V 2.20.0	Multichannel Systems GmbH
Fluorescence microscopy	LAS X software V 3.7.0.20979	Leica Microsystems Gmbh
Image processing	ImageJ 1.53s	NIH, USA
Statistical analysis	Microsoft Excel 2016	Microsoft Corporation

Appendix X. List of abbreviations

Acronym	Abbreviation
1D	1 dimension
2D	2 dimension
3D	3 dimension
AC	Alternating current
AFM	Atomic force microscopy
ANOVA	Analysis of variance
AP	Action potential
CE	Counter electrode
CLGNS	Collagen-like gold nanostructures
CNS	Central nervous system
CNT	Carbon nanotubes
D1	Low density CLGNS nanostructures
D2	High density CLGNS nanostructures
DAN	Deterministic aperiodic nanostructures
DAPI	DAPI (4',6-diamidino-2-phenylindole)
DAQ	Data acquisition system
DC	Direct current
DI	Distilled water
DIV	Day in vitro
DMEM	Dulbecco’s modified Eagle's medium
ECM	Extracellular matrix
EIS	Electrochemical impedance spectroscopy
FAC	Focal adhesion complex
GTPase	Guanosine triphosphate hydrolase enzymes
H1	CLGNS with 30 nm height
H2	CLGNS with 50 nm height
IC	Integrated circuit
ISFET	Ion-sensitive field-effect transistor
ITO	Indium Tin Oxide ceramic

MEA	Microelectrode array
NIL	Nanoimprint lithography
NS	Nanostructured macroelectrode surface
P2P	Peak-to-peak
PCB	Printed circuit board
PDF	Probability density function
PDMS	Polydimethylsiloxane
PMMA	Poly(methyl methacrylate)
PNS	Peripheral nervous system
PSP	Postsynaptic potentials
RE	Reference electrode
RPM	Revolutions per minute
RMS	Root mean square
SCCM	Standard cubic centimeters per minute
SEM	Scanning electron microscopy
SNR	Signal-to-noise ratio
SpO	Peripheral oxygen saturation electrode
TRITC	Tetramethylrhodamine
US	Unstructured macroelectrode surface
UV	Ultraviolet
WE	Working electrode

Acknowledgements

In this section I would like to briefly thank everyone who have supported me during the course of my doctoral studies. I would firstly like to thank my supervisors at University of Applied Sciences Kaiserslautern, Prof. Dr. Monika Saumer and Prof. Dr. Karl-Herbert Schäfer for giving me the opportunity to work in a scientific multidisciplinary environment. The process of brainstorming, ideation, application and realization of random nanostructures has been a wonderful experience and I would cherish it for the rest of my life. I would also like to thank my supervisor at Saarland University, Prof. Dr. Markus Hoth for giving me the opportunity to matriculate and undertake my doctoral examination. I would the like to thank 'The Federal Ministry of Education and Research, Germany' for providing the financial support to my work at the University of Applied Sciences Kaiserslautern.

I would like to thank the staff and co-workers at the University of Applied Sciences Kaiserslautern who have given me technical and moral support during my doctoral studies. I would firstly like to thank Prof. Dr. rer. nat. Holger Rabe for advising me issues related to electrophysiology. I would also like to thank Prof. Dr. Hans-Jürgen Steffens for advising with topics related to randomness and statistics. I would immensely like to thank Dr. Dominique Decker from the working group of Prof. Monika Saumer. It is safe to say that without your technical guidance, it would have been impossible to have completed my thesis. I would also like to thank Dr. Anette Britz-grell for advising me with her immense knowledge of chemistry. I would then like to Steven Schulte, Negin Jolfaei, Monika Martin and Dr. Manuela Gries from the working group of Prof. Karl-Herbert Schäfer for supporting me with the biological experiments. I would furthermore like to thank Detlev Cassel for preparing my gold substrates and also helping me with all kinds of cleanroom related issues. I would like to formally apologize for crashing different equipment several times during my experiments. I would like to thank Rainer Lilischkis for making the scanning electron microscopy measurements. I would also like to thank Petra Böswald, Heike Müller, Erik Engelmann, Christian Neu, Inge Neu and Peter Molter for helping me out on several occasions in chemistry lab, mechanical workshop, electrical workshop etc.

I would also like to thank my coworker friends for not only supporting me with work related issues but also moral support during the hard times. Michael Goeddel, Antoine Meyszner, Dr. Jessica Weyer, Dr. Walid Munief, Finnmerlin Deckert, Tobias Stephan, Tina Jene, Ian Sachs, Marc Fuhrmann, and others (please forgive me if I have forgotten to mention someone here), I would sincerely like to thank all of you. I finally would like to thank my friends and family from India who have always been there regardless of the situation. This work is dedicated to my father who has unfortunately passed away before he could read my thesis. He could not pursue his doctoral studies but gave me all the support to do so.

Publications

Peer-Reviewed Journal Publications

- Nowduri, B., Schulte, S., Decker, D., Schäfer, K., & Saumer, M. (2020). Biomimetic Nanostructures Fabricated by Nanoimprint Lithography for Improved Cell-Coupling. Advanced Functional Materials, 30(45), 2004227. https://doi.org/10.1002/adfm.202004227
- Nowduri, B., Britz-Grell, A., Saumer, M., & Decker, D. (2023). Nanoimprint lithography-based replication techniques for fabrication of metal and polymer biomimetic nanostructures for biosensor surface functionalization. Nanotechnology, 34(16), 165301. https://doi.org/10.1088/1361-6528/acb35b
- Nowduri, B., Schulte, S., Jolfaei, N. A., Decker, D., Rabe, H., Schäfer, K., & Saumer, M. (2023). Advanced Biomimetic Nanostructured Microelectrode Arrays for Enhanced Extracellular Recordings of Enteric Neurons. Advanced Materials Interfaces, 10(16). https://doi.org/10.1002/admi.202300023
- Schulte, S., Decker, D., Nowduri, B., Gries, M., Christmann, A., Meyszner, A., Rabe, H., Saumer, M., & Schäfer, K.-H. (2024). Improving morphological and functional properties of enteric neuronal networks in vitro using a novel upside-down culture approach. American Journal of Physiology-Gastrointestinal and Liver Physiology, 326(5), G567–G582. https://doi.org/10.1152/ajpgi.00170.2023

Conference Publications

- Nowduri, B., Britz, A., Schaefer, K. H., & Saumer, M. (July 4-6 2018, Reutlingen Germany). Fabrication of random nanostructured interfaces with nanoimprint lithography and porous alumina. 11th International Meeting on Substrate Integrated Microelectrode Arrays.
- Nowduri, B., Schulte, S., Jolfaei, N. A., Decker, D., Rabe, H., Schäfer, K., & Saumer, M. (July 6-8 2022, Tübingen Germany). Collagen-like gold nanostructures on microelectrodes promote neuronal adhesion and growth, 13th International Meeting on Substrate Integrated Microelectrode Arrays.
- Nowduri, B., Schulte, S., Decker, D., Schäfer, K., & Saumer, M. (September 19-23 2022, Leuven Belgium). Fabrication of metal and polymer biomimetic nanostructures replicating extracellular matrix biomolecules with nanoimprint lithography, 48th international conference on Micro and Nano Engineering - Eurosensors (MNE-ES).
- Nowduri, B., Britz, A., Henschke, R., Schaefer, K. H., & Saumer, M. (June 24 – 27, 2024, Lund Sweden) Nanostructuring flexible polyimide surfaces with nanoimprint lithography for biointerface applications. 23nd International Conference on Nanoimprint and Nanoprint Technologies.